Benchtop NMR Spectroscopy in Process Engineering

Vom Fachbereich Maschinenbau und Verfahrenstechnik

der Rheinland-Pfälzischen Technischen Universität

Kaiserslautern-Landau

zur Verleihung des akademischen Grades

Doktor-Ingenieur (Dr.-Ing.)

genehmigte

Dissertation

von

M.Sc. Johnnie The Phuong

aus Ludwigshafen am Rhein

Danksagung

Die vorliegende Arbeit entstand während meiner Tätigkeit als wissenschaftlicher Mitarbeiter am Lehrstuhl für Thermodynamik (LTD) der Rheinland-Pfälzischen Technischen Universität Kaiserslautern-Landau (ehemals Technische Universität Kaiserslautern). An dieser Stelle möchte ich mich bei allen Personen bedanken, die zum Erfolg dieser Arbeit beigetragen haben.

An erster Stelle möchte ich mich herzlichst bei meinem Doktorvater Prof. Dr.-Ing. Hans Hasse bedanken. Durch seinen offenen und ehrlichen Führungsstil fand ich ein äußerst kollegiales Arbeitsumfeld vor, in dem Eigeninitiative sowie Kreativität gefördert wurden. In dieser Atmosphäre konnte ich regelrecht aufblühen. Ich bedanke mich für die zahlreichen fruchtbaren Diskussionen, das von ihm erworbene Praxiswissen, die Möglichkeiten und Freiräume, die er mir gegeben hatte, und vor allem für das entgegengebrachte Vertrauen.

Ein herzlicher Dank gilt meiner Teamleiterin und Mentorin Dr. rer. nat. Kerstin Münnemann. Ihr ebenfalls offener, humorvoller und vertrauensvoller Führungsstil hat dazu beigetragen, dass ich trotz der Strapazen, die eine Promotion mit sich bringt, jeden Tag mit Spaß und Freude zur Arbeit gehen konnte. Ich habe es sehr geschätzt, dass ich mit ihr nicht nur über fachliche, sondern auch über außerfachliche Themen diskutieren konnte - und das jederzeit, wenn Bedarf bestand. Sie hat mir sehr viele Freiheiten gelassen und mich stets unterstützt, ohne die die vorliegende Arbeit nicht möglich gewesen wäre. Ich danke ihr sehr für die tolle Zusammenarbeit und die zahlreichen Erfahrungen.

Prof. Dr. Jan Korvink danke ich nicht nur für die Begutachtung der Arbeit, sondern auch für die Möglichkeiten, die er mir in dem von ihm geleiteten SFB HyPERiON geboten hat. Bei Prof. Dr.-Ing. Erik von Harbou bedanke ich mich für die Übernahme des Prüfungsvorsitz, besonders aber dafür, dass er mich letztendlich über die Betreuung meiner Masterarbeit an den LTD gebracht und mich für eine Promotion begeistert hat.

An dieser Stelle möchte ich mich auch bei den Projektpartnern bedanken, die ich während der Promotion kennenlernen durfte. Ich danke hierbei den Kolleginnen und Kollegen des SFB HyPERiON, des Weincampus Neustadt, der Universität Nantes, Prof. Daniel Holland sowie der Firma Magritek für die tolle Zusammenarbeit. Mein Dank

mich in schwierigen Zeiten aufgemuntert und mich immer wieder motiviert hast, weiter zu machen. Wir haben schon so viel gemeinsam erlebt und gemeistert. Wir sind ein sehr gutes und eingespieltes Team geworden. Ich hoffe sehr, dass wir noch viele weitere Abenteuer und Herausforderungen gemeinsam meistern und vor allem viele schöne Momente erleben werden. Danke Katrin!

Ludwigshafen am Rhein, November 2024

Johnnie The Phuong

Abstract

Nuclear magnetic resonance (NMR) is a highly attractive powerful method that enables non-invasive analysis of complex mixtures without requiring tedious calibration procedures. Benchtop NMR spectrometers are small, robust, and inexpensive, which makes them especially suited for process and reaction monitoring. However, the low magnetic field strength and the small premagnetization volume of these spectrometers are major drawbacks, resulting in low spectral resolution, peak overlap, low signal intensities, and insufficient magnetization build-up in flowing liquids. As a consequence, the quantitative analysis of complex mixtures is not always possible by benchtop NMR spectroscopy. This thesis tackles these challenges and introduces methods that extend the applications of benchtop NMR spectroscopy in process engineering. The first method is a model-based approach for resolving overlapping peaks in ^{1}H NMR spectra of complex multi-component mixtures. This method has been successfully tested by online monitoring of a wine fermentation. The second method uses dedicated NMR pulse sequences for ^{1}H-^{13}C polarization transfer and enables an improved quantitative analysis of mixtures in particular in flow experiments based on ^{13}C NMR spectroscopy. ^{13}C NMR spectroscopy is advantageous as the high chemical shift dispersion prevents peak overlap, albeit at the expense of low signal-to-noise ratio (SNR) and extended experimental time. The NMR pulse sequences provide an elegant solution to achieve ^{13}C signal enhancement and to shorten the experimental time by exploiting the higher polarization and favorable spin-lattice relaxation of protons. The method was also successfully applied for measuring diffusion coefficients by NMR. The third method uses the hyperpolarization technique Overhauser Dynamic Nuclear Polarization (ODNP) to significantly enhance ^{1}H and ^{13}C NMR signals. This enables the detection and quantification of components at low concentrations or at high flow velocities with just a single scan. These methods can also be applied together and significantly extend the NMR toolbox for process engineering and other applications.

Kurzfassung

Die Kernspinresonanz (NMR) ist eine äußerst attraktive und leistungsstarke Methode, die eine nicht-invasive Analyse komplexer Mischungen ermöglicht, ohne dass langwierige Kalibrierungsverfahren erforderlich sind. Benchtop NMR Spektrometer sind klein, robust und kostengünstig, was sie besonders für die Prozess- und Reaktionsüberwachung geeignet macht. Die geringe Magnetfeldstärke und das kleine Vormagnetisierungsvolumen dieser Spektrometer sind jedoch ein großer Nachteil, der zu geringer spektraler Auflösung, Peaküberlappung, geringen Signalintensitäten und unzureichendem Magnetisierungsaufbau in fließenden Proben führt. Infolgedessen ist die quantitative Analyse komplexer Mischungen mit der Benchtop NMR Spektroskopie nicht immer möglich. In dieser Arbeit werden diese Probleme angegangen und Methoden vorgestellt, die die Anwendungsmöglichkeiten der Benchtop NMR Spektroskopie in der Verfahrenstechnik erweitern. Die erste Methode ist ein modellbasierter Ansatz zur Auflösung überlappender Peaks in ^{1}H NMR-Spektren komplexer Mehrkomponentenmischungen. Diese Methode wurde bei der Online-Überwachung einer Weinfermentation erfolgreich getestet. Die zweite Methode verwendet spezielle NMR-Pulssequenzen für den ^{1}H-^{13}C-Polarisationstransfer und ermöglicht eine verbesserte quantitative Analyse von Mischungen, insbesondere in Strömungsexperimenten auf der Grundlage der ^{13}C NMR Spektroskopie. Die ^{13}C NMR Spektroskopie ist vorteilhaft, da die hohe Dispersion der chemischen Verschiebung eine Überlappung der Peaks verhindert, wenn auch auf Kosten eines geringen Signal-Rausch-Verhältnisses (SNR) und verlängerte Versuchsdauer. Die NMR-Pulssequenzen bieten eine elegante Lösung, um das ^{13}C-Signal zu verstärken und die Versuchszeit zu verkürzen, indem die höhere Polarisation und die kurze Spin-Gitter-Relaxation der Protonen ausgenutzt werden. Die Methode wurde auch erfolgreich für die Messung von Diffusionskoeffizienten mittels NMR eingesetzt. Die dritte Methode nutzt die Hyperpolarisationstechnik Overhauser Dynamic Nuclear Polarization (ODNP), um die ^{1}H und ^{13}C NMR-Signale deutlich zu verstärken. Dies ermöglicht den Nachweis und die Quantifizierung von Komponenten in niedrigen Konzentrationen oder bei hohen Flussgeschwindigkeiten mit nur einem einzigen Scan. Diese Methoden können auch gemeinsam angewendet werden und erweitern den NMR-Werkzeugkasten für die Verfahrenstechnik und andere Anwendungen erheblich.

Contents

List of Symbols

Latin symbols

a	Parameter a
B	Magnetic field strength
b	Parameter b
c	Molar concentration
c	Parameter c
d	Diameter
d	Time delay
D	Self-diffusion coefficient
E	Signal enhancement
f	Function
G	Magnetic field gradient
i	Component
I	Signal integral
l	Length
j	Component
J	Scalar coupling constant
m	Mass
M	Magnetization
M	Molar mass
M	Number of data points
n	Number of scans
N	Number of nuclei
p	Pressure
P	Power
S	Relative signal
t	Time
T	Temperature
T_1	Spin-lattice relaxation time
T_2^*	Spin-spin relaxation time

$\dot{V}$	Flow rate
V	Volume
v	Flow velocity
w	Weight
x	Mole fraction

Subscripts and Superscripts

0	Longitudinal
0	Native
1	Scalar coupling order 1
1	Spin-lattice
2	Spin-spin
*	Spin-spin with consideration of magnetic field inhomogenity
^{13}C	^{13}C Carbon
^{1}H	Proton
ACN	Acetonitrile
ACT	Acetone
C,H	Scalar coupling between carbon and proton
CF	Chloroform
coil	NMR coil
corr	Correlation
d	Delay
DC	Detection coil
DMSO	Dimethyl sulfoxide
DV	Detection volume
DX	1,4-Dioxane
EF	Ethyl formate
eff	Effective
EtOH	Ethanol
flow	Measurement of sample in continuous-flow
grad	Gradient
i	Component
I	Part I
II	Part II
j	Component
k	Data point
MeOH	Methanol

method	Method
ODNP	Overhauser dynamic nuclear polarization
PrOH	1-Propanol
ref	Reference
reference	Reference
rel	Relative
RM	Radical matrix
stationary	Measurement of sample at rest
thermal	Thermally equilibrated signal
TL	Transportation line
total	Total
W	Water
z	z-Direction

Greek symbols

δ	Chemical shift
Δ	Deviation
δ	Gradient pulse duration
Δ	Diffusion time
Δ	Difference
Δ	Error
ϵ	Void fraction
γ	Gyromagnetic ratio
ν	Frequency
τ	Gradient ramp time
τ	Residence time
Θ	Relative time
θ	Temperature

Abbreviations

ACN	Acetonitrile
Acq	Acquisition
ACT	Acetone
BT	Benchtop

corr	Correlation
CDEC	NMR experiment with ^{13}C decoupling
CF	Chloroform
DC	Detection coil
dDNP	Dissolution DNP
Dec	Proton decoupling
DECRA	Direct exponential curve resolution algorithm
DEPT	Distortionless enhancement by polarization transfer
DMSO	Dimethyl sulfoxide
DOSY	Diffusion ordered spectroscopy
DV	Detection volume
DX	1,4-Dioxane
EF	Ethyl formate
EtOH	Ethanol
FB	Fixed bed
FID	Free induction decay
FT-IR	Fourier transform infrared
GC-MS	Gas chromatography coupled to mass spectrometry
GSD	Global spectrum deconvolution
HF	High-field
HPLC	High pressure liquid chromatography
HSQC	Heteronuclear single quantum coherence spectroscopy
INEPT	Insensitive nuclei enhanced by polarization transfer
LOO	Leave-one-out
MAE	Mean absolute error
MCR	Multivariate curve resolution
MeOH	Methanol
MW	Microwave
NMR	Nuclear magnetic resonance
ODNP	Overhauser dynamic nuclear polarization
PAT	Process analytical tool
PCA	Principal component analysis
PEEK	Polyether ether ketone
PENDANT	Polarization enhancement nurtured during attached nucleus testing
PENPFG	Pulsed field gradient experiment combined with PENDANT NMR sequence
PFG	Pulsed field gradient
PFGSTE	Pulsed field gradient stimulated spin echo NMR experiment
PHIP	Parahydrogen induced polarization
PLS	Partial least squares

PRE	Paramagnetic relaxation enhancement
PrOH	1-Propanol
QM	Quantum mechanical
ref	Reference
RM	Radical matrix
RMSE	Root mean squared error
SABRE	Signal Amplification by Reversible Exchange
SCORE	Speedy component resolution
SE	Spin echo
SGP	Short gradient pulse
SINC	Simultaneous phase and baseline correction of NMR signals
SNR	Signal-to-noise ratio
STE	Stimulated spin echo
TL	Transportation line
UF	Ultrafast
UF-TOC	Ultrafiltration - total organic carbon
UV	Ultraviolet
UV-vis	Ultraviolet visible
W	Water

1 Introduction

In process engineering, time resolved information about chemical and biological reactions are crucial. Key questions that often arise in this context are: What is the current progress of the reaction? What are the conversion, selectivity and the yield? Are there any by-products that need to be considered? The answers to these questions are needed for designing future processes as well as for the optimization of existing plants.

Nuclear magnetic resonance (NMR) is a highly attractive and powerful analytical tool for reaction and process monitoring that can be used to address these important questions by combining several advantages: processes can be elucidated non-invasively, a tedious calibration is not required, and an application for continuous-flow analysis in a bypass setup is possible [1–11]. Therefore, NMR is widely used in science, medicine, and industry. However, conventional NMR spectrometers are expensive and require cryogenic media for cooling the superconducting magnets and extensive training of the operating personnel. This limits the use of NMR in process engineering to well-equipped laboratories with the appropriate infrastructure.

The advent of benchtop NMR spectrometers equipped with permanent magnets has substantially broadened the application horizon of NMR. These spectrometers are compact, robust, and affordable. In addition, benchtop NMR spectrometers are easy to maintain and to operate [12–21]. These features make them attractive as process analytical tools (PAT) in the industry [22]. Many studies have demonstrated the usefulness of benchtop NMR for solving process engineering problems [23–36]. However, the comparatively low magnetic field strength (current benchtop NMR spectrometers have a magnetic field strength of only up to 2.5 T) results in a low spectral resolution as well as in a low signal-to-noise ratio (SNR), which are major drawbacks and often result in strong peak overlap in ^{1}H NMR spectra and long times for experiments as many scans need to be acquired. The long experimental times are particularly problematic for benchtop ^{13}C NMR spectroscopy because the signal intensities are extremely low, making benchtop ^{13}C NMR spectroscopy unsuitable for process monitoring. In addition, the compact design of benchtop NMR spectrometers causes premagnetization issues when samples are analyzed in continuous-flow.

The present thesis contributed to overcoming these issues by the development and testing of new methods that faciliate the application in benchtop NMR spectroscopy in process engineering and related fields. The thesis is organized as follows:

In Chapter 2, benchtop NMR spectroscopy is used to monitor a wine fermentation process. However, the low spectral resolution of benchtop ^{1}H NMR spectroscopy and the complexity of the fermentation media hinder the direct quantification of important wine parameters and, thus, prevent its widespread use as an analytical tool in wineries. It is shown that these problems can be solved using model-based data processing. In a first step, the accuracy of this approach was evaluated by analyzing gravimetrically prepared test mixtures representing different fermentation stages. In a second step, benchtop ^{1}H NMR spectroscopy combined with model-based data processing was used for the online monitoring of real fermentation media. Wine fermentation processes with different feed strategies (batch and fed-batch) were investigated and compared and the evolution of important wine constituents as well as effects caused by the different feeding strategies were monitored.

In Chapter 3, the problem of peak overlap in benchtop ^{1}H NMR spectroscopy is addressed by applying ^{13}C NMR spectroscopy that exhibits a much larger chemical shift dispersion. However, low signal intensities and problems with the premagnetization of flowing samples in ^{13}C NMR hamper its use in process monitoring. In this work, it is shown that both problems can be overcome by using ^{1}H-^{13}C polarization transfer methods. Two ternary test mixtures (one with overlapping peaks in the ^{1}H NMR spectrum and one with well-resolved peaks, which was used as a reference) were studied with a 1 T benchtop NMR spectrometer using the polarization transfer sequence PENDANT. The mixtures were quantitatively analyzed by PENDANT-enhanced ^{13}C NMR experiments in stationary as well as in flow experiments, and the results were compared to the gravimetric sample preparation and with results of standard benchtop ^{1}H and ^{13}C NMR spectroscopy without polarization transfer. Furthermore, as a test for a process monitoring application, continuous dilution experiments were carried out and the composition of the mixture was monitored by benchtop ^{13}C NMR spectroscopy with PENDANT using a flow setup.

In Chapter 4, ^{1}H-^{13}C polarization transfer methods are applied for the determination of self-diffusion coefficients in liquids, since this important physical property can be measured with high precision by NMR. In most cases, ^{1}H NMR spectroscopy is used to determine self-diffusion coefficients but the signals of mixtures in ^{1}H NMR spectra often overlap. In contrast, the sensitivity of ^{13}C NMR is significantly lower than that of ^{1}H NMR spectroscopy leading to very long measurement times, which makes diffusion coefficient measurements based on ^{13}C NMR practically infeasible with benchtop NMR spectrometers. To circumvent this problem, two known pulse sequences were combined,

one for polarization transfer from ^{1}H to the ^{13}C nuclei (PENDANT) and one for the measurement of diffusion coefficients (PFG). The new method (PENPFG) was used to measure the self-diffusion coefficients of three pure solvents (acetonitrile, ethanol, 1-propanol) as well as in their binary mixtures and the ternary mixture at various compositions. For comparison, measurements of the same systems were also carried out with a standard PFG-NMR routine on a high-field NMR instrument.

In Chapter 5, the problem of insufficient premagnetization of flowing samples and low signal intensities is addressed by hyperpolarization by Overhauser Dynamic Nuclear Polarization (ODNP). ODNP operates on short time scales and results in strong ^{1}H and especially in very strong ^{13}C signal enhancements. Benchtop ^{13}C NMR spectra with ODNP enhancement acquired in continuous-flow are reported. Two ODNP approaches were investigated: direct ODNP, which transfers the polarization of unpaired electrons to ^{13}C nuclei via direct hyperfine coupling, and indirect ODNP, in which the electron polarization is first transferred to ^{1}H nuclei before a polarization transfer pulse sequence finally transfers the polarization to the ^{13}C nuclei. Experiments were carried out for three pure solvents and one mixture for different flow rates.

Finally, in Chapter 6, the hyperpolarization technique ODNP was used for quantitative analysis of binary mixtures. ODNP has never been used before for the quantitative analysis of mixtures - probably because NMR signal enhancements by ODNP can vary greatly for different molecules, making quantitative analysis of mixtures difficult. In this work, it is shown that this problem can be solved by a robust calibration: three binary mixtures were studied as test cases in a wide range of concentrations by ODNP-enhanced ^{1}H and ^{13}C NMR spectroscopy in continuous-flow experiments with a benchtop NMR spectrometer using a new tailored calibration procedure.

2 Online Monitoring of Fermentation Processes

2.1 Introduction

Wine production is among the oldest production technologies used by mankind and continues to evolve quickly. In 2023 the global wine market size was about 429 billion US-\$ [37]. The quality of the wine obviously depends critically on the grapes, but also on their processing, in which the fermentation plays a key role. For optimization and decision making during wine production, it is highly desirable to have reliable, informative, and quick methods for assessing the quality of the grape must obtained from pressing (the feed of the fermentation) and for monitoring the fermentation itself [38, 39].

Several analytical technologies are available, ranging from simple sensors for pH measurement and portable refractometers for juice density determination to more sophisticated methods such as high pressure liquid chromatography (HPLC) [40], gas chromatography coupled to mass spectrometry (GC-MS) [41, 42] and optical spectroscopy. For process monitoring applications, optical spectroscopy is established. Different techniques have been applied, such as Raman, UV-Vis and, in particular, Fourier transform infrared (FT-IR) spectroscopy [43–45]. Many studies have shown that FT-IR spectroscopy is able to monitor the entire winemaking process with little sample preparation; from the analysis of grape must, to the quantification of compounds during the vinification step, to the examination of finished wines [46–54]. However, FT-IR has some major drawbacks: The strong absorption bands of water in the IR spectrum cause problems with the sensitivity and the analysis of highly diluted compounds [44]; peak overlap is common and hinders quantification, and, last but not least, different components have different extinction coefficients, that also depend on the composition of the mixture, which makes a tedious calibration necessary [55]. The latter is especially problematic when analyzing temporal changes in the composition as during fermentation. To address the problems with peak overlap FT-IR data analysis requires statistical methods (chemometrics) such as Partial Least Squares (PLS) regression and Principal Compo-

nent Analysis (PCA) that require expert knowledge and have limitations for strongly overlapping peaks [55–58]. These drawbacks prevent the widespread use of FT-IR as an online/inline PAT in large wineries.

NMR spectroscopy is an excellent tool for reaction and process monitoring because it combines several advantages: it allows a non-invasive quantification of (even highly dilute) components in a complex mixture without prior external calibration, does not require extensive sample preparation and can be used in a bypass configuration [8]. Since many years, high-field NMR spectroscopy has been widely used to elucidate the composition of wine and other beverages, revealing details that even can be used to reliably detect product fraud [59–73]. Suppliers of NMR spectrometers offer automated wine profiling packages based on high-field NMR measurements. However, high-field NMR spectrometers have high acquisition and operating costs and are basically only used by specialized research and analytical laboratories. They are not suited for field studies.

The advent of compact, robust and comparatively inexpensive benchtop NMR spectrometers using permanent magnets has greatly extended the application field of NMR spectroscopy. However, the relatively low magnetic field strength of benchtop NMR spectrometers results in low spectral resolution, which causes significant peak overlap in ^{1}H NMR spectra of complex mixtures, such as wine or fruit juice, hindering quantitative analysis by conventional direct peak integration. The use of benchtop ^{13}C NMR spectroscopy, which offers a much higher chemical shift dispersion, is not an alternative in this case because of its low sensitivity hindering the detection of highly diluted species, that are of interest here, in a reasonable measurement time. However, benchtop NMR spectroscopy has already been used for online monitoring of fermentation processes from bioprocess engineering [24, 34, 36, 74], in which the systems were not as complex as wine and the task was the quantification of some key compounds and not a comprehensive analysis. In these studies, calibration procedures and internal standards were employed to enable quantitative analysis.

In recent work, Matviychuk et al. have developed a model-based data processing approach that addresses the issue of peak overlap in ^{1}H NMR spectroscopy by applying quantum mechanical models [75–77]. The quantum mechanical models are formulations that basically consist of only a few NMR parameters: the chemical shifts and the J-coupling constants, which can be determined either experimentally or, in particular, can be obtained from NMR databases, since these parameters are field invariant. The models of each individual component are then used to predict the NMR peaks, including the characteristic peak patterns of each species, and the corresponding ^{1}H NMR spectrum of the complex mixture as a whole. The model-based data processing approach incorporates an algorithm that uses a Bayesian formulation to robustly fit the generated

peaks to the experimental ^{1}H NMR spectrum, enabling the automated quantification of the complex mixture. This approach has been successfully applied to the reaction monitoring of the glycerol esterification using benchtop NMR spectrometer, demonstrating its ability to quantify a time-varying but less complex mixture than wine or grape must [78].

In another work, Matviychuk et al. [79] have successfully demonstrated that the model-based data processing approach can also be used to analyze wine and other beverages (samples at rest) with benchtop ^{1}H NMR spectroscopy. A software package with a graphical user interface has been developed that contains the quantum mechanical formulations of a large number of wine ingredients and can automatically identify as well as quantify the components. This software package will be referred to as AutoWine-tool. Quantitative analysis of the mixture required two ^{1}H NMR experiments, both with ^{13}C decoupling and one also using water presaturation. Maleic acid was added to adjust the pH, and potentially act as an internal standard. These measurements were able to quantify the major components of wine. For accurate quantification of the minor constituents, Matviychuk et al. [79] performed measurements on dry extracts, i.e. samples from which the ethanol was removed by evaporation and reconstituted in deuterated water. The requirement to add maleic acid and produce a dry extract mean the previously published method is not suitable for online monitoring of a fermentation process.

In this work, we explore the application of benchtop ^{1}H NMR spectroscopy together with the AutoWine-tool for online monitoring of wine fermentation - without using an internal standard and without the need to study a dry extract. The AutoWine-tool was used to quantify a large number of major (glucose, fructose, ethanol, glycerol, and malic acid) and of minor components (acetic acid, citric acid, and succinic acid) encountered in wine fermentation. The method was evaluated on gravimetrically prepared test mixtures representing different compositions similar to those found during a wine fermentation. The measurements were carried out by ^{1}H NMR spectroscopy with ^{13}C decoupling without water presaturation. Hence, the experimental workload was greatly simplified when compared to the previously published method.

Two different fermentation strategies were compared with each other: the standard batch fermentation and a fed-batch fermentation. In the latter strategy, grape juice is stepwise added to the bioreactor. This reduces the concentration of acetic acid, since the yeast (*Saccharomyces cerevisiae*) is less exposed to osmotic stress due to the reduced sugar concentration as shown by Frohmann & Orduña [80]. The goal was to find out whether the new analytical method can also be used to study kinetic processes during wine fermentation.

2.2 Experimental Section

2.2.1 Chemicals & Sample Preparation

An overview of the chemicals that were used for the preparation of the test mixtures is given in Table 1. Ultrapure water with a resistivity of 18.2 MΩ cm was produced in a Starpure's OmniaPure UV/UF-TOC water treatment system. For the fermentation experiments sterilized grape juice (Riesling of 2021 from the region Palatinate, Germany, prepared by Südpfalz Saft) was used. Yeast (*Sacharomyces cerevisiae*, Lalvin ICV D47, lyophilized) was purchased from Lallemand. For nitrogen supply during the fermentation, yeast nutrient Vitamon Combi of Erbslöh (containing $(NH_4)_2HPO_4$ and thiaminhydrochloride) was used.

Table 1: Chemicals used in this work including the suppliers and the purities as specified by the suppliers.

Chemical	Supplier	Purity
Acetic Acid	Sigma-Aldrich	≥ 99.7%
Citric Acid	Acros Organics	≥ 99.5%
Ethanol	Merck	≥ 99.9%
D(-)-Fructose	Tokyo Chemical Industry	≥ 99.0%
D(+)-Glucose	Carl Roth	ACS grade
Glycerol	Thermo Scientific	≥ 99.6%
DL-Malic Acid	Sigma Aldrich	≥ 99.0%
Maleic Acic	Carl Roth	≥ 99.0%
Succinic Acid	Tokyo Chemical Industry	≥ 99.0%

Three test mixtures of different compositions with a volume of 200 ml containing water, glucose, fructose, ethanol, glycerol, acetic acid, citric acid, malic acid, and succinic acid were prepared gravimetrically using a laboratory balance (XS603S DeltaRange, Mettler Toledo, accuracy: ± 0.001 g). The composition of these mixtures was chosen to resemble those encountered in wine fermentations. The mixtures are referred to as Mixture 1 (start of fermentation, high sugar concentration), Mixture 2 (middle of fermentation) and Mixture 3 (end of fermentation, high ethanol concentration). The density of each mixture (at 26.5 °C, the operating temperature of the benchtop NMR spectrometer) was determined by a densimeter (Anton Paar SVM 3000, validated on water at 20 °C, uncertainty: ± 1 g l^{-1} [81]) in order to calculate the concentration in

g l⁻¹ of the components. A detailed specification of the composition of these mixtures is given in the Appendix A. The uncertainty of the concentration of each component in the mixtures is about ±1 %. For the study of each mixture, three NMR sample tubes of each mixture (with an outer diameter of 5 mm, purchased from Magritek) were prepared each containing a volume of 0.7 ml.

2.2.2 Hardware and Experimental Procedure

2.2.2.1 Measurement of Synthetic Wine Mixtures

^{1}H NMR experiments with ^{13}C decoupling were performed on a Spinsolve 80 Carbon Ultra benchtop NMR spectrometer (Magritek) with a magnetic field strength of 1.88 T, corresponding to a ^{1}H Larmor frequency of 80 MHz. The pulse sequence is available in Magritek's Spinsolve pulse sequence library. The ^{1}H NMR experiments were conducted with the following parameters: 6.4 s acquisition time, 16 k data points, 90° excitation pulse, and 16 scans. The repetition time was set to 60 s to ensure full premagnetization of all components for quantitative analysis. The obtained ^{1}H NMR spectra were analyzed with the AutoWine-Tool (version 0.1.0) to determine the composition of the sample mixtures. Details regarding the quantum mechanical formulations and parameters, the fitting algorithm and the error calculations are given in the works of Matviychuck et al. [75–77, 79]. All three sample tubes of a mixture were analyzed to calculate mean values and standard deviations which are displayed as error bars in the corresponding figures. The results were compared to the known concentrations of the gravimetrical sample preparation which are considered as the ground truth.

2.2.2.2 Online Monitoring of Wine Fermentation

Figure 1 shows a scheme of the laboratory scale fermentation unit, in which the batch and fed-batch experiments were carried out. The fermentation was performed in a custom made double jacketed glass reactor with a total volume of 250 ml. The fermentation temperature was controlled with a thermostat (F25-HE, Julabo). The temperature and pH value of the fermentation broth were measured with a combined sensor (InPro3100/225/PT100, Mettler Toledo). An outlet for the CO_2 produced during the fermentation was provided by a fermentation airlock (filled with water), which also prevented contact with ambient air to keep anaerobic conditions in the fermenter. To provide additional grape juice in the fed-batch experiments, the reactor was connected to a dosing pump (765 Dosimat, Metrohm) that fed fresh juice from a storage container with a volume of 1 l into the reactor. The fermenter broth was continuously stirred with a magnetic stirrer (Topolino, IKA-Werke).

The composition in the fermenter was monitored by benchtop ^{1}H NMR spectroscopy. The NMR spectrometer (Spinsolve 80 Carbon Ultra, Magritek) was equipped with a glass flow cell (Spinsolve Reaction Monitoring Kit RM, Magritek) which had an inner diameter of 4 mm in the active region and an inner diameter of 1 mm at the inlet and outlet. The NMR spectrometer was connected to the fermenter by a sample loop driven by a peristaltic pump (Minipuls 3, Gilson). A 10 µm solvent filter (Upchurch Scientific) at the inlet of the loop was used to retain solids. A microfluidic bubble trap (Diba Omnifit) for CO_2 release was mounted in the sample loop of the benchtop NMR spectrometer. All components of the setup were connected with PEEK and PTFE capillaries (inner diameter 1.0 mm).

The flow rate in the sample loop was set to 0.3 ml min^{-1} and was permanently activated in all experiments, corresponding to a mean transport time from the fermenter to the active volume of 14 min, for details see Supporting Information. The large time delay is no problem as the fermentation is slow. The chosen flow rate is low enough to ensure a sufficient premagnetization for the quantitative analysis of the components as well as to prevent flushout of the sample from the active region during NMR acquisition.

Batch and fed-batch experiments were initiated by adding 0.06 g of yeast to 50 ml grape juice provided in the reactor. The grape juice was maintained at 35 °C and was stirred for at least 20 min to dissolve and activate the yeast before lowering the temperature to a fermentation temperature of 20 °C. Additional grape juice was added to the reactor: 150 ml for batch mode and 50 ml for fed-batch mode. After stirring, the sample loop was switched on and a script for automatic ^{1}H NMR spectra acquisition (^{13}C decoupling, 3.2 s acquisition time, 16 k data points, 90° excitation pulse, 16 scans, repetition time 15 s) was started on the benchtop NMR spectrometer, acquiring a ^{1}H NMR spectrum every 30 min. After 48 h of fermentation, yeast nutrient (0.01 g) was added to the reactor. In the fed-batch experiments, after an initial fermentation time of 48 h, 100 ml of additional grape juice was fed into the reactor in 4 tranches every 24 h. All fermentations were stopped after 200 h. The batch experiment was repeated once, the fed-batch experiment was repeated twice with the identical parameters to verify the reproducibility of the experiments.
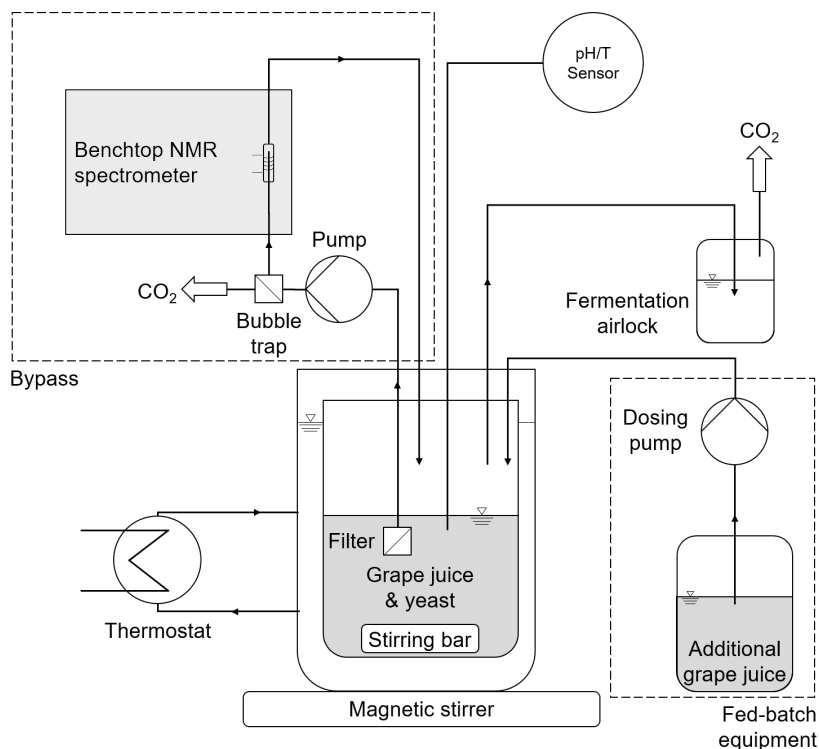
Figure 1: Scheme of the experimental setup for fermentation experiments in batch and fed-batch mode.

2.3 Results and Discussion

2.3.1 Measurement of Synthetic Wine Mixtures

Figure 2 shows the ^{1}H NMR spectra of Mixture 1, Mixture 2, and Mixture 3 (with peak assignments). The three mixtures contain 8 constituents at different concentrations, and represent the different stages of the wine fermentation (see Appendix A). The most important differences between these three mixtures are their sugar content (glucose and fructose) and their ethanol content, since these major components are consumed and produced, respectively, during fermentation. Due to the low chemical shift dispersion of the ^{1}H NMR spectra, major peak overlaps are observed. In particular, in the range of 3 to 4 ppm, the peaks of the components glucose, fructose and glycerol overlap with each other and with the CH_2-peak of ethanol, preventing a quantification by direct peak integration. This is why the AutoWine-tool of Matviychuck et al. [79] was used here. The NMR peaks of the acids (acetic acid, citric acid, malic acid and succinic acid) are located in the range of 2 to 3 ppm and are reasonably well resolved, but the acid content is very low and therefore difficult to quantify, due to the small SNR. The AutoWine-tool is able to identify each component and automatically fit the mathematical peak model of the molecules to the experimental ^{1}H NMR spectrum.

Figure 3 shows the results of the quantitative analysis of Mixture 1, Mixture 2, and Mixture 3 by the AutoWine-tool which are compared to the values of the gravimetric sample preparation. The numerical results are given in the Appendix A.
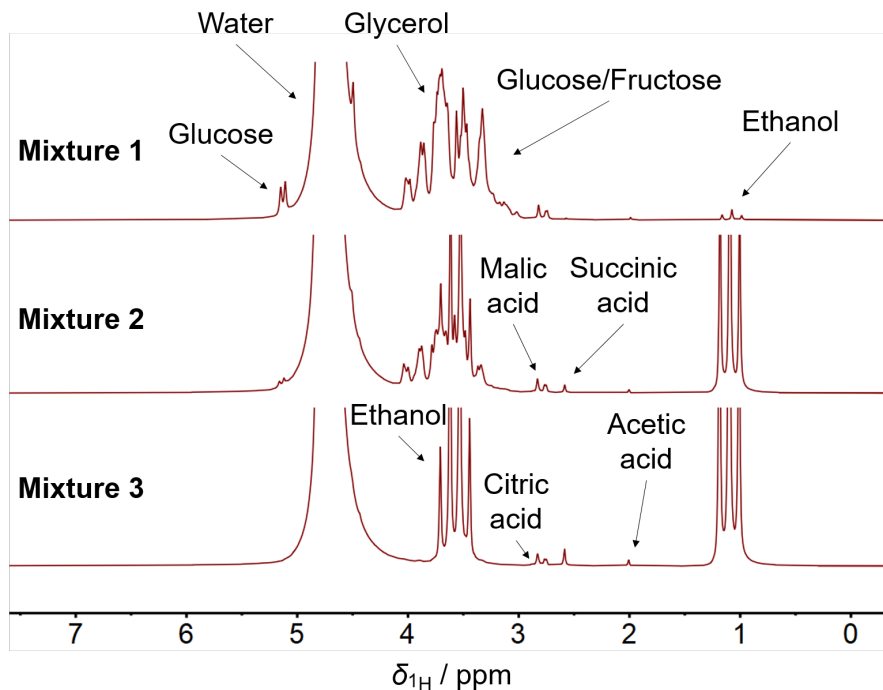
Figure 2: ^{1}H NMR spectra of Mixture 1, Mixture 2, and Mixture 3.

The results of the ^{1}H NMR experiments combined with the analysis by the AutoWine-tool are in overall good agreement with the ground truth for each mixture. It can be seen that both highly concentrated and, in particular, less concentrated components can be correctly quantified by the AutoWine-tool. For the minor components acetic acid and succinic acid, very good agreement with the ground truth was found. As these peaks are rather well separated (compare Figure 2), the AutoWine-tool robustly identifies and quantifies these components. In contrast, citric acid and malic acid strongly overlap with each other. The AutoWine-tool is still able to reliably distinguish the corresponding signals and accurately quantify both components.
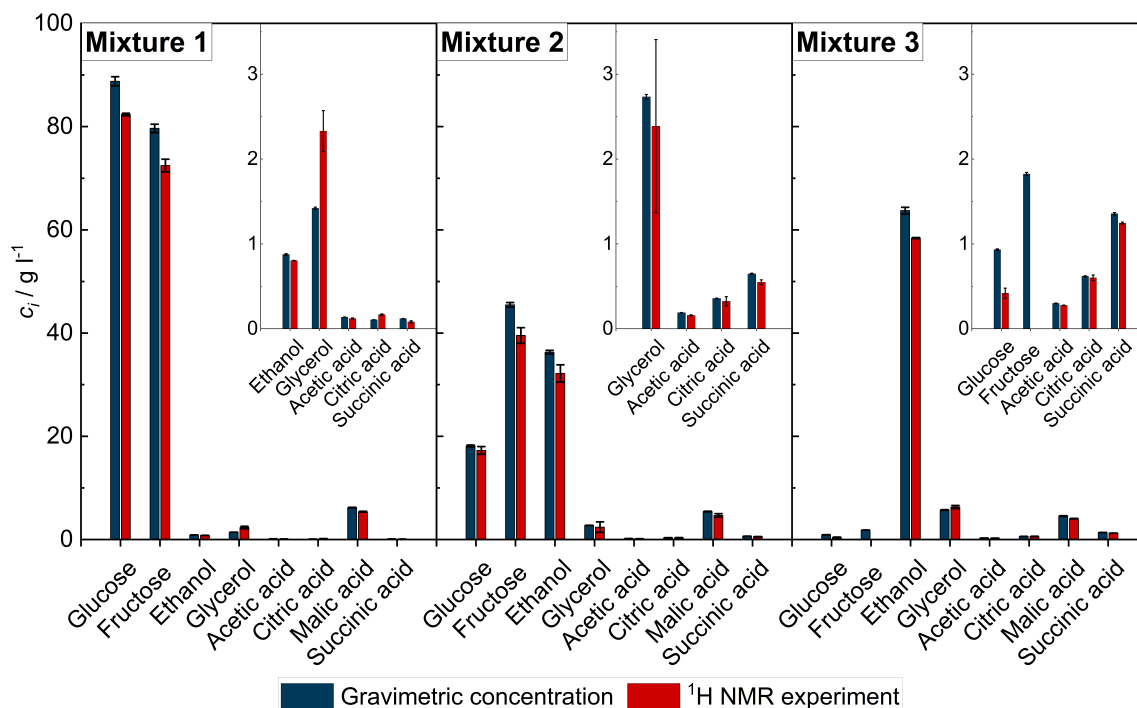
Figure 3: Comparison of the results of Mixture 1, Mixture 2, and Mixture 3 obtained by the ^{1}H NMR experiment combined with the quantitative analysis by the AutoWine-tool with the concentrations of the gravimetric sample preparation. Inserts are provided showing the concentration of the components that are less than 3.5 g l^{-1} in the corresponding mixture.

The largest deviations from the ground truth are found for glucose and fructose as well as for glycerol. Since the signals of these molecules strongly overlap with each other and are additionally disturbed by the CH_2-peak of ethanol, modeling and fitting of the corresponding peaks is challenging. In particular, the AutoWine-tool has issues in identifying and quantifying glucose and fructose if their respective concentrations are too low, which is the case for Mixture 3. Interestingly, for glucose the deviations from the ground truth are comparatively smaller as this carbohydrate has anomeric protons (located at 5.2 ppm) which can be used for the quantification. However, for lower concentrations these signals also disappear under the water signal, thereby limiting their detection (see Figure 2, Mixture 3). The application of ^{1}H NMR experiments with ^{13}C decoupling as the only acquisition method is not sufficient to quantify these components with high accuracy in this case.

Furthermore, there is a small systematic underestimation of the concentrations provided by the AutoWine-tool for nearly all components. One reason for this is the fitting error of the water peak due to its lineshape (see Appendix A): the water content is overestimated resulting in an underestimation of all other components. Another reason might be the density of the mixtures. The AutoWine-tool calculates the density by using the

densities of the pure components, weighted by the corresponding mole fractions of these components obtained from the ^{1}H NMR spectra (excess values are neglected). Details about the estimation of the density are described in the work of Matviychuk et al. [79]. The density is used to calculate the concentration of the mixture under investigation. The values obtained by the AutoWine-tool are underestimated compared to those from the measurement by the densimeter. The results are given in the Appendix A.

Matviychuk et al. [79] have suggested to perform additional ^{1}H NMR experiments with suppression of the water signal. In addition, the internal standard maleic acid was provided to improve the quantitative analysis. These experiments were also carried out but no significant improvements could be observed. Details regarding these experiments are given in the Appendix A.

In summary, it is possible to accurately quantify multiple species in complex mixtures over a wide concentration range by using only a simple ^{1}H NMR experiment in combination with the AutoWine-tool. This is beneficial for the online monitoring of a continuously changing system, such as the fermentation of grape juice. The quantification can be performed without any prior calibration or additional experimental efforts.

2.3.2 Online Monitoring of Wine Fermentation

The results of the online monitoring of the batch fermentation of grape juice are displayed in Figure 4. Only data points for each full hour are shown. Results from the replicated experiment as well as individual results for all studied components are provided in the Appendix A. Figure 4 shows that there are only a few outliers in the data; they can be explained by gas bubbles interfering with the signal acquisition. These bubbles were either not completely removed by the bubble trap or were formed in the transport line.

The evolution of the concentrations of the individual components can be resolved very well during the course of the 200 h fermentation. A significant change in the concentration is observed for the major components glucose, fructose and ethanol: glucose as well as fructose continuously decrease in concentration while ethanol increases after a lag-phase of about 24 h, as expected. Glucose is consumed significantly faster by the yeast than fructose, which is consistent with the general glucophilie of *saccharomyces* yeast [52]. At the end of the fermentation a maximum ethanol concentration of 70 g l^{-1} was achieved.
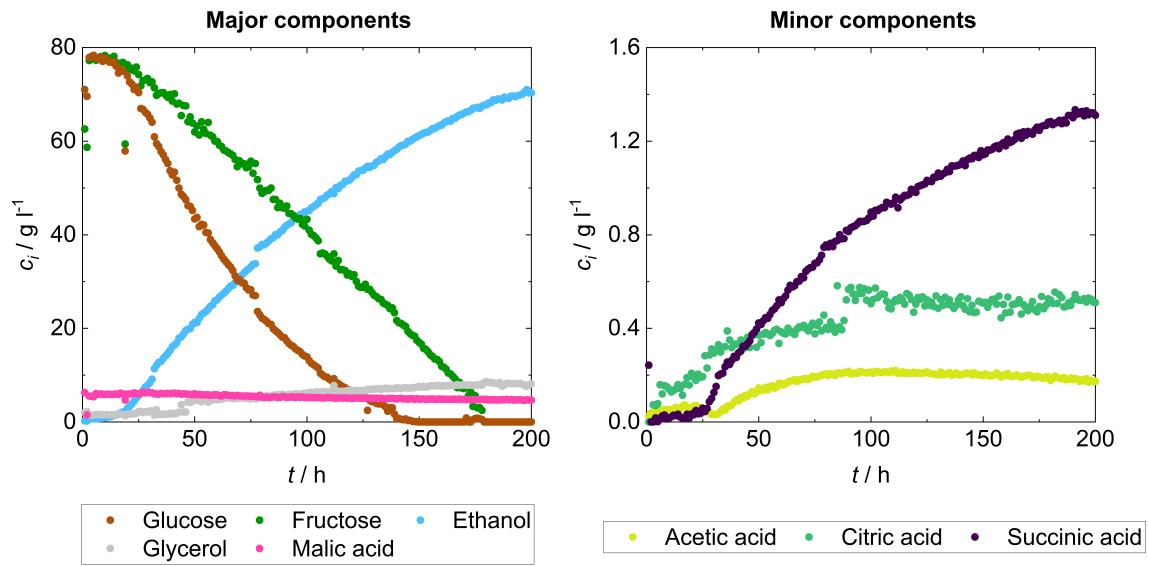
Figure 4: Results of the monitoring of the batch fermentation of grape juice (single experiment) by ^{1}H NMR spectroscopy over 200 h. Left: major components glucose, fructose, ethanol, glycerol, and malic acid. Right: minor components acetic acid, citric acid and succinic acid.

Glycerol is a by-product of the anaerobic fermentation of yeast. It is formed during the glycolysis of glyceraldehyde-3-phosphate. It it is known that, high initial sugar concentration of the grape juice induces high glycerol formation as it reduces the osmotic stress for the yeast [82]. Glycerol concentrations in commercial wines are in the range between 5 to 15 g l^{-1} [83], the average value is about 7 g l^{-1} [82]. In the batch fermentation shown in Figure 4, the concentration of glycerol continuously increases from an initial concentration of 1.4 g l^{-1} to about 8 g l^{-1}.

Malic acid is produced and degraded during the ripening process of the grapes and not by the yeast itself. Mature grapes contain between 2 and 6.5 g l^{-1} of malic acid [84]. Hence, the concentration of malic acid remains constant during the fermentation, it is about 5 g l^{-1} in the present study. The monitoring of the concentration of malic acid is important, as a decrease indicates malo-lactic fermentation induced by lactic acid bacteria, which did not occur here.

Succinic acid is a metabolite of the citric acid cycle of yeast [84, 85]. Due to the anaerobic conditions, the cycle is interrupted. This results in the production of large amounts of succinic acid which is indicated by the continuous increase in the concentration as shown in Figure 4. As a consequence, the pH drops, which was monitored here by the pH sensor (from pH = 2.9 to pH = 2.7, see Appendix A). Furthermore, the concentration evolution is similar to that of ethanol and a lag-phase can also be identified. The maximum concentration of succinic acid achieved in the batch fermentation is 1.3 g l^{-1}. Typical concentration levels of succinic acid are 0.2 to 2 g l^{-1} [85], which makes it the main acid

produced during alcoholic fermentation of wine. The measured concentration during the fermentation is in the range given in the literature [85].

Citric acid is also an intermediate in the citric acid cycle of yeast. It can also be present in the grapes [84], but in the juice only minor amounts were found, see Figure 4. During the fermentation some citric acid is formed. However, a sudden jump in the concentration to about 0.5 g l^{-1} is recognized due to unknown reasons at around 88 h of fermentation. After that, the concentration of citric acid remains constant, which is in the expected range [84].

In every wine fermentation, acetic acid is formed, leading to final concentrations between 0.1 and 0.3 g l^{-1} [86]. The formation mechanism is still subject of current research. In the experiment the formation of acetic acid was observed especially in the early phase of the fermentation when the sugar concentration is high and yeast produce acetic acid in osmotic stress reaction. In the later phase of the fermentation, the acetic acid concentration even slightly decreases. The observation supports the hypothesis that acetic acid is formed by enzymatic oxidation of acetaldehyde, which is known to be favored at high sugar concentration [86]. Thus, the fed-batch fermentation is a strategy to counteract the formation of acetic acid.

Figure 5 shows the results of the online monitoring of a fed-batch fermentation of grape juice. Again, only the data points for each full hour are given. The results of the two replicated experiments and the individual results for all studied components are provided in the Appendix A.

The evolution of the concentrations of the individual components during the fed-batch fermentation shows the same trend as already discussed for the batch fermentation. However, for the highly concentrated components glucose, fructose, and ethanol, four significant concentration jumps are recognized. This is attributed to the fact that additional grape juice was added to the reactor as feed at that time. Carbohydrates were added to the fermentation broth while ethanol was diluted. Glycerol and succinic acid also show concentration jumps, but they are less pronounced. In contrast, the malic acid concentration remains constant during the fermentation, similar to the batch fermentation, as this component is a constituent of the grape juice and occur in the same concentration in the fermenting wine and added grape juice. However, no significant concentration jumps due to the addition of grape juice are observed for acetic and citric acid, as these small concentration changes may be difficult to detect. But similar to the batch fermentation, for citric acid a sudden concentration increase is recognized at around 90 h of fermentation which is verified by the repetition experiment as well.
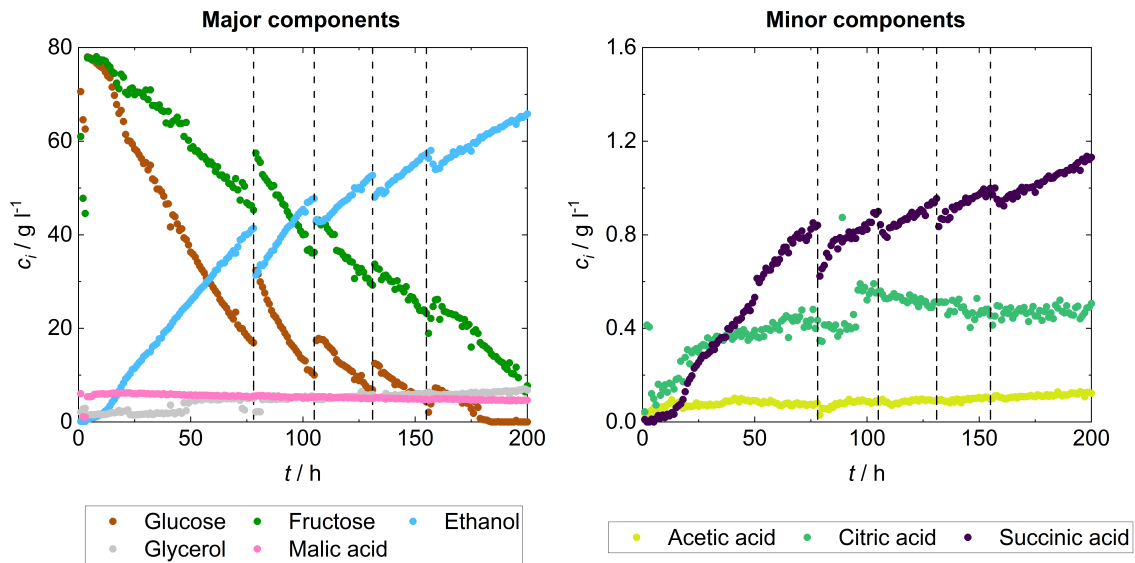
Figure 5: Results of the monitoring of the fed-batch fermentation of grape juice (single experiment) by ^{1}H NMR spectroscopy over 200 h. The vertical dashed lines indicate the times at which grape juice was added to the reactor. Left: major components glucose, fructose, ethanol, glycerol, and malic acid. Right: minor components acetic acid, citric acid and succinic acid.

Both operating modes, which only differ in the stepwise addition of grape juice, are explicitly compared for the components glucose, ethanol, glycerol, and acetic acid which is illustrated in Figure 6. The major components glucose and ethanol show the same overall concentration evolution for both batch and fed-batch fermentation. In addition, the same concentration levels were achieved at the end of the fermentation. For glycerol, a slight reduction of the glycerol concentration is observed in the fed-batch fermentation due to the reduced osmotic stress [82]. In contrast, for acetic acid, a significant difference can be observed when comparing the two operating modes: A lower acetic acid concentration is obtained for the fed-batch fermentation. The largest difference in the concentration is found for a fermentation time of about 100 h. The results are in agreement to the findings of Frohmann & Orduña, who also proposed the use of fed-batch fermentations to counteract acetic acid formation [80]. However, the concentrations of acetic acid in batch and fed-batch fermentations equalize over the course of the fermentation. The replicated experiments confirm this observation and indicate the same trend. This is due to the relatively low sugar concentration of the grape juice used in this work. In comparison, the sugar concentration of the juice used by Frohmann & Orduña was up to 340 g l^{-1}[80], leading to larger differences in the acetic acid concentration between the two fermentation strategies because of the significantly larger osmotic stress. Furthermore, the loss of the acetic acid can be partially reasoned by a formation of ethylacetate due to esterase activities of the *saccharomyces* yeast. However, the strengths of the analytical method were made clear here: In the wine production, it

is possible to stop or modify the fermentation at a certain time and to obtain a small acetic acid concentration, because the process can be continuously monitored with high temporal resolution.
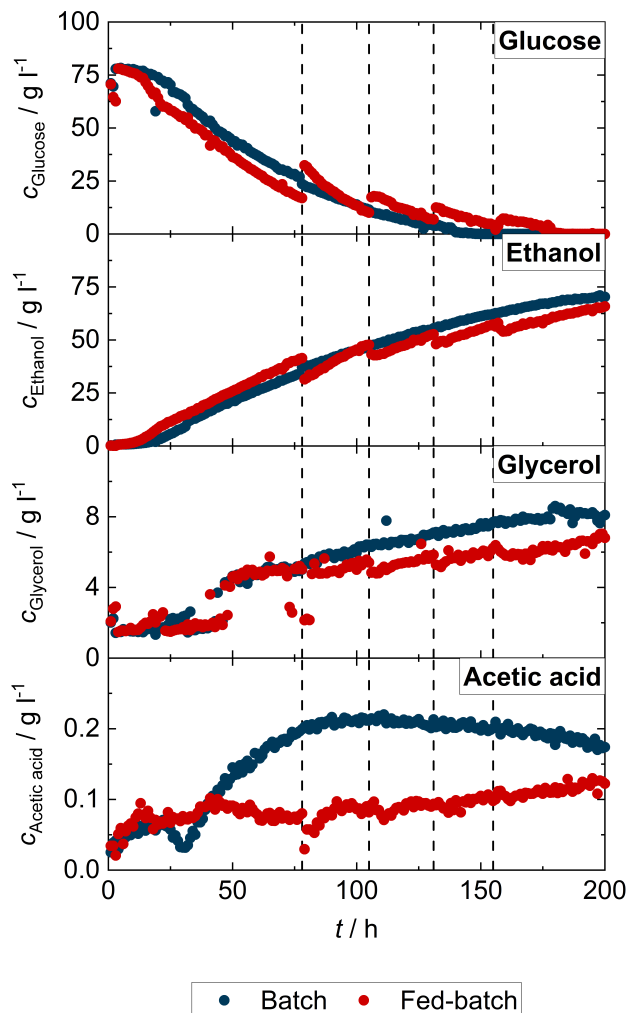
Figure 6: Comparison of the results of the batch and the fed-batch fermentation of grape juice for glucose, ethanol, acetic acid, and glycerol. The batch and fed-batch experiments are basically identical, the only difference is that in the fed-batch experiment, the addition of the grape juice was done stepwise. The times of the addition are indicated by vertical dashed lines.

2.4 Conclusions

In this work, the usefulness of benchtop ^{1}H NMR spectroscopy for online monitoring of wine fermentations has been successfully demonstrated. The application of the AutoWine-tool, which incorporates quantum mechanical formulations, for the analysis of the complex wine matrix enables the straightforward quantification of many parameters that are otherwise inaccessible due to large peak overlap in the ^{1}H NMR spectrum.

The approach was validated by the quantitative analysis of three test mixtures to prove the reliability of the method. In contrast to the previous work by Matviychuk et al. [79], it was found that a simple ^{1}H NMR experiment with ^{13}C decoupling is sufficient to provide accurate results. Based on these findings, batch and fed-batch fermentations were investigated using this method. Major as well as minor wine components could be quantified and their evolution during the fermentation was monitored.

The present study provides a tool for winemakers to gain a better insight of the wine production process and to use this information to suggest optimization measures. Since the quantification of many wine constituents during the fermentation can be conducted simultaneously without the need for any calibration or sample preparation, no extensive training or introduction to the technology is required. Furthermore, the analysis can be easily performed without disturbing the production process by implementing a bypass setup to existing fermentation tanks in wineries. High temporal resolution data can be obtained if desired. This provides a detailed insight into the fermentation process, allowing easy assessment of the yeast performance and its response to external manipulation or the detection of sluggish fermentation.

3 Polarization Transfer Methods for Quantitative Analysis of Flowing Mixtures

3.1 Introduction

The seemingly most simple way to tackle the peak overlap problem is to switch from ^{1}H NMR to ^{13}C NMR [87–89]. Peak overlap problems are rare in ^{13}C NMR spectroscopy, due to the higher chemical shift dispersion of ^{13}C compared with ^{1}H. Moreover, ^{1}H decoupling sequences can be used to avoid peak splitting resulting in ^{13}C NMR spectra consisting only of singlet peaks which provide larger sensitivity and selectivity. However, this big advantage of ^{13}C NMR comes at the cost of a much poorer SNR compared with ^{1}H NMR, caused by the low natural abundance of ^{13}C nuclei and their low gyromagnetic ratio. This is particularly detrimental for benchtop NMR spectrometers because of their low magnetic field strength, and often results in extremely long measurement times needed to obtain useful ^{13}C NMR spectra. In addition, ^{13}C nuclei have a long magnetization build-up time in flow applications due to the long spin-lattice relaxation time $T_{1,^{13}\mathrm{C}}$, which is several times higher than that of ^{1}H nuclei. This causes problems with the premagnetization of flowing samples, which are worsened by the fact that the premagnetization volumes in benchtop instruments are low, due to their compact design [2, 90]. The premagnetization problem can be tackled with paramagnetic relaxation agents which, however, complicate the measurement [91]. Furthermore, for routine measurements in industry, the agents must meet high stability requirements, and the technique is still far from being routine.

The application of polarization transfer pulse sequences can solve all problems mentioned above: They provide a fourfold signal enhancement of the ^{13}C signal via polarization transfer from scalar coupled ^{1}H spins. In addition, the repetition delay between successive scans can be reduced, since the much shorter spin-lattice relaxation time $T_{1,^{1}\mathrm{H}}$ of ^{1}H nuclei is used for magnetization build-up, which also substantially lessens the problems with flowing samples. This combination of advantages of polarization transfer

pulse sequences makes them highly attractive for process monitoring applications with benchtop NMR.

Commonly used polarization transfer pulse sequences are INEPT and DEPT [92–94]. However, these sequences cannot detect quaternary carbon atoms, i.e. the corresponding information is lost. The lesser known polarization transfer sequence PENDANT (abbreviation for polarization enhancement that is nurtured during attached nucleus testing) of Homer and Perry [95, 96] combines several advantages: enhancement of ^{13}C signals to which ^{1}H atoms are bound, selective excitation of functional carbon groups (CH$_3$, CH$_2$, CH) and detection of quaternary carbon atoms. Polarization transfer techniques have not been used before for quantitative process monitoring with benchtop NMR spectroscopy, particularly not for flowing samples.

To demonstrate the feasibility of using polarization transfer techniques for the quantitative analysis of mixtures with benchtop NMR, experiments have been carried out with two test mixtures using the polarization transfer sequence PENDANT. The mixtures were analyzed quantitatively in stationary and flow experiments. The results obtained with the polarization transfer sequence PENDANT were compared with the gravimetrically determined concentrations and results from standard ^{1}H and ^{13}C NMR analysis. Furthermore, a continuous dilution experiment was carried out that is considered here as a proxy of a dynamic process, and the ^{13}C NMR PENDANT technique was applied for its monitoring.

3.2 Experimental Section

3.2.1 Chemicals and Sample Preparation

The chemicals used in this work are summarized in the Appendix B. They were used without further purification. Two test systems were investigated:

- System 1: acetonitrile (ACN) + dimethyl sulfoxide (DMSO) + ethyl formate (EF), in which all peaks are well-separated in the ^{1}H NMR spectrum.

- System 2: acetonitrile (ACN) + acetone (ACT) + ethyl formate (EF), in which peaks overlap in the ^{1}H NMR spectrum.

Mixtures of different compositions were prepared gravimetrically with a laboratory balance (Delta Range XS603S, Mettler Toledo) with an accuracy of ± 0.001 g; Table 2 gives an overview.

Table 2: Overview of the studied mixtures.

System 1: ACN + DMSO + EF				System 2: ACN + ACT + EF			
	x_{ACN}	x_{DMSO}	x_{EF}		x_{ACN}	x_{ACT}	x_{EF}
Mixture	mol mol^{-1}			Mixture	mol mol^{-1}		
1.A	0.333	0.333	0.334	2.A	0.333	0.333	0.334
1.B	0.700	0.150	0.150	2.B	0.700	0.150	0.150
1.C	0.150	0.700	0.150	2.C	0.150	0.700	0.150
1.D	0.150	0.150	0.700	2.D	0.150	0.150	0.700

3.2.2 NMR Hardware and Experiments

All experiments were carried out with a benchtop NMR spectrometer from Magritek
(Spinsolve Carbon) with a magnetic field strength of B_0 = 1 T corresponding to a ^{1}H
Larmor frequency of v_0 = 42.5 MHz. The polarization transfer pulse sequence PEN-
DANT for the signal enhancement in the ^{13}C NMR spectrum was implemented on the
benchtop NMR spectrometer with the software Spinsolve Expert (Magritek). The evo-
lution delays as well as the phase cycle were adopted as published by Homer & Perry
[95, 96]. An inverse-gated decoupling sequence (WALTZ-16) for ^{1}H decoupling during
the acquisition of the FID is included. The experiment is referred to as ^{13}C NMR PEN-
DANT in the following and is illustrated in the Appendix B. The evolution delays of
the pulse sequence are given in the Appendix B. Depending on the setting for the scalar
coupling constant $^1J_{C,H}$ between the carbon and the scalarly coupled proton, either the
signal of CH$_3$-, CH$_2$- or CH-group is fully enhanced. In this work, the $^1J_{C,H}$ was set to
fully enhance the CH$_3$-group of each molecule.

3.2.2.1 Stationary Experiments

The stationary experiments were executed in NMR sample tubes with an outer diameter
of d = 5 mm (Magritek). The spin-lattice relaxation times $T_{1,^1H}$ and $T_{1,^{13}C}$ were deter-
mined with the inversion recovery experiment from the standard operating software of
the spectrometer.

The quantitative analysis of the mixtures was performed using a ^{1}H NMR, ^{13}C NMR
and the ^{13}C NMR PENDANT experiment controlled by the Spinsolve Expert software.
^{1}H NMR experiments were executed with an acquisition time of 6.4 s, 32 k data points,
4 scans and a 90° excitation pulse. The parameters for the ^{13}C NMR as well as the
^{13}C NMR PENDANT experiment were: 3.2 s acquisition time, 16 k data points, and

128 scans. For the ^{13}C NMR experiments a 90° excitation pulse and a WALTZ-16 decoupling sequence during the acquisition were applied. The repetition time in all experiments was set to guarantee a sufficient magnetization recovery of the sample with at least 5 times T_1.

All spectra were postprocessed with the automatic baseline and phase correction tool SINC [97, 98]. The determination of the SNR as well as the integration of the peaks for the quantitative analysis were performed in MestRenova. The overlapping peaks in the ^{1}H NMR spectrum in System 2 were analyzed with the Global Spectral Deconvolution (GSD) tool included in MestRenova. The mole fraction of a component in the ternary mixtures was determined by the normalized peak integral fraction of that component with respect to all components in the mixture. For the quantitative analysis only the signal of the CH_3-group of each component was considered. The uncertainties of the results for the mole fractions that are reported here were determined from the uncertainty of the peak areas as described in the Appendix B. For evaluating the ^{13}C NMR PEN-DANT experiment, the relative deviation ($\Delta_{i,\mathrm{rel}}$), the root mean squared error (RMSE) and the mean absolute error (MAE) are used:

$$\Delta_{i,\mathrm{rel}} = \left(\frac{x_{i,\mathrm{method}} - x_{i,\mathrm{reference}}}{x_{i,\mathrm{reference}}} \right) 100\% \tag{1}$$

$$\mathrm{RMSE} = \sqrt{\frac{\sum\limits_{i=1}^{N} \left(x_{i,\mathrm{method}} - x_{i,\mathrm{reference}} \right)^2}{N}} \tag{2}$$

$$\mathrm{MAE} = \frac{\sum\limits_{i=1}^{N} \left| x_{i,\mathrm{method}} - x_{i,\mathrm{reference}} \right|}{N} \tag{3}$$

Here, i denotes the component, N the total number of concentrations determined by that method and x_i the mole fraction of component i. Calculating the MAE and RMSE as error scores is a common practice in data science. While MAE provides a measure of the absolute error between the method and the reference, RMSE penalizes large errors more strongly, thus highlighting the impact of outliers. A direct comparison of MAE and RMSE provides insight into the underlying error distribution. If the RMSE is much higher than the MAE, the score is usually strongly influenced by outliers.

3.2.2.2 Flow Experiments

Figure 7 shows the closed loop setup used for the flow experiments. The liquid feed mixture was stored in a $V = 100$ ml feed container. A double piston high-pressure pump

with damping piston (WADose LITE HP, Flusys) was used to circulate the sample. The flow rate was measured with an accuracy of ±2 % with a Coriolis sensor (Mini Cori-Flow, Bronkhorst) that was also used to control the pump. The mixture was transported through PEEK capillaries with an inner diameter of $d = 1$ mm to the benchtop NMR spectrometer that was equipped with a glass flow cell (Spinsolve Reaction Monitoring Kit RM, Magritek). The flow cell has an inner diameter of $d = 1$ mm at the inlet and the outlet; in the active region the diameter is $d = 4$ mm.
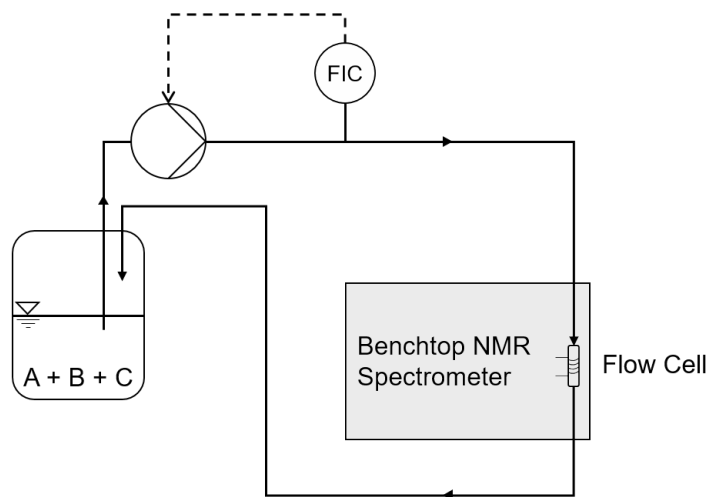
Figure 7: Scheme of the setup used for flow experiments.

Flow rates in the range of $\dot{V} = 0.5$ to 2 ml min^{-1} were set in 0.25 ml min^{-1} steps. These flow rates correspond to the following flow velocities: capillaries (1 - 4 cm s^{-1}); detection volume (0.1 - 0.3 cm s^{-1}). For the quantitative analysis of the flowing sample ^{1}H NMR, ^{13}C NMR, and ^{13}C NMR PENDANT experiments were performed with the same parameters as in the stationary experiments. ^{13}C NMR and ^{13}C NMR PENDANT experiments were executed with 64 scans. The accumulation of multiple scans was performed with a delay time t_{d} which depends on the investigated mixture as well as on the observed nucleus and was set according to Equation (4) [5, 13]:

$$t_{\mathrm{d}} = \frac{1}{\frac{1}{T_1} + \frac{1}{t_{\mathrm{DV}}}} \qquad (4)$$

Here, T_1 is the longest spin-lattice relaxation time of the mixture and t_{DV} the residence time of the spins inside the detection volume, which depends on the adjusted flow rate. An additional safety margin of 2 s was added to the delay time t_{d} calculated from Equation 4, to ensure a full replenishment of non-excited spins. The postprocessing steps as well as the quantitative analysis were performed as in the stationary experiments (see Section 3.2.2.1).

3.2.2.3 Process Monitoring Experiments

Figure 8 depicts the setup used for the process monitoring experiments, in which a continuous dilution process was monitored. The setup of flow experiments (see Figure 7) was adopted and extended by an additional feed container with a total volume of V = 100 ml as well as a second double piston high-pressure pump with damping piston (WADose PLUS HP, Flusys). A binary mixture (A + B) was placed in the first container. A third component (C) was stored in the second container and was continuously fed by the second pump into the container with the mixture. Two dosage rates were used: $\dot{V}$ = 0.2 ml min^{-1} and $\dot{V}$ = 0.833 ml min^{-1}. The initial volume of the liquid mixture was about V = 60 ml. A magnetic stirrer (Topolino, IKA-Werke) was used to homogenize the mixture in the first container.

The setup includes two identical benchtop NMR spectrometers (Spinsolve Carbon, Magritek). The additional benchtop NMR spectrometer was also equipped with a glass flow cell (Spinsolve Reaction Monitoring Kit RM, Magritek) and was connected with PEEK capillaries with an inner diameter of d = 1 mm to the setup. T-pieces in combination with a needle valve were used to evenly distribute the volume flow of the sample mixture to the two benchtop NMR spectrometers. The pump, that conveys the ternary mixture to the benchtop NMR spectrometers, was set to a flow rate of $\dot{V}$ = 1.5 ml min^{-1}. The first NMR spectrometer was used for ^{13}C NMR PENDANT experiments (3.2 s acquisition time, 16 k data points, 16 scans), the second NMR spectrometer was used for ^{1}H NMR experiments (6.4 s acquisition time, 32 data points, 1 scan) for referencing purposes. Data were acquired with the second spectrometer in intervals of 15 s.
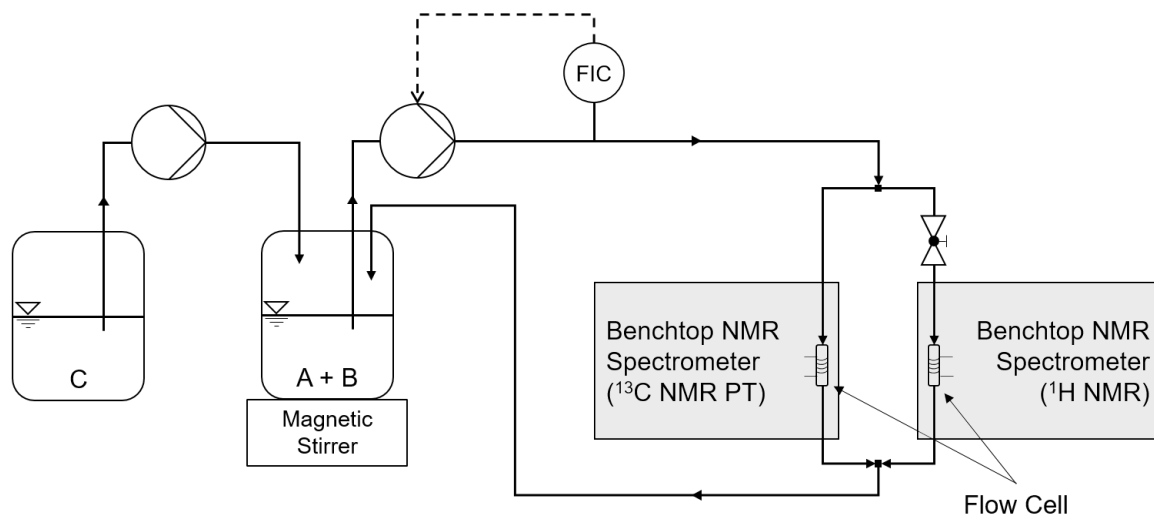
Figure 8: Scheme of the setup used for process monitoring experiments.

3.3 Results and Discussion

The $T_{1,{}^1\text{H}}$ and $T_{1,{}^{13}\text{C}}$ values of the CH$_3$-group of all components in the investigated mixtures are given in Table 3. In Figure 9, ^{1}H NMR as well as ^{13}C NMR and ^{13}C NMR PENDANT spectra are shown for Mixture 1.A and Mixture 2.A, respectively, including a peak assignment.

It can be seen from Figure 9 that the peaks in the ^{1}H NMR spectrum of Mixture 1.A are well separated, which holds also for all other mixtures from ACN, DMSO and EF. A quantification by direct peak integration can be carried out easily. In contrast, in Mixture 2.B, where DMSO is replaced by ACT, a peak overlap between the CH$_3$-groups of ACN and ACT occurs in the ^{1}H NMR spectrum. The components can no longer be quantified by direct peak integration and deconvolution methods must be applied.

In Figure 9, also ^{13}C NMR spectra of the studied mixtures are displayed together with the peak assignment. Due to the large chemical shift dispersion of ^{13}C there is no peak overlap. However, the SNR of the ^{13}C NMR spectra is relatively low, despite the high number of 128 scans. The signal of the CN-group of ACN (C5) is barely visible at 120 ppm, which is attributed to the short spin-spin relaxation time T_2 of that group resulting in a broad signal. Furthermore, the total measurement time of more than 4 h for a single ^{13}C NMR spectrum is extremely long because of the long repetition time of 5 times $T_{1,{}^{13}\text{C}}$ required for full magnetization recovery, which is necessary for a quantitative measurement. For use in process monitoring under continuous-flow, this is not practical.

Figure 9 also shows results from experiments that were carried out using ^{13}C NMR PENDANT. The settings were chosen so that the full enhancement is obtained for the signals from CH$_3$-groups, as only these were used for the quantification. The sequence could have been adjusted to enhance signals from CH$_2$- and CH-group likewise. For the CH$_3$-groups, an enhancement of the SNR of about 3.5 was obtained; see signals C1 - C3 in Figure 9. A signal from the quaternary C atom in ACT is obtained with PENDANT (however, as expected without enhancement). This is not the case for other polarization transfer sequences, such as INEPT and DEPT.

Another advantageous feature of PENDANT (and other polarization transfer methods such as DEPT) is its selectivity for different functional groups: signals from CH$_2$-groups as well as from quaternary C atoms are negative, while those from CH$_3$- and CH-groups are positive, see Figure 9. This is useful for the identification of components in complex mixtures.

Another important advantage of polarization transfer is that for the recycle delay, not the high $T_{1,^{13}C}$ is relevant, but the much lower $T_{1,^{1}H}$. Therefore, in the experiment shown in Figure 9, which both had 128 scans, the total experimental time for the ^{13}C NMR PENDANT experiment was reduced by a factor of 5 compared with the ^{13}C NMR experiment. In the following it is studied whether ^{13}C NMR PENDANT yields quantitative results in stationary as well as in flow experiments.

Table 3: Spin-lattice relaxation times $T_{1,^{1}H}$ and $T_{1,^{13}C}$ values of the CH_3-groups of each molecule in the studied ternary mixtures. The RMSE of three measurements is reported for $T_{1,^{1}H}$ in parentheses and refers to the last digit. For $T_{1,^{13}C}$ no RMSE is given as the measurement was done only once.

$T_{1,^{1}H}$ for System 1				$T_{1,^{1}H}$ for System 2			
	ACN	DMSO	EF		ACN	ACT	EF
Mixture		s		Mixture		s	
1.A	3.47 (28)	3.11 (3)	3.37 (2)	2.A	3.73 (4)	3.87 (2)	3.47 (1)
1.B	3.91 (2)	3.36 (2)	3.54 (3)	2.B	3.89 (4)	3.95 (13)	3.52 (16)
1.C	3.05 (5)	2.86 (3)	3.42 (5)	2.C	3.62 (4)	3.96 (1)	3.39 (3)
1.D	3.33 (1)	2.70 (1)	3.31 (1)	2.D	3.73 (2)	3.87 (3)	3.47 (1)
$T_{1,^{13}C}$ for System 1				$T_{1,^{13}C}$ for System 2			
	ACN	DMSO	EF		ACN	ACT	EF
Mixture		s		Mixture		s	
1.A	16.07	6.53	13.02	2.A	21.71	18.52	13.24
1.B	14.91	8.66	15.17	2.B	15.12	15.16	16.68
1.C	16.37	5.31	11.45	2.C	10.45	17.17	10.84
1.D	19.26	6.83	11.17	2.D	21.71	18.52	13.28
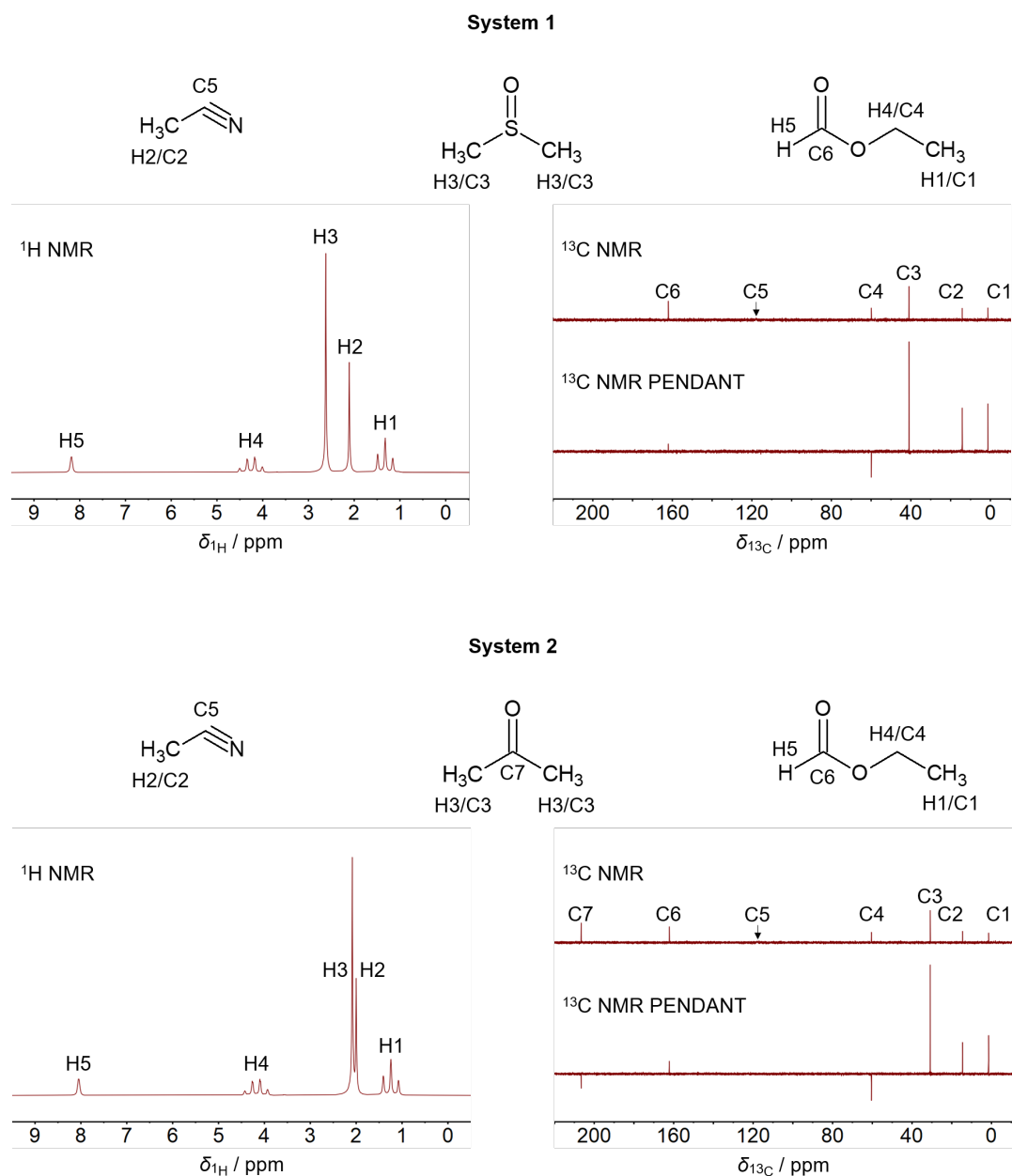
Figure 9: Comparison between ^{1}H NMR spectra as well as ^{13}C NMR and ^{13}C NMR PENDANT spectra for Mixture 1.A (top) and Mixture 2.A (bottom), respectively.

3.3.1 Stationary Experiments

Figure 10 shows results from the quantitative analysis of System 1 and System 2 with conventional ^{1}H NMR and ^{13}C NMR as well as ^{13}C NMR PENDANT experiments. For comparison also the results from the gravimetric sample preparation are shown, that are considered here as the ground truth and are depicted as horizontal dashed lines. Figure 10 shows the results for Mixture 1.C and Mixture 2.C; the corresponding results for the other mixtures are shown in the Appendix B. The MAE and RMSE values of the

quantification results of the analyzed mixtures are presented in Table 4. The numerical results of all experiments are provided in the Appendix B (Table A.11).
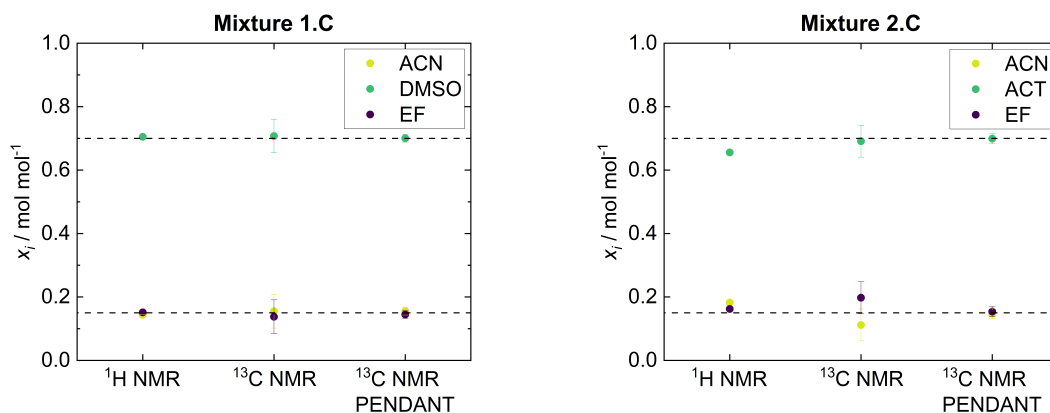
Figure 10: Results for the quantification of Mixture 1.C and Mixture 2.C by ^{1}H NMR, ^{13}C NMR and ^{13}C NMR PENDANT experiments. The horizontal dashed lines are results from the gravimetric sample preparation. The uncertainties (error bars) for the ^{1}H NMR experiments are within the symbol size. The concentrations of ACN and EF were equal in both cases.

Figure 10 shows that results from all three methods are generally in good agreement with the gravimetric reference, which also holds for the other studied mixtures. A closer inspection, however, reveals some differences (also see Table A.11 which contains the numerical results in the Appendix B): Firstly, the experimental uncertainty is generally much lower for ^{13}C NMR PENDANT compared with ^{13}C NMR. However, it is always higher than for ^{1}H NMR in System 1, which is a result of the fact that they are calculated from the SNR. Secondly, the results for all methods are quite good for System 1 with values for the MAE and RMSE of about 0.011 and 0.015, respectively. However, for System 2, which is analytically more demanding, the results from ^{13}C NMR PENDANT are better than for ^{1}H NMR and have even smaller errors than the ones obtained for System 1; see MAE (0.003) and RMSE (0.004). In contrast, the error values for ^{1}H NMR and ^{13}C NMR are distinctly higher. The larger deviation for the ^{1}H NMR method is due to difficulties in the deconvolution of the overlapping peaks. Moreover, in comparing the ^{13}C NMR results to the ^{13}C NMR PENDANT results, it has to be considered that the latter were obtained in experiments that were about 5 times faster.

Table 4: MAE and RMSE of the results from the quantification of the studied mixtures by ^{1}H NMR, ^{13}C NMR and ^{13}C NMR PENDANT.

Experiment	System 1		System 2	
	MAE	RMSE	MAE	RMSE
^{1}H NMR	0.0059	0.0067	0.0201	0.0232
^{13}C NMR	0.0100	0.0127	0.0214	0.0261
^{13}C NMR PENDANT	0.0114	0.0153	0.0029	0.0038

3.3.2 Flow Experiments

All test mixtures were analyzed with ^{1}H NMR, ^{13}C NMR and ^{13}C NMR PENDANT in flow experiments with different flow rates. The flow rate has an effect on the peak width determined by the spin-spin relaxation time T_2^*, and on the build-up of magnetization of the spins determined by the spin-lattice relaxation time T_1 [5, 13]. The effect of increasing flow rates on the ^{1}H NMR, ^{13}C NMR and ^{13}C PENDANT NMR spectra is shown in Figure 11, using Mixture 2.A as an example.

In the ^{1}H NMR spectra, the SNR is consistently high at all flow rates. However, the ^{13}C NMR spectra display a very low SNR which decreases at higher flow rates. In contrast, the ^{13}C NMR PENDANT spectra show a significantly higher SNR. Furthermore, it can be observed for all experiments that the peak heights decline at higher flow rates while the linewidths increase. This is due to the shortening of the spin-spin relaxation time T_2^* and the reduction of the premagnetization time. The peak broadening is especially disadvantageous in the ^{1}H NMR spectra as it may result in an increased peak overlap, as it can be seen in the ^{1}H NMR spectra near 2 ppm: the signals of the CH_3-groups of ACN and ACT strongly overlap at high flow rates which causes problems in the quantitative analysis.

The effect of the shorter premagnetization time at higher flow rates on the peak integrals acquired by ^{1}H NMR, ^{13}C NMR and ^{13}C PENDANT NMR experiments is illustrated in Figure 12, using again Mixture 2.A as an example. In all experiments the peak integrals decrease with higher flow rates. However, the decrease is particularly critical for the ^{13}C NMR experiment because of the large $T_{1,^{13}C}$ values. In addition, there are significant differences between the $T_{1,^{13}C}$ values of the different components (see Table 3) causing an uneven magnetization and, hence, deviations in the quantification. In the ^{13}C NMR PENDANT experiment, the premagnetization is sufficient throughout and the signal decrease is equal between each component at all flow rates (a signal drop of 10 % at $\dot{V}$ = 2.0 ml min^{-1} for each component), since the used $T_{1,^1H}$ values are small and in a

similar range, which allows quantitative analysis.
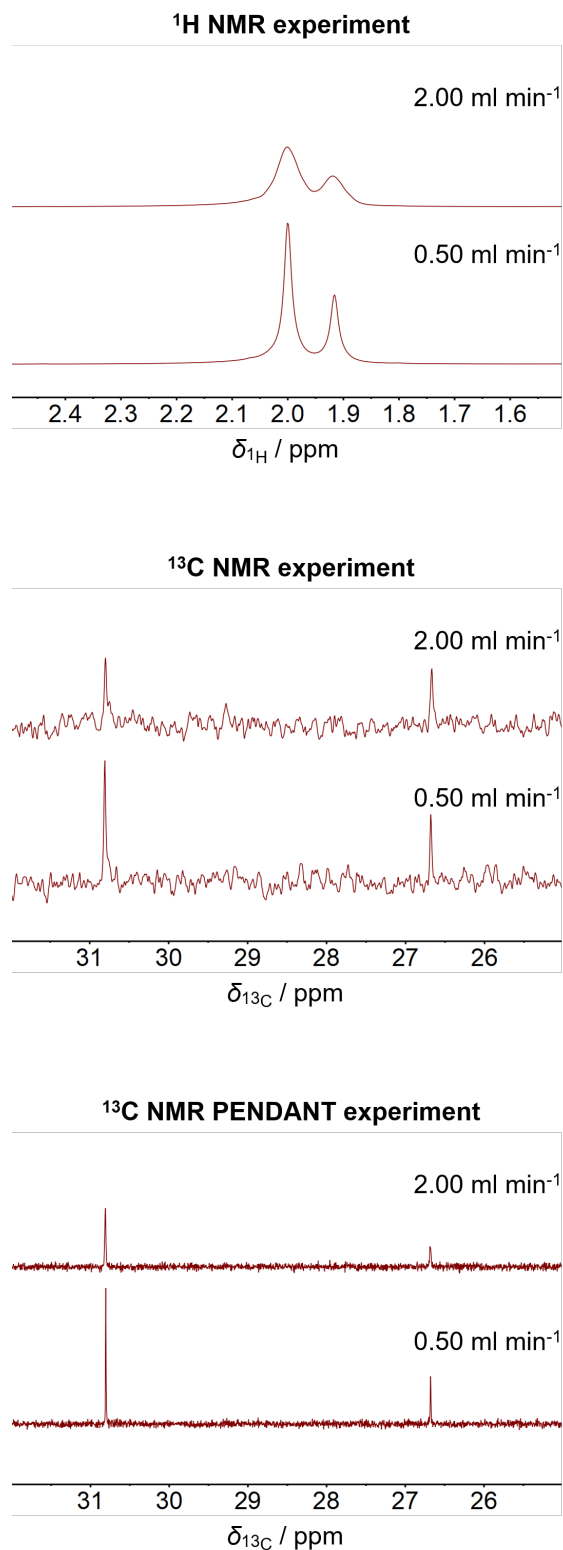
Figure 11: Spectra of the Mixture 2.A acquired with ^{1}H NMR, ^{13}C NMR and ^{13}C NMR PENDANT experiments at two different flow rates. The peaks of ACN and ACT are shown. The SNRs are given for the ^{13}C NMR and ^{13}C NMR PENDANT spectra.
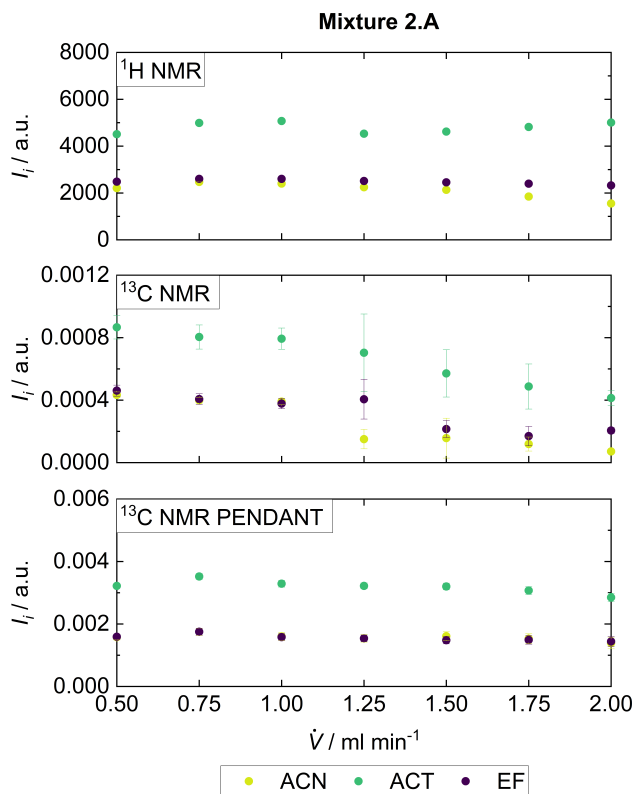
Figure 12: Peak integrals of the CH_3-groups of ACN, ACT and EF in Mixture 2.A acquired with ^{1}H NMR, ^{13}C NMR and ^{13}C NMR PENDANT experiments at various flow rates. The error bars are calculated by the SNR of the peak.

In the following, the influence of the flow effects on the quantification of the mixtures with ^{1}H NMR, ^{13}C NMR and ^{13}C NMR PENDANT experiments is discussed. In Figure 13 the results obtained in studies of the Mixture 1.C and Mixture 2.C at various flow rates are shown. The reference values are depicted as dashed horizontal lines. Similar representations of the results for the other mixtures as well as the numerical results are given in the Appendix B.

As shown in Figure 13 for System 1, the concentrations obtained by the ^{1}H NMR experiment are in very good agreement with the gravimetric reference, even at the highest flow rates. It is noteworthy that this agreement was obtained despite the fact that no full magnetization was achieved at high flow rates (for a calculation of the magnetization, see Appendix B). This is due to the fact that the $T_{1,^1\mathrm{H}}$ values for all components are very similar and hence the premagnetization is very similar. Furthermore, the error bars are small due to the high SNR of the ^{1}H NMR experiment resulting in an accurate quantification.
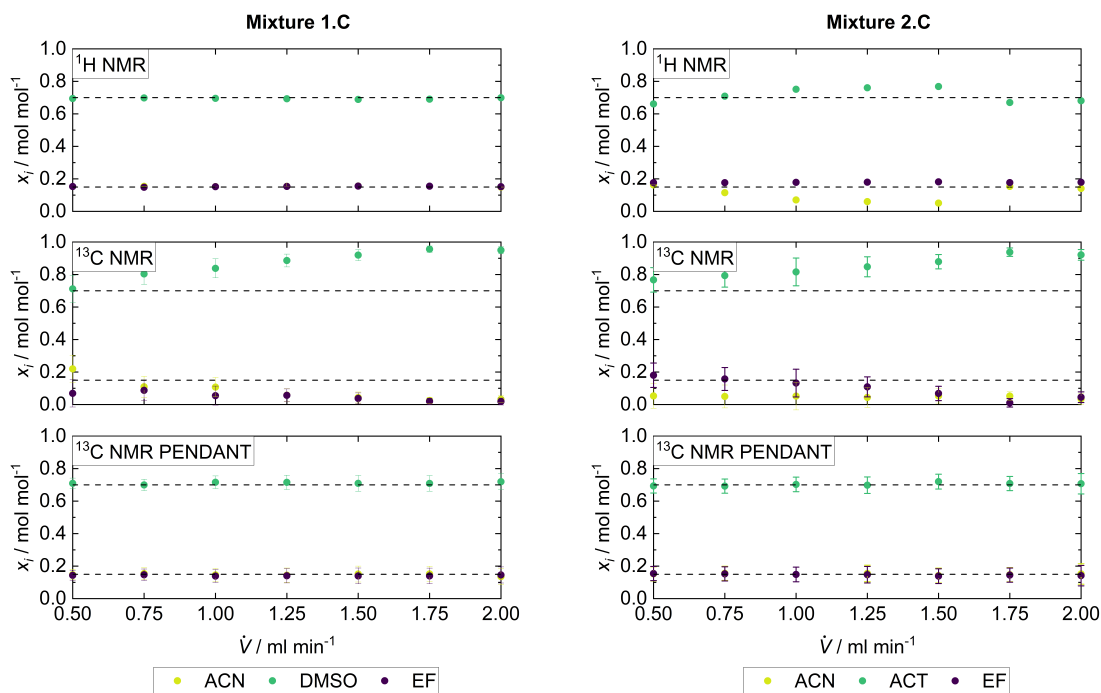
Figure 13: Results of the quantitative analysis of Mixture 1.C and Mixture 2.C by ^{1}H NMR, ^{13}C NMR and ^{13}C NMR PENDANT in flow experiments at different flow rates. The horizontal dashed lines represent the gravimetric reference. The error bars for the ^{1}H NMR experiments are within the symbol size.

The results from the ^{13}C NMR experiments deviate strongly from the gravimetric reference even at moderate flow rates. The concentration of DMSO is overestimated, those of ACN and EF are underestimated, with deviations that tend to increase with increasing flow rate. This observation can be explained by large differences in the spin-lattice relaxation times $T_{1,^{13}C}$ of the components (see Table 3). The negative effect of insufficient premagnetization of ACN and EF is amplified at high flow rates. The small SNR in the ^{13}C NMR spectrum leads to additional problems with the quantification resulting e.g. in large error bars.

In contrast, the ^{13}C NMR PENDANT experiment shows very good agreement with the gravimetric reference, also at the highest flow rates; see Figure 13. In addition, the error bars of the ^{13}C NMR PENDANT experiments are small compared with the ^{13}C NMR experiment due to the signal enhancement, which leads to higher SNR.

For System 2, the results from the ^{1}H NMR flow experiments deviate from the gravimetric reference, as it was the case in the stationary experiments. However, the deviations show no clear dependency on the flow rate. While the results for the concentration of EF are fair for all flow rates, there are important deviations for ACN and ACT, due to the strongly overlapping peaks. For Mixture 2.C, even a fusion of both singlets was observed which is challenging for the deconvolution and results in incorrect concentrations.

The results of the ^{13}C NMR experiments for System 1 and System 2 show similar and important deviations from the gravimetric reference. In contrast, the results obtained by ^{13}C NMR PENDANT are in very good agreement with the reference. The reasons for this excellent performance are the same as already discussed for System 1. In System 2, however, the advantage of the ^{13}C NMR PENDANT experiment is more pronounced, as peak overlap problems occur in this system in the ^{1}H NMR experiments.

3.3.3 Process Monitoring Experiments

A continuous dilution experiment to mimic a dynamic process was performed with the setup shown in Figure 8 which enables the simultaneous acquisition of ^{1}H NMR and ^{13}C NMR PENDANT spectra. System 1 was used for this study which allows to consider the results of ^{1}H NMR experiments as reference as there is no peak overlap in the ^{1}H NMR spectrum. Furthermore, the effect of two dosage rates on the quality of the determined concentrations by the ^{13}C NMR PENDANT experiment was investigated. In both cases, DMSO was continuously added to a mixture of ACN + EF with an initial concentration of x_{ACN} = 0.6 mol mol^{-1}. In the first experiment a DMSO dosage rate of $\dot{V}$ = 0.2 ml min^{-1} was used, resulting in a total study time of 4 h. In the second experiment the dosage rate was increased to $\dot{V}$ = 0.833 ml min^{-1}, which reduces the study time to 1 h. The ^{1}H NMR and ^{13}C NMR PENDANT spectra from the second experiment are shown in Figure 14. The effective flow rate in each spectrometer was $\dot{V}$ = 0.75 ml min^{-1}.

Figure 14 shows that the NMR signal of DMSO continuously increases in the ^{1}H NMR as well as in the ^{13}C NMR PENDANT spectra during the progress of the dilution experiment. The ^{1}H NMR experiment has a high temporal resolution because only one scan is required for the quantitative analysis as the SNR in the ^{1}H NMR spectra is sufficiently high. The ^{13}C NMR PENDANT experiment requires 16 scans to obtain a sufficient SNR for the quantification resulting in a measurement time of 2.7 min so that 24 ^{13}C NMR PENDANT spectra were taken in the course of the experiment. The results of the quantitative analysis of both dilution experiments are shown in Figure 15.
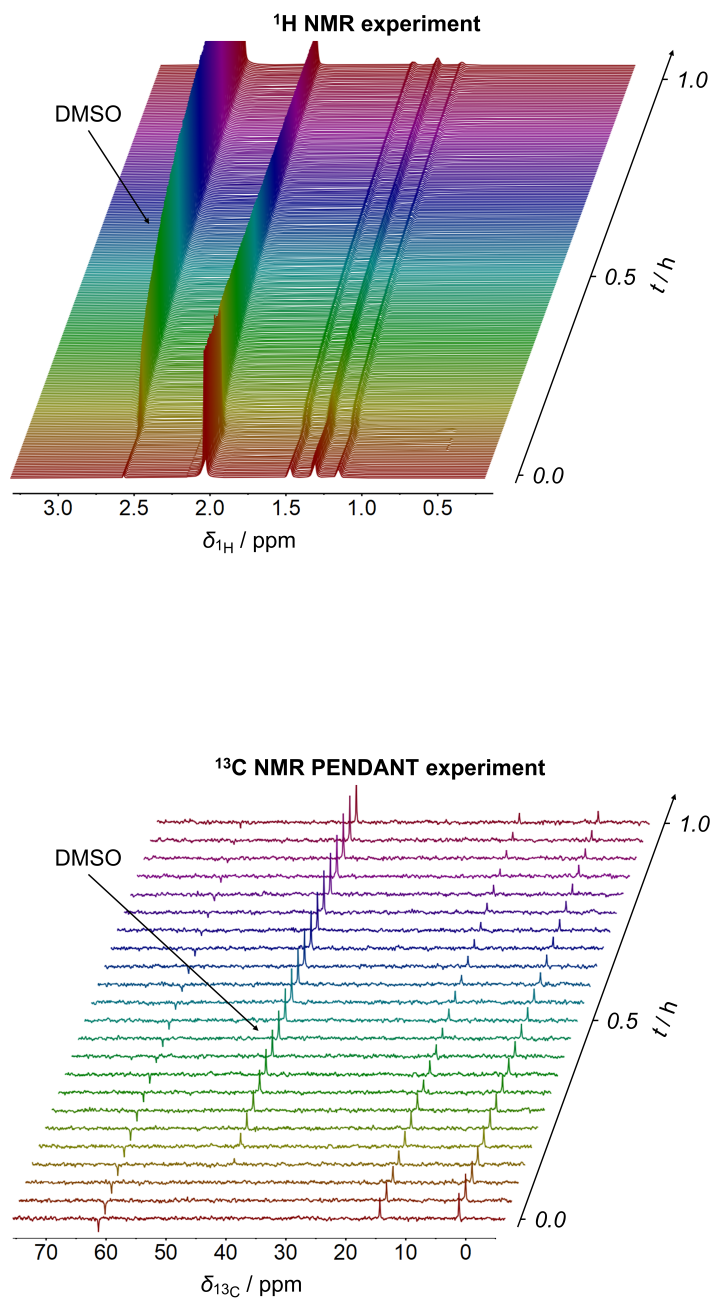
Figure 14: Monitoring of a dilution experiment in System 1 with ^{1}H NMR and ^{13}C NMR PENDANT experiments. DMSO was continuously added to a binary mixture of ACN + EF (initial concentration x_{ACN} = 0.6 mol mol^{-1}) within a time interval of 1 h (corresponding to a dosage rate of $\dot{V}$ = 0.833 ml min^{-1}).
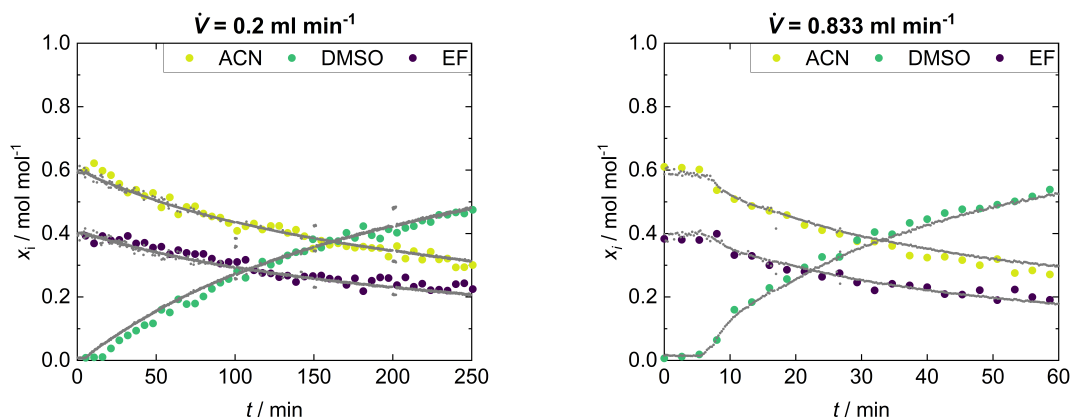
Figure 15: Results of the quantitative analysis of System 1 with ^{1}H NMR and ^{13}C NMR PENDANT during the monitoring of a continuous dilution experiment. DMSO was continuously added to a binary mixture of ACN + EF (initial concentration x_{ACN} = 0.6 mol mol^{-1}) within 4 h (dosage rate: $\dot{V}$ = 0.2 ml min^{-1}, left) and 1 h (dosage rate: $\dot{V}$ = 0.833 ml min^{-1}, right), respectively. The gray circles (appearing as gray lines due to the high acquisition rate) represent the concentrations determined by ^{1}H NMR. The colored circles are from ^{13}C NMR PENDANT. The error bars are not shown for clarity.

For both experiments, there is a time lag of about 5 min, until the concentration change can be observed, which is, however, better visible in the results for the high dosage rate. As expected, the concentration changes, resulting from the addition of DMSO with a constant flow rate, are not linear. The concentrations determined with ^{13}C NMR PENDANT are in very good agreement with those from ^{1}H NMR. The scattering of the results from ^{13}C NMR PENDANT is about 0.04 mol mol^{-1}, which is a consequence of the low number of 16 scans that was used, but a smoothing of the results obtained at different times would obviously lead to a result that is very close to the ^{1}H NMR reference. Similar results from ^{13}C NMR PENDANT could be expected for System 2, for which, however, ^{1}H NMR would have given only poor results due to the peak overlap (see Section 3.3.2), and ^{13}C NMR could not be reasonably used with only 16 scans due to the low SNR.

3.4 Conclusions

The polarization transfer sequence PENDANT was applied for the first time for the quantitative analysis of mixtures in stationary and flow experiments with benchtop ^{13}C NMR spectroscopy. The new method combines three advantages: fast premagnetization, high spectral resolution, and good SNR. The accuracy and reliability of quantitative results obtained with ^{13}C NMR PENDANT were evaluated and compared with

results from ^{1}H NMR, ^{13}C NMR, and a gravimetric reference. It was shown that ^{13}C NMR PENDANT gives excellent results also at conditions where ^{13}C NMR without polarization transfer cannot be applied, e.g. in measurements at high flow rates that cause problems in the analysis with benchtop NMR spectrometers, due to their low premagnetization volume. The new method is particularly attractive for the analysis of mixtures that are difficult to quantify with ^{1}H NMR due to overlapping peaks. Furthermore, it was demonstrated that ^{13}C NMR PENDANT is useful for monitoring dynamic processes.

4 Determination of Self-Diffusion Coefficients in Mixtures via Polarization Transfer

4.1 Introduction

In this work, the approach described in the previous chapter to apply PENDANT in benchtop ^{13}C NMR spectroscopy is used to determine self-diffusion coefficients.

The self-diffusion coefficient characterizes the mobility of individual molecules and is, hence, of fundamental interest in many fields of science and engineering [99, 100]. Data of self-diffusion coefficients are used e.g. to test molecular models and to characterize molecular interactions [99, 101–105]; for determining hydrodynamic radii [106]; to characterize restricted diffusion in pores and cells [107–111]; and for the characterization of complex mixtures such as process streams in biotechnology, lubricants or beverages [100, 112–116]. They are also used in pharmaceutical quality control for the detection of possible product frauds [117, 118].

The self-diffusion coefficient of an infinitely dilute component in a mixture is equal to the mutual diffusion coefficient [119, 120]. The mutual diffusion coefficient is an extremely important property for the design of all mass transfer processes [121, 122]. Methods used for predicting mutual diffusion coefficients at finite concentrations usually need data at infinite dilution as input [122]. Therefore, results from measurements of absolute values of self-diffusion coefficients of highly diluted species are directly relevant for many technical applications.

Self-diffusion coefficients can be determined experimentally with dynamic light scattering [123], tracer measurements [124], neutron scattering [125], and nuclear magnetic resonance (NMR) with pulsed field gradients (PFG) [126]. From these methods, PFG-NMR is well established as it allows chemically resolved measurements of self-diffusion coefficients even in complex mixtures without perturbing the investigated systems.

The measurement of self-diffusion coefficients in PFG-NMR experiments can be achieved by applying two gradient pulses to spatially label the molecules. The first gradient

pulse alters the precession phase and encodes the molecules in dependency of their position in the sample. The second decoding gradient pulse reverses the phase shifts in stationary molecules. However, due to the molecular motion by self-diffusion in the magnetic gradient field the phase shift cannot be fully reversed. The resulting spin echo (SE) or stimulated spin echo (STE) is attenuated depending on the magnitude of the self-diffusion coefficient of the observed molecules. The experiment is repeated several times with incrementally increasing gradient strength. The Stejskal-Tanner equation is fitted to the attenuated NMR signals from which the self-diffusion coefficient can be determined as a fitting parameter [127]. Note, that flow and temperature gradients induce convection within the sample which can cause additional signal attenuation and can lead to wrong results for the self-diffusion coefficient. Special pulse sequences with flow compensation are available which tackle this issue [128]. In PFG-NMR experiments the gradient has to be calibrated only once. Afterwards, it is a calibration free method. Usually, high-field NMR spectrometers are used for such measurements of self-diffusion coefficients but also benchtop instruments equipped with a gradient system can be used [129].

The ^{1}H nucleus is mostly used for benchtop NMR measurements, especially for the determination of self-diffusion coefficients, because of its high gyromagnetic ratio resulting in high sensitivity of this nucleus. However, the investigation of multi-component mixtures is often hindered by peak overlapping problems in the ^{1}H NMR spectrum because of the low chemical shift dispersion. This is particularly serious for benchtop NMR due to the restricted field strength and thus inherently low resolution. Some pulse sequences exist, for example pure-shift or Oneshot 45, which are able to partly fix this issue and are already tested on benchtop NMR spectrometers [130–133]. There are also studies to use lanthanide shift reagents to enhance the chemical shift dispersion [134]. But the differentiation of single species and therefore the precise determination of the self-diffusion coefficient is often infeasible with benchtop NMR in mixtures.

Another way of tackling this problem is to use mathematical methods such as Direct Exponential Curve Resolution Algorithm (DECRA) [135], Multivariate Curve Resolution (MCR) [136], Speedy Component Resolution (SCORE) [137] or a QM model-based approach [138]. However, all these methods need additional software packages and expert knowledge to apply the fitting procedure properly on the crowded ^{1}H NMR spectrum and cannot fully resolve the problems resulting from overlapping peaks. In Diffusion Ordered Spectroscopy (DOSY) NMR experiments species in complex mixture are distinguished by correlating the NMR signals with corresponding self-diffusion coefficients via a data inversion process [99, 139, 140] (Note, that the acronyms PFG-NMR and DOSY experiments might be used as synonyms to describe the measurement of self-diffusion coefficients [110].) However, in ^{1}H NMR spectra where peak overlap is severe,

the discrimination of different molecules by DOSY is hampered by large uncertainties in the determined self-diffusion coefficients.

Hence, the usage of nuclei with greater chemical shift dispersion, such as the ^{13}C nucleus, is highly desirable [141–144]. However, ^{13}C NMR experiments suffer from a low SNR due to the low natural abundance and gyromagnetic ratio of ^{13}C. Furthermore, the low gyromagnetic ratio requires the application of stronger magnetic field gradients than for the diffusion encoding via ^{1}H nuclei. In addition, the spin-lattice relaxation time T_1 of ^{13}C nuclei is much longer than that of ^{1}H nuclei, leading to long measurement times.

To overcome these problems, polarization transfer methods have been developed, which transfer the high and rapidly restored polarization of ^{1}H nuclei to ^{13}C nuclei. These methods considerably improve the sensitivity of ^{13}C NMR spectroscopy and greatly reduce the experimental time because fewer scans are required. Moreover, the experiments can be repeated at a high rate as the repetition time for the polarization transfer is dictated by the T_1 of the ^{1}H instead of that of the ^{13}C nuclei which further reduces the experimental time. However, in the diffusion encoding step of a PFG-NMR experiment, the ^{13}C nuclei still relax with their inherent relaxation time. This is advantageous because the longer relaxation times T_1 and T_2 of the ^{13}C nucleus can be used to achieve longer diffusion times which is beneficial for the measurement of macromolecules. Several pulse sequences have been described in the literature in which polarization transfer techniques were coupled to ^{13}C DOSY sequences: INEPT-DOSY, DEPT-DOSY and DEPTSE as well as the 3D sequence HSQC-iDOSY [145–152]. The mentioned pulse sequences are frequently implemented on high-field NMR spectrometers.

However, ^{13}C PFG-NMR with signal enhancement by polarization transfer methods has not yet been studied on benchtop NMR spectrometers. In addition, the often used polarization transfer pulse sequences INEPT and DEPT sacrifice the signals of quaternary carbons. In contrast, the less popular polarization transfer pulse sequence PENDANT of Homer & Perry combines the features of sufficient signal enhancement and the selective excitation of functional carbon groups (CH$_3$, CH$_2$, CH) with the additional ability to detect quaternary carbons [95, 96].

In this work, the polarization transfer sequence PENDANT is combined with the PFG-SE sequence in order to obtain absolute values of self-diffusion coefficients via ^{13}C NMR spectroscopy on a 1 T benchtop NMR spectrometer [127]. The SE sequence was chosen here rather than the more common STE sequence due to its simplicity and because there is no significant problem with homonuclear coupling for ^{13}C nuclei (unless labelled samples are measured). Furthermore, the ^{13}C spin-spin relaxation time T_2 is nearly the same as the ^{13}C spin-lattice relaxation time T_1 for small molecules allowing the use of the SE sequence [150, 153]. The new combined pulse sequence is called PENPFG. The PENPFG experiment was implemented on a 1 T benchtop NMR spectrometer and

was applied to determine the self-diffusion coefficients of acetonitrile (ACN), ethanol (EtOH) and 1-propanol (PrOH) in the pure substances as well as in their three binary mixtures and in their ternary mixture at different compositions. All experiments were carried out at ambient pressure and at T = 301.65 K, which is the operating temperature of the benchtop NMR spectrometer that was used. For comparison, the measurements were repeated with a high-field NMR spectrometer using standard PFG-NMR routines previously used for studying many other systems and which were validated by comparison with literature data [104, 121, 122]. For completeness, the PENPFG sequence was also implemented on the high-field NMR spectrometer and the corresponding results are reported here and included in the comparison. The aim of this work is to demonstrate that the absolute value of the self-diffusion coefficient can be precisely and reliably determined by PENPFG on a benchtop NMR spectrometer.

4.2 Experimental Section

4.2.1 Hardware and Experimental Procedure

The PENPFG experiment is a combination of the polarization transfer sequence PENDANT (signal enhancement) and the PFG-SE sequence (diffusion encoding) as illustrated in Figure 16. The PENDANT sequence, including the evolution delays and pulse phases, was implemented as published by Homer & Perry [95, 96]. The evolution delays are given by Equations (5) and (6).

$$d_1 = \frac{1}{4\,^1J_{C,H}} \tag{5}$$

$$d_2 = \frac{5}{8\,^1J_{C,H}} \tag{6}$$

Here, $^1J_{C,H}$ is the coupling constant between the carbon and the scalar coupled proton. The coupling constant was set to $^1J_{C,H}$ = 140 Hz for all PENPFG experiments. The value was determined by experiments and is a compromise for $^1J_{C,H}$ so that CH_3, CH_2 and CH-groups are all enhanced. The enhancement does not reach the possible maximum for each group, but this is not necessary since only the relative signal attenuation is considered during the PFG-NMR experiments. In the PENPFG experiment, the first 90° pulse of the original PFG-SE sequence is replaced by the PENDANT sequence. The refocusing 180° pulse of the regular PFG-SE sequence is following which separates the two gradient pulses for the phase encoding. Decoupling (WALTZ-16) is applied during the acquisition.
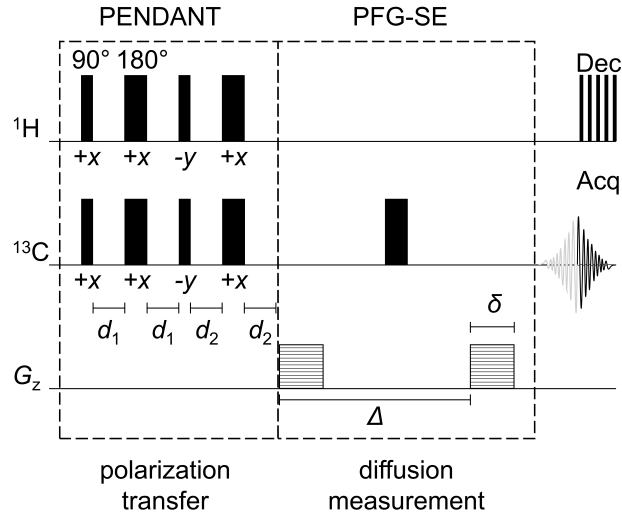
Figure 16: Illustration of the PENPFG pulse sequence for the measurement of self-diffusion coefficients with ^{13}C NMR spectroscopy, consisting of the polarization transfer pulse sequence PENDANT for signal enhancement and the PFG-SE sequence for diffusion encoding. The delays d_1 and d_2 depend on the ^{13}C-^{1}H $^1J_{\text{C,H}}$-coupling constants. Δ denotes the diffusion time and δ the gradient pulse duration.

PENPFG and ^{1}H PFG-NMR (for the evaluation of PENPFG) experiments were carried out on a benchtop NMR spectrometer from Magritek (Spinsolve Carbon) with a magnetic field strength of B_0 = 1 T corresponding to a ^{1}H Larmor frequency of ν_0 = 42.5 MHz. The benchtop NMR spectrometer is equipped with a gradient coil with a maximum gradient strength of G = 15.7 G cm^{-1} and operates at a temperature of T = 301.65 K. The gradient is aligned perpendicular to the NMR tube in order to reduce influences from convection. Standard sample tubes with an outer diameter of d = 5.0 mm from Magritek were used for the measurements. The PENPFG experiment was implemented with the software Spinsolve Expert (Magritek) for the operation on the benchtop NMR spectrometer and is referred to as ^{13}C BT PENPFG in the following. The code of the pulse sequence is given in the Appendix C. For the reference ^{1}H PFG-NMR experiments, the PFG-STE sequence (referred to as ^{1}H BT PFGSTE here) was used as provided by the standard Magritek operating software Spinsolve. The self-diffusion coefficients of the species were determined from the acquired NMR signals with a modified Stejskal-Tanner equation according to Equation (7):

$$I_i = I_{0,i} \exp\left(-D_i \gamma^2 G^2 \left(\delta_{\text{eff}}^2 \left(\Delta - \frac{\delta_{\text{eff}}}{3}\right)\right)\right) \tag{7}$$

Here, I is the signal intensity, I_0 is the signal intensity without gradient, γ is the gyromagnetic ratio of the investigated nucleus, G is the gradient strength and Δ is the diffusion time. As the applied magnetic field gradient has a trapezoidal shape, δ_{eff} (which is defined as the sum of the gradient pulse duration δ and the gradient ramp time τ_{grad} as shown in Equation 8) needs to be used in the Stejskal-Tanner equation to assume a rectangular pulse. The linear ramp prevents distortion of the acquired NMR signal. A complete Stejskal-Tanner equation, which also includes the correction of the trapezoidal shape of the gradient pulse, is given in the Appendix C. However, the correction can be neglected as τ_{grad} is small.

$$\delta_{\text{eff}} = \delta + \tau_{\text{grad}} \tag{8}$$

For ^{1}H BT PFGSTE as well as for ^{13}C BT PENPFG the diffusion time was set to Δ = 50 ms. The gradient strength was incrementally increased in 16 steps ranging from G = 1.8 to 15.7 G cm^{-1} for both cases (in equal steps of G^2). The gradient ramp time τ_{grad} was set to τ_{grad} = 0.1 ms for all experiments. The gradient pulse duration δ of ^{13}C BT PENPFG was longer than in the ^{1}H BT PFGSTE because of the lower gyromagnetic ratio of the ^{13}C nucleus and the benchtop NMR spectrometer's weak maximum gradient strength. In order to obtain a NMR signal attenuation of approximately 90 to 95 % at the strongest gradient strength the duration of the gradient pulse δ was set to values between δ = 2 to 7 ms for ^{1}H BT PFGSTE and to values between δ = 9 to 23 ms for ^{13}C BT PENPFG, respectively. The diffusion time Δ includes the gradient pulse duration δ in order to keep the absolute diffusion time constant for each experiment. However, the effective Δ (defined as the delay between the end of the dephasing and the beginning of the rephasing gradient) is different. Note, that the short gradient pulse approximation (SGP) needs to be considered if porous systems are investigated [154–156]. Spectra of ^{1}H BT PFGSTE were acquired with 4 scans and an acquisition time (time for acquiring the FID) of 3.2 s. For ^{13}C BT PENPFG 128 scans and an acquisition time of 3.2 s were applied. In all experiments a relaxation delay of 25 s was used to ensure sufficient relaxation of the sample with at least 5 times T_1 regarding the relaxation time of the ^{1}H nuclei. This set of parameters results in a total measurement time of about 14 h for one ^{13}C BT PENPFG experiment, which could be reduced by the modification of the repetition delay as well as the number of gradient steps. In comparison, the measurement of self-diffusion coefficients on ^{13}C nuclei without polarization transfer is not feasible because it requires at least a doubling of the number of scans, which is incompatible with the lock stability of the benchtop NMR spectrometer during this long measurement time.

For the validation of the results obtained on the benchtop NMR spectrometer ^{1}H and ^{13}C PFG-NMR as well as PENPFG experiments were also performed on a high-field NMR spectrometer with a superconducting magnet and a magnetic field strength of B_0 = 9.4 T corresponding to a [1]H Larmor frequency of ν_0 = 400.25 MHz (Bruker Biospin magnet Ascend 400, console Avance III HD 400, probe BBFO). Special sample tubes optimized for diffusion measurements with an outer diameter of d = 2.5 mm (Deutero) were used to prevent radiation damping and to reduce sample convection. The temperature of the high-field NMR spectrometer was set to T = 301.65 K to match the operation tempe-rature of the benchtop NMR spectrometer. ^{1}H as well as ^{13}C PFG-NMR experiments were executed with STE pulse sequences with bipolar pulsed gradients (called ^{1}H HF PFGSTE and ^{13}C HF PFGSTE in the following, respectively). These sequences were already implemented (as stebpgp1s) in the spectrometer's operating software TopSpin. The PENPFG sequence was manually implemented on the high-field NMR spectrometer with TopSpin (referred to as ^{13}C HF PENPFG). All sequences on the high-field NMR spectrometer apply the SMSQ10.100 gradient pulse. Self-diffusion coefficients of the species were determined with Equation (7) for ^{13}C HF PENPFG experiments while a modified Stejskal-Tanner equation was used for the evaluation of ^{1}H HF PFGSTE and ^{13}C HF PFGSTE. This modified Stejskal-Tanner equation is displayed in Equation (9):

$$I_i = I_{0,i} \exp\left(-D_i \gamma^2 G^2 \left(\Delta - \frac{\delta}{3} - \frac{\tau}{2}\right)\right) \tag{9}$$

In Equation (9), τ is the correction parameter for the usage of bipolar gradients and was chosen as τ = 0.2 ms. Similar to the benchtop NMR spectrometer experiments the diffusion time was set to Δ = 50 ms in all experiments. The gradient strength G of the high-field NMR spectrometer was incremented in 16 steps from G = 2.3 to 43.1 G cm⁻¹ (again in equal steps of G^2). To obtain a NMR signal attenuation of approximately 90 to 95 % at the strongest gradient strength the duration of the gradient pulse δ was adjusted between δ = 0.6 to 1.0 ms for ^{1}H HF PFGSTE and to values between δ = 2.1 to 7.0 ms for ^{13}C HF PFGSTE as well as ^{13}C HF PENPFG, respectively. Each high-field diffusion experiment consisted of 16 scans with an acquisition time of 5 s for ^{1}H HF PFGSTE and 4 s for ^{13}C HF PFGSTE as well as for ^{13}C HF PENPFG. The repetition delays for ^{1}H HF PFGSTE, ^{13}C HF PFGSTE and ^{13}C HF PENPFG are given in the Appendix C and are set to ensure a complete relaxation of the sample (5 x T_1). The molecule with the longest T_1, which was determined in the pure component, is considered to be decisive for the repetition delays in the mixture.

From previous work, it is known that the expanded relative uncertainty for the mea-surement of self-diffusion coefficients with the high-field NMR spectrometer used in this work can be estimated to be 2 % [104]. All experiments were repeated three times to

calculate the root mean squared error (RMSE) of the self-diffusion coefficients which are depicted as error bars in this work. The baseline and the phase of the acquired spectra of all experiments from the benchtop NMR as well as the high-field NMR spectrometer were manually corrected with MestRenova (Mestrelab Research). The analysis of the signal attenuation was also executed in MestRenova by direct peak integration. The determination of the self-diffusion coefficients with the Stejskal-Tanner equations (Equation (7) and (9), respectively) was performed with nonlinear least-square fits using MATLAB's (MathWorks Inc.) *lsqnonlin* solver.

4.2.2 Chemicals and Studied Mixtures

Table 5 gives an overview of the chemicals that were used in this work, including their formulas, the suppliers, and the specified purities. In this study, the self-diffusion coefficients of the molecules were determined in pure components as well as in binary and ternary mixtures. The molecular structures of the components are not complex, however, they are suitable to demonstrate the methodology since the ^{1}H NMR spectrum's complexity is considerably increasing from pure components to ternary mixtures. Figure 17 gives an overview of the mixtures investigated in this work. The samples were prepared gravimetrically using a laboratory balance (AG204, Mettler Toledo Inc.) with an accuracy of $\pm\,0.0001$ g. The total mass of each sample was approximately $m = 2$ g, from which the required amount of sample for the NMR experiments was taken.

Table 5: Chemicals used in this work including the suppliers and the purities as specified by the suppliers.

Chemical	Formula	Supplier	Purity
Acetonitrile (ACN)	C_2H_3N	Carl Roth	$\geq 99.9\%$
Ethanol (EtOH)	C_2H_6O	Merck	$\geq 99.9\%$
1-Propanol (PrOH)	C_3H_8O	Honeywell Specialty Chemicals	$\geq 99.5\%$
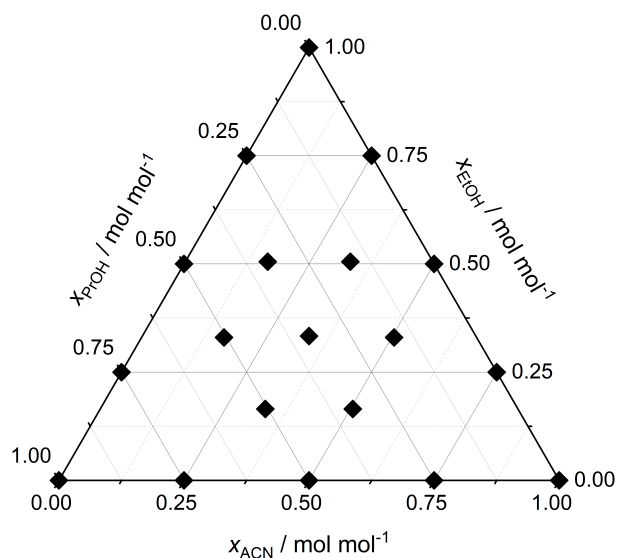
Figure 17: Overview of the studied mixtures consisting of acetonitrile ACN, ethanol EtOH and 1-propanol PrOH.

4.3 Results and Discussion

Figure 18 presents ^{1}H NMR spectra of an equimolar mixture of ACN + EtOH + PrOH acquired with a benchtop NMR spectrometer and a high-field NMR spectrometer to illustrate the problem of peak overlap in the benchtop NMR spectrometer due to reduced spectral resolution. The peak nomenclature and the assignment of the protons of the single species to the corresponding NMR signals is included. Note, that there is a peak splitting observed for the OH-groups of EtOH and PrOH (H4/H8) because the sample is free of water.

The signals acquired at high-field are well resolved, sharp and well separated enabling quantification by direct integration. In contrast, the signals of the different species strongly overlap in the benchtop ^{1}H NMR spectrum. Especially, the CH$_3$-group signals of EtOH and PrOH as well as the CH$_2$-group signal of PrOH in the region of 0.5 to 2 ppm cannot be distinguished from each other. The same holds for the CH$_2$-group signals of both alcohol molecules in the area around 3.5 ppm. Standard analysis methods, such as a direct integration of peak areas, fail in this situation. Only the signal of ACN can be clearly identified due to the singlet signal of its CH$_3$-group. This illustrates that the distinction of molecules and the integration of the signals is often challenging in benchtop ^{1}H NMR spectra, even for only moderately complex systems.
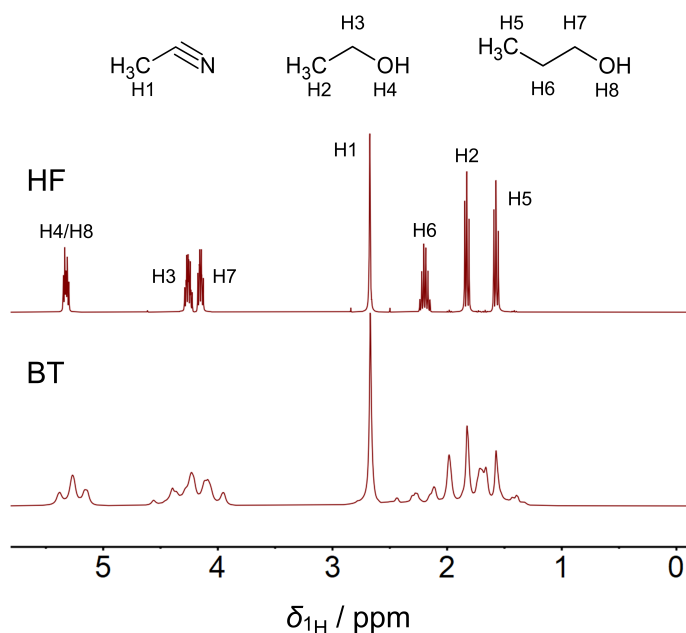
Figure 18: Comparison of ^{1}H NMR spectra of an equimolar mixture of ACN + EtOH + PrOH acquired in a high-field (HF, top) and a benchtop NMR spectrometer (BT, bottom). Also the peak assignment is indicated.

Figure 19 displays ^{13}C NMR spectra of the same mixture, for which the ^{1}H NMR spectra are shown in Figure 18, without and with polarization transfer acquired with the benchtop NMR spectrometer. Due to the large chemical shift dispersion of ^{13}C NMR, the signals of all components can be easily distinguished. However, measurements relying only on the thermal polarization of ^{13}C spins (top panel in Figure 19) at the low magnetic field strength of the benchtop NMR spectrometer result in low SNR and long measurement times because of the huge number of scans required for sufficient signal accumulation. This problem is amplified by the long T_1 relaxation time of ^{13}C resulting in a total measurement time for the ^{13}C NMR spectrum of 3.2 h. Figure 19 also shows a ^{13}C NMR spectrum acquired using polarization transfer with PENDANT. This increases the SNR by a factor of about 3.5. The theoretical maximum enhancement of the SNR of 4 is not reached since an average $^1J_{C,H}$-coupling constant was chosen. Note, that the signal of the CN-group of ACN at around 120 ppm is not clearly visible in the ^{13}C NMR spectrum regardless the application of polarization transfer. This observation is attributed to the fact that the T_2 relaxation time for the CN-group is short, leading to a broadening of this peak. The polarization transfer is not able to enhance the CN-group signal due to the lack of scalar coupled protons attached directly at the respective carbon atom.

The total measurement time for the ^{13}C PENDANT NMR spectrum is considerably shortened (total measurement time 0.9 h) due to two reasons: the signal enhancement reduces the necessary number of scans and also the repetition time is reduced due to the shorter T_1 time of protons. In addition, PENDANT allows a discrimination between the CH$_3$-, CH$_2$- and CH-groups of the organic molecules that result in either positive or negative peaks in the spectrum (cf. Figure 19). This is highly beneficial for the identification of components in complex multi-component mixtures.
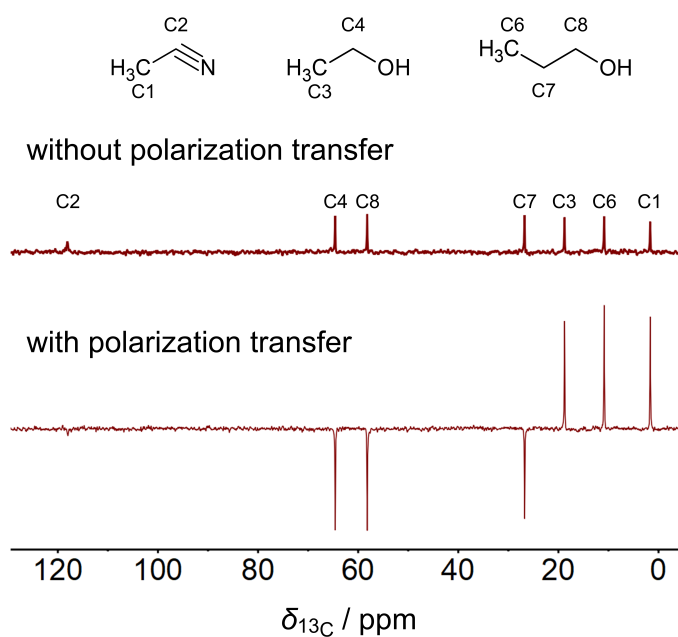
Figure 19: Comparison of ^{13}C NMR spectra of an equimolar mixture of ACN + EtOH + PrOH acquired without (top) and with the polarization transfer sequence PENDANT (bottom) in a benchtop NMR spectrometer. Also the peak assignment is indicated.

4.3.1 Pure Components

Figure 20 displays self-diffusion coefficients of the pure components ACN, EtOH and PrOH measured with different experiments with the high-field as well as with the bench-top NMR spectrometer. The numerical results are given in the Appendix C. Furthermore, the error bars calculated by the RMSE as well as the errors caused by the fit of Stejskal-Tanner equation are shown in the Appendix C. In each experiment, only the signals of the CH$_3$-groups were used for the analysis of the self-diffusion coefficients. The self-diffusion coefficients obtained with ^{1}H HF PFGSTE are considered as the ground truth in this work and are used to evaluate the results of the other experiments. They are additionally depicted as horizontal lines in Figure 20. The relative deviations of all experiments is provided on the right side of Figure 20.
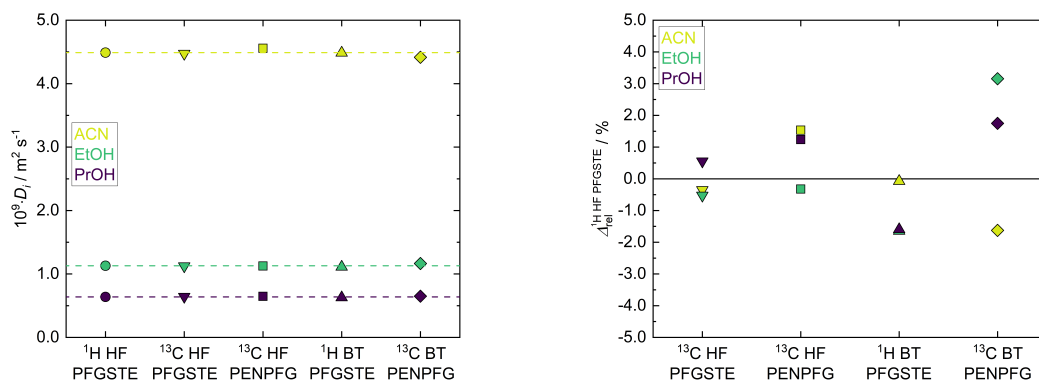
Figure 20: Left: Comparison of the experimental results of different NMR techniques for the self-diffusion coefficients of the pure components ACN, EtOH and PrOH at T = 301.65 K. The symbols indicate results obtained with the different methods and instruments (HF high-field, BT benchtop; PFG-STE standard experiment, PENPFG experiment with polarization transfer). The dashed horizontal lines represent the reference measurement with ^{1}H HF PFGSTE. All error bars are within the symbol size (further details are given in the Appendix C). Right: Relative deviations of the results obtained by different NMR techniques compared with the reference method ^{1}H HF PFGSTE.

As expected, the self-diffusion coefficient of ACN is the highest due to its molar mass of M_{ACN} = 41.05 g mol^{-1}, which is the lowest of the three substances studied. PrOH has the lowest self-diffusion coefficient due to its high molar mass of M_{PrOH} = 60.09 g mol^{-1} and because it forms H-bonded clusters.

The results for the self-diffusion coefficients of all studied substances obtained with the different methods are in excellent agreement. The relative deviation of the results from the reference value from ^{1}H HF PFGSTE is below 3 %. The results from ^{13}C HF PENPFG agree well with those from ^{1}H HF PFGSTE and ^{13}C HF PFGSTE experiments. Therefore, it can be concluded that the combination of the polarization transfer sequence PENDANT with the selected diffusion encoding sequence PFG-SE is suitable for the accurate measurement of self-diffusion coefficients.

There is also an excellent agreement of the values obtained with ^{1}H BT PFGSTE and ^{13}C BT PENPFG with the reference values from ^{1}H HF PFGSTE proving the benchtop NMR spectrometer's reliability to deliver precise self-diffusion coefficients. It should be noted that the acquisition with ^{1}H BT PFGSTE is only possible in simple systems, in which peaks do not overlap. This approach fails already for the mixture of the three solvents as shown in Figure 18. Therefore, ^{13}C BT PENPFG expands the horizon of systems for which diffusion coefficients can be measured with benchtop NMR spectrometers. All in all, Figure 20 shows that the new method PENPFG delivers reliable results

on a benchtop NMR spectrometer.

4.3.2 Binary Mixtures

In the studies of binary mixtures the ^{13}C BT PENPFG experiments are compared with the reference experiments carried out with ^{1}H HF PFGSTE. Figure 21 shows the measured self-diffusion coefficients of ACN, EtOH and PrOH in the three binary mixtures. The numerical results are given in the Appendix C. Again, only the CH$_3$-groups of the specific molecules were considered for the determination of the self-diffusion coefficients. The diagrams in Figure 21 display the self-diffusion coefficients of each component in dependency of the mixture's composition. Because of the small differences between the self-diffusion coefficient of EtOH and PrOH, the ordinate of the respective diagram is magnified by a factor of 10 for better visualization. In all mixtures, the component with the higher self-diffusion coefficient as pure component has also the higher value in the binary mixtures. By increasing the mole fraction of the fast diffusing component, the self-diffusion coefficients of both components gradually increase.

In the binary mixtures ACN + EtOH and ACN + PrOH the self-diffusion coefficient of ACN substantially exceeds those of EtOH and PrOH. These two mixtures show a similar behaviour: the relative small molecule ACN forms no hydrogen-bonds in the bulk phase resulting in a fast molecular motion. However, in the binary mixture EtOH + PrOH the components EtOH and PrOH have similar molar masses and associate via hydrogen-bonding. This results in very similar self-diffusion coefficients.

The results from ^{13}C BT PENPFG are in very good agreement with the results from ^{1}H HF PFGSTE. The mean relative deviation of the results from ^{13}C BT PENPFG to the reference values from ^{1}H HF PFGSTE is typically below 3 %. A maximum relative deviation of 6 % to the reference values is identified for EtOH in the binary system EtOH + PrOH. However, the ability to distinguish between the two alcohols EtOH and PrOH, which have similar molar masses as well as molecular dynamics and therefore similar self-diffusion coefficients, shows that the benchtop NMR spectrometer in combination with the PENPFG sequence is a powerful tool.
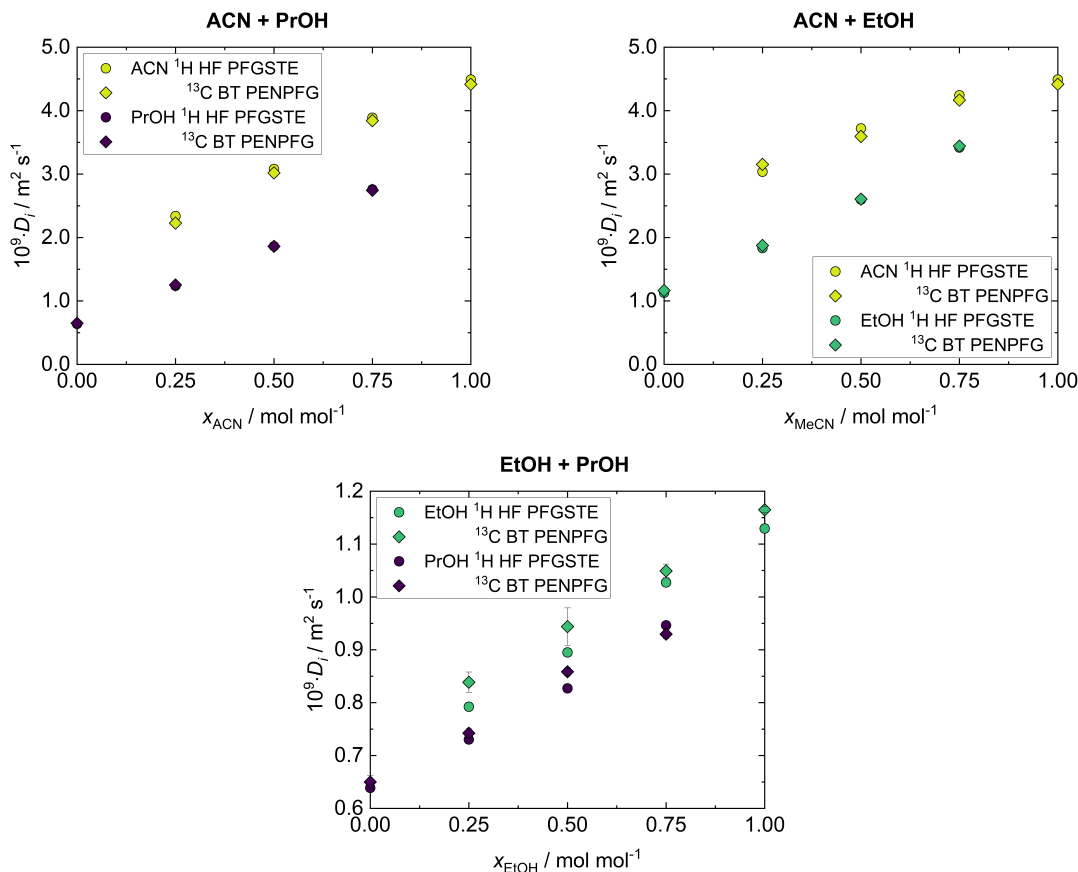
Figure 21: Comparison of results of measurements of self-diffusion coefficients of ACN, EtOH and PrOH in the binary mixtures ACN + PrOH, ACN + EtOH and EtOH + PrOH at T = 301.65 K. The diamonds stand for results obtained with ^{13}C BT PENPFG, the circles for the results from ^{1}H HF PFGSTE. For the binary mixture EtOH + PrOH the vertical scale is magnified by a factor of 10. Error bars are only shown if they are larger than the symbol size.

4.3.3 Ternary Mixtures

Figure 22 depicts the self-diffusion coefficients of the seven investigated ternary mixtures of ACN + EtOH + PrOH obtained with ^{13}C BT PENPFG and ^{1}H HF PFGSTE. The numerical results are summarized in the Appendix C. Self-diffusion coefficients obtained from the CH$_3$-groups of ACN, EtOH and PrOH were used for the comparison of ^{13}C BT PENPFG with the reference measurements ^{1}H HF PFGSTE. In the parity plot in Figure 22 the self-diffusion coefficients of each species obtained with ^{13}C BT PENPFG are plotted against the results from ^{1}H HF PFGSTE. An overview of all self-diffusion coefficients of the pure components ACN, EtOH and PrOH as well as the obtained values in the binary and ternary mixtures determined with ^{13}C BT PENPFG is given in the Appendix C.
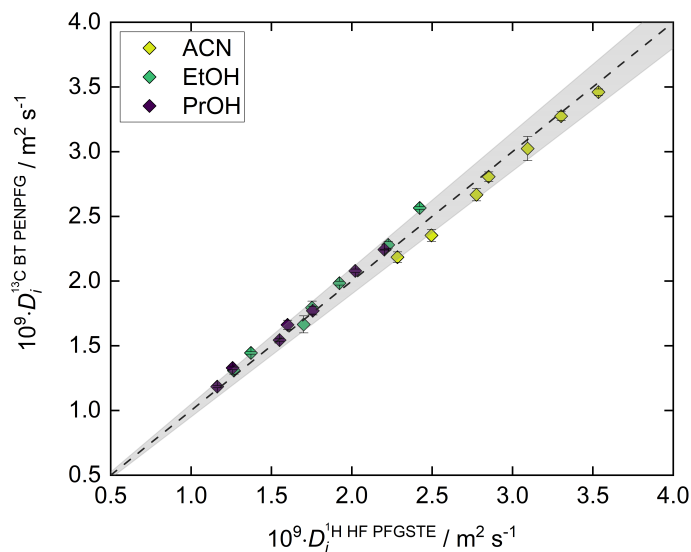
Figure 22: Self-diffusion coefficients of ACN, EtOH and PrOH in ternary mixtures of ACN + EtOH + PrOH at T = 301.65 K measured with ^{13}C BT PENPFG. The parity plot compares the results from ^{13}C BT PENPFG to the reference values from ^{1}H HF PFGSTE. The gray shaded area indicates relative deviations below 5 %.

The comparison of the results of ^{13}C BT PENPFG with the corresponding results from ^{1}H HF PFGSTE shows very good agreement. The maximum relative deviation does not exceed 5 %, the mean relative deviation is again only about 3 %. The comparison shows that the benchtop NMR spectrometer in combination with the PENPFG experiment is able to measure precisely the self-diffusion coefficients of a complex mixture.

Figure 23 shows the self-diffusion coefficients obtained from the analysis of all individual peaks of the ^{13}C NMR spectrum of the ternary system ACN + EtOH + PrOH by ^{13}C BT PENPFG as well as ^{13}C HF PENPFG. The numerical results are given in the Appendix C. For the reference experiment ^{1}H HF PFGSTE only the CH$_3$-groups of the specific molecules were considered. They are depicted as horizontal lines in Figure 23. The resulting 2D NMR spectrum allows a differentiation of the molecules in the mixture due to their specific self-diffusion coefficients (DOSY spectrum).

Despite the fact that ACN has two carbon atoms, only one value is shown in Figure 23 because the ^{13}C SNR of the CN-group is insufficient for quantitative evaluation. All values are in good agreement with the corresponding reference values from the high-field NMR spectrometer indicated by the horizontal lines. In addition, the results obtained by ^{13}C BT PENPFG are in very good agreement with the results of ^{13}C HF PENPFG. It can therefore be concluded that differentiation between ACN, EtOH and PrOH in a DOSY experiment is possible by using a benchtop NMR spectrometer in combination

with the ^{13}C BT PENPFG experiment. This differentiation is even successful for EtOH and PrOH which have very similar self-diffusion coefficients.
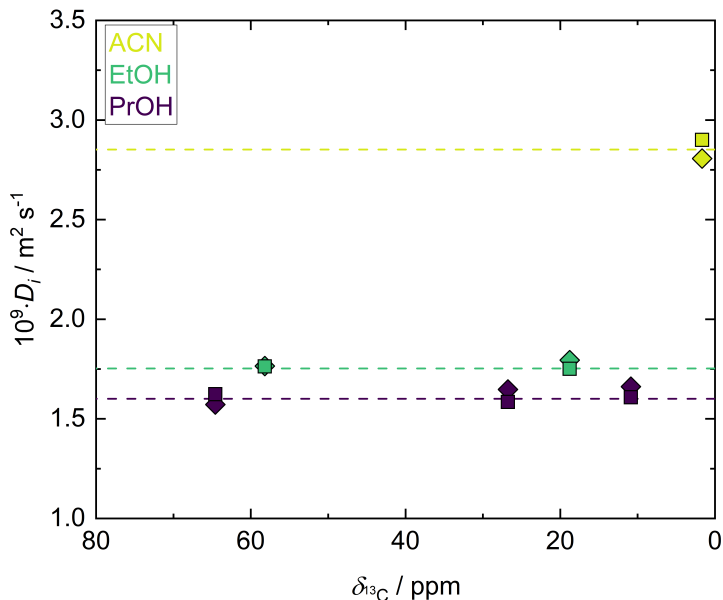
Figure 23: DOSY representation of an equimolar mixture of ACN + EtOH + PrOH at T = 301.65 K. The squares and diamonds indicate results from ^{13}C HF PENPFG and ^{13}C BT PENPFG. The dashed horizontal lines represent the reference measurement with ^{1}H HF PFGSTE, obtained by the analysis of the CH$_3$-group of the specific molecules. All error bars are within the symbol size.

4.4 Conclusions

In this work, a new pulse sequence, PENPFG, was developed which combines the proton-carbon polarization transfer sequence PENDANT with the diffusion encoding sequence PFG-SE. The sequence enables the determination of self-diffusion coefficients in mixtures on benchtop NMR spectrometer by ^{13}C nuclei as it combines the following advantages: high chemical shift dispersion, signal enhancement and fast measurement times. The new sequence was tested by measuring the self-diffusion coefficients of acetonitrile (ACN), ethanol (EtOH), and 1-propanol (PrOH) as pure components as well as in binary and ternary mixtures on a 1 T benchtop NMR spectrometer. For reference, the same systems were investigated by high-field ^{1}H and ^{13}C PFG-NMR, and, where possible, by ^{1}H PFG-NMR experiments on the benchtop instrument. Good agreement was found in all cases. All experiments were performed at T = 301.65 K, the operating temperature of the benchtop NMR system used. Recently, however, benchtop NMR spectrometers have

become available that operate at temperatures up to 338.15 K, which greatly increases the applicability of the new method. Moreover, new benchtop NMR spectrometers with higher magnetic field strengths are expected to become available in the near future from which the new method will greatly benefit. They will allow to further reduce the measurement time and to study compounds at high dilution. The new methodology is especially attractive for small laboratories which do not have the suitable infrastructure for expensive high-field NMR spectrometers. In addition, expert knowledge is not required for operating benchtop NMR spectrometers and applying the new method for measuring self-diffusion coefficients.

5 Overhauser Dynamic Nuclear Polarization for Benchtop ^{13}C NMR Spectroscopy

5.1 Introduction

The scope of ^{1}H-^{13}C polarization transfer techniques for benchtop ^{13}C NMR spectroscopy is limited. This technique only allows for a maximum signal enhancement of up to a factor of 4. Furthermore, if the flow rate is too high, even the ^{1}H polarization build-up in the premagnetization volume becomes insufficient.

The premagnetization issue could in principle be solved by the use of paramagnetic relaxation enhancement (PRE) agents [157, 158]. Immobilized PRE agents can be positioned in the flow path in front of the NMR coil, enabling a much faster premagnetization of the molecules and thus facilitating quantitative analysis at high flow velocities [91, 159, 160]. Kircher et al. [161] have successfully applied this technique to a 1 T benchtop NMR spectrometer. However, despite the accelerated polarization build-up, this method is not suitable for quantitative studies of kinetic effects with flow ^{13}C NMR, because a large number of scans is still required to achieve a sufficient SNR. However, this problem can be solved by the application of NMR hyperpolarization methods which result in large signal enhancements.

Among various hyperpolarization techniques [162–164], such as parahydrogen induced polarization (PHIP) [165–171] or optical pumping [172–174], ODNP is particularly suitable for reaction and process monitoring [175–179]. In ODNP, the high polarization of electron spins is transferred to surrounding nuclear spins via hyperfine coupling, enabling a maximum theoretical signal enhancement of 658 for ^{1}H and 2640 for ^{13}C nuclei, respectively [180–189]. This can be a game changer for sensitivity in NMR spectroscopy. For ^{13}C NMR spectroscopy, several studies have already demonstrated the potential of ODNP and have discussed the different hyperfine interactions in liquids [190–198]. These studies were done on samples at rest and utilized dissolved radicals, which is not suitable for reaction and process monitoring, because radicals alter the sample and interfere

with the NMR detection. In some works [160, 199–207], it was demonstrated that the required radicals can be immobilized in fixed beds while largely retaining their ODNP performance. In ex-situ ODNP applications, this allows flow-induced separation of the hyperpolarized fluid from the radical matrix and thus undisturbed NMR detection. This approach is especially well suited for continuously flowing samples, eventually allowing online monitoring of fast processes and reactions. Appropriate mobile ODNP setups compatible with benchtop NMR spectrometers are available which have been applied for benchtop ^{1}H NMR spectroscopy under continuous-flow in previous benchtop studies [206, 208–211]. However, this approach has not been used in ^{13}C NMR studies.

In this work the usefulness of ODNP for benchtop ^{13}C NMR spectroscopy in continuous-flow are explored. Two approaches were studied: direct and indirect ODNP. In direct ODNP, the electron polarization is transferred directly to the ^{13}C nuclei, which is the common approach in ODNP. In contrast, indirect ODNP transfers the electron polarization to the ^{1}H nuclei in an intermediate step before the polarization is finally transferred to ^{13}C nuclei via polarization transfer pulse sequences (e.g. INEPT or DEPT). Cheng et al. [212] and Dey et al. [213] have compared these approaches and refer to indirect ODNP as J-mediated and t-ODNP (transferred Overhauser DNP), respectively. Dissolved radicals were used in Cheng's and Dey's work and their measurements were performed on samples at rest, and not on flowing samples as it was done in the present work. The authors report that indirect ODNP resulted in larger enhancements than direct ODNP for some molecules, due to cancellation of site-specific positive (scalar coupling) or negative (dipolar coupling) enhancements in the same molecule.

In this work, both approaches were investigated for acetonitrile (ACN), chloroform (CF), and methanol (MeOH). No ^{13}C enriched materials were used. The direct as well as indirect approach were also applied to a binary mixture of ACN and CF. Direct and indirect ^{13}C ODNP experiments were performed on continuously flowing samples at different flow rates and the obtained signals (with respect to the signals obtained at thermal equilibrium) were compared. For the ^{1}H to ^{13}C polarization transfer, the pulse sequences PENDANT [95, 96] and refocused INEPT$^+$ [214, 215] were used.

5.2 Experimental Section

5.2.1 Hardware and Experimental Procedure

The setup used for the continuous-flow ODNP experiments is illustrated in Figure 24. It was adapted from Kircher et al. [206, 207]; a detailed description of the setup is given in these references. The setup consists of two main parts: a Halbach magnet, in

which hyperpolarization by ODNP is performed, and a benchtop NMR spectrometer for signal detection. Liquid was taken from a storage vessel (volume V = 100 ml) stored at room temperature and pumped through the setup by a double piston high pressure pump (WADose Plus HP, Flusys, accuracy: < 3 %). The pump speed was calibrated for a flow range of $\dot{V}$ = 0.5 to 10 ml min^{-1}. The liquid first passes the Halbach magnet with the microwave resonator and the fixed bed containing the radical matrix. The ODNP probe was not thermostated; the temperature in the MW resonator is higher than the ambient temperature, for details see Kircher et al. [206]. As in the studies of Kircher et al. [206, 207], the fixed bed was mounted in a PEEK tube with an inner diameter of $d_{\text{flow cell}}$ = 1.0 mm. The length over which the microwave (MW) field acted on the fixed bed in the MW resonator was 4 mm in height. The fixed bed was adjusted so that this MW active zone was at its end. After leaving the fixed bed, the liquid is fed to the benchtop NMR spectrometer through a PEEK capillary with an inner diameter of $d_{\text{capillary}}$ = 0.25 mm.
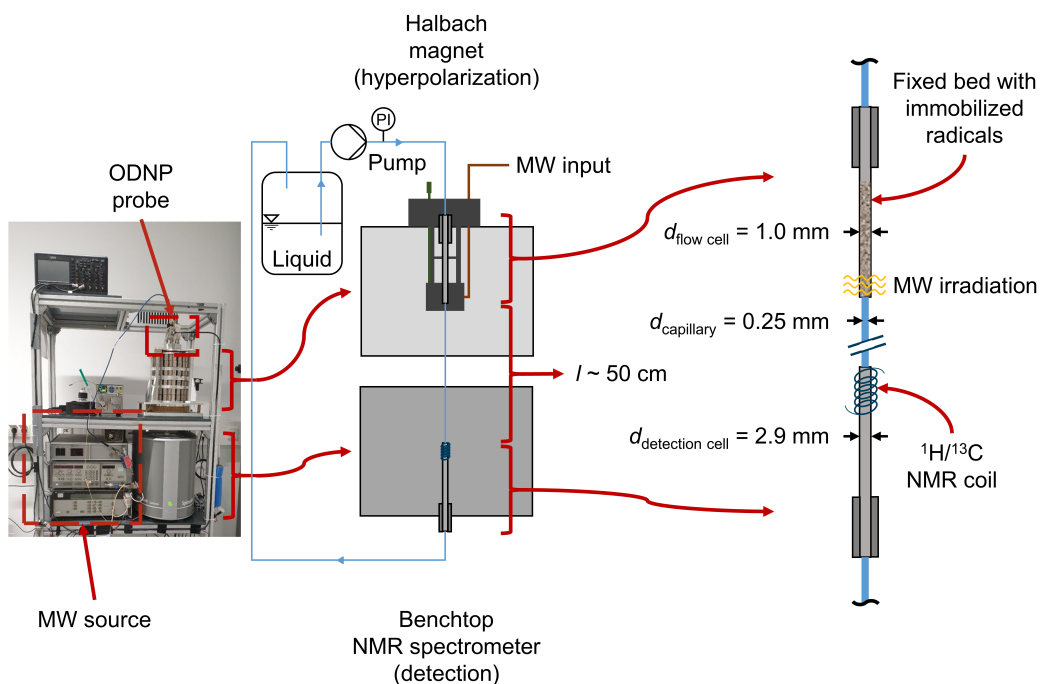
Figure 24: Photo and scheme of the experimental setup for continuous-flow ODNP experiment. MW: microwave.

The benchtop NMR spectrometer was from Magritek (Spinsolve Carbon) and had a magnetic field strength of B_0 = 1.0 T, corresponding to a ^{1}H Larmor frequency of ν_0 = 42.5 MHz. The magnet of the benchtop NMR spectrometer was thermostated to ϑ = 28.5 °C. The maximum ODNP enhancement achievable with this setup is 220 for ^{1}H and 880 for ^{13}C, as the magnetic field strength used for detection is three times higher than the field strength used for hyperpolarization. In contrast to Kircher et al.

[206, 207], a PEEK tube with an inner diameter of $d_{\text{detection cell}}$ = 2.9 mm was used as detection cell. The detection cell was positioned inside the benchtop NMR spectrometer so that the sensitive region of the NMR coil was located close to the expansion from 0.25 to 2.9 mm in order to minimize hyperpolarization losses caused by T_1 relaxation. The total length of the line between the MW resonator and the detection cell was about $l \approx 52$ cm. After leaving the NMR spectrometer, the liquid was recirculated to the storage vessel.

The flow rate was varied in the range between $\dot{V}$ = 0.5 and $\dot{V}$ = 7.0 ml min^{-1}, corresponding to flow velocities of v = 0.17 to 2.38 m s^{-1} in the capillary between the Halbach magnet and benchtop NMR spectrometer. The pressure in the storage vessel was ambient, the pressure increase by the pump was between Δp = 1 and 40 bar, and was indicated by the pressure gauge integrated in the pump (accuracy: 0.5 %). ODNP experiments were performed at a MW frequency of v = 9.687 GHz and a power of P = 5 W. Figure 25 illustrates the polarization conditions as well as the fluid dynamics in each section of the current experimental setup.

Section	Spin-Lattice Relaxation	Polarization	Fluid Dynamics
Hyperpolarization	reduced T_1	Build-Up	Plug-Flow
Transportation	native T_1	Decay	Laminar-Flow
Detection	native T_1	Decay	Jet-Flow
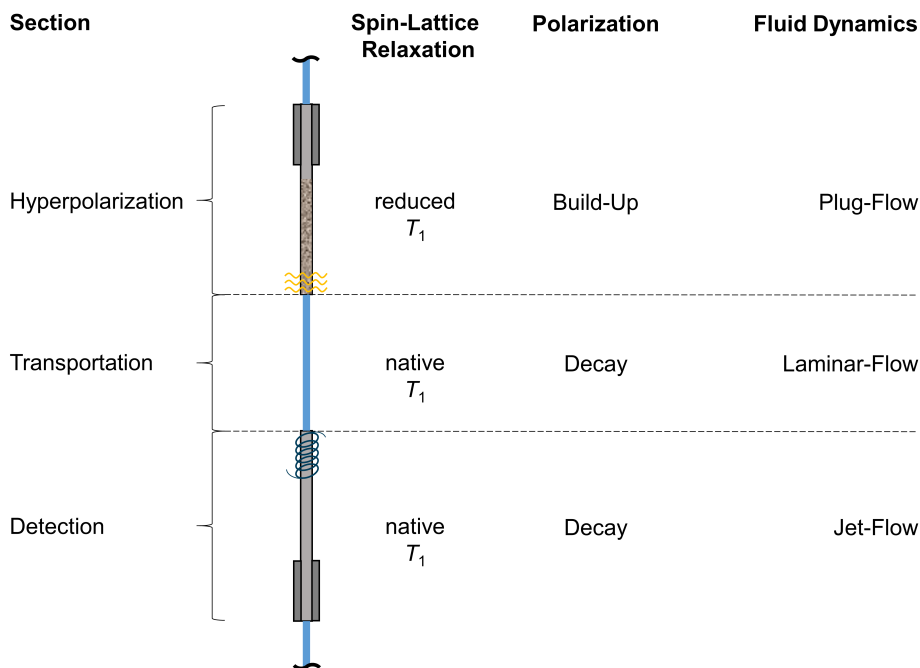
Figure 25: Illustration of the apparent spin-lattice relaxation, polarization and fluid dynamics conditions in each section of the experimental setup.

In the Halbach magnet, the T_1 time of the molecules is shortened by paramagnetic relaxation due to the contact with the radical matrix. The residence time of the liquid in the fixed bed (FB) located in the MW resonator is between τ_{FB} = 0.1 and τ_{FB} = 0.01 s for the lowest and highest flow rates, respectively. These numbers were calculated assuming plug-flow and a void fraction of the fixed bed of ϵ = 0.26, which corresponds

to that of the closest packing of spheres of the diameter used in the fixed bed. After the fluid has left the fixed bed, the ODNP hyperpolarization starts to decay at the rate of the native T_1. The flow in the line connecting the fixed bed to the NMR detection cell (TL) is laminar. The mean transport time in that line is τ_{TL} = 3.1 and τ_{TL} = 0.2 s for the smallest and highest flow rates, respectively. In the detection cell, the sudden expansion from d = 0.25 to d = 2.9 mm in combination with the high flow velocity leads a jet-flow (jet with a small diameter in a larger cylindrical tube). Thus, near the axis of the detection cell, there is a fast flow of hyperpolarized fluid, whereas near the walls, only weakly polarized fluid flows in reverse direction and there are also zones in which the fluid is almost stagnant. This flow pattern severely reduces the observed enhancements. Interestingly, Lingwood et al has carried out NMR imaging experiments to study such free jets [205]. A step experiment was carried out to characterize the flow regime in the detection cell, which are discussed in the Appendix D. The mean residence time of the liquid in the active region of the NMR coil (DC; estimated length l_{coil} = 8 mm) is between τ_{DC} = 6.3 to τ_{DC} = 0.5 s. The microwave irradiation was activated for at least 2 s before a NMR spectrum was acquired in the detection cell.

NMR experiments were controlled by the Spinsolve Expert software (Magritek). ^{13}C NMR experiments with direct ODNP enhancement (referred to as ^{13}C ODNP) were performed with an acquisition time of 1.6 s, 16 k data points, 1 scan and a 90° excitation pulse. ^{13}C NMR experiments with indirect ODNP enhancement via the intermediate step of applying a polarization transfer sequence (PENDANT and refocused INEPT$^+$) were also performed with an acquisition time of 1.6 s, 16 k data points and 1 scan (referred to as ^{13}C ODNP PENDANT and ^{13}C ODNP INEPT, respectively). The pulse sequences for both polarization transfer techniques are provided in the Appendix D.

Furthermore, ^{13}C NMR experiments performed at Boltzmann (thermal) equilibrium were used as a reference for calculating the ^{13}C signal enhancements. The ^{13}C NMR experiments without ODNP enhancement and in the absence of flow (referred to as ^{13}C thermal) were performed with the same acquisition parameters except for the number of scans, which was 256 in order to obtain a sufficient SNR. The repetition delay was set to t = 120 s to ensure a full magnetization build-up of at least 5 times $T_{1,^{13}C}$. All ^{13}C NMR experiments were performed with an inverse-gated decoupling sequence (WALTZ-16). Additional ^1H NMR experiments with ODNP enhancement (referred to as ^1H ODNP) were performed with an acquisition time of 0.4 s, 2048 data points, 1 scan and a 90° excitation pulse. The signal enhancements of the ^1H ODNP experiments were calculated by using the signal obtained without ODNP at the same flow velocity which was also acquired with only 1 scan (referred to as ^1H thermal). Furthermore, the spin-lattice relaxation times $T_{1,^1H}$ and $T_{1,^{13}C}$ of the molecules without and with contact to the immobilized radical matrix were determined with the inversion recovery

experiment. NMR sample tubes with an inner diameter of $d = 5$ mm (Magritek) were used for the experiments without matrices, while NMR sample tubes with an inner diameter of $d = 2.5$ mm (Deutero) were used for the measurements with matrices. The latter were chosen in order to completely fill the sensitive region of the NMR coil with molecules that are in contact with the matrix. Only in this case ^{13}C enriched solvents were used.

All experiments were repeated three times to calculate average signal integrals, enhancements as well as standard deviations which are used for an error propagation. Details regarding the calculation of the error of the signal enhancement and the respective error bars are given in the Appendix D. The signal enhancement E of the ODNP experiments was calculated by scaling the spectra to the same noise level and by dividing the signal and the noise by the square root of the number of scans acquired, which was applied for the thermally polarized NMR spectra as well as for the NMR spectra with ODNP enhancement [196, 197]; see Equation (10).

$$E = \frac{I_{\text{ODNP, scaled}}}{I_{\text{thermal, scaled}}} \cdot \frac{\sqrt{n_{\text{thermal}}}}{\sqrt{n_{\text{ODNP}}}} \tag{10}$$

Here, $I_{\text{ODNP, scaled}}$ denotes the integral of the scaled signal obtained with ODNP enhancement, $I_{\text{thermal, scaled}}$ the integral of the scaled signal obtained at Boltzmann equilibrium, and n the number of scans. A correction for the receiver gain is not necessary since this parameter was kept constant in all ^{1}H and ^{13}C NMR experiments.

5.2.2 Chemicals and Materials

Table 6 provides an overview of the chemicals used in this work. All chemicals were used without further purification. For preparing the binary mixture, a laboratory balance (XS6032S DeltaRange, Mettler Toledo, accuracy: ± 0.01 mol mol^{-1}) was used. ^{13}C enriched chemicals were only used for the determination of the $T_{1,^{13}\text{C}}$ in contact with the radical matrix (marked with (^{13}C) in Table 6) due to the low sample volume in the matrices.

The immobilized radical matrix was synthesized at the Laboratory of Engineering Thermodynamics (RPTU Kaiserslautern) and consists of the nitroxide radical glycidyl-oxytetramethylpiperidinyloxyl (TEMPO) immobilized on an aminopropyl-functionalized controlled porous glass (CPG) with a pore size of 50 nm. TEMPO was attached to the CPG via a polyethylene-imine (PEI)-linker (molecular mass of 25,000 g mol^{-1}) and an intermediate linker 1,4-butanediol diglycidyl ether (BDGE). A detailed description of the properties of this immobilized radical matrix as well as its synthesis is given by Kircher et al. [207].

Table 6: Chemicals used in this work. Purity as specified by the supplier. ^{13}C enriched chemicals are marked with ^{13}C.

Chemical	Formula	Supplier	Purity
ACN	CH_3CN	Carl Roth	$\geq 99.9\%$
ACN (^{13}C)	$^{13}CH_3CN$	Cambridge Isotope Laboratories	$\geq 99.9\%$
CF	$CHCl_3$	Merck	$\geq 99.0\%$
CF (^{13}C)	$^{13}CHCl_3$	Cambridge Isotope Laboratories	$\geq 99.9\%$
MeOH	CH_3OH	Sigma-Aldrich	$\geq 99.9\%$
MeOH (^{13}C)	$^{13}CH_3OH$	Sigmal-Aldrich	$\geq 99.9\%$

5.3 Results and Discussion

In the following, the absolute signal integrals of the ^{1}H ODNP, ^{13}C ODNP as well as ^{13}C ODNP PENDANT and ^{13}C ODNP INEPT are shown for each studied substance as a function of the flow velocity. Negative signal enhancement due to dipolar coupling are also explicitly displayed as absolute values. For comparison, the corresponding results of the ^{1}H and ^{13}C thermal experiments are also reported. The numerical values are provided in the Appendix D. Before entering into a detailed discussion of the results for each substance, we would like to address some general facts that are apparent in the experimental setup.

The analysis of the ODNP parameters (coupling, leakage, and saturation factors) was not the focus of this work. We focus here on the influence of the different T_1 times in combination with the different residence times in the microwave cavity on the enhancement. In Table 7, the $T_{1,^1H}$ and $T_{1,^{13}C}$ values of ACN, CF and MeOH without and with contact to the radical matrix are reported. As expected, a significant reduction of the T_1 values due to paramagnetic relaxation is found. Furthermore, as expected, the $T_{1,^{13}C}$ values are significantly larger than the corresponding $T_{1,^1H}$ values for all substances. A short T_1 during the matrix interaction is advantageous as it enables a faster and, hence, a complete hyperpolarization build-up in the Halbach magnet during continuous-flow. On the other hand, a long native T_1 is desirable because it reduces hyperpolarization losses during the transport from the Halbach magnet to the benchtop NMR spectrometer.

Table 7: $T_{1,^1\mathrm{H}}$ and $T_{1,^{13}\mathrm{C}}$ times values of ACN, CF and MeOH without ($T_{1,i}^0$) and with contact to the radical matrix ($T_{1,i}^{\mathrm{RM}}$) at B_0 = 1 T. Mean value and standard uncertainty from three identical experiments are reported. For ACN and MeOH, the $T_{1,^{13}\mathrm{C}}$ and $T_{1,^1\mathrm{H}}$ values refer to the CH$_3$-group of these molecules.

Molecule	^{1}H		^{13}C	
	$T_{1,^1\mathrm{H}}^0$ / s	$T_{1,^1\mathrm{H}}^{\mathrm{RM}}$ / s	$T_{1,^{13}\mathrm{C}}^0$ / s	$T_{1,^{13}\mathrm{C}}^{\mathrm{RM}}$ / s
ACN	3.82 ± 0.05	0.10 ± 0.01	15.41 ± 0.30	0.54 ± 0.01
CF	5.25 ± 0.06	0.06 ± 0.01	21.69 ± 0.70	0.87 ± 0.06
MeOH	2.96 ± 0.04	0.11 ± 0.01	14.05 ± 0.46	0.80 ± 0.01

The ^{13}C thermal signal cannot be measured in continuous-flow, so this signal was measured for a stagnant fluid with 256 scans. As a result, the ^{13}C thermal experiments are not affected by insufficient polarization build-up and back-mixing effects due to the jet-flow. In contrast, all direct and indirect ODNP experiments are strongly influenced by the jet, since hyperpolarized and thermally polarized molecules are detected simultaneously. Another effect can reduce the enhancement further: For signal enhancements that originally have a negative sign (dipolar coupling), the signal can be canceled by a positive thermal signal. These effects greatly reduce the observed enhancements compared to the theoretically possible enhancements. Thus, the obtained enhancements are largely underestimated and are numerically provided in the Appendix D.

5.3.1 ODNP Experiments with ACN

Figure 26 displays the ^{13}C NMR spectra of ACN obtained by the ^{13}C ODNP, ^{13}C ODNP PENDANT, and ^{13}C ODNP INEPT experiments in continuous-flow. For comparison, a spectrum of the ^{13}C thermal experiment is given. All ODNP-enhanced spectra show the CH$_3$-signal (C1) of ACN with single scan acquisition. This is impossible with thermal ^{13}C NMR detection due to insufficient premagnetization and SNR as discussed before.
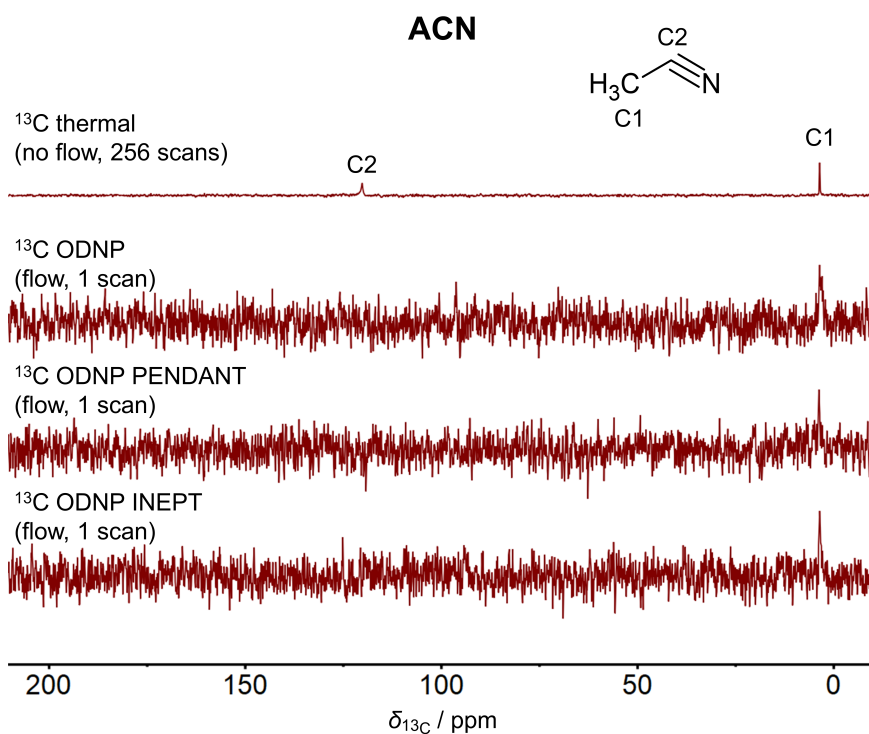
Figure 26: Comparison of ^{13}C NMR spectra of ACN acquired by the ^{13}C thermal, ^{13}C ODNP, ^{13}C ODNP PENDANT, and ^{13}C ODNP INEPT experiment. The spectrum of the ^{13}C thermal experiment was scaled with respect to its number of scans $(\sqrt{n})$. The experiments with ODNP enhancement were performed at a flow velocity of $v = 0.85$ m s^{-1}.

An overview of the signal integrals of ACN obtained at different flow velocities is given in Figure 27. The integrals of the ^{1}H thermal experiment decrease slightly with increasing flow velocity due to premagnetization issues. However, the effect of insufficient premagnetization is not significant because fully premagnetized molecules are present in the detection cell due to the back-mixing effects of the jet-flow. In contrast, the corresponding integral of the ^{1}H ODNP experiment first increases with increasing flow velocity and reaches a plateau for values larger than $v = 1.0$ m s^{-1}. The initial increase and the plateau are consequences of the reduction of the transport time and therefore of the reduction of the hyperpolarization losses. The maximum signal enhancement is about $E_{^1\text{H}} = 5$.
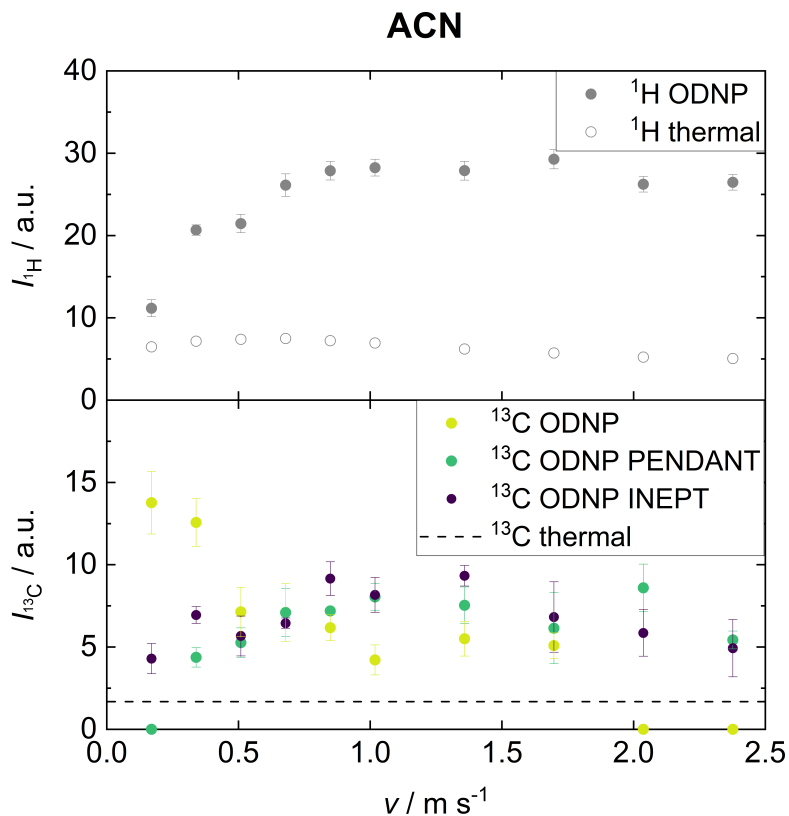
Figure 27: Integrals of signals from ACN (C1) obtained by single scan ^{1}H ODNP, ^{13}C ODNP, ^{13}C ODNP PENDANT, and ^{13}C ODNP INEPT at different flow velocities. Also the corresponding integrals obtained in ^{1}H and ^{13}C thermal experiments, that were obtained with 256 scans, are shown.

The largest integral of the ^{13}C ODNP experiment is detected at the lowest flow velocity (v = 0.17 m $^{-1}$) and corresponds to a signal enhancement of $E_{^{13}C}$ = 8. At higher flow velocities, the performance of the ^{13}C ODNP experiment decreases significantly, as the time for the interaction with the radical matrix is not sufficient for a complete ODNP hyperpolarization build-up (compare the $T_{1,^{13}C}^{\mathrm{RM}}$ value of ACN in Table 7). Therefore, the application of low flow velocities is beneficial for direct ^{13}C ODNP. Moreover, since the native $T_{1,^{13}C}^{0}$ value is much larger than that of ^{1}H the small loss of ODNP hyperpolarization during the transport to the benchtop NMR spectrometer is not important here.

In contrast, the ^{13}C ODNP PENDANT and ^{13}C ODNP INEPT experiments yield larger integrals with increasing flow velocity. Both indirect ODNP methods rely on the hyperpolarization build-up of the ^{1}H nuclei, which occurs on a much shorter time scale than for the ^{13}C nuclei. The use of high flow rates is, hence, less problematic. As seen before, ^{1}H ODNP hyperpolarization losses occur during the transport. Therefore, the application of higher flow velocities preserves the ^{1}H ODNP hyperpolarization, which can then

be transferred to the ^{13}C nuclei. However, a new effect occurs that leads to a decrease in signal at flow velocities above v = 1.70 m s^{-1}: the application of the polarization transfer sequences takes time. Consequently, a flow rate that is too high results in a less efficient transfer of the ^{1}H ODNP hyperpolarization to the ^{13}C nuclei. The differences between PENDANT and INEPT results are not significant.

Both approaches, direct ODNP (^{13}C ODNP) and indirect ODNP (^{13}C ODNP PENDANT/^{13}C ODNP INEPT), when applied to ACN, have their advantages at different flow regimes: If low flow velocities are applied, direct ODNP is preferable because higher ^{13}C signal enhancements can be achieved. The contact time with the radical matrix is sufficient and since the $T_{1,^{13}C}$ is long, no significant loss of ODNP hyperpolarization occurs. If high flow velocities are used, indirect ODNP gives better results, as the much shorter $T_{1,^1H}^{RM}$ provides a much faster hyperpolarization build-up. However, both approaches share the ability to detect the ACN signal in continuous-flow within a single scan which is impossible without ODNP. Hence, ODNP is an enabling technology for benchtop ^{13}C NMR spectroscopy.

5.3.2 ODNP Experiments with CF

Figure 28 illustrates the ^{13}C NMR spectra of CF obtained by the ^{13}C ODNP, ^{13}C ODNP PENDANT, and ^{13}C ODNP INEPT experiments in continuous-flow. For comparison, a spectrum of the ^{13}C thermal experiment is given. It can be seen that applying ODNP increases the SNR tremendously, although only a single scan was acquired. The direct ODNP shows the best performance.

The integrals of all experiments as a function of the flow velocity are given in Figure 29. The results of the ^{1}H thermal as well as the ^{1}H ODNP experiments show the same behaviour as observed for ACN. However, compared to the ^{13}C results of ACN, a significantly larger signal enhancement was observed for CF in all experiments. E.g., for the ^{13}C ODNP experiment the largest signal enhancement was about $E_{^{13}C}$ = 72 compared to a corresponding value of $E_{^{13}C}$ = 8 for ACN. This observation can be explained by the scalar coupling mechanism, which is strongly dominant for CF due to its molecular structure. A reduction of the net signal enhancement by the contribution of the dipolar coupling and its negative signal is thus prevented. This is in agreement with the results from other groups [197, 200–202]. The observed signal enhancements are in a similar range as those found by Dorn et al. [200] and Stevenson et al. [201].
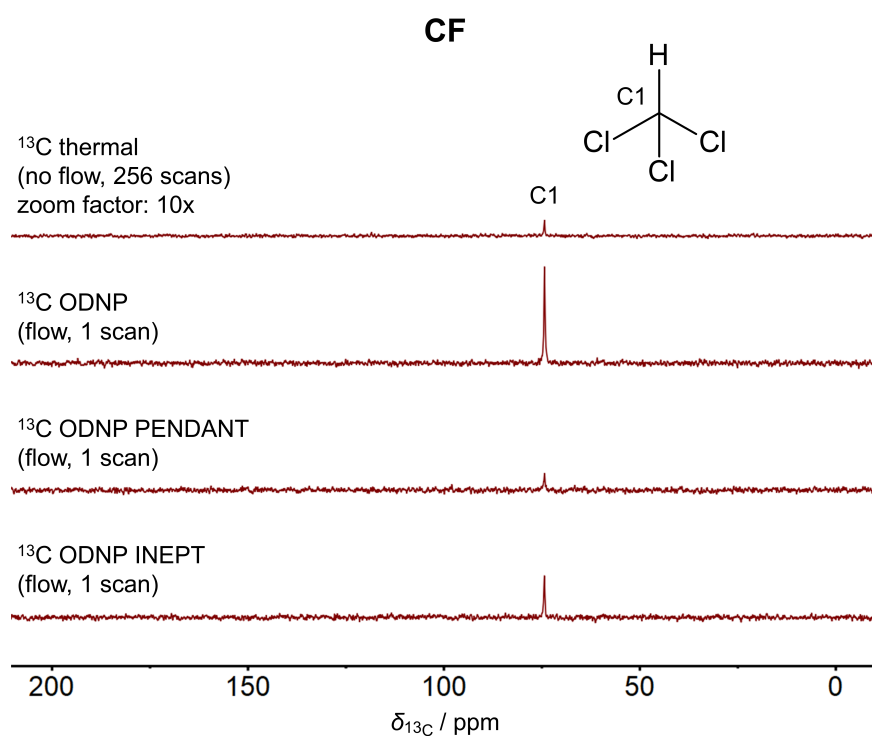
Figure 28: Comparison of ^{13}C NMR spectra of CF acquired by the ^{13}C thermal, ^{13}C ODNP, ^{13}C ODNP PENDANT, and ^{13}C ODNP INEPT experiment. The spectrum of the ^{13}C thermal experiment was scaled with respect to its number of scans ($\sqrt{n}$). The experiments with ODNP enhancement were performed at a flow velocity of $v = 1.02$ m s^{-1}.

In contrast to ACN, the largest ^{13}C ODNP signal enhancement is not observed for the lowest flow rate for CF - instead, the signal first rises with increasing flow rate, similar to the results for ^{1}H ODNP. A reason for the important differences of the results for the direct ^{13}C ODNP between ACN and CF may be a difference in the hyperfine interaction of these molecules to the TEMPO radical. For CF, the scalar coupling is largely dominant, whereas for ACN both scalar and dipolar coupling mechanisms should play a role. However, scalar and dipolar coupling lead to signals of different sign that cancel out. The direct ^{13}C ODNP experiments of ACN show a small positive signal indicating that both coupling mechanisms are present. Moreover, the strength of the scalar hyperfine interaction is different for both molecules which could also be reflected in different times required for hyperpolarization build-up (usually stronger couplings result in faster polarization transfer). However, a clarification of this issue was out of the scope of the present work, but the effect will be investigated in the future work.
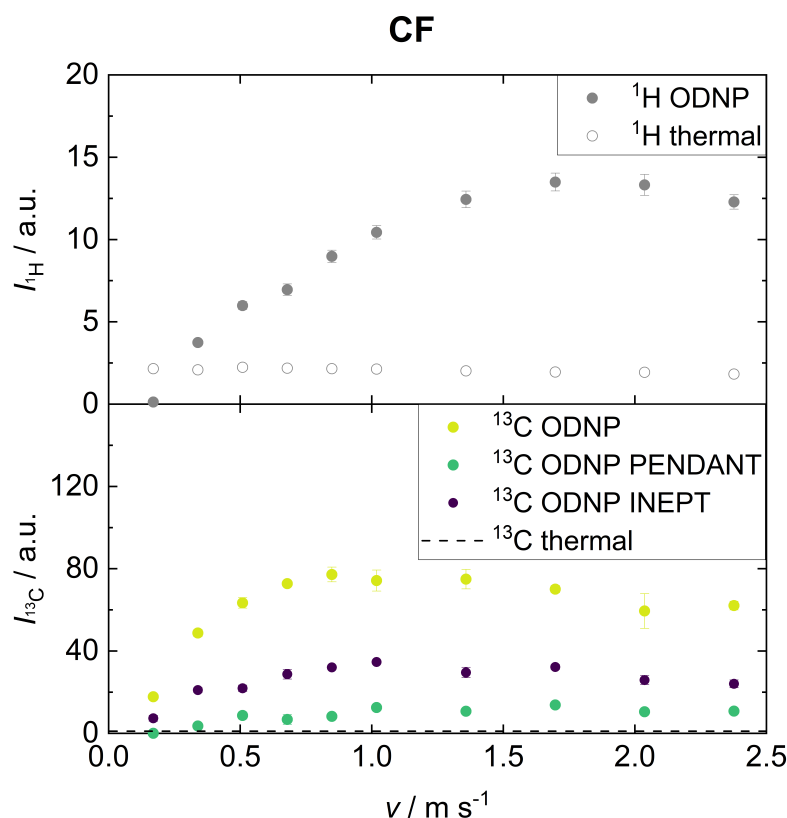
Figure 29: Integrals of signals from CF (C1) obtained by single scan ^{1}H ODNP, ^{13}C ODNP, ^{13}C ODNP PENDANT, and ^{13}C ODNP INEPT at different flow velocities. Also the corresponding integrals obtained in ^{1}H and ^{13}C thermal experiments, that were obtained with 256 scans, are shown.

For ^{13}C ODNP PENDANT and ^{13}C ODNP INEPT the observations made for ACN also apply to CF. In general, the indirect ODNP approach results in significantly lower ^{13}C signal enhancement than the direct ^{13}C ODNP because this method uses the weaker dipolar ^{1}H signal enhancement. The signal enhancements obtained by ^{13}C ODNP PEN-DANT are significantly lower than those of ^{13}C ODNP INEPT. This is due to the nature of the PENDANT pulse sequence, which allows the simultaneous detection of the original ^{13}C polarization and the transferred polarization from ^{1}H (this is the reason why quaternary carbons can be detected with PENDANT). In ODNP, the signal enhancements resulting from scalar and dipolar interactions are of opposite sign, thus, reducing the net signal enhancement. In contrast, the refocused INEPT$^+$ pulse sequence only permits the detection of ^{13}C polarization that originates from transfer from ^{1}H.

In summary, ^{13}C NMR spectra with very good SNR were obtained with a single scan for CF with a 1 T benchtop NMR spectrometer without using ^{13}C enriched substance and in continuous-flow in a flow cell with an inner diameter of only d = 2.9 mm.

5.3.3 ODNP Experiments with MeOH

^{13}C NMR spectra of MeOH obtained by ^{13}C thermal, ^{13}C ODNP, and ^{13}C ODNP PEN-DANT in continuous-flow are given in Figure 30. ^{13}C ODNP INEPT experiments were not conducted due to failure of the MW amplifier. The results of these experiments were expected to be similiar to those of the ACN experiments.

Again, the integrals as a function of the flow velocity are shown in Figure 31. For the ^{1}H thermal and ^{1}H ODNP experiments, comparable observations were made for MeOH as already noticed for ACN and CF. However, it can be seen that the direct ODNP approach does not result in detectable ^{13}C polarization at any flow velocity. In contrast, with ^{13}C ODNP PENDANT a signal can be acquired, but with only moderate enhancement.
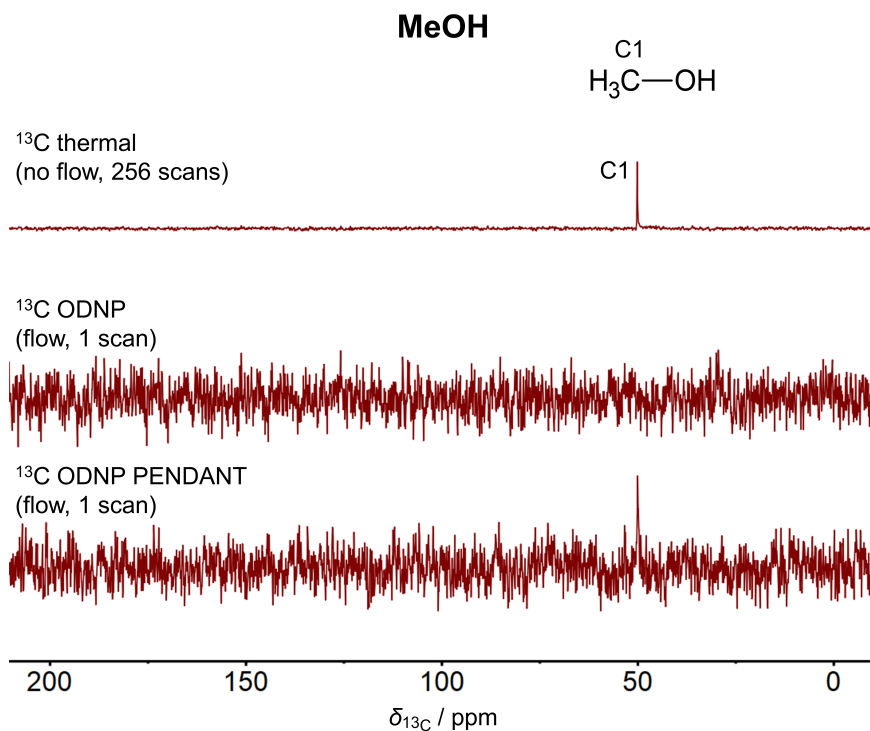
Figure 30: Comparison of ^{13}C NMR spectra of MeOH acquired by the ^{13}C thermal, ^{13}C ODNP, and ^{13}C ODNP PENDANT experiment. The spectrum of the ^{13}C thermal experiment was scaled with respect to its number of scans ($\sqrt{n}$). The experiments with ODNP enhancement were performed at a flow velocity of v = 2.38 m s^{-1}.

In comparison to ACN and CF, a much lower signal enhancement was obtained on the ^{1}H (max $E_{^1\text{H}}$ = 3) as well as on the ^{13}C nucleus (max $E_{^{13}\text{C}}$ = 3, for ^{13}C ODNP PENDANT).

The low enhancements can be explained by the poor hyperfine interaction of the CH_3-group of MeOH with the TEMPO radical. The polar molecular structure of the radical interacts preferentially with the equally polar OH-group of MeOH, resulting in a low ODNP hyperpolarization of the ^1H and ^{13}C nuclei of the CH_3-group. This is especially critical for the direct ^{13}C ODNP technique, since the weak ^{13}C ODNP hyperpolarization can be additionally cancelled by the competing dipolar (negative signal) and scalar coupling (positive signal). However, indirect ODNP still allows MeOH to be detected by ^{13}C NMR spectroscopy in a single scan in continuous-flow mode because it relies entirely on the available ^1H ODNP hyperpolarization. This highlights that there are situations where indirect ODNP can be used when direct ODNP fails.
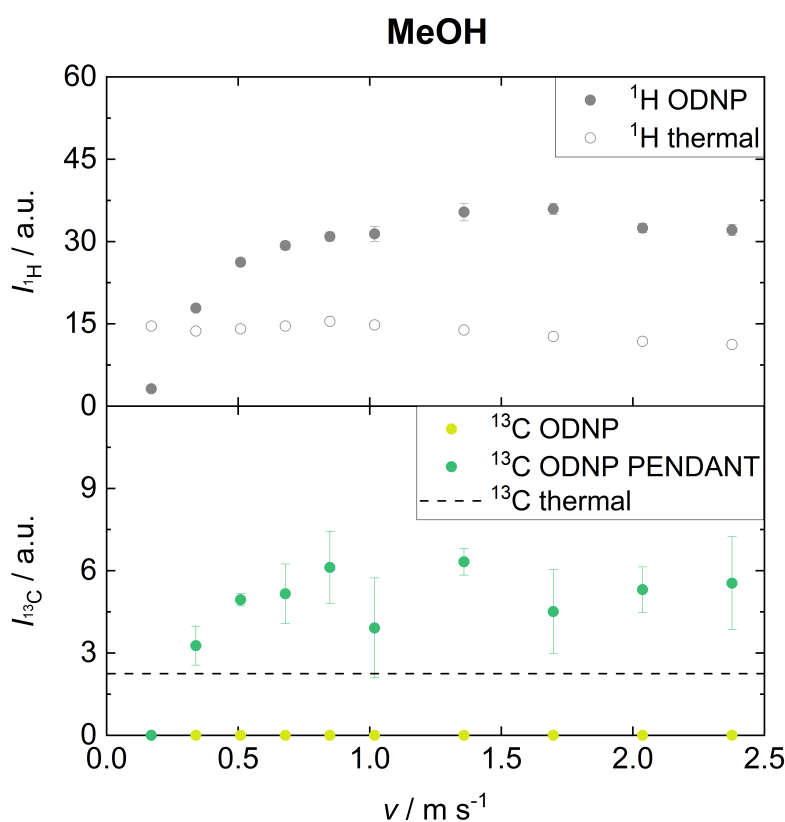
Figure 31: Integrals of signals from MeOH (C1) obtained by single scan ^1H ODNP, ^{13}C ODNP, and ^{13}C ODNP PENDANT at different flow velocities. Also the corresponding integrals obtained in ^1H and ^{13}C thermal experiments, that were obtained with 256 scans, are shown.

5.3.4 ODNP Experiments with ACN + CF

To investigate the potential of ODNP on ^{13}C for process monitoring, also a binary mixture was studied. ^{13}C NMR spectra of the binary mixture consisting of ACN and CF (x_{ACN} = 0.75 mol mol^{-1}) obtained by ^{13}C thermal, ^{13}C ODNP, and ^{13}C ODNP PENDANT in continuous-flow are shown in Figure 32. Again, ^{13}C ODNP INEPT experiments could not be performed due to hardware issues. A significant improvement of the SNR in the ^{13}C NMR spectrum by the direct as well as the indirect approach is recognizable for both components.

ACN + CF

^{13}C thermal
(no flow, 256 scans)

^{13}C ODNP
(flow, 1 scan)

^{13}C ODNP PENDANT
(flow, 1 scan)

200   150   100   50   0

$\delta_{^{13}\mathrm{C}}$ / ppm
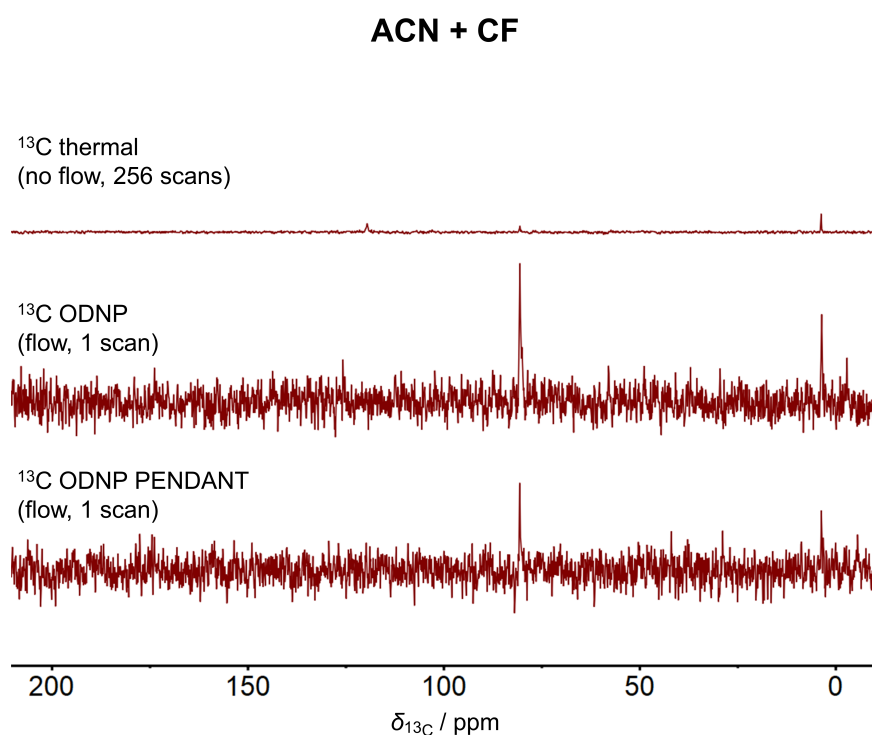
Figure 32: Comparison of ^{13}C NMR spectra of the binary mixture ACN and CF (x_{ACN} = 0.75 mol mol^{-1}) acquired by the ^{13}C thermal, ^{13}C ODNP, and ^{13}C ODNP PENDANT experiment. The spectrum of the ^{13}C thermal experiment was scaled with respect to its number of scans ($\sqrt{n}$). The experiments with ODNP enhancement were performed at a flow velocity of v = 0.68 m s^{-1}.

Figure 33 shows the integrals of ACN and CF in the binary mixture obtained from the ^{13}C ODNP and the ^{13}C ODNP PENDANT experiments as a function of the flow velocity. The observations made for the pure components also apply to the studied binary mixture (compare Figure 27 and Figure 29). Compared to the pure components, lower absolute signal integrals are observed due to the lower total amount of spins of

each molecule in the detection cell. However, the signal enhancements obtained in the binary mixture, with the exception of the ^{13}C ODNP experiment of CF, are in the same range as for the pure components. The exception for CF can be explained by the fact that in the binary mixture, CF molecules compete with ACN for the limited radical binding sites.

In summary, in the ODNP experiments the detection of the ^{13}C signals of both components is possible even in continuous-flow. This is not the case for ^{13}C thermal experiments. The application of ^{13}C ODNP hyperpolarization therefore opens the route for quantifying the composition of flowing mixtures by ^{13}C NMR e.g. in reaction kinetic studies. The present results suggest that this is possible, but requires a calibration. In preliminary studies, a suitable flow rate should be chosen, for which at least one signal for each component is detectable. Then, the calibration can be carried out with mixtures of known composition.
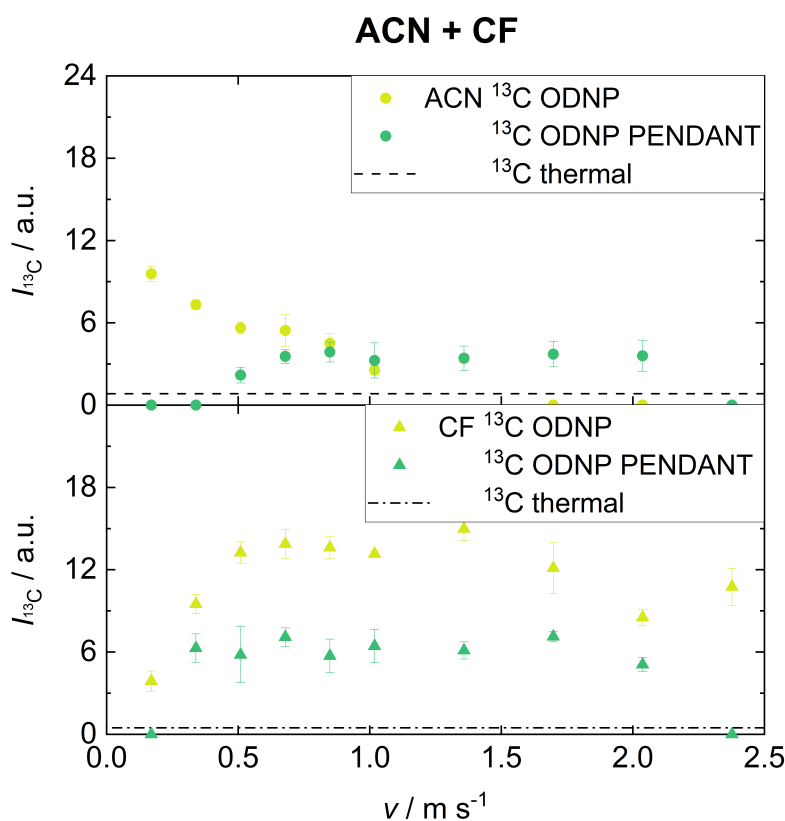
Figure 33: Integrals of signals from ACN + CF (C1 for both molecules) in a binary mixture (x_{ACN} = 0.75 mol mol^{-1}) obtained by single scan ^{13}C ODNP and ^{13}C ODNP PENDANT at different flow velocities. Also the corresponding integrals obtained in ^{13}C thermal experiments, that were obtained with 256 scans, are shown.

5.4 Conclusions

In this work, ODNP hyperpolarization has been applied for enabling continuous-flow benchtop ^{13}C NMR spectroscopy. This is highly attractive for reaction and process monitoring. Three ODNP methods were studied: direct ODNP (^{13}C ODNP) and two indirect ^{1}H-^{13}C ODNP methods (^{13}C ODNP PENDANT and ^{13}C ODNP INEPT). Their performance was evaluated at different flow velocities for pure acetonitrile (ACN), chloroform (CF), methanol (MeOH) and a mixture of acetonitrile (ACN), chloroform (CF). Significant ^{13}C signal enhancements were found in basically all cases. Even though no ^{13}C enriched substances were used, it was shown that single scan ODNP experiments can yield ^{13}C NMR spectra with good SNR even at high flow velocities. The size of the signal enhancement and its dependency on the flow velocity is different for the different studied ODNP techniques and it also depends on the investigated substance. The actual outcome is determined by several effects, starting with the efficiency of the polarization transfer in the fixed bed (to the ^{13}C nuclei in the direct method and to the ^{1}H nuclei in the indirect method) and the loss of polarization on the way from the fixed bed to the NMR detection volume. These two effects depend on the corresponding T_1 times which are much lower for ^{1}H than for ^{13}C. Furthermore, effects in the detection volume are important, where in the indirect methods the transfer of the polarization from ^{1}H to ^{13}C has to be accomplished as well as in all cases the final ^{13}C NMR experiment must be carried out. The influence of all these effects on the results of the different ODNP methods was elucidated and discussed for the different studied substances and conditions. Besides these results of studies on ^{13}C ODNP, also results from corresponding ^{1}H NMR measurements are reported, in which also important enhancements were observed.

The studies should be extended in several directions: the design of the NMR detection flow cell should be improved. The jump of the diameter at the inlet of the present cell is certainly not an optimal design, a smooth transition, that avoids back-mixing and dead zones will enable much higher enhancements than those obtained in the present work. Furthermore, a combination with ultrafast (UF)-2D NMR [216–219] techniques could be explored.

The present work lays the foundation for the application of benchtop ^{13}C NMR spectroscopy in flow for the quantification of mixtures. This would open new perspectives for reaction and process monitoring.

6 Quantitative Analysis with Overhauser Dynamic Nuclear Polarization

6.1 Introduction

ODNP is particularly attractive because of its ability to hyperpolarize a wide range of molecules and because it is fast, so that it can be used in continuous-flow setups for real-time process monitoring [199–202, 206, 207, 209–211]. Stable radicals, such as nitroxides, are added to the sample as a source of electron spin polarization [190–192]. For an application in process monitoring, it is advantageous to immobilize the radicals in a fixed bed which allows flow-induced separation of the radicals and thus a measurement of a radical free sample [199, 200, 206, 207]. This avoids chemical contamination of the sample and interference of the radicals with NMR detection.

However, the quantitative analysis of hyperpolarized mixtures is a challenge because the integral of the signal does not only depend on the number of spins in the sample but also on the polarization level. In ODNP, unequal nuclear spin polarization levels are observed for different components of mixtures and sometimes even for different nuclei on the same molecule, due to different hyperfine interactions of the molecular sites with the radicals. This prevents applying the common quantification based only on the peak integrals. Different methods to solve the problem of unequal polarization levels have been described in the literature: the Signal Amplification by Reversible Exchange (SABRE) hyperpolarization technique uses a second ligand which binds at the mediating metal complex to achieve a linear dependence of the SABRE signal on the concentration of the studied component [165, 220]. Using a calibration, the SABRE technique has been applied successfully, e.g. to quantify metabolites in urine samples or sugars solved in dimethylformamide [167, 221]. A different approach has been developed for dissolution DNP (dDNP) and applied for the quantification of metabolic pathways and networks using an internal standard [222–232]. Although originally proposed for biomedical applications, including in vivo imaging, applications of dDNP for online

monitoring of chemical and biological reactions have emerged [175, 233]. However, both SABRE and dDNP have drawbacks in online applications: SABRE can only be applied to molecules that are able to bind to the metal complex which mediates the contact with p-H_2, while dDNP is limited to the detection of very fast processes and cannot be used in continuous-flow applications because the spin polarization produced is non-renewable, allowing only studies on the time scale of the T_1 time of the observed nucleus. Hyperpolarization by ODNP is particularly suitable in this respect because it can polarize a wide range of different molecules at different concentrations, works also in continuous-flow, and is technically straightforward.

In the present work, the quantitative analysis of ODNP hyperpolarized mixtures with ^{1}H and ^{13}C NMR spectroscopy was explored. This is the first study that reports on this interesting new option for quantitative hyperpolarized NMR. To demonstrate the feasibility of this approach, ^{1}H and ^{13}C ODNP experiments on three binary mixtures over a wide concentration range without the use of any internal standard were carried out. The experiments were performed in continuous-flow. Immobilized radical matrices were used for the ODNP build-up and the hyperpolarized mixtures were analyzed with a benchtop NMR spectrometer. It is shown that no tedious study of the different factors that influence ODNP (coupling, leakage and saturation factor) is necessary for the quantification. The effect of uneven hyperpolarization on the different molecules was addressed by a calibration that was tailored for the application to ODNP experiments and works reliably in the entire concentration range.

6.2 Experimental Section

6.2.1 Chemicals and Materials

Three binary systems were investigated (the suppliers and the purities of the chemicals are given in the Appendix E):

- System 1: acetonitrile + water (ACN + W)

- System 2: acetonitrile + 1,4-dioxane (ACN + DX)

- System 3: acetonitrile + chloroform (ACN + CF)

For each system, mixtures of different composition were prepared gravimetrically using a laboratory balance (Delta Range XS603S, Mettler Toledo, accuracy: ±0.001 g). The uncertainty of the concentrations obtained gravimetrically is ±0.001 mol mol^{-1}. The immobilized paramagnetic radical matrix used here is the same as used in the work described in Chapter 5 and consists of the nitroxide radical TEMPO immobilized via

a polymeric linker on controlled porous glass beads [207]. More details on the radical matrix are given in the Appendix E.

6.2.2 Experimental Setup and Procedure

Figure 34 illustrates the setup for the continuous-flow ODNP experiments. The setup is adapted from Kircher et al. [206]. It is only briefly described here, details as well as component specifications are given in the Appendix E.
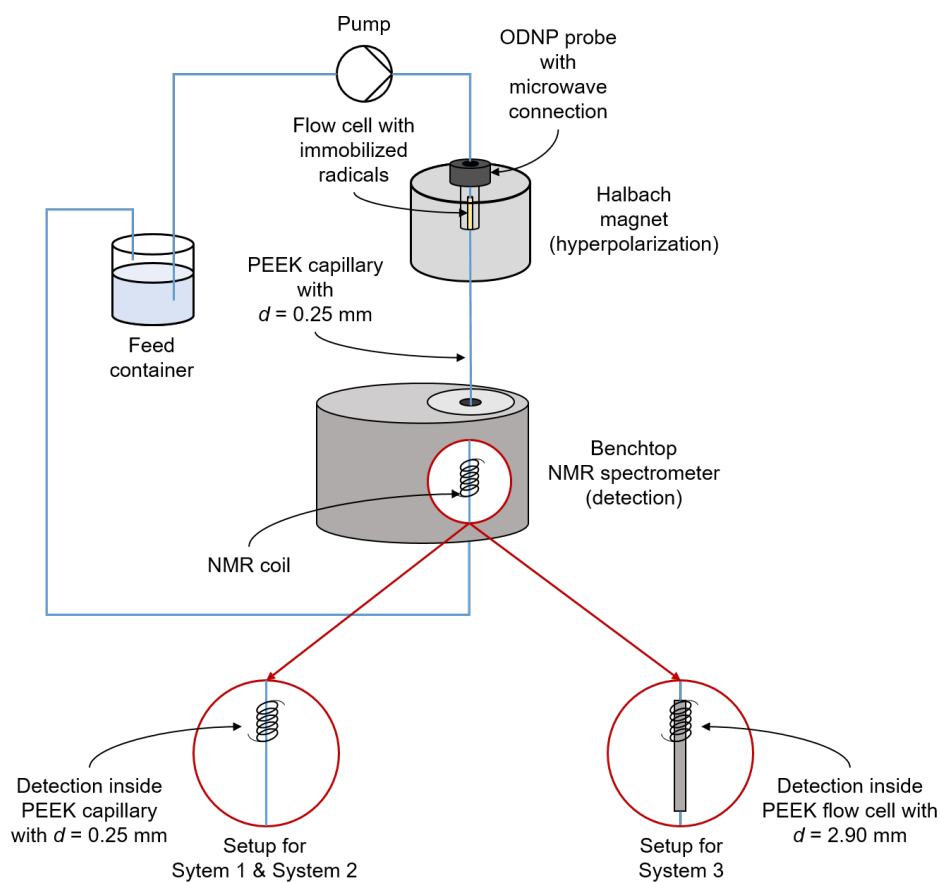
Figure 34: Scheme of the experimental setup for the continuous-flow ODNP experiments.

The main components of the setup are a custom-built Halbach magnet (magnetic field strength 0.35 T) and a Magritek benchtop NMR spectrometer (Spinsolve Carbon, magnetic field strength 1.0 T). The sample mixture was pumped from a storage vessel to the ODNP probe inside the Halbach magnet containing the radical matrix in a fixed bed. Inside the ODNP probe, the sample is irradiated with microwave (MW) radiation at a frequency of 9.687 GHz to accomplish the hyperpolarization. After hyperpolarization, the sample flows through a PEEK capillary to the benchtop NMR spectrometer which was placed directly under the Halbach magnet. The inner diameter of the capillary

connecting the ODNP probe and the detection cell of the benchtop NMR spectrometer was 0.25 mm, its length 0.52 m.

^{1}H NMR experiments with ODNP hyperpolarization (referred to as ^{1}H NMR ODNP) were carried out for all systems, ^{13}C NMR experiments with ODNP hyperpolarization (referred to as ^{13}C NMR ODNP) were additionally carried out for System 3. Furthermore, corresponding thermally polarized ^{1}H and ^{13}C NMR experiments without MW irradiation (referred to as ^{1}H NMR and ^{13}C NMR) were carried out to enable the calculation of the signal enhancement. Hence, there are four data sets: Three for the ^{1}H NMR ODNP experiments in the Systems 1 to 3 and another one for the ^{13}C NMR ODNP experiments in the System 3. All ODNP experiments were conducted with a single scan in continuous-flow. Details of the experimental procedure as well as the calculation of the signal enhancement are provided in the Appendix E.

Two different detection cells were used: For the studies of System 1 and System 2, a PEEK-capillary with an inner diameter of 0.25 mm was used, since only ^{1}H NMR experiments, which yield large signals, were performed [206]; for System 3, a custom-built PEEK-detection cell with an an inner diameter of 2.90 mm was used to enable analysis by ^{13}C NMR spectroscopy without the use of isotopically enriched samples (see Chapter 5). After passing the NMR spectrometer the sample was recycled to the storage vessel.

The flow rate $\dot{V}$ and the MW power P were set individually for each system based on experience from previous works [206] and the previous chapter. The experimental parameters are summarized in Table 8, which also provides the corresponding flow velocities v (calculated assuming plug-flow) in the capillary between the ODNP probe and the NMR detection cell. The MW irradiation was activated 2 s before signal acquisition to allow sufficient ODNP hyperpolarization build-up.

Table 8: Experimental parameters: flow rate $\dot{V}$ and microwave power P for each studied system. Also the flow velocity v in the capillary between the ODNP probe and the NMR detection cell is provided. d is the inner diameter of the detection cell.

System	NMR	$\dot{V}$ / ml min⁻¹	v / m s⁻¹	P / W	d / mm
1, 2	[1]H	1.0	0.34	10	0.25
3	[1]H	7.0	2.38	5	2.90
	[13]C	1.0	0.34		

The (uncorrected) mole fraction x_i^{ODNP} of component i in the binary systems was determined from the normalized peak integral with respect to the second component j in that system (see Equation (11)).

$$x_i^{\mathrm{ODNP}} = \frac{\frac{I_i^{\mathrm{ODNP}}}{N_i}}{\frac{I_i^{\mathrm{ODNP}}}{N_i} + \frac{I_j^{\mathrm{ODNP}}}{N_j}} \tag{11}$$

Here, I_i^{ODNP} denotes the integral of the signal of the component i and N_i is the number of protons or carbon nuclei assigned to this signal. All ^{1}H NMR ODNP experiments were repeated 5 times, while ^{13}C NMR ODNP experiments were repeated 3 times. From the results the mean value x_i^{ODNP} and the standard deviation, that are reported here, were calculated.

6.2.3 Calibration Function

Unequal hyperpolarization efficiencies for different components as well as differences in the hyperpolarization losses due to relaxation processes during the transport to the NMR detection result in differences between x_i^{ODNP} and the true concentration. In this work, the gravimetrical concentration x_i^{ref} is taken as ground truth. The concentrations x_i^{ODNP} obtained from the ^{1}H NMR ODNP and ^{13}C NMR ODNP experiments were correlated to x_i^{ref} of the corresponding mixture. A typical result for the relation of x_i^{ref} and x_i^{ODNP} is given in Figure 35.
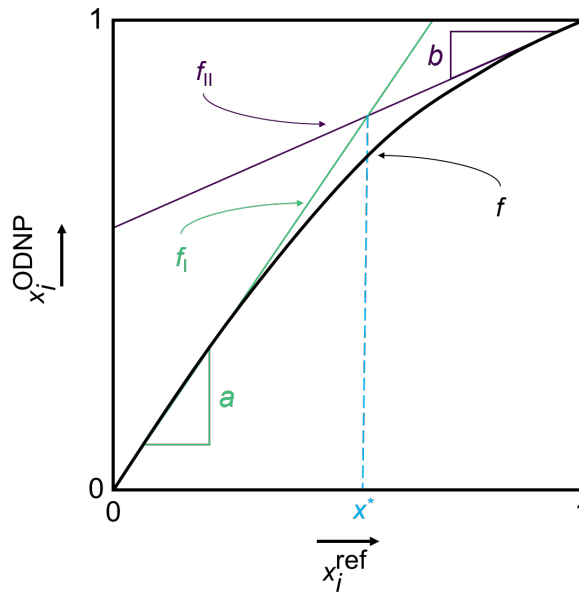
Figure 35: Illustration of the calibration function that relates x_i^{ODNP} and x_i^{ref}. The calibration function f is basically a combination of two linear functions (green and purple) with a smooth transition between both.

In both concentration corners, the relation between x_i^{ref} and x_i^{ODNP} is basically linear, but the slopes of the linear functions differ. At intermediate concentrations, there is a smooth transition between these two lines. This observation has led to the empirical correlation function which is given in Equation (12). The function was chosen after preliminary tests with the aim of representing the observed relations $x_i^{\text{ODNP}}(x_i^{\text{ref}})$ with a flexible function with a minimal number of parameters.

$$x_i^{\text{ODNP}} = f(x_i^{\text{ref}}) = w_{\text{I}}(x_i^{\text{ref}}) \cdot f_{\text{I}}(x_i^{\text{ref}}) + w_{\text{II}}(x_i^{\text{ref}}) \cdot f_{\text{II}}(x_i^{\text{ref}}) \tag{12}$$

with:

$$f_{\text{I}}(x_i^{\text{ref}}) = a \cdot x_i^{\text{ref}} \tag{13}$$

$$f_{\text{II}}(x_i^{\text{ref}}) = (1 - b) + b \cdot x_i^{\text{ref}} \tag{14}$$

The parameters a and b describe the slopes of the linear calibration curves in the highly diluted regions and are fitted to the experimental data points. The weights w_{I} and w_{II} are defined such that the following conditions are satisfied:

$$w_{\text{I}}(0) = 1 \text{ and } w_{\text{I}}(1) = 0$$

$$w_{\text{II}}(0) = 0 \text{ and } w_{\text{II}}(1) = 1$$

The weight functions are given in Equation (15) and Equation (16).

$$w_{\text{I}}(x_i^{\text{ref}}) = \frac{\tanh\left(c\left(x_i^* - x_i^{\text{ref}}\right)\right) - \tanh\left(c\left(x_i^* - 1\right)\right)}{\tanh\left(c\left(x_i^* - 0\right)\right) - \tanh\left(c\left(x_i^* - 1\right)\right)} \tag{15}$$

$$w_{\text{II}}(x_i^{\text{ref}}) = \frac{\tanh\left(c\left(x_i^{\text{ref}} - x_i^*\right)\right) - \tanh\left(c\left(0 - x_i^*\right)\right)}{\tanh\left(c\left(1 - x_i^*\right)\right) - \tanh\left(c\left(0 - x_i^*\right)\right)} \tag{16}$$

where x^* is

$$x^* = \frac{1 - b}{a - b} \tag{17}$$

which is the value of x_i^{ref} for which the two functions $f_{\text{I}}(x_i^{\text{ref}})$ and $f_{\text{II}}(x_i^{\text{ref}})$ intersect. The parameter c controls the steepness of the transition between these two branches of the calibration curve. It can be adjusted, but also a default value can be chosen, as it was done in the present work. Based on preliminary studies the value $c = 3$ was selected and used for all evaluations. Hence, even though the mathematical form of the calibration curve described by Equations (12) - (17) may seem intricate, the function

itself is simple to handle and has only two adjustable parameters a and b (or three if c is not set). Furthermore, it also contains the fully linear correlation as a limiting case (for $a = b$). Formally, the component i can be chosen to be either 1 or 2. As the mole fractions of the two components of the binary mixture sum up to 1, both choices are equivalent. In the present work, we always refer to component 1, which was ACN in all three studied systems.

For each of the studied systems, the parameters a and b were determined from a fit to the experimental data points, which was performed with the nonlinear least-squares solver *lsqcurvefit* of MATLAB using the following target function

$$S = \sum_{k=1}^{M} \left(f\left(x_{\mathrm{ACN},k}^{\mathrm{ref}}\right) - x_{\mathrm{ACN},k}^{\mathrm{ODNP}} \right)^2 \tag{18}$$

where M is the number of data points in the system.

To quantify the accuracy of the obtained correlation, the mean absolute error ($\mathrm{MAE_{corr}}$) is calculated according to Equation (19).

$$\mathrm{MAE_{corr}} = \frac{\sum_{k=1}^{M} \left| f\left(x_{\mathrm{ACN},k}^{\mathrm{ref}}\right) - x_{\mathrm{ACN},k}^{\mathrm{ODNP}} \right|}{M} \tag{19}$$

The robustness of this calibration approach was evaluated using a leave-one-out (LOO) analysis [234]: One data point (here: the result for one mixture $k^\star$) of the data set (here: the set of results for a given system) was left out, while the others were used for the fit. The obtained calibration function was then used to calculate $\left| f\left(x_{\mathrm{ACN},k^*}^{\mathrm{ref}}\right) - x_{\mathrm{ACN},k^*}^{\mathrm{ODNP}} \right|$. This procedure was repeated for all M data points (mixtures) of the studied system and the mean absolute error of the LOO analysis ($\mathrm{MAE_{LOO}}$) was calculated in the same way as for $\mathrm{MAE_{corr}}$, cf. Equation (19).

6.3 Results and Discussion

The signal integrals from the ODNP experiments were used to calculate $x_{\mathrm{ACN}}^{\mathrm{ODNP}}$ for all data points using Equation (11). Furthermore, for all data points $x_{\mathrm{ACN}}^{\mathrm{ref}}$ is known. Based on these data, for the studied system the calibration function (Equation (12) - (17)) was fitted to the data points $(x_{\mathrm{ACN}}^{\mathrm{ref}}, x_{\mathrm{ACN}}^{\mathrm{ODNP}})$ and the LOO analysis was carried out, yielding $\mathrm{MAE_{corr}}$ and $\mathrm{MAE_{LOO}}$. In Table 9, these values are reported together with the numbers for a and b found from the correlation of the full data set. The values for $\mathrm{MAE_{corr}}$ are below about 0.02 mol mol^{-1} for the ^{1}H NMR as well as for the ^{13}C NMR data, which is remarkable, considering the fact that the data stem from single-scan experiments in

flow. The values of MAE_{LOO} are somewhat higher, but underline the robustness of the method. A detailed discussion of the results is given in the next sections. Additional data on the signal integrals, the signal enhancements, and the spin-lattice relaxation time T_1 as well as the relative deviations of data points from the calibration curve are reported in the Appendix E.

In general, there are two effects that affect the ODNP enhancement and consequently may result in a nonlinear calibration curve: 1) the different types and strengths of hyperfine interactions of the molecules with the radical; 2) the unequal hyperpolarization losses due to differences in T_1 during the transport from the fixed bed to the benchtop NMR spectrometer.

Table 9: Results from the fits of the calibration curves. Parameters a and b of the calibration function (Equation (12) - (17)) were obtained from a fit to all available experimental data points of the studied system. Additionally, the resulting value of x^*_{ACN} is provided. The number for c was not adjusted to the data and set to $c = 3$ for all systems. The numbers for the mean absolute error of the correlation of all data points (MAE_{corr}) and that found in the leave-one-out analysis (MAE_{LOO}) are also reported.

System	NMR	a	b	x^*_{ACN} / mol mol^{-1}	MAE_{corr} / mol mol^{-1}	MAE_{LOO} / mol mol^{-1}
System 1	^{1}H	1.3023	0.4959	0.625	0.007	0.013
System 2	^{1}H	1.0498	0.9467	0.517	0.018	0.015
System 3	^{1}H	0.6624	1.1946	0.366	0.021	0.039
	^{13}C	0.5064	2.1848	0.706	0.023	0.040

6.3.1 System 1: Acetonitrile (ACN) + Water (W)

Figure 36 shows the ^{1}H NMR spectra of the different studied mixtures of System 1: ACN + W obtained with the ^{1}H NMR ODNP experiments in continuous-flow. For comparison, also the results of the corresponding thermally polarized experiments are shown. Two singlet peaks can be identified which are assigned to ACN and W. Both peaks are broad due to flow effects that reduce the spin-spin relaxation time T_2 [13]. However, the peaks do not overlap, allowing a quantification by direct integration of the signals. The thermally polarized ^{1}H NMR experiments show a low SNR. By switching on the MW and performing the ^{1}H NMR ODNP experiment, a significant improvement

in the SNR is achieved. The average signal enhancements were $E_{\text{ACN}}^{1\text{H}}$ = 35 for ACN and $E_{\text{W}}^{1\text{H}}$ = 19 for W for System 1.

In both types of experiments, the signal integral of W increases linearly as more W is added to the mixture. However, for ACN a deviation from the linear relationship is observed in the ^{1}H NMR ODNP experiment: the maximum signal integral for ACN is not found for the pure substance, but for a mole fraction of $x_{\text{ACN}}^{\text{ref}}$ = 0.584 mol mol^{-1}. This is due to a change in the molecular dynamics of the system as the composition of the samples changes, which affects the interaction of the molecules with the radicals and, hence, the corresponding signal enhancement.
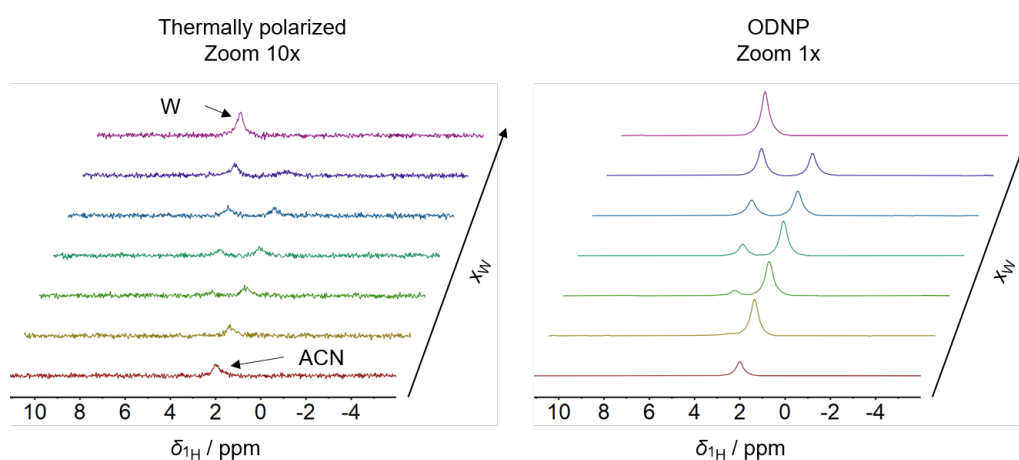
Figure 36: ^{1}H NMR spectra of System 1: ACN + W for mixtures with different composition acquired with a single scan in continuous-flow (flow velocity v = 0.34 m s^{-1}).

Figure 37 shows the results of the quantitative analysis of System 1 with the ^{1}H NMR ODNP experiments. The results for $x_{\text{ACN}}^{\text{ODNP}}$ obtained in the ^{1}H NMR ODNP experiment are plotted over the gravimetric reference value $x_{\text{ACN}}^{\text{ref}}$ and the calibration curve resulting from the fit to all data points is shown.

The concentrations of ACN were systematically overestimated in the ODNP experiment (and, as consequence, those for the concentrations of W were systematically underestimated). This is a result of the significant difference in the observed signal enhancements which are mainly due to differences in the $T_{1,^1\text{H}}$ values between ACN and W. The T_1 values of ACN are much larger than those of W; see Appendix E. This leads to lower hyperpolarization losses during the transport from the fixed bed to the detection zone for ACN compared to those for W. Furthermore, the results shown in Figure 37 indicate that the different affinities of the two component to the radical matrix do not play a significant role here because it is expected that W has a higher preference to the matrix than ACN which would lead to data points below the diagonal line.

However, the excellent description of the results by the correlation is evident in Figure 37. The calibration function fits the experimental data points very well. In particular, the almost linear data for ACN mole fractions below about 0.5 mol mol^{-1} is described very well. The MAE_{corr} is less than 0.007 mol mol^{-1}, which is a very good result for quantitative NMR measured in a 0.25 mm capillary in a benchtop NMR spectrometer in continuous-flow. The MAE obtained in the LOO analysis is only 0.013 mol mol^{-1}, indicating that the approach provides a robust calibration function.
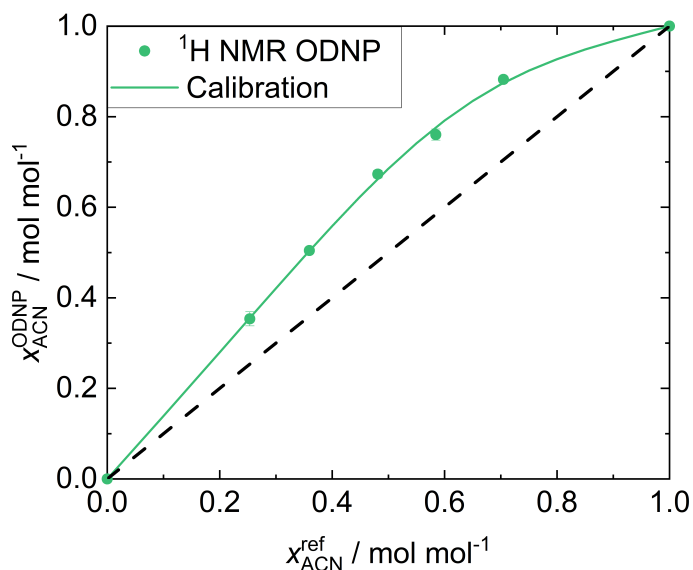
Figure 37: Results for System 1: ACN + W. x_{ACN}^{ODNP} obtained in the ^{1}H NMR ODNP experiments (symbols) are plotted over the gravimetric reference values x_{ACN}^{ref}. The calibration curve (solid line) resulting from the fit to all data as well as the ideal diagonal line (dashed line) are given.

6.3.2 System 2: Acetonitrile (ACN) + 1,4-Dioxane (DX)

Figure 38 shows the results of the quantitative analysis with the ^{1}H NMR ODNP experiment and the calibration curve for System 2: ACN + DX. The ^{1}H NMR spectra of the thermally polarized ^{1}H NMR and ^{1}H NMR ODNP experiments in continuous-flow are provided in the Appendix E.

In Figure 38, a linear dependence of x_{ACN}^{ODNP} on x_{ACN}^{ref} can be observed over almost the entire concentration range. In contrast to System 1, the results are close to the ideal diagonal line. Also this behavior is described very well by the calibration function. The MAE_{corr} is 0.018 mol mol^{-1} and the MAE_{LOO} is 0.015 mol mol^{-1}, respectively, which is a good result for quantitative benchtop NMR of fast flowing samples.

The slopes of both linear functions and, thus, the parameters a and b do not differ much

from each other for this system. The calibration function collapses to a simple linear correlation. There are two reasons for this observation: First, the difference in the T_1 values of ACN and DX is small compared to System 1 (see Appendix E). Therefore, hyperpolarization losses during the transport are not relevant for the quantification in this system. Second, the hyperfine interactions of both molecules with the radicals are expected to be similar. This is supported by the similar enhancement values obtained for ACN and DX in the different mixtures (see Appendix E).
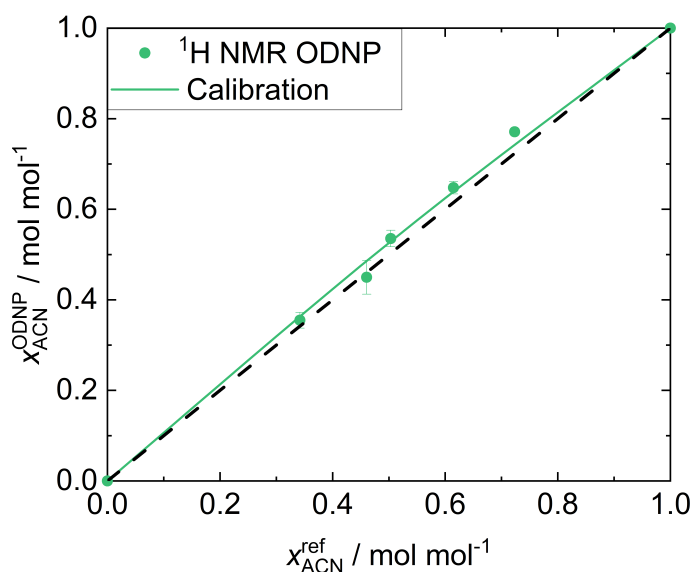
Figure 38: Results for System 2: ACN + DX. $x_{\text{ACN}}^{\text{ODNP}}$ obtained in the ^{1}H NMR ODNP experiments (symbols) are plotted over the gravimetric reference values $x_{\text{ACN}}^{\text{ref}}$. The calibration curve (solid line) resulting from the fit to all data as well as the ideal diagonal line (dashed line) are given.

6.3.3 System 3: Acetonitrile (ACN) + Chloroform (CF)

Figure 39 shows the results of the quantitative analysis with the ^{1}H NMR ODNP experiments and the calibration curve for System 3: ACN + CF. Again, the ^{1}H NMR spectra of the thermally polarized ^{1}H NMR and ^{1}H NMR ODNP experiments in continuous-flow are provided in the Appendix E. The detection cell for this system had an inner diameter of 2.9 mm to enable the ^{13}C NMR experiments at natural abundance described later. Therefore, the ^{1}H NMR experiments for this system were carried out at a much higher flow velocity than for System 1 and System 2 (v = 0.34 m s^{-1} for System 1 and System 2 compared to v = 2.38 m s^{-1} for System 3) to allow the larger detection cell to be filled within the $T_{1,^1\text{H}}$ relaxation time of the molecules. Furthermore, the MW power was reduced in these experiments because of the high volatility of CF, resulting in lower enhancement values and lower SNR. Moreover, the sudden expansion at the inlet of the

detection cell from 0.25 to 2.9 mm leads to the formation of a jet-flow (see Chapter 5). Therefore, a high degree of back-mixing is present in the detection cell, which further reduces hyperpolarization and affects quantification.

Despite these changes, the calibration function correlates the data very well. The $\mathrm{MAE_{corr}}$ is 0.021 mol mol^{-1}. However, an outlier is identified at an ACN mole fraction of $x^{\mathrm{ref}}_{\mathrm{ACN}}$ = 0.383 mol mol $^{-1}$. As a consequence, a larger $\mathrm{MAE_{LOO}}$ of 0.039 mol mol^{-1} is found. Nevertheless, the results underline the robustness of the calibration method.

In contrast to System 1, the ACN concentration is systematically underestimated by the ^{1}H NMR ODNP experiment whereas the CF concentration is overestimated. This observation can be explained by the T_1 values, which are reversed in this system: ACN has a significantly shorter ^{1}H spin-lattice relaxation time than CF, resulting in larger hyperpolarization losses for ACN.
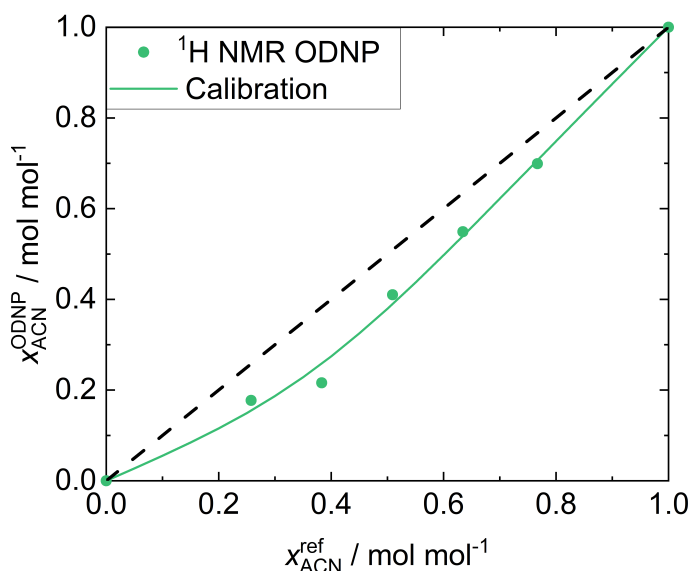
Figure 39: Results for System 3: ACN + CF. $x^{\mathrm{ODNP}}_{\mathrm{ACN}}$ obtained in the ^{1}H NMR ODNP experiments (symbols) are plotted over the gravimetric reference values $x^{\mathrm{ref}}_{\mathrm{ACN}}$. The calibration curve (solid line) resulting from the fit to all data as well as the ideal diagonal line (dashed line) are given.

Figure 40 shows ^{13}C NMR spectra of the different mixtures of System 3 obtained by the ^{13}C NMR ODNP experiment with only one scan in continuous-flow. Without ODNP a similar experiment would have yielded no signals at all. The flow rate for the ^{13}C NMR experiments of this system was reduced (v = 0.34 m s^{-1}) compared to the one for the ^{1}H NMR experiments due to the much longer $T_{1,^{13}\mathrm{C}}$ relaxation times. The two singlet peaks in the spectra can be clearly assigned to the methyl group of ACN and CF, respectively. The large chemical shift dispersion prevents peak overlap, which is

particularly beneficial for benchtop NMR spectroscopy. A mean signal enhancement of $E_{\text{ACN}}^{^{13}\text{C}}$ = 14 and $E_{\text{CF}}^{^{13}\text{C}}$ = 45 was achieved. The higher enhancement of CF is a consequence of its molecular structure (electron withdrawing effect of the chlorine atoms) which results in a stronger hyperfine interaction to TEMPO radicals [197, 200–202].
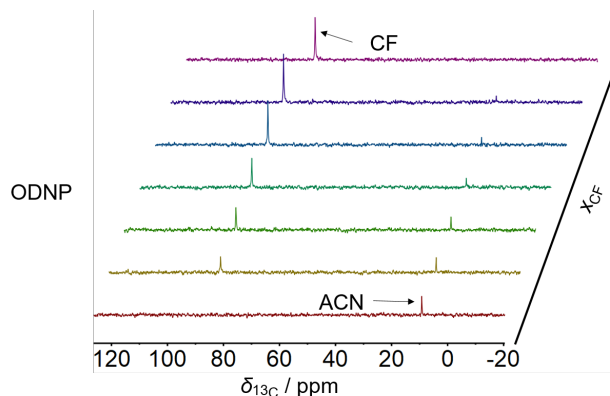
**Figure 40:** ODNP-enhanced ^{13}C NMR spectra of System 3: ACN + CF for mixtures with different composition acquired with a single scan in continuous-flow (flow velocity v = 0.34 m s^{-1}).

In Figure 41, the results of the quantitative analysis with the ^{13}C NMR ODNP experiment and the calibration curve for System 3: ACN + CF are shown. Similar to the experiments with ^{1}H NMR ODNP, an overestimation of CF is observed, which is explained by the larger ODNP enhancement of CF compared to ACN. Relaxation effects on the ^{13}C nuclei must also be considered, as the chosen flow velocity of 0.34 m s^{-1} results in a mean transport time of 1.5 s. An additional time delay occurs due to the filling of the large detection volume with hyperpolarized fluid. For the pure components ACN and CF the $T_{1,\,^{13}\text{C}}$ values were determined experimentally (for ACN: 15.4 s; for CF: 21.7 s; see Chapter 5), which leads to higher polarization losses for ACN. The combination of both effects (stronger hyperfine interaction and larger T_1 time) leads to an overestimation of the CF concentration, and consequently an underestimation of the ACN concentration, as observed in Figure 41 and as expected.

For the ^{13}C NMR ODNP experiments, the obtained $x_{\text{ACN}}^{\text{ODNP}}$ mole fractions deviate strongly from the diagonal line. The calibration function is still able to correlate the experimental data satisfactorily, but the MAE$_{\text{corr}}$ of 0.023 mol mol^{-1} and the MAE$_{\text{LOO}}$ of 0.040 mol mol^{-1} are the highest of all quantitative analyses. This is explained by the significantly lower SNRs of the ^{13}C NMR spectra compared to those of the ^{1}H NMR spectra, which is due to the low natural abundance of ^{13}C, resulting in larger uncertainties. In addition, the quantification is disturbed by the jet-flow present in the detection cell. Improving the accuracy of the ^{13}C NMR quantification with ODNP by improving the experimental setting is the subject of ongoing research in our group. However, even

the first experiments demonstrate that ODNP enables a reasonable quantitative analysis of mixtures by single-scan benchtop ^{13}C NMR spectroscopy in continuous-flow, which is impossible without ODNP. This is particularly useful when NMR signals overlap in the ^{1}H NMR spectrum as it is often the case for mixtures measured with benchtop NMR spectrometers.
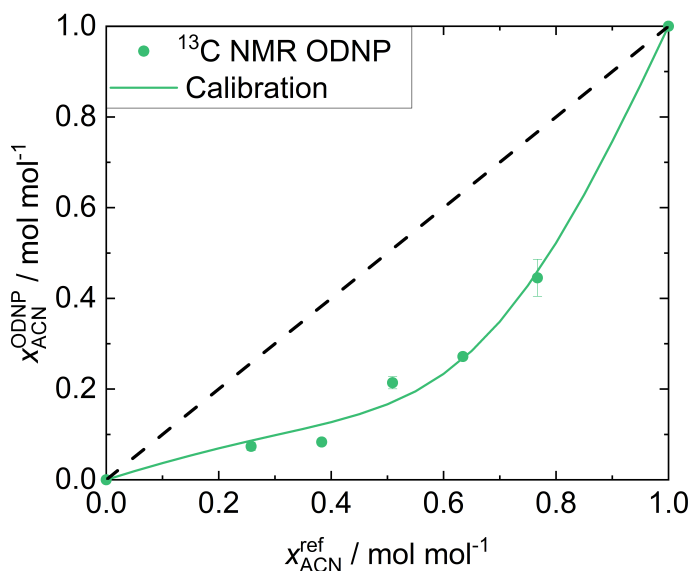
Figure 41: Results for System 3: ACN + W. $x_{\mathrm{ACN}}^{\mathrm{ODNP}}$ obtained in the ^{13}C NMR ODNP experiments (symbols) are plotted over the gravimetric reference values $x_{\mathrm{ACN}}^{\mathrm{ref}}$. The calibration curve (solid line) resulting from the fit to all data as well as the ideal diagonal line (dashed line) are given.

6.4 Conclusions

ODNP can be used for overcoming sensitivity issues of NMR spectroscopy as it greatly increases the signal intensity and thereby the SNR. This is especially important in continuous-flow NMR, where the analysis must often be carried out with single-scan experiments. However, as the signal enhancement is generally different for different components and many factors influence the individual enhancements, a quantification of NMR spectra obtained with ODNP is difficult. This is the first study in which this issue is tackled. It has been shown that a quantification of both ^{1}H NMR and ^{13}C NMR spectra of mixtures obtained in continuous-flow experiments with ODNP with a benchtop NMR spectrometer is possible using a simple calibration – without having to elucidate and quantify all effects that lead to the different signal enhancements for the different components. A special calibration function was developed for that purpose that describes the non-linear data for the different studied binary systems very well with

only two parameters. The results indicate that the most important parameters that influence the enhancements and, hence, the type of calibration curve that is obtained, are the strengths of the hyperfine interaction of the components of the mixture with the radicals in the fixed bed and the polarization losses during transport from the fixed bed to the NMR detection, that basically depend on the T_1 time of the components. To apply ODNP for quantitative analysis in a flow setup as used in this work, the following procedure is recommended: in a preliminary study, suitable experimental parameters, such as the microwave intensity and flow rate should be determined. Alternatively, they could be set based on experience. For these parameters, a calibration can be carried out. Then, routine analysis is possible, including single-scan experiments with ^{13}C NMR on benchtop instruments in continuous-flow. In future work, the approach should be extended to multi-component systems, but the route to apply ODNP in quantitative flow NMR is now open.

7 Conclusions

Benchtop NMR spectroscopy is a highly promising process analytical technique (PAT): it is non-invasive, enable quantification without calibration, and is robust and affordable. However, three major drawbacks currently hinder the widespread use of this emerging technology: peak overlap, typically observed for ^{1}H NMR spectroscopy, low signal intensity, commonly an issue in ^{13}C NMR spectroscopy, and the insufficient premagnetization in continuous-flow, which is a consequence of the compact design of the benchtop NMR spectrometers. In the present thesis, these challenges are addressed by applying various strategies: 1) the application of a novel method for model-based quantitative analysis of spectra with overlapping peaks, 2) using special pulse sequences to enhance the ^{13}C NMR signal without the need for additional hardware, and 3) employing hyperpolarization techniques to enhance ^{13}C NMR signals.

Grape must and wine products are characterized by a complex matrix with many components which result in strong peak overlap in the ^{1}H NMR spectra. Hence, these samples are challenging for quantitative benchtop NMR spectroscopy. The AutoWine-tool of Matviychuck et al. [79] was used to monitor and to quantify a wine fermentation online. In a preliminary study, the procedure was validated using test mixtures representing the different stages of a wine fermentation. Good agreement with the corresponding gravimetric concentrations was found. Subsequently, a laboratory scale wine fermentation was monitored by benchtop ^{1}H NMR spectroscopy and quantified with the AutoWine-tool. Two different fermentation modes were investigated. Both major and minor components were successfully monitored with a high temporal resolution.

^{13}C NMR spectroscopy with its large chemical shift dispersion is highly interesting for the quantification of complex mixtures. However, quantifying mixtures with ^{13}C NMR spectroscopy is time-consuming as the SNR and the spin-lattice relaxation times are unfavorable. The latter is particularly problematic for applications in continuous-flow, as the magnetization is insufficient, especially in the compact benchtop NMR spectrometers. NMR pulse sequences, e.g. PENDANT, which involve ^{1}H-^{13}C polarization transfer, are attractive because they tackle these issues by enhancing the ^{13}C NMR signal up to fourfold and additionally reduce the experimental time as well as solve the premagnetization issue by utilizing the much faster spin-lattice relaxation of protons.

Therefore, PENDANT has been applied for the quantitative analysis of mixtures in stationary and flow experiments with a benchtop NMR spectrometer. The results obtained by PENDANT were compared to those from standard NMR experiments and gravimetric references, showing excellent agreement in both stationary and flow conditions. A dynamic process was successfully studied with PENDANT, demonstrating the method's applicability in process monitoring.

Moreover, the advantages of the polarization transfer method were used in measurements of self-diffusion coefficients with benchtop ^{13}C NMR spectroscopy. The self-diffusion coefficient is an important physical property that characterizes the mobility of individual molecules and is, thus, important in many fields of science and engineering. Usually ^{1}H NMR is used for diffusion measurements but it is not applicable to complex mixtures resulting in heavily overlapping peaks in the ^{1}H NMR spectrum. Therefore, the polarization transfer sequence PENDANT was extended with a diffusion encoding sequence for the determination of diffusion coefficients based on ^{13}C NMR spectroscopy. The new pulse sequence - named PENPFG - was tested by measuring the self-diffusion coefficients of pure components as well as in binary and ternary mixtures with a benchtop NMR spectrometer. As a reference, the same systems were investigated with standard NMR experiments using a high-field NMR spectrometer. Good agreement between the results of PENPFG and those of the reference experiments was found.

ODNP is hyperpolarization technique in which the polarization of electron spins is transferred to nuclear spins by MW irradiation, resulting in impressive signal enhancements. ODNP is well-suited for reaction and process monitoring applications due to its very rapid polarization build-up which solves the premagnetization issue of flowing samples in benchtop NMR. Direct as well as indirect ODNP techniques were studied to obtain signal enhanced ^{13}C NMR spectra. All techniques were evaluated at different flow rates. Significant ^{13}C signal enhancements were observed in all cases, which depend on the flow velocity, the investigated substance, and its molecular interaction with the radical fixed bed. The outcome is determined by the efficiency of hyperpolarization build-up in the fixed bed as well as hyperpolarization loss on the way to the detection zone. It was demonstrated that ODNP enables ^{13}C NMR acquisition with a single scan even at high flow velocities.

In ODNP, unequal nuclear spin polarization levels are observed for different components in the mixture, causing complications in the quantification of those mixtures. This challenge has been addressed, allowing the application of ODNP for the quantitative analysis of binary mixtures on a benchtop NMR spectrometer in continuous-flow in a wide concentration range for the first time. A robust calibration approach was developed to handle the non-uniform ODNP efficiencies. The approach was evaluated by a LOO analysis. The calibration function described the experimental data successfully and

quantified the mixtures with good precision. It was demonstrated that quantitative NMR spectroscopy with ODNP-enhanced signals is feasible.

In conclusion, this thesis introduces methods and strategies to considerably improve benchtop NMR spectroscopy in terms of sensitivity, selectivity and temporal resolution and opens up new routes for the application of this powerful analytical technique in process engineering and related fields.

Literature

[1] Y. Ben-Tal, P. J. Boaler, H. J. Dale, R. E. Dooley, N. A. Fohn, Y. Gao, A. García-Domínguez, K. M. Grant, A. M. Hall, H. L. Hayes, M. M. Kucharski, R. Wei, G. C. Lloyd-Jones: Mechanistic analysis by NMR spectroscopy: A users guide, Progress in Nuclear Magnetic Resonance Spectroscopy 129 (2022) 28–106. DOI: `10.1016/j.pnmrs.2022.01.001`.

[2] A. Brächer, R. Behrens, E. von Harbou, H. Hasse: Application of a new micro-reactor ^{1}H NMR probe head for quantitative analysis of fast esterification reactions, Chemical Engineering Journal 306 (2016) 413–421. DOI: `10.1016/j.cej.2016.07.045`.

[3] P. Giraudeau, F.-X. Felpin: Flow reactors integrated with in-line monitoring using benchtop NMR spectroscopy, Reaction Chemistry & Engineering 3 (2018) 399–413. DOI: `10.1039/c8re00083b`.

[4] L. F. Gladden, F. J. Abegão, C. P. Dunckley, D. J. Holland, M. H. Sankey, A. J. Sederman: MRI: Operando measurements of temperature, hydrodynamics and local reaction rate in a heterogeneous catalytic reactor, Catalysis Today 155 (2010) 157–163. DOI: `10.1016/j.cattod.2009.10.012`.

[5] A. M. R. Hall, J. C. Chouler, A. Codina, P. T. Gierth, J. P. Lowe, U. Hintermair: Practical aspects of real-time reaction monitoring using multi-nuclear high resolution FlowNMR spectroscopy, Catalysis Science & Technology 6 (2016) 8406–8417. DOI: `10.1039/c6cy01754a`.

[6] E. von Harbou, R. Behrens, J. Berje, A. Brächer, H. Hasse: Studying Fast Reaction Kinetics with Online NMR Spectroscopy, Chemie Ingenieur Technik 89 (2016) 369–378. DOI: `10.1002/cite.201600068`.

[7] M. Maiwald, H. H. Fischer, Y.-K. Kim, H. Hasse: Quantitative on-line high-resolution NMR spectroscopy in process engineering applications, Analytical and Bioanalytical Chemistry 375 (2003) 1111–1115. DOI: `10.1007/s00216-002-1723-y`.

[8] M. Maiwald, H. H. Fischer, Y.-K. Kim, K. Albert, H. Hasse: Quantitative high-resolution on-line NMR spectroscopy in reaction and process monitoring, Journal of Magnetic Resonance 166 (2004) 135–146. DOI: `10.1016/j.jmr.2003.09.003`.

[9] A. Nordon, C. A. McGill, D. Littlejohn: Process NMR spectrometry, The Analyst 126 (2001) 260–272. DOI: `10.1039/b009293m`.

[10] M. Sankey, D. Holland, A. Sederman, L. Gladden: Magnetic resonance velocity imaging of liquid and gas two-phase flow in packed beds, Journal of Magnetic Resonance 196 (2009) 142–148. DOI: `10.1016/j.jmr.2008.10.021`.

[11] N. Zientek, K. Meyer, S. Kern, M. Maiwald: Quantitative Online NMR Spectroscopy in a Nutshell, Chemie Ingenieur Technik 88 (2016) 698–709. DOI: `10.1002/cite.201500120`.

[12] B. Blümich: Introduction to compact NMR: A review of methods, TrAC Trends in Analytical Chemistry 83 (2016) 2–11. DOI: `10.1016/j.trac.2015.12.012`.

[13] F. Dalitz, M. Cudaj, M. Maiwald, G. Guthausen: Process and reaction monitoring by low-field NMR spectroscopy, Progress in Nuclear Magnetic Resonance Spectroscopy 60 (2012) 52–70. DOI: `10.1016/j.pnmrs.2011.11.003`.

[14] E. Danieli, J. Perlo, A. L. L. Duchateau, G. K. M. Verzijl, V. M. Litvinov, B. Blümich, F. Casanova: On-Line Monitoring of Chemical Reactions by using Bench-Top Nuclear Magnetic Resonance Spectroscopy, ChemPhysChem 15 (2014) 3060–3066. DOI: `10.1002/cphc.201402049`.

[15] M. V. S. Elipe, R. R. Milburn: Monitoring chemical reactions by low-field benchtop NMR at 45 MHz: pros and cons, Magnetic Resonance in Chemistry 54 (2015) 437–443. DOI: `10.1002/mrc.4189`.

[16] M. Grootveld, B. Percival, M. Gibson, Y. Osman, M. Edgar, M. Molinari, M. L. Mather, F. Casanova, P. B. Wilson: Progress in low-field benchtop NMR spectroscopy in chemical and biochemical analysis, Analytica Chimica Acta 1067 (2019) 11–30. DOI: `10.1016/j.aca.2019.02.026`.

[17] T. Maschmeyer, P. L. Prieto, S. Grunert, J. E. Hein: Exploration of continuous-flow benchtop NMR acquisition parameters and considerations for reaction monitoring, Magnetic Resonance in Chemistry (2020). DOI: `10.1002/mrc.5094`.

[18] K. Meyer, S. Kern, N. Zientek, G. Guthausen, M. Maiwald: Process control with compact NMR, TrAC Trends in Analytical Chemistry 83 (2016) 39–52. DOI: `10.1016/j.trac.2016.03.016`.

[19] S. D. Riegel, G. M. Leskowitz: Benchtop NMR spectrometers in academic teaching, TrAC Trends in Analytical Chemistry 83 (2016) 27–38. DOI: `10.1016/j.trac.2016.01.001`.

[20] T. Rudszuck, H. Nirschl, G. Guthausen: Perspectives in process analytics using low field NMR, Journal of Magnetic Resonance 323 (2021) 106897. DOI: `10.1016/j.jmr.2020.106897`.

[21] K. Singh, B. Blümich: NMR spectroscopy with compact instruments, TrAC Trends in Analytical Chemistry 83 (2016) 12–26. DOI: `10.1016/j.trac.2016.02.014`.

[22] R. Hotop: Neue Methoden der Prozeßanalysentechnik für die verfahrenstechnische Produktion, Chemie Ingenieur Technik 65 (1993) 921–928. DOI: `10.1002/cite.330650805`.

[23] T. A. Beek: Low-field benchtop NMR spectroscopy: status and prospects in natural product analysis, Phytochemical Analysis 32 (2020) 24–37. DOI: `10.1002/pca.2921`.

[24] D. Bouillaud, J. Farjon, O. Gonçalves, P. Giraudeau: Benchtop NMR for the monitoring of bioprocesses, Magnetic Resonance in Chemistry 57 (2019) 794–804. DOI: `10.1002/mrc.4821`.

[25] T. Castaing-Cordier, D. Bouillaud, J. Farjon, P. Giraudeau: Recent advances in benchtop NMR spectroscopy and its applications, in: Annual Reports on NMR Spectroscopy, Elsevier, 2021, pp. 191–258. DOI: `10.1016/bs.arnmr.2021.02.003`.

[26] C. Claaßen, K. Mack, D. Rother: Benchtop NMR for Online Reaction Monitoring of the Biocatalytic Synthesis of Aromatic Amino Alcohols, ChemCatChem 12 (2020) 1190–1199. DOI: `10.1002/cctc.201901910`.

[27] F. Dalitz, L. Kreckel, M. Maiwald, G. Guthausen: Quantitative Medium-Resolution NMR Spectroscopy Under Non-Equilibrium Conditions, Studied on the Example of an Esterification Reaction, Applied Magnetic Resonance 45 (2014) 411–425. DOI: `10.1007/s00723-014-0522-x`.

[28] A. Friebel, A. Fröscher, K. Münnemann, E. von Harbou, H. Hasse: In situ measurement of liquid-liquid equilibria by medium field nuclear magnetic resonance, Fluid Phase Equilibria 438 (2017) 44–52. DOI: `10.1016/j.fluid.2017.01.027`.

[29] A. Friebel, E. von Harbou, K. Münnemann, H. Hasse: Reaction Monitoring by Benchtop NMR Spectroscopy Using a Novel Stationary Flow Reactor Setup, Industrial & Engineering Chemistry Research 58 (2019) 18125–18133. DOI: `10.1021/acs.iecr.9b03048`.

[30] A. Friebel, E. von Harbou, K. Münnemann, H. Hasse: Online process monitoring of a batch distillation by medium field NMR spectroscopy, Chemical Engineering Science 219 (2020) 115561. DOI: `10.1016/j.ces.2020.115561`.

[31] D. Galvan, L. M. de Aguiar, J. J. R. Rohwedder, D. Borsato, M. H. M. Killner: Online monitoring of transesterification reaction by medium-resolution benchtop ^{1}H NMR and NIR spectroscopy, Fuel Processing Technology 208 (2020) 106511. DOI: `10.1016/j.fuproc.2020.106511`.

[32] S. Kern, L. Wander, K. Meyer, S. Guhl, A. R. G. Mukkula, M. Holtkamp, M. Salge, C. Fleischer, N. Weber, R. King, S. Engell, A. Paul, M. P. Remelhe, M. Maiwald: Flexible automation with compact NMR spectroscopy for continuous production of pharmaceuticals, Analytical and Bioanalytical Chemistry 411 (2019) 3037–3046. DOI: `10.1007/s00216-019-01752-y`.

[33] S. Kern, S. Liehr, L. Wander, M. Bornemann-Pfeiffer, S. Müller, M. Maiwald, S. Kowarik: Artificial neural networks for quantitative online NMR spectroscopy, Analytical and Bioanalytical Chemistry 412 (2020) 4447–4459. DOI: `10.1007/s00216-020-02687-5`.

[34] D. Kreyenschulte, E. Paciok, L. Regestein, B. Blümich, J. Büchs: Online monitoring of fermentation processes via non-invasive low-field NMR, Biotechnology and Bioengineering 112 (2015) 1810–1821. DOI: `10.1002/bit.25599`.

[35] M. Leutzsch, A. J. Sederman, L. F. Gladden, M. D. Mantle: In situ reaction monitoring in heterogeneous catalysts by a benchtop NMR spectrometer, Magnetic Resonance Imaging 56 (2019) 138–143. DOI: `10.1016/j.mri.2018.09.006`.

[36] A. Soyler, D. Bouillaud, J. Farjon, P. Giraudeau, M. H. Oztop: Real-time benchtop NMR spectroscopy for the online monitoring of sucrose hydrolysis, LWT 118 (2020) 108832. DOI: `10.1016/j.lwt.2019.108832`.

[37] https://www.expertmarketresearch.com/reports/wine-market, Expert Market Research, 2024.

[38] M. Schwinn, D. Durner, A. Delgado, U. Fischer: Distribution of Yeast Cells, Temperature, and Fermentation By-Products in White Wine Fermentations, American Journal of Enology and Viticulture 70 (2019) 339–350. DOI: `10.5344/ajev.2019.18092`.

[39] M. Schwinn, D. Durner, M. Wacker, A. Delgado, U. Fischer: Impact of fermentation temperature on required heat dissipation, growth and viability of yeast, on sensory characteristics and on the formation of volatiles in Riesling, Australian Journal of Grape and Wine Research 25 (2019) 173–184. DOI: `10.1111/ajgw.12386`.

[40] S. Gómez-Alonso, I. Hermosín-Gutiérrez, E. García-Romero: Simultaneous HPLC Analysis of Biogenic Amines, Amino Acids, and Ammonium Ion as Aminoenone Derivatives in Wine and Beer Samples, Journal of Agricultural and Food Chemistry 55 (2007) 608–613. DOI: `10.1021/jf062820m`.

[41] R. López, M. Aznar, J. Cacho, V. Ferreira: Determination of minor and trace volatile compounds in wine by solid-phase extraction and gas chromatography with mass spectrometric detection, Journal of Chromatography A 966 (2002) 167–177. DOI: `10.1016/s0021-9673(02)00696-9`.

[42] M. Stupak, V. Kocourek, I. Kolouchova, J. Hajslova: Rapid approach for the determination of alcoholic strength and overall quality check of various spirit drinks and wines using GC–MS, Food Control 80 (2017) 307–313. DOI: `10.1016/j.foodcont.2017.05.008`.

[43] L. S. Mendes, F. C. Oliveira, P. A. Suarez, J. C. Rubim: Determination of ethanol in fuel ethanol and beverages by Fourier transform (FT)-near infrared and FT-Raman spectrometries, Analytica Chimica Acta 493 (2003) 219–231. DOI: `10.1016/s0003-2670(03)00870-5`.

[44] C.-D. Patz, A. Blieke, R. Ristow, H. Dietrich: Application of FT-MIR spectrometry in wine analysis, Analytica Chimica Acta 513 (2004) 81–89. DOI: `10.1016/j.aca.2004.02.051`.

[45] Q. Wang, Z. Li, Z. Ma, L. Liang: Real time monitoring of multiple components in wine fermentation using an on-line auto-calibration raman spectroscopy, Sensors and Actuators B: Chemical 202 (2014) 426–432. DOI: `10.1016/j.snb.2014.05.109`.

[46] A. Urtubia, J. Ricardo Pérez-Correa, M. Meurens, E. Agosin: Monitoring large scale wine fermentations with infrared spectroscopy, Talanta 64 (2004) 778–784. DOI: `10.1016/j.talanta.2004.04.005`.

[47] M. Gishen, R. Dambergs, D. Cozzolino: Grape and wine analysis - enhancing the power of spectroscopy with chemometrics. A review of some applications in the Australian wine industry, Australian Journal of Grape and Wine Research 11 (2005) 296–305. DOI: `10.1111/j.1755-0238.2005.tb00029.x`.

[48] J. L. Moreira, L. Santos: Analysis of organic acids in wines by Fourier-transform infrared spectroscopy, Analytical and Bioanalytical Chemistry 382 (2005) 421–425. DOI: `10.1007/s00216-005-3062-2`.

[49] M. Sáiz-Abajo, J. González-Sáiz, C. Pizarro: Prediction of organic acids and other quality parameters of wine vinegar by near-infrared spectroscopy. A feasibility study, Food Chemistry 99 (2006) 615–621. DOI: `10.1016/j.foodchem.2005.08.006`.

[50] D. Cozzolino, R. Dambergs, L. Janik, W. Cynkar, M. Gishen: Analysis of Grapes and Wine by near Infrared Spectroscopy, Journal of Near Infrared Spectroscopy 14 (2006) 279–289. DOI: `10.1255/jnirs.679`.

[51] A. Urtubia, J. R. Pérez-correa, F. Pizarro, E. Agosin: Exploring the applicability of MIR spectroscopy to detect early indications of wine fermentation problems, Food Control 19 (2008) 382–388. DOI: `10.1016/j.foodcont.2007.04.017`.

[52] V. Di Egidio, N. Sinelli, G. Giovanelli, A. Moles, E. Casiraghi: NIR and MIR spectroscopy as rapid methods to monitor red wine fermentation, European Food Research and Technology 230 (2010) 947–955. DOI: `10.1007/s00217-010-1227-5`.

[53] D. W. Lachenmeier, R. Godelmann, M. Steiner, B. Ansay, J. Weigel, G. Krieg: Rapid and mobile determination of alcoholic strength in wine, beer and spirits using a flow-through infrared sensor, Chemistry Central Journal 4 (2010). DOI: `10.1186/1752-153x-4-5`.

[54] C. Canal, B. Ozen: Monitoring of Wine Process and Prediction of Its Parameters with Mid-Infrared Spectroscopy, Journal of Food Process Engineering 40 (2015). DOI: `10.1111/jfpe.12280`.

[55] R. Bauer, H. Nieuwoudt, F. F. Bauer, J. Kossmann, K. R. Koch, K. H. Esbensen: FTIR Spectroscopy for Grape and Wine Analysis, Analytical Chemistry 80 (2008) 1371–1379. DOI: `10.1021/ac086051c`.

[56] D. Cozzolino, M. Parker, R. G. Dambergs, M. Herderich, M. Gishen: Chemometrics and visible-near infrared spectroscopic monitoring of red wine fermentation in a pilot scale, Biotechnology and Bioengineering 95 (2006) 1101–1107. DOI: `10.1002/bit.21067`.

[57] R. Dambergs, M. Gishen, D. Cozzolino: A Review of the State of the Art, Limitations, and Perspectives of Infrared Spectroscopy for the Analysis of Wine Grapes, Must, and Grapevine Tissue, Applied Spectroscopy Reviews 50 (2014) 261–278. DOI: `10.1080/05704928.2014.966380`.

[58] D. Cozzolino: State-of-the-art advantages and drawbacks on the application of vibrational spectroscopy to monitor alcoholic fermentation (beer and wine), Applied Spectroscopy Reviews 51 (2015) 302–317. DOI: `10.1080/05704928.2015.1132721`.

[59] A. Rapp, A. Markowetz, H. Niebergall: Anwendung der ^{13}C-NMR-Spektroskopie in der Aminosäureanalytik in Wein und Fruchtsäften, Zeitschrift für Lebensmittel-Untersuchung und -Forschung 192 (1991) 1–6. DOI: `10.1007/bf01201432`.

[60] A. Rapp, A. Markowetz: NMR-Spektroskopie in der Weinanalytik, Chemie in unserer Zeit 27 (1993) 149–155. DOI: `10.1002/ciuz.19930270307`.

[61] I. Kosir, M. Kocjancic, J. Kidric: Wine analysis by 1D and 2D NMR spectroscopy, Analusis 26 (1998) 97–101. DOI: `10.1051/analusis:1998118`.

[62] E. López-Rituerto, S. Cabredo, M. López, A. Avenoza, J. H. Busto, J. M. Peregrina: A Thorough Study on the Use of Quantitative ^{1}H NMR in Rioja Red Wine Fermentation Processes, Journal of Agricultural and Food Chemistry 57 (2009) 2112–2118. DOI: `10.1021/jf803245r`.

[63] A. Weekley, P. Bruins, M. Sisto, M. Augustine: Using NMR to study full intact wine bottles, Journal of Magnetic Resonance 161 (2003) 91–98. DOI: `10.1016/s1090-7807(02)00177-5`.

[64] M. Nilsson, I. F. Duarte, C. Almeida, I. Delgadillo, B. J. Goodfellow, A. M. Gil, G. A. Morris: High-Resolution NMR and Diffusion-Ordered Spectroscopy of Port Wine, Journal of Agricultural and Food Chemistry 52 (2004) 3736–3743. DOI: `10.1021/jf049797u`.

[65] A. Avenoza, J. H. Busto, N. Canal, J. M. Peregrina: Time Course of the Evolution of Malic and Lactic Acids in the Alcoholic and Malolactic Fermentation of Grape Must by Quantitative ^{1}H NMR (qHNMR) Spectroscopy, Journal of Agricultural and Food Chemistry 54 (2006) 4715–4720. DOI: `10.1021/jf060778p`.

[66] S. Clark, N. W. Barnett, M. Adams, I. B. Cook, G. A. Dyson, G. Johnston: Monitoring a commercial fermentation with proton nuclear magnetic resonance spectroscopy with the aid of chemometrics, Analytica Chimica Acta 563 (2006) 338–345. DOI: `10.1016/j.aca.2005.11.033`.

[67] R. Godelmann, F. Fang, E. Humpfer, B. Schütz, M. Bansbach, H. Schäfer, M. Spraul: Targeted and Nontargeted Wine Analysis by ^{1}H NMR Spectroscopy Combined with Multivariate Statistical Analysis. Differentiation of Important Parameters: Grape Variety, Geographical Origin, Year of Vintage, Journal of Agricultural and Food Chemistry 61 (2013) 5610–5619. DOI: `10.1021/jf400800d`.

[68] R. Godelmann, C. Kost, C.-D. Patz, R. Ristow, H. Wachter: Quantitation of Compounds in Wine Using ^{1}H NMR Spectroscopy: Description of the Method and Collaborative Study, Journal of AOAC INTERNATIONAL 99 (2016) 1295–1304. DOI: `10.5740/jaoacint.15-0318`.

[69] J. Herbert-Pucheta, C. Pino-Villar, F. Rodríguez-González, G. Padilla-Maya, D. Milmo-Brittingham, L. Zepeda-Vallejo: "One-shot" analysis of wine parameters in non-Saccharomyces large-scale alcohol reduction processes with one- and two-dimensional nuclear magnetic resonance, BIO Web of Conferences 15 (2019) 02016. DOI: `10.1051/bioconf/20191502016`.

[70] E. López-Rituerto, K. M. Sørensen, F. Savorani, S. B. Engelsen, A. Avenoza, J. M. Peregrina, J. H. Busto: Monitoring of the Rioja red wine production process by ^{1}H-NMR spectroscopy, Journal of the Science of Food and Agriculture 102 (2021) 3808–3816. DOI: `10.1002/jsfa.11729`.

[71] P. A. Solovyev, C. Fauhl-Hassek, J. Riedl, S. Esslinger, L. Bontempo, F. Camin: NMR spectroscopy in wine authentication: An official control perspective, Comprehensive Reviews in Food Science and Food Safety 20 (2021) 2040–2062. DOI: `10.1111/1541-4337.12700`.

[72] M. Viskić, L. M. Bandić, A.-M. J. Korenika, A. Jeromel: NMR in the Service of Wine Differentiation, Foods 10 (2021) 120. DOI: `10.3390/foods10010120`.

[73] A. Webb, C. Najac, I. Ronen: Rapid Quantification of Alcohol Content in Intact Bottles of Wine Using Scalar-Coupled Spectroscopy at Low Field, Applied Magnetic Resonance 54 (2023) 1321–1328. DOI: `10.1007/s00723-023-01585-0`.

[74] P. Burkhardtsmaier, K. Pavlovskaja, D. Maier, S. Schäfer, U. Salat, M. S. Schmidt: Quantitative Monitoring of the Fermentation Process of a Barley Malt Mash by Benchtop ^{1}H NMR Spectroscopy, Food Analytical Methods 14 (2021) 1425–1431. DOI: `10.1007/s12161-021-01991-9`.

[75] Y. Matviychuk, E. von Harbou, D. J. Holland: An experimental validation of a Bayesian model for quantification in NMR spectroscopy, Journal of Magnetic Resonance 285 (2017) 86–100. DOI: `10.1016/j.jmr.2017.10.009`.

[76] Y. Matviychuk, J. Yeo, D. J. Holland: A field-invariant method for quantitative analysis with benchtop NMR, Journal of Magnetic Resonance 298 (2019) 35–47. DOI: `10.1016/j.jmr.2018.11.010`.

[77] Y. Matviychuk, E. Steimers, E. von Harbou, D. J. Holland: Bayesian approach for automated quantitative analysis of benchtop NMR data, Journal of Magnetic Resonance 319 (2020) 106814. DOI: `10.1016/j.jmr.2020.106814`.

[78] E. Steimers, Y. Matviychuk, A. Friebel, K. Münnemann, E. Harbou, D. J. Holland: A comparison of non-uniform sampling and model-based analysis of NMR spectra for reaction monitoring, Magnetic Resonance in Chemistry 59 (2020) 221–236. DOI: `10.1002/mrc.5095`.

[79] Y. Matviychuk, S. Haycock, T. Rutan, D. J. Holland: Quantitative analysis of wine and other fermented beverages with benchtop NMR, Analytica Chimica Acta 1182 (2021) 338944. DOI: `10.1016/j.aca.2021.338944`.

[80] C. Frohman, R. Mira de Orduña: Cellular viability and kinetics of osmotic stress associated metabolites of Saccharomyces cerevisiae during traditional batch and fed-batch alcoholic fermentations at constant sugar concentrations, Food Research International 53 (2013) 551–555. DOI: `10.1016/j.foodres.2013.05.020`.

[81] B. Kunstmann, M. Kohns, H. Hasse: Thermophysical Properties of Mixtures of 2-Ethylhexanoic Acid and Ethanol, Journal of Chemical & Engineering Data 68 (2023) 330–338. DOI: `10.1021/acs.jced.2c00689`.

[82] K. Scanes, S. Hohrnann, B. Prior: Glycerol Production by the Yeast Saccharomyces cerevisiae and its Relevance to Wine: A Review, South African Journal of Enology & Viticulture 19 (1998). DOI: `10.21548/19-1-2239`.

[83] A. L. Waterhouse, G. L. Sacks, D. W. Jeffery: Understanding Wine Chemistry, Wiley, 2016. DOI: `10.1002/9781118730720`.

[84] B. Chidi, F. Bauer, D. Rossouw: Organic Acid Metabolism and the Impact of Fermentation Practices on Wine Acidity: A Review, South African Journal of Enology and Viticulture 39 (2018). DOI: `10.21548/39-2-3172`.

[85] R. Torres-Guardado, N. Rozès, B. Esteve-Zarzoso, C. Reguant, A. Bordons: Succinic acid production by wine yeasts and the influence of GABA and glutamic acid, International Microbiology 27 (2023) 505–512. DOI: `10.1007/s10123-023-00410-9`.

[86] P. Ribéreau-Gayon, D. Dubourdieu, B. Donèche, A. Lonvaud: Handbook of Enology: The Microbiology of Wine and Vinifications, Wiley, 2005. DOI: `10.1002/0470010363`.

[87] X. Li, K. Hu: Quantitative NMR Studies of Multiple Compound Mixtures, in: Annual Reports on NMR Spectroscopy, Elsevier, 2017, pp. 85–143. DOI: `10.1016/bs.arnmr.2016.08.001`.

[88] D. A. L. Otte, D. E. Borchmann, C. Lin, M. Weck, K. A. Woerpel: ^{13}C NMR Spectroscopy for the Quantitative Determination of Compound Ratios and Polymer End Groups, Organic Letters 16 (2014) 1566–1569. DOI: `10.1021/ol403776k`.

[89] J. van Duynhoven, E. van Velzen, D. M. Jacobs: Quantification of Complex Mixtures by NMR, in: Annual Reports on NMR Spectroscopy, Elsevier, 2013, pp. 181–236. DOI: `10.1016/b978-0-12-408097-3.00003-2`.

[90] A. Friebel, T. Specht, E. von Harbou, K. Münnemann, H. Hasse: Prediction of flow effects in quantitative NMR measurements, Journal of Magnetic Resonance 312 (2020) 106683. DOI: `10.1016/j.jmr.2020.106683`.

[91] H. H. Fischer, M. Seiler, T. S. Ertl, U. Eberhardinger, H. Bertagnolli, H. Schmitt-Willich, K. Albert: Quantification Studies in Continuous-Flow ^{13}C Nuclear Magnetic Resonance Spectroscopy by Use of Immobilized Paramagnetic Relaxation Agents, The Journal of Physical Chemistry B 107 (2003) 4879–4886. DOI: `10.1021/jp021631d`.

[92] T. J. Henderson: Sensitivity-Enhanced Quantitative ^{13}C NMR Spectroscopy via Cancellation of $^{1}J_{\mathrm{CH}}$ Dependence in DEPT Polarization Transfers, Journal of the American Chemical Society 126 (2004) 3682–3683. DOI: `10.1021/ja039261+`.

[93] K. Albert, M. Nieder, E. Bayer, M. Spraul: Continuous-flow nuclear magnetic resonance, Journal of Chromatography A 346 (1985) 17–24. DOI: `10.1016/s0021-9673(00)90489-8`.

[94] A. Mäkelä, I. Kilpeläinen, S. Heikkinen: Quantitative ^{13}C NMR spectroscopy using refocused constant-time INEPT, Q-INEPT-CT, Journal of Magnetic Resonance 204 (2010) 124–130. DOI: `10.1016/j.jmr.2010.02.015`.

[95] J. Homer, M. C. Perry: New method for NMR signal enhancement by polarization transfer, and attached nucleus testing, Journal of the Chemical Society, Chemical Communications (1994) 373. DOI: `10.1039/c39940000373`.

[96] J. Homer, M. C. Perry: Enhancement of the NMR spectra of insensitive nuclei using PENDANT with long-range coupling constants, Journal of the Chemical Society, Perkin Transactions 2 (1995) 533. DOI: `10.1039/p29950000533`.

[97] M. Sawall, E. von Harbou, A. Moog, R. Behrens, H. Schröder, J. Simoneau, E. Steimers, K. Neymeyr: Multi-objective optimization for an automated and simultaneous phase and baseline correction of NMR spectral data, Journal of Magnetic Resonance 289 (2018) 132–141. DOI: `10.1016/j.jmr.2018.02.012`.

[98] E. Steimers, M. Sawall, R. Behrens, D. Meinhardt, J. Simoneau, K. Münnemann, K. Neymeyr, E. von Harbou: Application of a new method for simultaneous phase and baseline correction of NMR signals (SINC), Magnetic Resonance in Chemistry 58 (2019) 260–270. DOI: `10.1002/mrc.4964`.

[99] C. Johnson: Diffusion ordered nuclear magnetic resonance spectroscopy: principles and applications, Progress in Nuclear Magnetic Resonance Spectroscopy 34 (1999) 203–256. DOI: `10.1016/s0079-6565(99)00003-5`.

[100] G. Pagès, V. Gilard, R. Martino, M. Malet-Martino: Pulsed-field gradient nuclear magnetic resonance measurements (PFG NMR) for diffusion ordered spectroscopy (DOSY) mapping, The Analyst 142 (2017) 3771–3796. DOI: `10.1039/c7an01031a`.

[101] G. A. Fernández, J. Vrabec, H. Hasse: Self-Diffusion and Binary Maxwell–Stefan Diffusion Coefficients of Quadrupolar Real Fluids from Molecular Simulation, International Journal of Thermophysics 26 (2005) 1389–1407. DOI: `10.1007/s10765-005-8093-6`.

[102] J. T. Bullerjahn, S. von Bülow, G. Hummer: Optimal estimates of self-diffusion coefficients from molecular dynamics simulations, The Journal of Chemical Physics 153 (2020) 024116. DOI: `10.1063/5.0008312`.

[103] I. N. Tsimpanogiannis, O. A. Moultos, L. F. M. Franco, M. B. de M. Spera, M. Erdős, I. G. Economou: Self-diffusion coefficient of bulk and confined water: a critical review of classical molecular simulation studies, Molecular Simulation 45 (2018) 425–453. DOI: `10.1080/08927022.2018.1511903`.

[104] D. Bellaire, H. Kiepfer, K. Münnemann, H. Hasse: PFG-NMR and MD Simulation Study of Self-Diffusion Coefficients of Binary and Ternary Mixtures Containing Cyclohexane, Ethanol, Acetone, and Toluene, Journal of Chemical & Engineering Data 65 (2020) 793–803. DOI: `10.1021/acs.jced.9b01016`.

[105] A. Muhammad, G. D. Carmine, L. Forster, C. D'Agostino: Solvent Effects in the Homogeneous Catalytic Reduction of Propionaldehyde with Aluminium Isopropoxide Catalyst: New Insights from PFG NMR and NMR Relaxation Studies, ChemPhysChem 21 (2020) 1101–1106. DOI: `10.1002/cphc.202000267`.

[106] E. R. McCarney, C. J. Breaux, P. M. Rendle: Measurement of the hydrodynamic radii of PEE-g dendrons by diffusion spectroscopy on a benchtop NMR spectrometer, Magnetic Resonance in Chemistry 58 (2020) 641–647. DOI: `10.1002/mrc.4997`.

[107] E. O. Stejskal: Use of Spin Echoes in a Pulsed Magnetic-Field Gradient to Study Anisotropic, Restricted Diffusion and Flow, The Journal of Chemical Physics 43 (1965) 3597–3603. DOI: `10.1063/1.1696526`.

[108] V. Busignies, P. Porion, B. Leclerc, P. Evesque, P. Tchoreloff: Application of PGSTE-NMR technique to characterize the porous structure of pharmaceutical tablets, European Journal of Pharmaceutics and Biopharmaceutics 69 (2008) 1160–1170. DOI: `10.1016/j.ejpb.2008.02.008`.

[109] L. Forster, M. Lutecki, H. Fordsmand, L. Yu, C. D'Agostino: Tailoring morphology of hierarchical catalysts for tuning pore diffusion behaviour: a rational guideline exploiting bench-top pulsed-field gradient (PFG) nuclear magnetic resonance (NMR), Molecular Systems Design & Engineering 5 (2020) 1193–1204. DOI: `10.1039/d0me00036a`.

[110] J. Kärger, M. Avramovska, D. Freude, J. Haase, S. Hwang, R. Valiullin: Pulsed field gradient NMR diffusion measurement in nanoporous materials, Adsorption 27 (2021) 453–484. DOI: `10.1007/s10450-020-00290-9`.

[111] I. A. Avilova, V. I. Volkov: Water and Molecular Exchange in Biological Cells Studied Using ^{1}H Pulsed Field Gradient NMR, Membranes 13 (2023) 567. DOI: `10.3390/membranes13060567`.

[112] G. S. Kapur, S. Berger: Pulsed field gradient (PFG) NMR spectroscopy: An effective tool for the analysis of mixtures of lubricating oil components, Tribotest 6 (2000) 323–336. DOI: `10.1002/tt.3020060402`.

[113] E. Förster, C. Fraenza, J. Küstner, E. Anoardo, H. Nirschl, G. Guthausen: Monitoring of engine oil aging by diffusion and low-field nuclear magnetic resonance relaxation, Measurement 137 (2019) 673–682. DOI: `10.1016/j.measurement.2019.02.019`.

[114] J. P. M. van Duynhoven, G. J. W. Goudappel, G. van Dalen, P. C. van Bruggen, J. C. G. Blonk, A. P. A. M. Eijkelenboom: Scope of droplet size measurements in food emulsions by pulsed field gradient NMR at low field, Magnetic Resonance in Chemistry 40 (2002) S51–S59. DOI: `10.1002/mrc.1115`.

[115] Y. S. Hong, C. H. Lee: Self-Diffusion Coefficient of Water in Tofu Determined by Pulsed Field Gradient Nuclear Magnetic Resonance, Journal of Agricultural and Food Chemistry 54 (2005) 219–223. DOI: `10.1021/jf0519360`.

[116] A. Gil, I. Duarte, E. Cabrita, B. Goodfellow, M. Spraul, R. Kerssebaum: Exploratory applications of diffusion ordered spectroscopy to liquid foods: an aid

towards spectral assignment, Analytica Chimica Acta 506 (2004) 215–223. DOI:
`10.1016/j.aca.2003.11.006`.

[117] V. Gilard, S. Trefi, S. Balayssac, M.-A. Delsuc, T. Gostan, M. Malet-Martino,
R. Martino, Y. Prigent, F. Taulelle: DOSY NMR for drug analysis, in: NMR
Spectroscopy in Pharmaceutical Analysis, Elsevier, 2008, pp. 269–289. DOI: `10.`
`1016/b978-0-444-53173-5.00011-1`.

[118] G. Assemat, B. Gouilleux, D. Bouillaud, J. Farjon, V. Gilard, P. Giraudeau,
M. Malet-Martino: Diffusion-ordered spectroscopy on a benchtop spectrometer
for drug analysis, Journal of Pharmaceutical and Biomedical Analysis 160 (2018)
268–275. DOI: `10.1016/j.jpba.2018.08.011`.

[119] E. Cussler: Diffusion: Mass Transfer in Fluid Systems, Cambridge Series in Chem-
ical Engineering, Cambridge University Press, 2009.

[120] H. Weingärtner: The Microscopic Basis of Self Diffusion - Mutual Diffusion
Relationships in Binary Liquid Mixtures, Berichte der Bunsengesellschaft für
physikalische Chemie 94 (1990) 358–364. DOI: `10.1002/bbpc.19900940331`.

[121] D. Bellaire, O. Großmann, K. Münnemann, H. Hasse: Diffusion coefficients at
infinite dilution of carbon dioxide and methane in water, ethanol, cyclohexane,
toluene, methanol, and acetone: A PFG-NMR and MD simulation study, The
Journal of Chemical Thermodynamics 166 (2022) 106691. DOI: `10.1016/j.`
`jct.2021.106691`.

[122] D. Bellaire, K. Münnemann, H. Hasse: Mutual diffusion coefficients from NMR
imaging, Chemical Engineering Science 255 (2022) 117655. DOI: `10.1016/j.`
`ces.2022.117655`.

[123] J. Stetefeld, S. A. McKenna, T. R. Patel: Dynamic light scattering: a practical
guide and applications in biomedical sciences, Biophysical Reviews 8 (2016) 409–
427. DOI: `10.1007/s12551-016-0218-6`.

[124] J. H. Wang: Self-Diffusion and Structure of Liquid Water. I. Measurement of Self-
Diffusion of Liquid Water with Deuterium as Tracer, Journal of the American
Chemical Society 73 (1951) 510–513. DOI: `10.1021/ja01146a002`.

[125] J. R. D. Copley, S. W. Lovesey: The dynamic properties of monatomic liquids,
Reports on Progress in Physics 38 (1975) 461–563. DOI: `10.1088/0034-4885/`
`38/4/001`.

[126] H. Weingärtner: Chapter 3. NMR studies of self-diffusion in liquids, Annu. Rep. Prog. Chem., Sect. C: Phys. Chem. 91 (1994) 37–69. DOI: `10.1039/pc9949100037`.

[127] E. O. Stejskal, J. E. Tanner: Spin Diffusion Measurements: Spin Echoes in the Presence of a Time-Dependent Field Gradient, The Journal of Chemical Physics 42 (1965) 288–292. DOI: `10.1063/1.1695690`.

[128] A. Jerschow, N. Müller: Suppression of Convection Artifacts in Stimulated-Echo Diffusion Experiments. Double-Stimulated-Echo Experiments, Journal of Magnetic Resonance 125 (1997) 372–375. DOI: `10.1006/jmre.1997.1123`.

[129] B. Gouilleux, J. Farjon, P. Giraudeau: Gradient-based pulse sequences for benchtop NMR spectroscopy, Journal of Magnetic Resonance 319 (2020) 106810. DOI: `10.1016/j.jmr.2020.106810`.

[130] M. D. Pelta, G. A. Morris, M. J. Stchedroff, S. J. Hammond: A one-shot sequence for high-resolution diffusion-ordered spectroscopy, Magnetic Resonance in Chemistry 40 (2002) S147–S152. DOI: `10.1002/mrc.1107`.

[131] M. Nilsson, G. A. Morris: Pure shift proton DOSY: diffusion-ordered ^{1}H spectra without multiplet structure, Chemical Communications (2007) 933. DOI: `10.1039/b617761a`.

[132] A. Botana, J. A. Aguilar, M. Nilsson, G. A. Morris: J-modulation effects in DOSY experiments and their suppression: The Oneshot45 experiment, Journal of Magnetic Resonance 208 (2011) 270–278. DOI: `10.1016/j.jmr.2010.11.012`.

[133] E. R. McCarney, R. Dykstra, P. Galvosas: Evaluation of benchtop NMR Diffusion Ordered Spectroscopy for small molecule mixture analysis, Magnetic Resonance Imaging 56 (2019) 103–109. DOI: `10.1016/j.mri.2018.09.033`.

[134] A. K. Rogerson, J. A. Aguilar, M. Nilsson, G. A. Morris: Simultaneous enhancement of chemical shift dispersion and diffusion resolution in mixture analysis by diffusion-ordered NMR spectroscopy, Chemical Communications 47 (2011) 7063. DOI: `10.1039/c1cc12456k`.

[135] W. Windig, B. Antalek: Direct exponential curve resolution algorithm (DECRA): A novel application of the generalized rank annihilation method for a single spectral mixture data set with exponentially decaying contribution profiles, Chemometrics and Intelligent Laboratory Systems 37 (1997) 241–254. DOI: `10.1016/s0169-7439(97)00028-2`.

[136] L. C. V. Gorkom, T. M. Hancewicz: Analysis of DOSY and GPC-NMR Experiments on Polymers by Multivariate Curve Resolution, Journal of Magnetic Resonance 130 (1998) 125–130. DOI: `10.1006/jmre.1997.1292`.

[137] M. Nilsson: The DOSY Toolbox: A new tool for processing PFG NMR diffusion data, Journal of Magnetic Resonance 200 (2009) 296–302. DOI: `10.1016/j.jmr.2009.07.022`.

[138] E. Steimers, Y. Matviychuk, D. J. Holland, H. Hasse, E. von Harbou: Accurate measurements of self-diffusion coefficients with benchtop NMR using a QM model-based approach, Magnetic Resonance in Chemistry 60 (2022) 1113–1130. DOI: `10.1002/mrc.5300`.

[139] K. F. Morris, C. S. Johnson: Diffusion-ordered two-dimensional nuclear magnetic resonance spectroscopy, Journal of the American Chemical Society 114 (1992) 3139–3141. DOI: `10.1021/ja00034a071`.

[140] M. Khajeh, A. Botana, M. A. Bernstein, M. Nilsson, G. A. Morris: Reaction Kinetics Studied Using Diffusion-Ordered Spectroscopy and Multiway Chemometrics, Analytical Chemistry 82 (2010) 2102–2108. DOI: `10.1021/ac100110m`.

[141] P. Stilbs: Molecular self-diffusion coefficients in Fourier transform nuclear magnetic resonance spectrometric analysis of complex mixtures, Analytical Chemistry 53 (1981) 2135–2137. DOI: `10.1021/ac00236a044`.

[142] M. Zhou, V. Frydman, L. Frydman: NMR Analyses of Order and Dynamics in Poly(p-Benzamide)/Sulfuric Acid Solutions, Macromolecules 30 (1997) 5416–5428. DOI: `10.1021/ma970233j`.

[143] K. Vermillion, N. P. Price: Stable isotope-enhanced two- and three-dimensional diffusion ordered ^{13}C NMR spectroscopy (SIE-DOSY ^{13}C NMR), Journal of Magnetic Resonance 198 (2009) 209–214. DOI: `10.1016/j.jmr.2009.02.008`.

[144] M. Yemloul, V. Castola, S. Leclerc, D. Canet: Self-diffusion coefficients obtained from proton-decoupled carbon-13 spectra for analyzing a mixture of terpenes, Magnetic Resonance in Chemistry 47 (2009) 635–640. DOI: `10.1002/mrc.2442`.

[145] D. Wu, A. Chen, J. Charles S. Johnson: Heteronuclear-Detected Diffusion-Ordered NMR Spectroscopy through Coherence Transfer, Journal of Magnetic Resonance, Series A 123 (1996) 215–218. DOI: `10.1006/jmra.1996.0239`.

[146] N. E. Schlörer, E. J. Cabrita, S. Berger: Characterization of Reactive Intermediates by Diffusion-Ordered NMR Spectroscopy: A Snapshot of the Reaction of $^{13}CO_2$ with $[Cp_2Zr(Cl)H]$, Angewandte Chemie International Edition 41 (2002) 107–109. DOI: `10.1002/1521-3773(20020104)41:1<107::aid-anie107>3.0.co;2-n`.

[147] J. Hou, Y. He, P. Sabatino, L. Yuan, D. Redwine: Generic applications of ^{13}C-detected NMR diffusion to formulated systems with suppression of thermal convection induced by proton decoupling, Magnetic Resonance in Chemistry 54 (2016) 584–591. DOI: `10.1002/mrc.4404`.

[148] D. Li, R. Hopson, W. Li, J. Liu, P. G. Williard: ^{13}C INEPT Diffusion-Ordered NMR Spectroscopy (DOSY) with Internal References, Organic Letters 10 (2008) 909–911. DOI: `10.1021/ol703039v`.

[149] D. Li, I. Keresztes, R. Hopson, P. G. Williard: Characterization of Reactive Intermediates by Multinuclear Diffusion-Ordered NMR Spectroscopy (DOSY), Accounts of Chemical Research 42 (2008) 270–280. DOI: `10.1021/ar800127e`.

[150] A. Botana, P. W. Howe, V. Caër, G. A. Morris, M. Nilsson: High resolution ^{13}C DOSY: The DEPTSE experiment, Journal of Magnetic Resonance 211 (2011) 25–29. DOI: `10.1016/j.jmr.2011.03.016`.

[151] B. Vitorge, D. Jeanneat: NMR Diffusion Measurements in Complex Mixtures Using Constant-Time-HSQC-IDOSY and Computer-Optimized Spectral Aliasing for High Resolution in the Carbon Dimension, Analytical Chemistry 78 (2006) 5601–5606. DOI: `10.1021/ac060744g`.

[152] A. S. McLachlan, J. J. Richards, A. R. Bilia, G. A. Morris: Constant time gradient HSQC-iDOSY: practical aspects, Magnetic Resonance in Chemistry 47 (2009) 1081–1085. DOI: `10.1002/mrc.2518`.

[153] A. M. Torres, G. Zheng, W. S. Price: *J*-compensated PGSE: an improved NMR diffusion experiment with fewer phase distortions, Magnetic Resonance in Chemistry 48 (2009) 129–133. DOI: `10.1002/mrc.2555`.

[154] P. Linse, O. Soderman: The Validity of the Short-Gradient-Pulse Approximation in NMR Studies of Restricted Diffusion. Simulations of Molecules Diffusing between Planes, in Cylinders and Spheres, Journal of Magnetic Resonance, Series A 116 (1995) 77–86. DOI: `10.1006/jmra.1995.1192`.

[155] W. S. Price, P. Stilbs, O. Söderman: Determination of pore space shape and size in porous systems using NMR diffusometry. beyond the short gradient pulse

approximation, Journal of Magnetic Resonance 160 (2003) 139–143. DOI: 10.1016/s1090-7807(02)00134-9.

[156] C. Malmborg, D. Topgaard, O. Söderman: NMR diffusometry and the short gradient pulse limit approximation, Journal of Magnetic Resonance 169 (2004) 85–91. DOI: 10.1016/j.jmr.2004.04.004.

[157] I. Solomon: Relaxation Processes in a System of Two Spins, Physical Review 99 (1955) 559–565. DOI: 10.1103/physrev.99.559.

[158] N. Bloembergen, L. O. Morgan: Proton Relaxation Times in Paramagnetic Solutions. Effects of Electron Spin Relaxation, The Journal of Chemical Physics 34 (1961) 842–850. DOI: 10.1063/1.1731684.

[159] D. Bruck, R. Dudley, C. Fyfe, J. Van Delden: Sample magnetization using immobilized free radicals for use in flow NMR systems, Journal of Magnetic Resonance (1969) 42 (1981) 51–59. DOI: 10.1016/0022-2364(81)90009-3.

[160] Y. Zhang, D. A. Laude: Immobilized free-radical substrates for magnetization of carbon-13 nuclei in flow NMR measurements, Journal of Magnetic Resonance (1969) 87 (1990) 46–55. DOI: 10.1016/0022-2364(90)90084-m.

[161] R. Kircher, S. Mross, H. Hasse, K. Münnemann: Quantitative Analysis in Continuous-Flow ^{1}H Benchtop NMR Spectroscopy by Paramagnetic Relaxation Enhancement, Applied Magnetic Resonance 54 (2023) 1555–1569. DOI: 10.1007/s00723-023-01626-8.

[162] J. H. Lee, Y. Okuno, S. Cavagnero: Sensitivity enhancement in solution NMR: Emerging ideas and new frontiers, Journal of Magnetic Resonance 241 (2014) 18–31. DOI: 10.1016/j.jmr.2014.01.005.

[163] M. E. Halse: Perspectives for hyperpolarisation in compact NMR, TrAC Trends in Analytical Chemistry 83 (2016) 76–83. DOI: 10.1016/j.trac.2016.05.004.

[164] J. Eills, D. Budker, S. Cavagnero, E. Y. Chekmenev, S. J. Elliott, S. Jannin, A. Lesage, J. Matysik, T. Meersmann, T. Prisner, J. A. Reimer, H. Yang, I. V. Koptyug: Spin Hyperpolarization in Modern Magnetic Resonance, Chemical Reviews 123 (2023) 1417–1551. DOI: 10.1021/acs.chemrev.2c00534.

[165] N. Eshuis, B. J. A. van Weerdenburg, M. C. Feiters, F. P. J. T. Rutjes, S. S. Wijmenga, M. Tessari: Quantitative Trace Analysis of Complex Mixtures Using SABRE Hyperpolarization, Angewandte Chemie International Edition 54 (2014) 1481–1484. DOI: 10.1002/anie.201409795.

[166] P. M. Richardson, A. J. Parrott, O. Semenova, A. Nordon, S. B. Duckett, M. E. Halse: SABRE hyperpolarization enables high-sensitivity ^{1}H and ^{13}C benchtop NMR spectroscopy, The Analyst 143 (2018) 3442–3450. DOI: `10.1039/c8an00596f`.

[167] P. M. Richardson, W. Iali, S. S. Roy, P. J. Rayner, M. E. Halse, S. B. Duckett: Rapid ^{13}C NMR hyperpolarization delivered from *para*-hydrogen enables the low concentration detection and quantification of sugars, Chemical Science 10 (2019) 10607–10619. DOI: `10.1039/c9sc03450a`.

[168] O. Semenova, P. M. Richardson, A. J. Parrott, A. Nordon, M. E. Halse, S. B. Duckett: Reaction Monitoring Using SABRE-Hyperpolarized Benchtop (1 T) NMR Spectroscopy, Analytical Chemistry 91 (2019) 6695–6701. DOI: `10.1021/acs.analchem.9b00729`.

[169] L. Sellies, I. Reile, R. L. E. G. Aspers, M. C. Feiters, F. P. J. T. Rutjes, M. Tessari: Parahydrogen induced hyperpolarization provides a tool for NMR metabolomics at nanomolar concentrations, Chemical Communications 55 (2019) 7235–7238. DOI: `10.1039/c9cc02186h`.

[170] H. Chae, S. Min, H. J. Jeong, S. K. Namgoong, S. Oh, K. Kim, K. Jeong: Organic Reaction Monitoring of a Glycine Derivative Using Signal Amplification by Reversible Exchange-Hyperpolarized Benchtop Nuclear Magnetic Resonance Spectroscopy, Analytical Chemistry 92 (2020) 10902–10907. DOI: `10.1021/acs.analchem.0c01270`.

[171] R. Kircher, J. Xu, D. A. Barskiy: In Situ Hyperpolarization Enables ^{15}N and ^{13}C Benchtop NMR at Natural Isotopic Abundance, Journal of the American Chemical Society 146 (2023) 514–520. DOI: `10.1021/jacs.3c10030`.

[172] S. Appelt, A. B.-A. Baranga, C. J. Erickson, M. V. Romalis, A. R. Young, W. Happer: Theory of spin-exchange optical pumping of ^{3}He and ^{129}Xe, Physical Review A 58 (1998) 1412–1439. DOI: `10.1103/physreva.58.1412`.

[173] T. G. Walker, W. Happer: Spin-exchange optical pumping of noble-gas nuclei, Reviews of Modern Physics 69 (1997) 629–642. DOI: `10.1103/revmodphys.69.629`.

[174] D. A. Barskiy, A. M. Coffey, P. Nikolaou, D. M. Mikhaylov, B. M. Goodson, R. T. Branca, G. J. Lu, M. G. Shapiro, V. Telkki, V. V. Zhivonitko, I. V. Koptyug, O. G. Salnikov, K. V. Kovtunov, V. I. Bukhtiyarov, M. S. Rosen, M. J. Barlow, S. Safavi, I. P. Hall, L. Schröder, E. Y. Chekmenev: NMR Hyperpolarization

Techniques of Gases, Chemistry – A European Journal 23 (2016) 725–751. DOI: `10.1002/chem.201603884`.

[175] H. Zeng, Y. Lee, C. Hilty: Quantitative Rate Determination by Dynamic Nuclear Polarization Enhanced NMR of a Diels-Alder Reaction, Analytical Chemistry 82 (2010) 8897–8902. DOI: `10.1021/ac101670n`.

[176] E. Ravera, C. Luchinat, G. Parigi: Basic facts and perspectives of Overhauser DNP NMR, Journal of Magnetic Resonance 264 (2016) 78–87. DOI: `10.1016/j.jmr.2015.12.013`.

[177] J. van Bentum, B. van Meerten, M. Sharma, A. Kentgens: Perspectives on DNP-enhanced NMR spectroscopy in solutions, Journal of Magnetic Resonance 264 (2016) 59–67. DOI: `10.1016/j.jmr.2016.01.010`.

[178] J. G. Krummenacker, V. P. Denysenkov, M. Terekhov, L. M. Schreiber, T. F. Prisner: DNP in MRI: An in-bore approach at 1.5 T, Journal of Magnetic Resonance 215 (2012) 94–99. DOI: `10.1016/j.jmr.2011.12.015`.

[179] N. Abhyankar, V. Szalai: Challenges and Advances in the Application of Dynamic Nuclear Polarization to Liquid-State NMR Spectroscopy, The Journal of Physical Chemistry B 125 (2021) 5171–5190. DOI: `10.1021/acs.jpcb.0c10937`.

[180] A. W. Overhauser: Polarization of Nuclei in Metals, Physical Review 92 (1953) 411–415. DOI: `10.1103/physrev.92.411`.

[181] A. Abragam: Overhauser Effect in Nonmetals, Physical Review 98 (1955) 1729–1735. DOI: `10.1103/physrev.98.1729`.

[182] T. R. Carver, C. P. Slichter: Experimental Verification of the Overhauser Nuclear Polarization Effect, Physical Review 102 (1956) 975–980. DOI: `10.1103/physrev.102.975`.

[183] K. Hausser, D. Stehlik: Dynamic Nuclear Polarization in Liquids, Elsevier, 1968, pp. 79–139. DOI: `10.1016/b978-1-4832-3116-7.50010-2`.

[184] B. D. Armstrong, S. Han: A new model for Overhauser enhanced nuclear magnetic resonance using nitroxide radicals, The Journal of Chemical Physics 127 (2007). DOI: `10.1063/1.2770465`.

[185] T. Maly, G. T. Debelouchina, V. S. Bajaj, K.-N. Hu, C.-G. Joo, M. L. Mak–Jurkauskas, J. R. Sirigiri, P. C. A. van der Wel, J. Herzfeld, R. J. Temkin, R. G. Griffin: Dynamic nuclear polarization at high magnetic fields, The Journal of Chemical Physics 128 (2008). DOI: `10.1063/1.2833582`.

[186] B. D. Armstrong, S. Han: Overhauser Dynamic Nuclear Polarization To Study Local Water Dynamics, Journal of the American Chemical Society 131 (2009) 4641–4647. DOI: `10.1021/ja809259q`.

[187] A. Krahn, P. Lottmann, T. Marquardsen, A. Tavernier, M.-T. Türke, M. Reese, A. Leonov, M. Bennati, P. Hoefer, F. Engelke, C. Griesinger: Shuttle DNP spectrometer with a two-center magnet, Physical Chemistry Chemical Physics 12 (2010) 5830. DOI: `10.1039/c003381b`.

[188] C. Griesinger, M. Bennati, H. Vieth, C. Luchinat, G. Parigi, P. Höfer, F. Engelke, S. Glaser, V. Denysenkov, T. Prisner: Dynamic nuclear polarization at high magnetic fields in liquids, Progress in Nuclear Magnetic Resonance Spectroscopy 64 (2012) 4–28. DOI: `10.1016/j.pnmrs.2011.10.002`.

[189] M. Goldman: Dynamic nuclear polarization, Comptes Rendus Physique 20 (2019) 694–705. DOI: `10.1016/j.crhy.2019.05.010`.

[190] W. Müller-Warmuth, R. Vilhjalmsson, P. Gerlof, J. Smidt, J. Trommel: Intermolecular interactions of benzene and carbon tetrachloride with selected free radicals in solution as studied by ^{13}C and ^{1}H dynamic nuclear polarization, Molecular Physics 31 (1976) 1055–1067. DOI: `10.1080/00268977600100811`.

[191] N. M. Loening, M. Rosay, V. Weis, R. G. Griffin: Solution-State Dynamic Nuclear Polarization at High Magnetic Field, Journal of the American Chemical Society 124 (2002) 8808–8809. DOI: `10.1021/ja026660g`.

[192] M. D. Lingwood, S. Han: Dynamic nuclear polarization of ^{13}C in aqueous solutions under ambient conditions, Journal of Magnetic Resonance 201 (2009) 137–145. DOI: `10.1016/j.jmr.2009.09.002`.

[193] M. J. Prandolini, V. P. Denysenkov, M. Gafurov, B. Endeward, T. F. Prisner: High-Field Dynamic Nuclear Polarization in Aqueous Solutions, Journal of the American Chemical Society 131 (2009) 6090–6092. DOI: `10.1021/ja901496g`.

[194] M. Reese, M.-T. Türke, I. Tkach, G. Parigi, C. Luchinat, T. Marquardsen, A. Tavernier, P. Höfer, F. Engelke, C. Griesinger, M. Bennati: ^{1}H and ^{13}C Dynamic Nuclear Polarization in Aqueous Solution with a Two-Field (0.35 T/14 T) Shuttle DNP Spectrometer, Journal of the American Chemical Society 131 (2009) 15086–15087. DOI: `10.1021/ja905959n`.

[195] X. Wang, W. C. Isley III, S. I. Salido, Z. Sun, L. Song, K. H. Tsai, C. J. Cramer, H. C. Dorn: Optimization and prediction of the electron–nuclear dipolar and scalar interaction in ^{1}H and ^{13}C liquid state dynamic nuclear polarization, Chemical Science 6 (2015) 6482–6495. DOI: `10.1039/c5sc02499d`.

[196] G. Liu, M. Levien, N. Karschin, G. Parigi, C. Luchinat, M. Bennati: One-thousand-fold enhancement of high field liquid nuclear magnetic resonance signals at room temperature, Nature Chemistry 9 (2017) 676–680. DOI: `10.1038/nchem.2723`.

[197] T. Orlando, R. Dervişoğlu, M. Levien, I. Tkach, T. F. Prisner, L. B. Andreas, V. P. Denysenkov, M. Bennati: Dynamic Nuclear Polarization of ^{13}C Nuclei in the Liquid State over a 10 Tesla Field Range, Angewandte Chemie International Edition 58 (2018) 1402–1406. DOI: `10.1002/anie.201811892`.

[198] D. Dai, X. Wang, Y. Liu, X.-L. Yang, C. Glaubitz, V. Denysenkov, X. He, T. Prisner, J. Mao: Room-temperature dynamic nuclear polarization enhanced NMR spectroscopy of small biological molecules in water, Nature Communications 12 (2021). DOI: `10.1038/s41467-021-27067-0`.

[199] H. Dorn, R. Gitti, K. Tsai, T. Glass: The flow transfer of a bolus with ^{1}H dynamic nuclear polarization from low to high magnetic fields, Chemical Physics Letters 155 (1989) 227–232. DOI: `10.1016/0009-2614(89)85354-0`.

[200] H. C. Dorn, T. E. Glass, R. Gitti, K. H. Tsai: Transfer of ^{1}H and ^{13}C dynamic nuclear polarization from immobilized nitroxide radicals to flowing liquids, Applied Magnetic Resonance 2 (1991) 9–27. DOI: `10.1007/bf03166265`.

[201] S. Stevenson, H. C. Dorn: ^{13}C Dynamic Nuclear Polarization: A Detector for Continuous-Flow, Online Chromatography, Analytical Chemistry 66 (1994) 2993–2999. DOI: `10.1021/ac00091a003`.

[202] S. Stevenson, T. Glass, H. C. Dorn: ^{13}C Dynamic Nuclear Polarization: an Alternative Detector for Recycled-Flow NMR Experiments, Analytical Chemistry 70 (1998) 2623–2628. DOI: `10.1021/ac971337v`.

[203] E. R. McCarney, S. Han: Spin-labeled gel for the production of radical-free dynamic nuclear polarization enhanced molecules for NMR spectroscopy and imaging, Journal of Magnetic Resonance 190 (2008) 307–315. DOI: `10.1016/j.jmr.2007.11.013`.

[204] M. D. Lingwood, T. A. Siaw, N. Sailasuta, B. D. Ross, P. Bhattacharya, S. Han: Continuous flow Overhauser dynamic nuclear polarization of water in the fringe field of a clinical magnetic resonance imaging system for authentic image contrast, Journal of Magnetic Resonance 205 (2010) 247–254. DOI: `10.1016/j.jmr.2010.05.008`.

[205] M. D. Lingwood, A. J. Sederman, M. D. Mantle, L. F. Gladden, S. Han: Overhauser dynamic nuclear polarization amplification of NMR flow imaging, Journal of Magnetic Resonance 216 (2012) 94–100. DOI: `10.1016/j.jmr.2012.01.007`.

[206] R. Kircher, H. Hasse, K. Münnemann: High Flow-Rate Benchtop NMR Spectroscopy Enabled by Continuous Overhauser DNP, Analytical Chemistry 93 (2021) 8897–8905. DOI: `10.1021/acs.analchem.1c01118`.

[207] R. Kircher, S. Mross, H. Hasse, K. Münnemann: Functionalized Controlled Porous Glasses for Producing Radical-Free Hyperpolarized Liquids by Overhauser DNP, Molecules 27 (2022) 6402. DOI: `10.3390/molecules27196402`.

[208] B. D. Armstrong, M. D. Lingwood, E. R. McCarney, E. R. Brown, P. Blümler, S. Han: Portable X-band system for solution state dynamic nuclear polarization, Journal of Magnetic Resonance 191 (2008) 273–281. DOI: `10.1016/j.jmr.2008.01.004`.

[209] K. Münnemann, C. Bauer, J. Schmiedeskamp, H. W. Spiess, W. G. Schreiber, D. Hinderberger: A Mobile DNP Polarizer for Clinical Applications, Applied Magnetic Resonance 34 (2008) 321–330. DOI: `10.1007/s00723-008-0130-8`.

[210] S. Ebert, A. Amar, C. Bauer, M. Kölzer, P. Blümler, H. W. Spiess, D. Hinderberger, K. Münnemann: A Mobile DNP Polarizer for Continuous Flow Applications, Applied Magnetic Resonance 43 (2012) 195–206. DOI: `10.1007/s00723-012-0344-7`.

[211] O. Neudert, D. G. Zverev, C. Bauer, P. Blümler, H. W. Spiess, D. Hinderberger, K. Münnemann: Overhauser DNP and EPR in a Mobile Setup: Influence of Magnetic Field Inhomogeneity, Applied Magnetic Resonance 43 (2012) 149–165. DOI: `10.1007/s00723-012-0347-4`.

[212] C.-Y. Cheng, O. J. Goor, S. Han: Quantitative Analysis of Molecular Transport across Liposomal Bilayer by J-Mediated ^{13}C Overhauser Dynamic Nuclear Polarization, Analytical Chemistry 84 (2012) 8936–8940. DOI: `10.1021/ac301932h`.

[213] A. Dey, A. Banerjee, N. Chandrakumar: Transferred Overhauser DNP: A Fast, Efficient Approach for Room Temperature ^{13}C ODNP at Moderately Low Fields and Natural Abundance, The Journal of Physical Chemistry B 121 (2017) 7156–7162. DOI: `10.1021/acs.jpcb.7b05081`.

[214] G. A. Morris, R. Freeman: Enhancement of nuclear magnetic resonance signals by polarization transfer, Journal of the American Chemical Society 101 (1979) 760–762. DOI: `10.1021/ja00497a058`.

[215] O. Sørensen, R. Ernst: Elimination of spectral distortion in polarization transfer experiments. Improvements and comparison of techniques, Journal of Magnetic Resonance (1969) 51 (1983) 477–489. DOI: `10.1016/0022-2364(83)90300-1`.

[216] P. Giraudeau, G. S. Remaud, S. Akoka: Evaluation of Ultrafast 2D NMR for Quantitative Analysis, Analytical Chemistry 81 (2008) 479–484. DOI: `10.1021/ac8021168`.

[217] P. Giraudeau, L. Frydman: Ultrafast 2D NMR: An Emerging Tool in Analytical Spectroscopy, Annual Review of Analytical Chemistry 7 (2014) 129–161. DOI: `10.1146/annurev-anchem-071213-020208`.

[218] B. Gouilleux, B. Charrier, E. Danieli, J.-N. Dumez, S. Akoka, F.-X. Felpin, M. Rodriguez-Zubiri, P. Giraudeau: Real-time reaction monitoring by ultrafast 2D NMR on a benchtop spectrometer, The Analyst 140 (2015) 7854–7858. DOI: `10.1039/c5an01998b`.

[219] B. Gouilleux, B. Charrier, S. Akoka, F.-X. Felpin, M. Rodriguez-Zubiri, P. Giraudeau: Ultrafast 2D NMR on a benchtop spectrometer: Applications and perspectives, TrAC Trends in Analytical Chemistry 83 (2016) 65–75. DOI: `10.1016/j.trac.2016.01.014`.

[220] N. Eshuis, N. Hermkens, B. J. A. van Weerdenburg, M. C. Feiters, F. P. J. T. Rutjes, S. S. Wijmenga, M. Tessari: Toward Nanomolar Detection by NMR Through SABRE Hyperpolarization, Journal of the American Chemical Society 136 (2014) 2695–2698. DOI: `10.1021/ja412994k`.

[221] N. Reimets, K. Ausmees, S. Vija, I. Reile: Developing Analytical Applications for Parahydrogen Hyperpolarization: Urinary Elimination Pharmacokinetics of Nicotine, Analytical Chemistry 93 (2021) 9480–9485. DOI: `10.1021/acs.analchem.1c01281`.

[222] J. H. Ardenkjær-Larsen, B. Fridlund, A. Gram, G. Hansson, L. Hansson, M. H. Lerche, R. Servin, M. Thaning, K. Golman: Increase in signal-to-noise ratio of >10,000 times in liquid-state NMR, Proceedings of the National Academy of Sciences 100 (2003) 10158–10163. DOI: `10.1073/pnas.1733835100`.

[223] M. H. Lerche, S. Meier, P. R. Jensen, S. Hustvedt, M. Karlsson, J. o. Duus, J. H. Ardenkjær-Larsen: Quantitative dynamic nuclear polarization-NMR on blood plasma for assays of drug metabolism, NMR in Biomedicine 24 (2010) 96–103. DOI: `10.1002/nbm.1561`.

[224] S. Meier, M. Karlsson, P. R. Jensen, M. H. Lerche, J. o. Duus: Metabolic pathway visualization in living yeast by DNP-NMR, Molecular BioSystems 7 (2011) 2834. DOI: `10.1039/c1mb05202k`.

[225] F. A. Gallagher, M. I. Kettunen, S. E. Day, D. Hu, M. Karlsson, A. Gisselsson, M. H. Lerche, K. M. Brindle: Detection of tumor glutamate metabolism in vivo using ^{13}C magnetic resonance spectroscopy and hyperpolarized [1-^{13}C]glutamate, Magnetic Resonance in Medicine 66 (2011) 18–23. DOI: `10.1002/mrm.22851`.

[226] M. H. Lerche, P. R. Jensen, M. Karlsson, S. Meier: NMR Insights into the Inner Workings of Living Cells, Analytical Chemistry 87 (2014) 119–132. DOI: `10.1021/ac501467x`.

[227] J.-N. Dumez, J. Milani, B. Vuichoud, A. Bornet, J. Lalande-Martin, I. Tea, M. Yon, M. Maucourt, C. Deborde, A. Moing, L. Frydman, G. Bodenhausen, S. Jannin, P. Giraudeau: Hyperpolarized NMR of plant and cancer cell extracts at natural abundance, The Analyst 140 (2015) 5860–5863. DOI: `10.1039/c5an01203a`.

[228] M. H. Lerche, D. Yigit, A. B. Frahm, J. H. Ardenkjær-Larsen, R. M. Malinowski, P. R. Jensen: Stable Isotope-Resolved Analysis with Quantitative Dissolution Dynamic Nuclear Polarization, Analytical Chemistry 90 (2017) 674–678. DOI: `10.1021/acs.analchem.7b02779`.

[229] A. Dey, B. Charrier, E. Martineau, C. Deborde, E. Gandriau, A. Moing, D. Jacob, D. Eshchenko, M. Schnell, R. Melzi, D. Kurzbach, M. Ceillier, Q. Chappuis, S. F. Cousin, J. G. Kempf, S. Jannin, J.-N. Dumez, P. Giraudeau: Hyperpolarized NMR Metabolomics at Natural ^{13}C Abundance, Analytical Chemistry 92 (2020) 14867–14871. DOI: `10.1021/acs.analchem.0c03510`.

[230] A. B. Frahm, P. R. Jensen, J. H. Ardenkjær-Larsen, D. Yigit, M. H. Lerche: Stable isotope resolved metabolomics classification of prostate cancer cells using hyperpolarized NMR data, Journal of Magnetic Resonance 316 (2020) 106750. DOI: `10.1016/j.jmr.2020.106750`.

[231] A. B. Frahm, D. Hill, S. Katsikis, T. Andreassen, J. H. Ardenkjær-Larsen, T. F. Bathen, S. A. Moestue, P. R. Jensen, M. H. Lerche: Classification and biomarker identification of prostate tissue from TRAMP mice with hyperpolarized ^{13}C-SIRA, Talanta 235 (2021) 122812. DOI: `10.1016/j.talanta.2021.122812`.

[232] V. Ribay, A. Dey, B. Charrier, C. Praud, J. Mandral, J. Dumez, M. P. M. Letertre, P. Giraudeau: Hyperpolarized ^{13}C NMR Spectroscopy of Urine Samples at Natural Abundance by Quantitative Dissolution Dynamic Nuclear Polar-

ization, Angewandte Chemie International Edition 62 (2023). DOI: `10.1002/anie.202302110`.

[233] G. Zhang, C. Hilty: Applications of dissolution dynamic nuclear polarization in chemistry and biochemistry, Magnetic Resonance in Chemistry 56 (2018) 566–582. DOI: `10.1002/mrc.4735`.

[234] I. H. Witten, E. Frank, M. A. Hall: Data Mining: Practical Machine Learning Tools and Techniques, 3rd ed., Morgan Kaufmann Publishers Inc., San Francisco, CA, USA, 2011.

Appendix

A Supporting Information for Chapter 2

A.1 Experimental Section

A.1.1 Synthetic Wine Mixtures

Three test mixtures were prepared gravimetrically. The masses of the components in each test mixture are given in Table A.1.

Table A.1: Masses of the components in the three test mixtures.

Component	Mixture 1	Mixture 2	Mixture 3
	m / g		
Acetic Acid	0.031	0.042	0.066
Citric Acid	0.024	0.079	0.136
Ethanol	0.198	8.005	14.003
D(-)-Fructose	18.002	10.029	0.401
D(+)-Glucose	20.061	3.998	0.205
Glycerol	0.321	0.603	1.256
DL-Malic Acid	1.397	1.199	1.003
Succinic Acid	0.027	0.143	0.298
Water	200.07	200.18	200.15

A.1.2 Determination of the Transport Time

Tracer experiments were performed to determine the delay between sample uptake and acquisition in the benchtop NMR spectrometer. For this purpose, dimethylsulfoxide (DMSO) was injected to the reactor filled with 200 ml of water while the pump was running at a constant flow rate of $\dot{V}$ = 0.3 ml min^{-1}. In parallel to the injection, the benchtop ^{1}H NMR measurements were started and 300 scans were acquired (acquisition time 1.6 s, 8192 data points, 90° excitation pulse, 1 scan) every 5 s. The signal of DMSO was continuously tracked during the experiment to calculate the transport time. Three experiments were performed to calculate a mean value. The results are displayed in Figure A.1. The mean dwell time was 14.4 min.
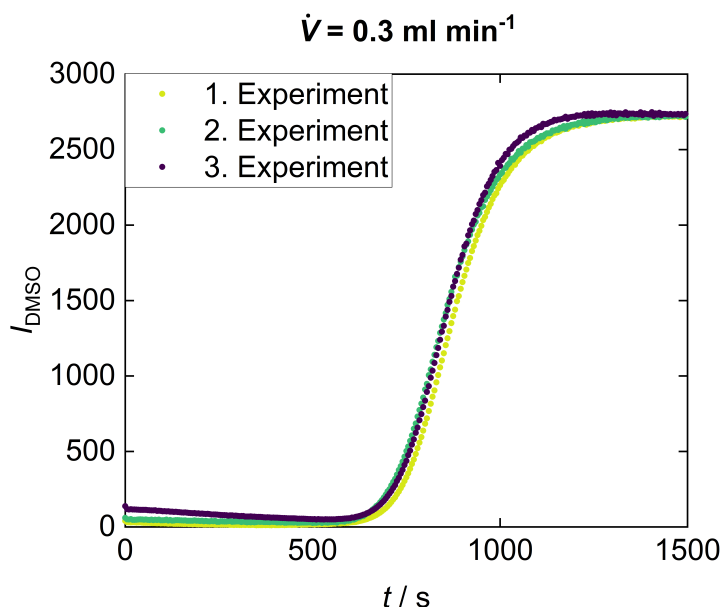
Figure A.1: Three tracer experiments to determine the delay between sample uptake and NMR acquisition. The signal integral of DMSO was continuously tracked during the experiment while the pump was running at a flow rate of $\dot{V}$ = 0.3 ml min^{-1}.

A.2 Results and Discussion

A.2.1 Measurement of Synthetic Wine Mixtures

Mixture 1, Mixture 2, and Mixture 3 were quantified by the AutoWine-tool. The results of the ^{1}H NMR experiment are compared with the gravimetric concentrations which are considered as ground truth. The numerical values are given in Table A.2, Table A.3, and Table A.4.

Table A.2: Concentrations of Mixture 1 determined by the ^{1}H NMR experiment combined with the AutoWine-tool. The results are compared to the gravimetric concentrations. Errors are calculated from three repetitions using the standard uncertainty.

	Mixture 1	
Component	Gravimetric	^{1}H NMR experiment
	c_i / g l^{-1}	
Acetic Acid	0.137	0.121±0.006
Citric Acid	0.106	0.167±0.008
Ethanol	0.876	0.804±0.002
D(-)-Fructose	79.660	72.465±1.227
D(+)-Glucose	88.772	82.345±0.247
Glycerol	1.420	2.330±0.241
DL-Malic Acid	6.182	5.392±0.082
Succinic Acid	0.119	0.082±0.012

Table A.3: Concentrations of Mixture 2 determined by the ^{1}H NMR experiment combined with the AutoWine-tool. The results are compared to the gravimetric concentrations. Errors are calculated from three repetitions using the standard uncertainty.

	Mixture 2	
Component	Gravimetric	^{1}H NMR experiment
	c_i / g l^{-1}	
Acetic Acid	0.190	0.159±0.006
Citric Acid	0.358	0.324±0.054
Ethanol	36.299	32.173±1.693
D(-)-Fructose	45.477	39.538±1.509
D(+)-Glucose	18.129	17.253±0.743
Glycerol	2.734	2.388±1.021
DL-Malic Acid	5.437	4.665±0.340
Succinic Acid	0.648	0.549±0.028

Table A.4: Concentrations of Mixture 3 determined by the ^{1}H NMR experiment combined with the AutoWine-tool. The results are compared to the gravimetric concentrations. Errors are calculated from three repetitions using the standard uncertainty.

	Mixture 3	
Component	Gravimetric	^{1}H NMR experiment
	c_i / g l^{-1}	
Acetic Acid	0.300	0.277±0.003
Citric Acid	0.619	0.601±0.032
Ethanol	63.739	58.411±0.098
D(-)-Fructose	1.825	0
D(+)-Glucose	0.933	0.420±0.060
Glycerol	5.717	6.301±0.303
DL-Malic Acid	4.565	4.045±0.044
Succinic Acid	1.356	1.245±0.011

Figure A.2 displays the fit of the water peak for Mixture 1 by the AutoWine-tool. It can be seen, that the water peak is overestimated resulting in an underestimation of the other components.
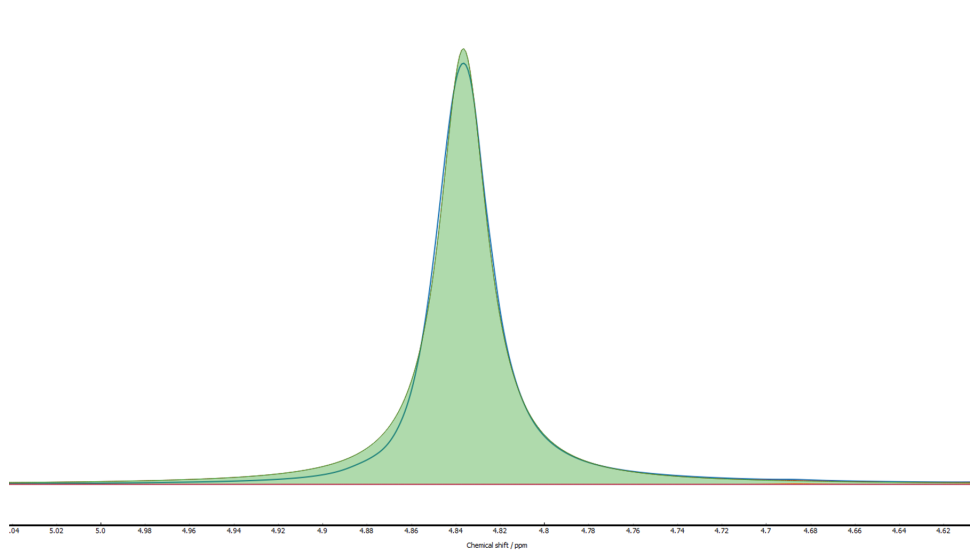
Figure A.2: Fit of the water peak by the AutoWine-tool for Mixture 1.

The density of Mixture 1, Mixture 2, and Mixture 3 (at 26.5°C) was determined by the densimeter as well as the AutoWine-tool and are provided in Table A.5.

Table A.5: Densities of Mixture 1, Mixture 2, and Mixture 3 at 26.5 °C. The values were determined with a densimeter and the AutoWine-tool. For the AutoWine-tool, errors are calculated from three repetitions using the standard uncertainty.

Mixture	Densimeter	AutoWine-tool
	c_i / g $\mathrm{l^{-1}}$	
Mixture 1	1062.6	1032.6±0.3
Mixture 2	1017.0	1004.9±0.3
Mixture 3	990.1	989.2±0.1

Matviychuk et al. [79] reported that their model-based data processing approach gives more accurate results when maleic acid with a concentration of 0.01 g $\mathrm{g^{-1}}$ is added to the sample as an internal standard. Therefore, about 5 g were taken from the stock of each mixture and the appropriate amount of maleic acid was added to the sample. Furthermore, additional ^{1}H NMR experiments with ^{13}C decoupling and water presaturation (available in Magritek's Spinsolve pulse sequence library) should aid the quantification by the AutoWine-tool. The experiments were conducted with an acquisition time of 6.4 s, 16 k data points, a 90° excitation pulse, and 16 scans with a repetition time of 60 s. For the water presaturation, a presaturation duration of 3 s with a power of -65 dBm was applied. Mixture 1, Mixture 2, and Mixture 3 were quantified by the AutoWine-tool. The results are compared to the gravimetric sample preparation and are shown in Figure A.3. The numerical values are given in Table A.6, Table A.7, and Table A.8.
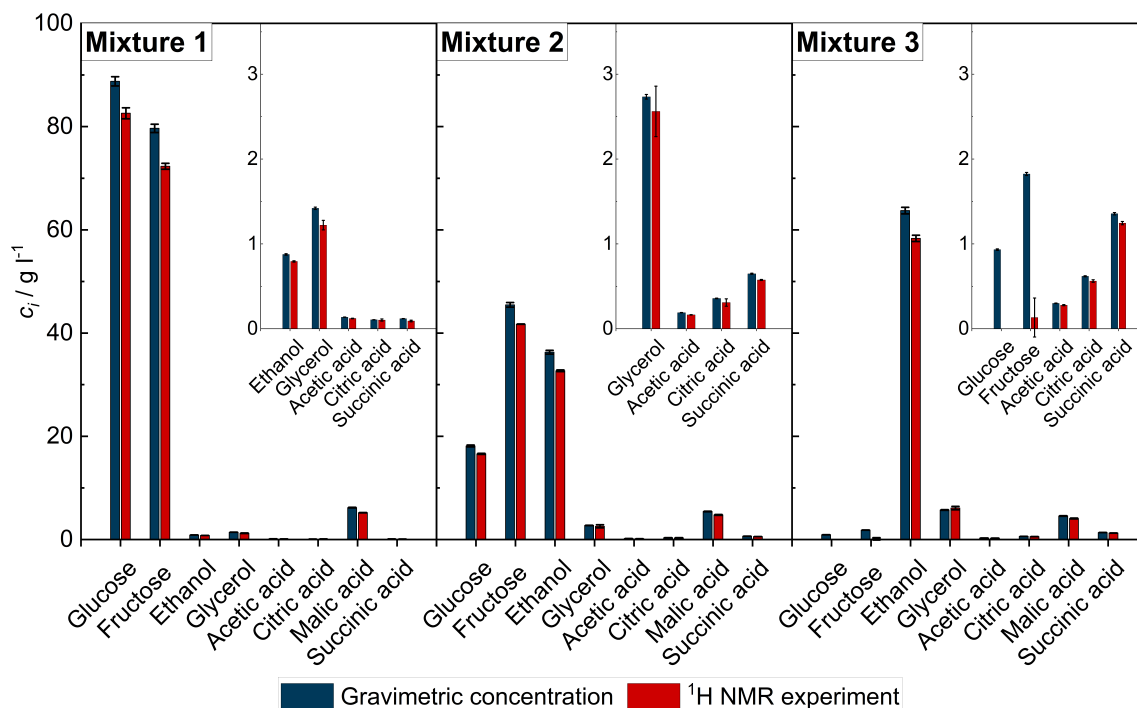
Figure A.3: Comparison of the results of Mixture 1, Mixture 2, and Mixture 3 obtained by the ^{1}H NMR experiment (with water presaturation and internal standard maleic acid) combined with the quantitative analysis by the AutoWine-tool with the concentrations of the gravimetric sample preparation. Inserts are provided showing the concentration of the components that are less than 3.5 g l^{-1} in the corresponding mixture.

When comparing the two approaches with each other, no significant differences were found, which is surprising. However, except for the outliers of the approach without water presaturation and internal standard for glycerol and citric acid in Mixture 1, the results of both approaches are almost identical. It was expected that the approach consisting of water presaturation and an internal standard would result in a better quantification of the components. The addition of maleic acid should aid quantification as the AutoWine-tool can refer to this peak to scale the intensities of the other signals accordingly, especially when a water suppression is applied. Furthermore, the addition of maleic acid lowers the pH value, which shifts the peak positions and sharpens the peaks, resulting in less peak overlap and better quantification [79].

It is assumed that significant improvements can only be achieved by analyzing the reconstituted dry extract, as recommended by Matviychuk et al. [79]. This approach would eliminate the important peak overlap with ethanol and allows detection of the sugars and glycerol at much lower concentrations. We did not apply this approach because it is not practical for the online monitoring of wine fermentations under field conditions.

Table A.6: Concentrations of Mixture 1 determined by the ^{1}H NMR experiment (with water presaturation and the internal standard maleic acid) combined with the AutoWine-tool. The results are compared to the gravimetric concentrations. Errors are calculated from three repetitions using the standard uncertainty.

	Mixture 1	
Component	Gravimetric	^{1}H NMR experiment
	c_i / g l^{-1}	
Acetic Acid	0.137	0.122±0.003
Citric Acid	0.106	0.103±0.012
Ethanol	0.876	0.794±0.007
D(-)-Fructose	79.660	72.316±0.582
D(+)-Glucose	88.772	82.583±1.065
Glycerol	1.420	1.222±0.056
DL-Malic Acid	6.182	5.197±0.030
Succinic Acid	0.119	0.092±0.010

Table A.7: Concentrations of Mixture 2 determined by the ^{1}H NMR experiment (with water presaturation and the internal standard maleic acid) combined with the AutoWine-tool. The results are compared to the gravimetric concentrations. Errors are calculated from three repetitions using the standard uncertainty.

Component	Gravimetric	^{1}H NMR experiment
	c_i / g l^{-1}	
Acetic Acid	0.190	0.164±0.002
Citric Acid	0.358	0.310±0.043
Ethanol	36.299	32.706±0.163
D(-)-Fructose	45.477	41.737±0.032
D(+)-Glucose	18.129	16.588±0.100
Glycerol	2.734	2.562±0.297
DL-Malic Acid	5.437	4.770±0.080
Succinic Acid	0.648	0.576±0.006

Table A.8: Concentrations of Mixture 3 determined by the ^{1}H NMR experiment (with water presaturation and the internal standard maleic acid) combined with the AutoWine-tool. The results are compared to the gravimetric concentrations. Errors are calculated from three repetitions using the standard uncertainty.

	Mixture 3	
Component	Gravimetric	^{1}H NMR experiment
	c_i / g l^{-1}	
Acetic Acid	0.300	0.278±0.007
Citric Acid	0.619	0.563±0.014
Ethanol	63.739	58.352±0.604
D(-)-Fructose	1.825	0.133±0.230
D(+)-Glucose	0.933	0
Glycerol	5.717	6.093±0.331
DL-Malic Acid	4.565	4.069±0.084
Succinic Acid	1.356	1.246±0.020

A.2.2 Online Monitoring Of Wine Fermentation

The evolution of the components in the batch fermentation of grape juice and the repetition experiment as well as the mean values are displayed in Figure A.4.
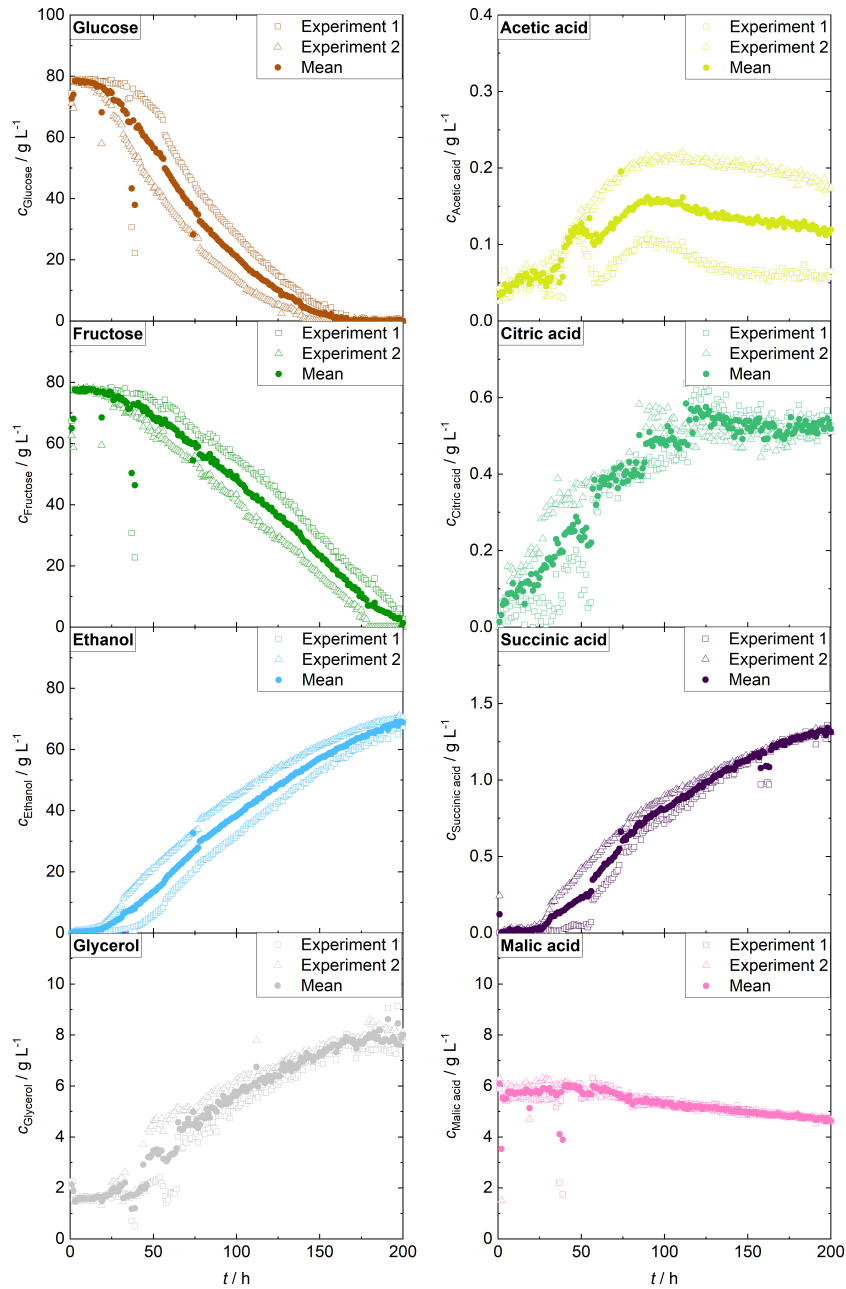
Figure A.4: Results of the batch fermentation of grape juice and the repetition experiment over 200 h. Mean values were formed from these two experiments.

The evolution of the pH value during the batch fermentation of grape juice over 200 h is shown in Figure A.5.
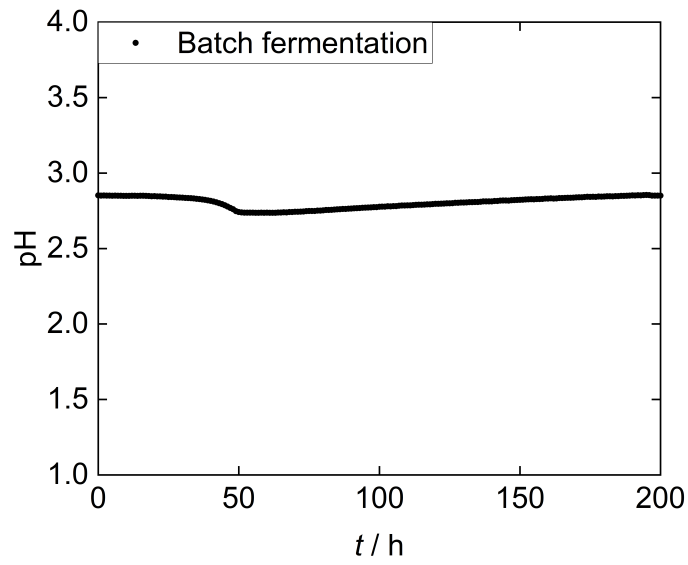
Figure A.5: Evolution of the pH value in the batch fermentation of grape juice.

The evolution of the components in the fed-batch fermentation of grape juice and the two repetition experiments as well as the mean values are displayed in Figure A.6.
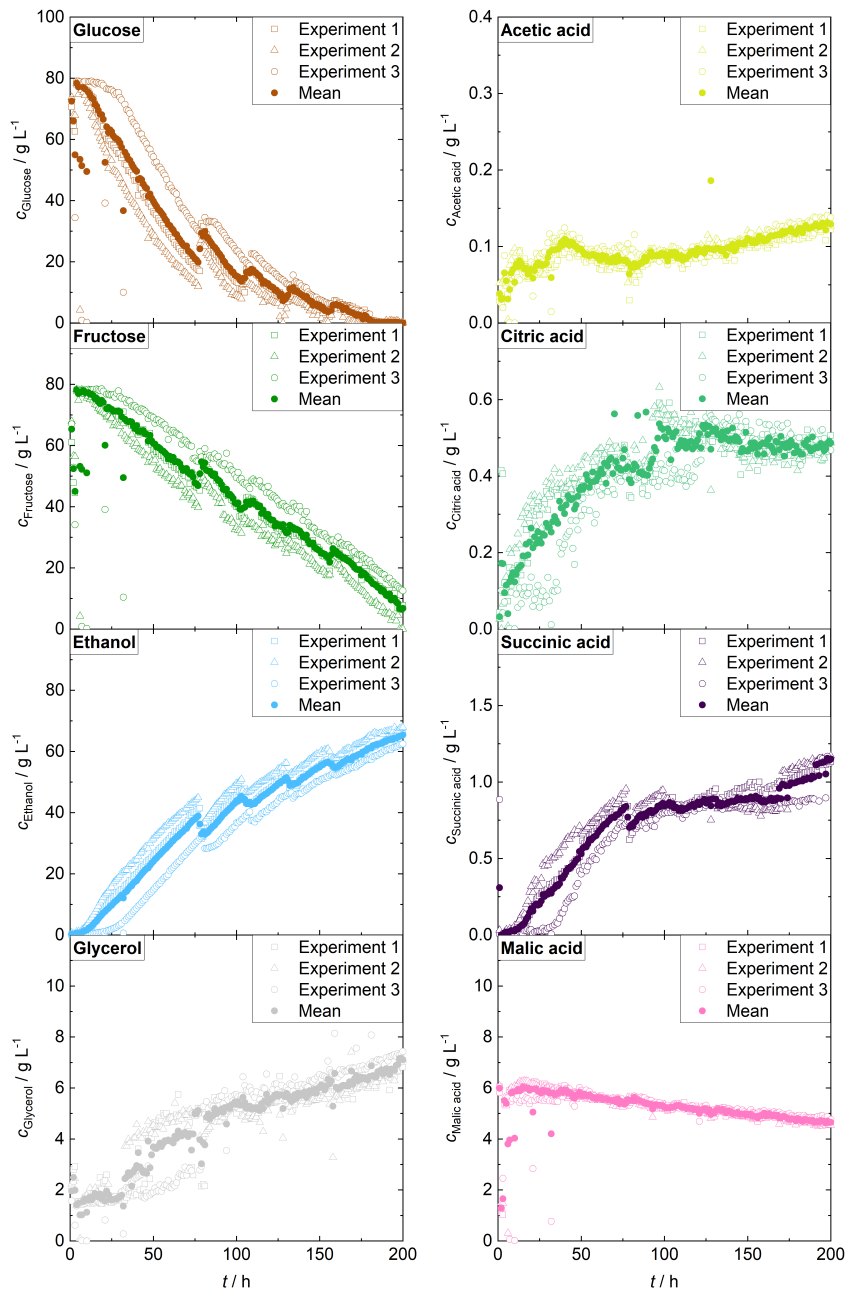
Figure A.6: Results of the fed-batch fermentation of grape juice and the two repetition experiment over 200 h. Mean values were formed from these three experiments.

B Supporting Information for Chapter 3

B.1 Experimental Section

Table A.9 displays the chemicals used in this work as well as their purities.

Table A.9: Chemicals that were used in this work including the suppliers and their respective purities.

Chemical	Formula	Supplier	Purity
Acetonitrile (ACN)	C_2H_3N	VWR Chemicals	$\geq 99.90\%$
Acetone (ACT)	C_3H_6O	Sigma Aldrich	$\geq 99.95\%$
Dimethyl sulfoxide (DMSO)	C_2H_6OS	VWR Chemicals	$\geq 99.97\%$
Ethyl formate (EF)	$C_3H_6O_2$	Acros Organics	$\geq 98.00\%$

Figure A.7 illustrates the implemented pulse sequence PENDANT for the polarization transfer from ^{1}H to the ^{13}C nuclei. The applied evolution delays are given in Equation (20) and (21).
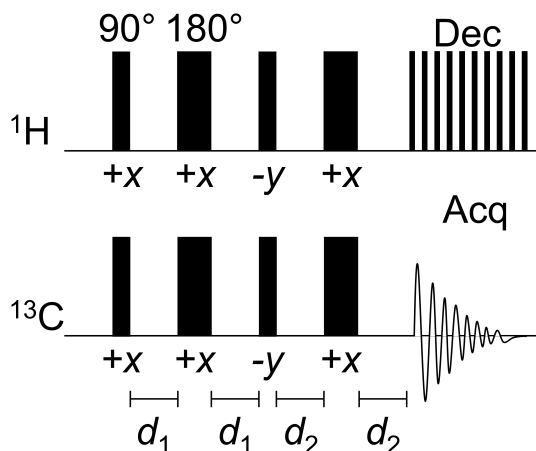
Figure A.7: Illustration of the used polarization transfer pulse sequence PENDANT.

$$d_1 = \frac{1}{4\,^1J_{\mathrm{C,H}}} \tag{20}$$

$$d_2 = \frac{5}{8\,^1J_{\mathrm{C,H}}} \tag{21}$$

For the determination of the T_1 values the program MestRenova was used (Mestrelab Research) to integrate the peaks. A custom MATLAB program (MathWorks Inc.) was used to obtain the T_1 values by fitting the peak integrals to the Bloch-Equation (see Equation (22)) with the nonlinear regression fit function *nlinfit*. All signal peaks of each molecule were evaluated and the highest T_1 value is determined to be decisive for the mixture. The selected parameters for the inversion recovery experiment are provided in Table A.10.

$$M_{\mathrm{z}}\left(t\right) = M_{\mathrm{z,0}}\left(1 - \exp\left(-\frac{t}{T_1}\right)\right) \tag{22}$$

Table A.10: Parameters applied for the execution of the inversion recovery experiment for the determination of the spin-lattice relaxation time $T_{1,{}^1\mathrm{H}}$ and $T_{1,{}^{13}\mathrm{C}}$.

Parameter	$T_{1,{}^1\mathrm{H}}$	$T_{1,{}^{13}\mathrm{C}}$
Number of scans / 1	2	32
Acquisition time / s	6.4	1.6
Repetition time / s	60	60
Max inversion time / s	20	30
Number of steps / 1	21	21

The mole fraction is calculated with Equation (23). The equations to calculate the uncertainty of the measured concentrations by the NMR experiments are given in Equation (24) and (25) (error propagation).

$$x_i = \frac{I_i}{I_1 + I_2 + I_3} \tag{23}$$

$$\Delta x = \frac{I_2 + I_3}{\left(\sum\limits_{i=1}^{K} I_i\right)^2}\Delta I_1 + \frac{I_1 + I_3}{\left(\sum\limits_{i=1}^{K} I_i\right)^2}\Delta I_2 + \frac{I_1 + I_2}{\left(\sum\limits_{i=1}^{K} I_i\right)^2}\Delta I_3 \tag{24}$$

$$\Delta I = \frac{I}{SNR} \tag{25}$$

B.2 Results and Discussion

B.2.1 Stationary Experiments

Figure A.8 shows the results of the quantitative analysis of Mixture 1.A, Mixture 1.B, Mixture 1.D, Mixture 2.A, Mixture 2.B and Mixture 2.D by ^{1}H NMR, ^{13}C NMR and ^{13}C NMR PENDANT experiments. The results of the gravimetric sample preparation are depicted as dashed horizontal lines. The numerical results are given in Table A.11.
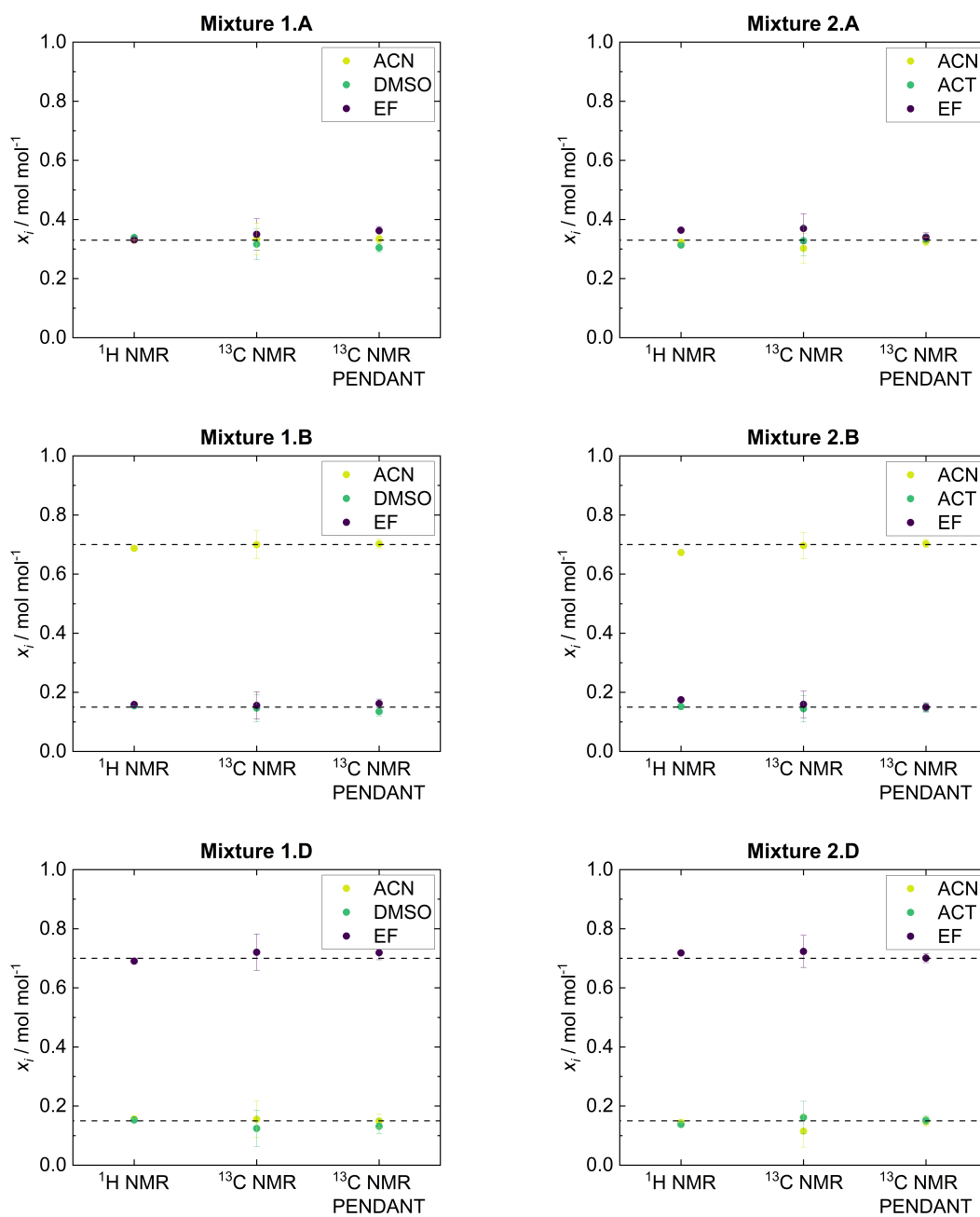
Figure A.8: Results for the quantification of Mixture 1.A, Mixture 1.B, Mixture 1.D, Mixture 2.A, Mixture 2.B, Mixture 2.D by ^{1}H NMR, ^{13}C NMR and ^{13}C NMR PENDANT experiments. The horizontal dashed lines are results from the gravimetric sample preparation. The uncertainties (error bars) for the ^{1}H NMR experiments are within the symbol size.

Table A.11: Results from the quantification of the studied mixtures by ^{1}H NMR, ^{13}C NMR and ^{13}C NMR PENDANT. The first line gives the experimental results, together with the uncertainty, that is reported in parentheses and refers to the last digit. The second line gives the relative deviation to the gravimetric reference value (compare Table 1).

	System 1								
	^{1}H NMR			^{13}C NMR			^{13}C NMR PENDANT		
Experiment	x_{ACN}	x_{DMSO}	x_{EF}	x_{ACN}	x_{DMSO}	x_{EF}	x_{ACN}	x_{DMSO}	x_{EF}
Mixture		mol mol^{-1}			mol mol^{-1}			mol mol^{-1}	
1.A	0.330 (1)	0.339 (1)	0.331 (1)	0.334 (53)	0.316 (53)	0.350 (53)	0.334 (14)	0.304 (14)	0.362 (14)
	-1.25 %	1.44 %	-1.02 %	0.09 %	-5.36 %	4.62 %	0.18 %	-8.95 %	8.30 %
1.B	0.687 (1)	0.154 (1)	0.159 (1)	0.699 (47)	0.146 (47)	0.155 (47)	0.703 (15)	0.135 (15)	0.162 (15)
	-1.88 %	2.92 %	5.85 %	-0.10 %	-2.33 %	3.76 %	0.37 %	-9.93 %	8.20 %
1.C	0.144 (1)	0.705 (1)	0.151 (1)	0.155 (53)	0.707 (53)	0.138 (53)	0.155 (12)	0.700 (12)	0.145 (12)
	-4.21 %	0.70 %	0.96 %	3.34 %	1.06 %	-8.30 %	3.39 %	0.05 %	-3.64 %
1.D	0.157 (1)	0.153 (1)	0.690 (1)	0.155 (62)	0.124 (62)	0.721 (62)	0.150 (62)	0.132 (62)	0.718 (62)
	4.43 %	1.97 %	-1.37 %	3.51 %	-17.13 %	2.92 %	-0.33 %	-12.29 %	2.70 %

Experiment	¹H NMR			¹³C NMR			¹³C NMR PENDANT		
Mixture	x_{ACN}	x_{ACT} mol mol^{-1}	x_{EF}	x_{ACN}	x_{ACT} mol mol^{-1}	x_{EF}	x_{ACN}	x_{ACT} mol mol^{-1}	x_{EF}
2.A	0.323 (1)	0.313 (1)	0.364 (1)	0.302 (50)	0.328 (50)	0.370 (50)	0.325 (15)	0.335 (15)	0.340 (15)
	-3.34 %	-6.29 %	8.80 %	-9.55 %	-1.88 %	10.60 %	-2.68 %	0.16 %	1.68 %
2.B	0.673 (1)	0.152 (1)	0.175 (1)	0.696 (45)	0.145 (45)	0.159 (45)	0.703 (14)	0.147 (14)	0.150 (14)
	-3.87 %	1.37 %	16.70 %	-0.52 %	-3.81 %	6.25 %	0.45 %	-2.29 %	0.21 %
2.C	0.182 (1)	0.656 (1)	0.162 (1)	0.112 (50)	0.691 (50)	0.197 (50)	0.147 (15)	0.699 (15)	0.154 (15)
	21.47 %	-6.36 %	8.20 %	-25.60 %	-1.31 %	31.73 %	-1.96 %	-0.14 %	2.63 %
2.D	0.144 (1)	0.138 (1)	0.718 (1)	0.115 (54)	0.162 (54)	0.723 (54)	0.148 (15)	0.152 (15)	0.700 (15)
	-4.01 %	-8.15 %	2.60 %	-23.27 %	7.75 %	3.33 %	-1.76 %	1.49 %	0.06 %

System 2

B.2.2 Flow Experiments

The results for the concentrations of the components by the ^{1}H NMR, ^{13}C NMR and ^{13}C NMR PENDANT experiments at various flow rates are illustrated in Figure A.9 to A.14. The reference values are depicted as dashed horizontal lines. The numerical results are given in Table A.12.
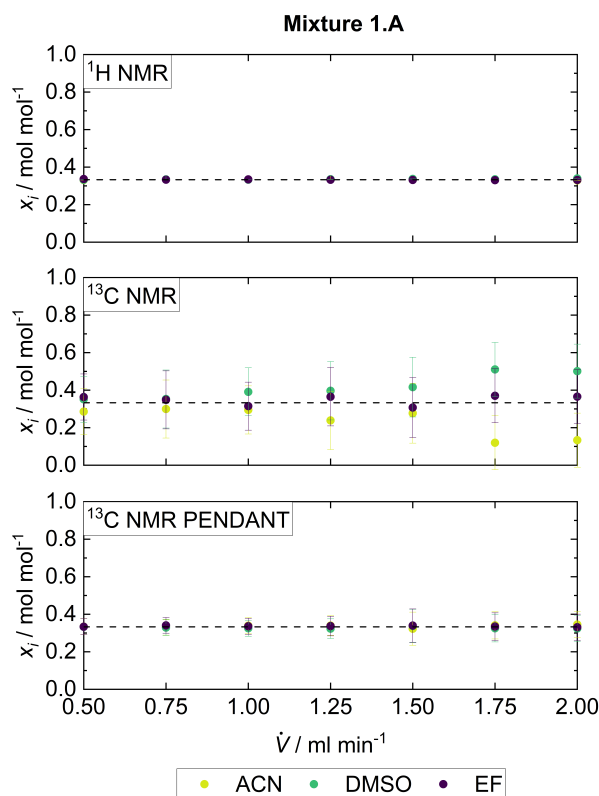
Figure A.9: Results of the quantitative analysis of Mixture 1.A by ^{1}H NMR, ^{13}C NMR and ^{13}C NMR PENDANT in flow experiments at different flow rates. The horizontal dashed lines represent the gravimetric reference. The error bars for the ^{1}H NMR experiments are within the symbol size.
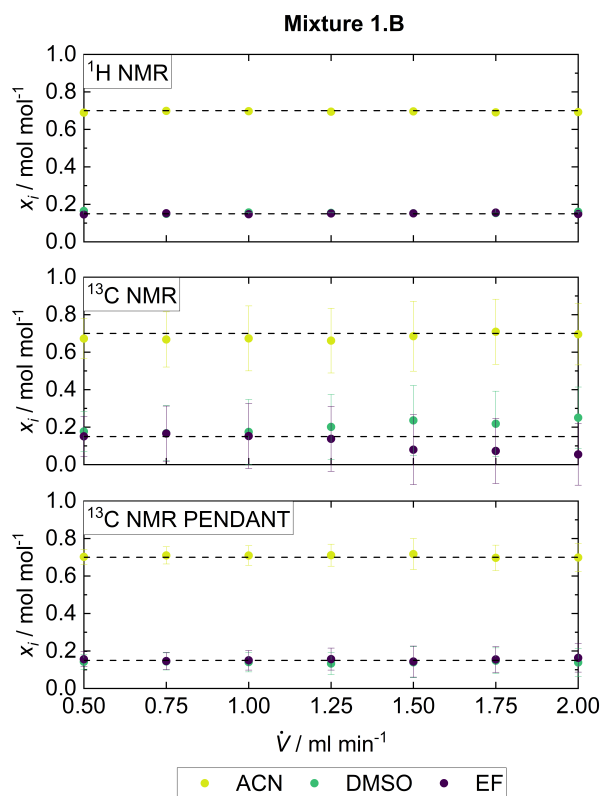
Figure A.10: Results of the quantitative analysis of Mixture 1.B by ^{1}H NMR, ^{13}C NMR and ^{13}C NMR PENDANT in flow experiments at different flow rates. The horizontal dashed lines represent the gravimetric reference. The error bars for the ^{1}H NMR experiments are within the symbol size.
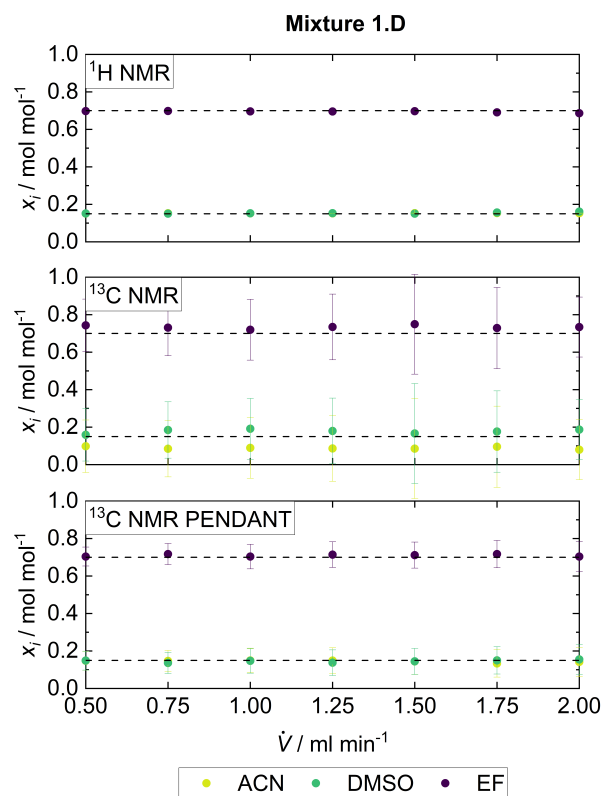
Figure A.11: Results of the quantitative analysis of Mixture 1.D by ^{1}H NMR, ^{13}C NMR and ^{13}C NMR PENDANT in flow experiments at different flow rates. The horizontal dashed lines represent the gravimetric reference. The error bars for the ^{1}H NMR experiments are within the symbol size.
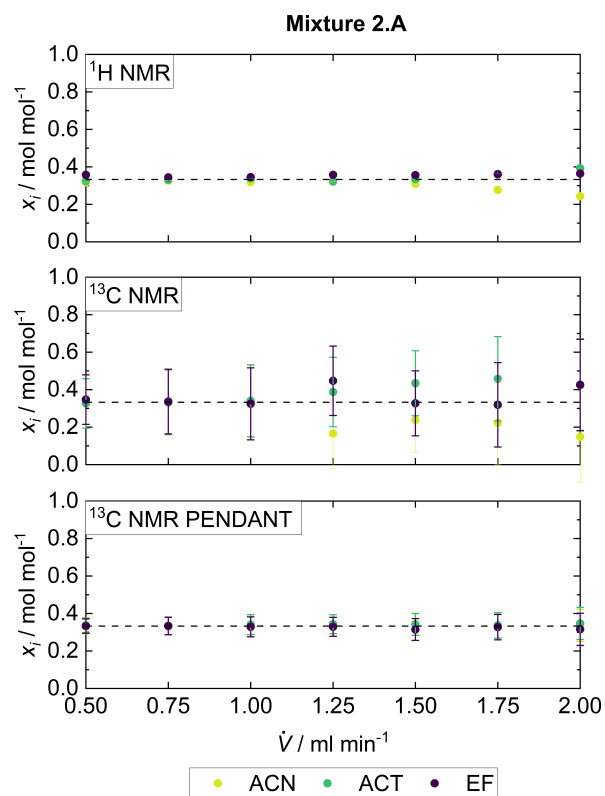
Figure A.12: Results of the quantitative analysis of Mixture 2.A by ^{1}H NMR, ^{13}C NMR and ^{13}C NMR PENDANT in flow experiments at different flow rates. The horizontal dashed lines represent the gravimetric reference. The error bars for the ^{1}H NMR experiments are within the symbol size.
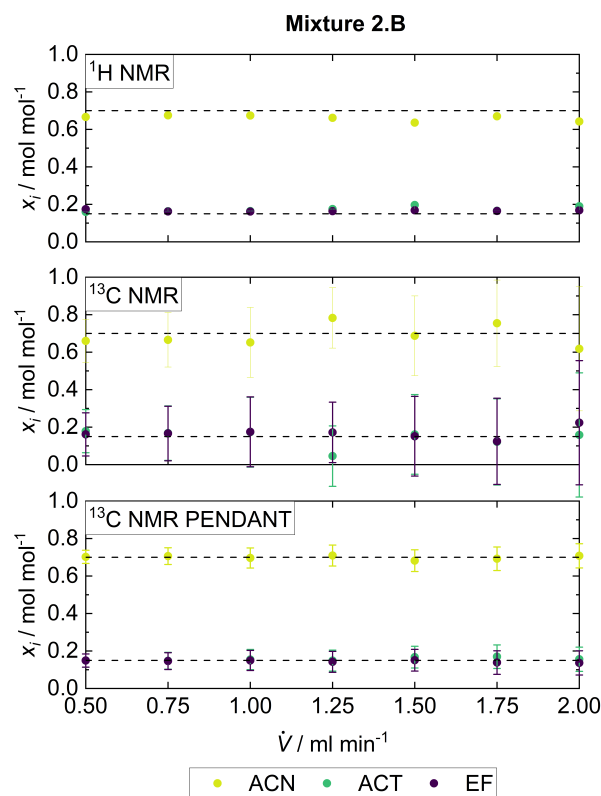
Figure A.13: Results of the quantitative analysis of Mixture 2.B by ^{1}H NMR, ^{13}C NMR and ^{13}C NMR PENDANT in flow experiments at different flow rates. The horizontal dashed lines represent the gravimetric reference. The error bars for the ^{1}H NMR experiments are within the symbol size.
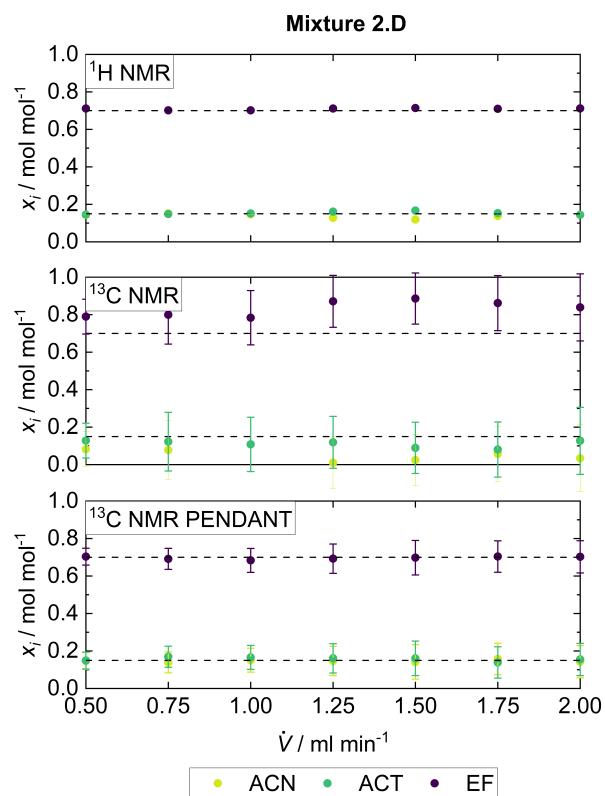
Figure A.14: Results of the quantitative analysis of Mixture 2.D by ^{1}H NMR, ^{13}C NMR and ^{13}C NMR PENDANT in flow experiments at different flow rates. The horizontal dashed lines represent the gravimetric reference. The error bars for the ^{1}H NMR experiments are within the symbol size.

Table A.12: Results of the quantitative analysis of the studied mixtures by ^{1}H NMR, ^{13}C NMR and ^{13}C NMR PENDANT in flow experiments at different flow rates. The uncertainty is reported in parentheses and refers to the last digit.

Experiment	Mixture 1.A								
	^{1}H NMR			^{13}C NMR			^{13}C NMR PENDANT		
Flow Rate	x_{ACN}	x_{ACT}	x_{EF}	x_{ACN}	x_{ACT}	x_{EF}	x_{ACN}	x_{ACT}	x_{EF}
ml min^{-1}		mol mol^{-1}			mol mol^{-1}			mol mol^{-1}	
0.50	0.331 (1)	0.332 (1)	0.337 (1)	0.286 (123)	0.351 (123)	0.363 (123)	0.334 (43)	0.333 (43)	0.333 (43)
0.75	0.333 (1)	0.335 (1)	0.332 (1)	0.299 (155)	0.353 (155)	0.348 (155)	0.331 (42)	0.329 (42)	0.340 (42)
1.00	0.333 (1)	0.333 (1)	0.334 (1)	0.294 (128)	0.391 (128)	0.315 (128)	0.339 (43)	0.325 (43)	0.336 (43)
1.25	0.333 (1)	0.335 (1)	0.332 (1)	0.239 (156)	0.397 (156)	0.364 (156)	0.340 (52)	0.323 (52)	0.337 (52)
1.50	0.332 (1)	0.337 (1)	0.331 (1)	0.277 (159)	0.416 (159)	0.307 (159)	0.322 (89)	0.338 (89)	0.340 (89)
1.75	0.335 (1)	0.335 (1)	0.330 (1)	0.120 (144)	0.511 (144)	0.369 (144)	0.341 (73)	0.325 (73)	0.334 (73)
2.00	0.329 (1)	0.340 (1)	0.331 (1)	0.133 (144)	0.501 (144)	0.366 (144)	0.345 (69)	0.324 (73)	0.331 (73)

Mixture 1.B

Experiment		^{1}H NMR			^{13}C NMR			^{13}C NMR PENDANT		
Flow Rate		x_ACN	x_DMSO	x_EF	x_ACN	x_DMSO	x_EF	x_ACN	x_DMSO	x_EF
ml min^{-1}			mol mol^{-1}			mol mol^{-1}			mol mol^{-1}	
0.50		0.689 (1)	0.165 (1)	0.146 (1)	0.672 (106)	0.177 (106)	0.151 (106)	0.702 (40)	0.142 (40)	0.156 (40)
0.75		0.699 (1)	0.149 (1)	0.152 (1)	0.668 (147)	0.167 (147)	0.165 (147)	0.710 (46)	0.144 (46)	0.146 (46)
1.00		0.697 (1)	0.156 (1)	0.147 (1)	0.673 (173)	0.174 (173)	0.153 (173)	0.709 (52)	0.141 (52)	0.150 (52)
1.25		0.694 (1)	0.155 (1)	0.151 (1)	0.662 (173)	0.201 (173)	0.137 (173)	0.711 (59)	0.133 (59)	0.156 (59)
1.50		0.696 (1)	0.152 (1)	0.152 (1)	0.685 (186)	0.236 (186)	0.079 (186)	0.717 (83)	0.140 (83)	0.143 (83)
1.75		0.691 (1)	0.154 (1)	0.155 (1)	0.709 (174)	0.218 (174)	0.073 (174)	0.697 (68)	0.148 (68)	0.155 (68)
2.00		0.692 (1)	0.160 (1)	0.148 (1)	0.696 (164)	0.250 (164)	0.054 (164)	0.699 (76)	0.138 (76)	0.163 (76)

Mixture 1.C

Experiment	1H NMR			13C NMR			13C NMR PENDANT		
Flow Rate ml min^{-1}	x_{ACN}	x_{ACT} mol mol^{-1}	x_{EF}	x_{ACN}	x_{ACT} mol mol^{-1}	x_{EF}	x_{ACN}	x_{ACT} mol mol^{-1}	x_{EF}
0.50	0.153 (1)	0.694 (1)	0.153 (1)	0.220 (84)	0.712 (84)	0.068 (84)	0.147 (32)	0.709 (32)	0.144 (32)
0.75	0.154 (1)	0.698 (1)	0.148 (1)	0.109 (64)	0.803 (64)	0.088 (64)	0.154 (35)	0.700 (35)	0.146 (35)
1.00	0.153 (1)	0.696 (1)	0.151 (1)	0.107 (59)	0.838 (59)	0.055 (59)	0.146 (39)	0.716 (39)	0.138 (39)
1.25	0.154 (1)	0.693 (1)	0.153 (1)	0.058 (40)	0.886 (40)	0.056 (40)	0.144 (44)	0.715 (44)	0.141 (44)
1.50	0.156 (1)	0.689 (1)	0.155 (1)	0.043 (34)	0.919 (34)	0.038 (34)	0.151 (49)	0.709 (49)	0.140 (49)
1.75	0.155 (1)	0.690 (1)	0.155 (1)	0.025 (20)	0.956 (20)	0.019 (20)	0.152 (48)	0.709 (48)	0.139 (48)
2.00	0.149 (1)	0.699 (1)	0.152 (1)	0.032 (22)	0.950 (22)	0.018 (22)	0.135 (49)	0.719 (49)	0.146 (49)

Mixture 1.D

Experiment	¹H NMR			¹³C NMR			¹³C NMR PENDANT		
Flow Rate ml min⁻¹	x_{ACN}	x_{ACT} mol mol⁻¹	x_{EF}	x_{ACN}	x_{ACT} mol mol⁻¹	x_{EF}	x_{ACN}	x_{ACT} mol mol⁻¹	x_{EF}
0.50	0.151 (1)	0.151 (1)	0.698 (1)	0.098 (140)	0.159 (140)	0.743 (140)	0.148 (50)	0.149 (50)	0.703 (50)
0.75	0.152 (1)	0.150 (1)	0.698 (1)	0.085 (150)	0.185 (150)	0.730 (150)	0.147 (56)	0.136 (56)	0.717 (56)
1.00	0.152 (1)	0.152 (1)	0.696 (1)	0.089 (162)	0.191 (162)	0.720 (162)	0.149 (66)	0.147 (66)	0.704 (66)
1.25	0.152 (1)	0.153 (1)	0.695 (1)	0.086 (175)	0.179 (175)	0.735 (175)	0.149 (68)	0.137 (68)	0.714 (68)
1.50	0.153 (1)	0.150 (1)	0.697 (1)	0.085 (266)	0.166 (266)	0.749 (266)	0.144 (70)	0.144 (70)	0.712 (70)
1.75	0.153 (1)	0.156 (1)	0.691 (1)	0.095 (217)	0.176 (217)	0.729 (217)	0.134 (73)	0.150 (73)	0.716 (73)
2.00	0.153 (1)	0.161 (1)	0.686 (1)	0.079 (160)	0.187 (160)	0.734 (160)	0.141 (79)	0.155 (79)	0.704 (79)

Mixture 2.A

Experiment	^{1}H NMR			^{13}C NMR			^{13}C NMR PENDANT		
Flow Rate ml min^{-1}	x_{ACN}	x_{ACT} mol mol^{-1}	x_{EF}	x_{ACN}	x_{ACT} mol mol^{-1}	x_{EF}	x_{ACN}	x_{ACT} mol mol^{-1}	x_{EF}
0.50	0.318 (1)	0.325 (1)	0.357 (1)	0.327 (132)	0.326 (132)	0.347 (132)	0.330 (39)	0.337 (39)	0.333 (39)
0.75	0.326 (1)	0.330 (1)	0.344 (1)	0.331 (173)	0.333 (173)	0.336 (173)	0.333 (47)	0.334 (47)	0.333 (47)
1.00	0.318 (1)	0.336 (1)	0.346 (1)	0.335 (192)	0.341 (192)	0.324 (192)	0.331 (53)	0.340 (53)	0.329 (53)
1.25	0.320 (1)	0.323 (1)	0.357 (1)	0.166 (185)	0.387 (185)	0.447 (185)	0.328 (50)	0.343 (50)	0.329 (50)
1.50	0.309 (1)	0.335 (1)	0.356 (1)	0.238 (173)	0.434 (173)	0.328 (173)	0.344 (58)	0.341 (58)	0.315 (58)
1.75	0.278 (1)	0.362 (1)	0.360 (1)	0.223 (225)	0.458 (225)	0.319 (225)	0.336 (68)	0.337 (68)	0.327 (68)
2.00	0.243 (1)	0.393 (1)	0.364 (1)	0.148 (244)	0.427 (244)	0.425 (244)	0.337 (86)	0.347 (86)	0.316 (86)

Mixture 2.B

Experiment	^{1}H NMR			^{13}C NMR			^{13}C NMR PENDANT		
Flow Rate	x_{ACN}	x_{ACT}	x_{EF}	x_{ACN}	x_{ACT}	x_{EF}	x_{ACN}	x_{ACT}	x_{EF}
ml min^{-1}	mol mol^{-1}			mol mol^{-1}			mol mol^{-1}		
0.50	0.666 (1)	0.160 (1)	0.174 (1)	0.660 (115)	0.179 (115)	0.161 (115)	0.702 (35)	0.149 (35)	0.149 (35)
0.75	0.675 (1)	0.163 (1)	0.162 (1)	0.666 (145)	0.168 (145)	0.166 (145)	0.706 (35)	0.148 (35)	0.146 (35)
1.00	0.674 (1)	0.164 (1)	0.162 (1)	0.652 (186)	0.173 (186)	0.175 (186)	0.696 (45)	0.154 (45)	0.150 (45)
1.25	0.661 (1)	0.175 (1)	0.164 (1)	0.783 (161)	0.045 (161)	0.172 (161)	0.709 (54)	0.149 (54)	0.142 (54)
1.50	0.636 (1)	0.196 (1)	0.168 (1)	0.687 (213)	0.161 (213)	0.152 (213)	0.682 (58)	0.167 (58)	0.151 (58)
1.75	0.670 (1)	0.165 (1)	0.165 (1)	0.754 (230)	0.121 (230)	0.125 (230)	0.692 (63)	0.170 (63)	0.138 (63)
2.00	0.642 (1)	0.190 (1)	0.168 (1)	0.617 (331)	0.159 (331)	0.224 (331)	0.708 (65)	0.156 (65)	0.136 (65)

Mixture 2.C

Experiment	¹H NMR			¹³C NMR			¹³C NMR PENDANT		
Flow Rate ml min⁻¹	x_{ACN}	x_{ACT} mol mol⁻¹	x_{EF}	x_{ACN}	x_{ACT} mol mol⁻¹	x_{EF}	x_{ACN}	x_{ACT} mol mol⁻¹	x_{EF}
0.50	0.163 (1)	0.661 (1)	0.176 (1)	0.053 (75)	0.767 (75)	0.180 (75)	0.152 (44)	0.694 (44)	0.154 (44)
0.75	0.115 (1)	0.709 (1)	0.176 (1)	0.050 (70)	0.793 (70)	0.157 (70)	0.155 (44)	0.693 (44)	0.152 (44)
1.00	0.070 (1)	0.751 (1)	0.179 (1)	0.052 (85)	0.816 (85)	0.132 (85)	0.149 (45)	0.702 (45)	0.149 (45)
1.25	0.060 (1)	0.760 (1)	0.180 (1)	0.044 (62)	0.847 (62)	0.109 (62)	0.155 (51)	0.698 (51)	0.147 (51)
1.50	0.051 (1)	0.768 (1)	0.181 (1)	0.053 (44)	0.879 (44)	0.068 (44)	0.142 (46)	0.720 (46)	0.138 (46)
1.75	0.153 (1)	0.670 (1)	0.177 (1)	0.052 (26)	0.938 (26)	0.010 (26)	0.147 (44)	0.708 (44)	0.145 (44)
2.00	0.141 (1)	0.680 (1)	0.179 (1)	0.034 (34)	0.921 (34)	0.045 (34)	0.152 (63)	0.707 (63)	0.141 (63)

Mixture 2.D

Experiment		¹H NMR			¹³C NMR			¹³C NMR PENDANT		
Flow Rate		x_{ACN}	x_{ACT}	x_{EF}	x_{ACN}	x_{ACT}	x_{EF}	x_{ACN}	x_{ACT}	x_{EF}
ml min⁻¹		mol mol⁻¹			mol mol⁻¹			mol mol⁻¹		
0.50		0.144 (1)	0.145 (1)	0.711 (1)	0.082 (93)	0.128 (93)	0.790 (93)	0.147 (45)	0.149 (45)	0.704 (45)
0.75		0.151 (1)	0.148 (1)	0.701 (1)	0.078 (157)	0.122 (157)	0.800 (157)	0.139 (56)	0.169 (56)	0.692 (56)
1.00		0.147 (1)	0.151 (1)	0.702 (1)	0.108 (145)	0.108 (145)	0.784 (145)	0.151 (64)	0.166 (64)	0.683 (64)
1.25		0.128 (1)	0.161 (1)	0.711 (1)	0.010 (138)	0.119 (138)	0.871 (138)	0.146 (78)	0.161 (78)	0.693 (78)
1.50		0.119 (1)	0.167 (1)	0.714 (1)	0.025 (137)	0.089 (137)	0.886 (137)	0.142 (92)	0.160 (92)	0.698 (92)
1.75		0.137 (1)	0.153 (1)	0.710 (1)	0.057 (147)	0.081 (147)	0.862 (147)	0.157 (84)	0.139 (84)	0.704 (84)
2.00		0.144 (1)	0.144 (1)	0.712 (1)	0.034 (179)	0.127 (179)	0.839 (179)	0.143 (86)	0.155 (86)	0.702 (86)

The investigation of the achieved ^{1}H and ^{13}C magnetization for ACN, DMSO and EF at the detection zone of the benchtop NMR spectromer at different flow rates is shown in Figure A.15 at the example of Mixture 1.C. The relative magnetization of a molecule is plotted against the flow rate. The relative magnetization is calculated by Equation (26).

$$I_{\text{rel}} = \frac{I_{\text{flow}}}{I_{\text{stationary}}} \tag{26}$$
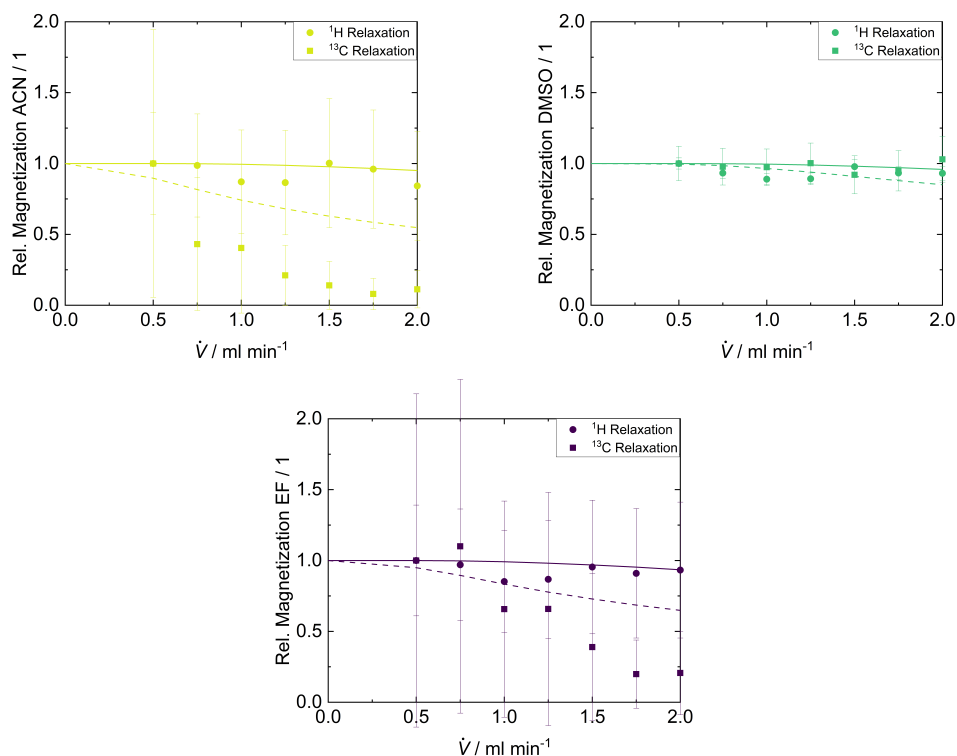
Figure A.15: Evaluation of the achieved relative magnetization of ACN, DMSO and EF of Mixture 1.C when arriving at the detection zone at various flow rates. The calculated magnetizations for the relaxation via ^{1}H (solid line) and ^{13}C nuclei (dashed line) are presented. The experimental determined magnetization by ^{13}C NMR PENDANT (circle) and ^{13}C NMR experiments (square) is additionally given.

C Supporting Information for Chapter 4

C.1 Experimental Section

The code of the pulse sequence PENPFG for Spinsolve Expert 1.26 is given in the following.

```
1   procedure(pulse_program,dir,mode)
2
3   # Interface description (name, label, x, y, ctrl, vartype)
4      interface = ["nucleus",          "Nucleus",                      "0","0", "tb",
        "readonly_string",
5                  "b1Freq13C",         "13C Frequency (MHz)",          "0","1",
                   "tbw","freq",
6                  "offFreq",           "Offset Frequency (Hz)",        "0","2",
                   "tbw","float",
7                  "acqShift",          "Acq shift (us)",               "1","4",
                   "tbw","float,[0,2000]",
8                  "pulseLength13C",    "Pulse length 13C (us)",        "0","3",
                   "tbw","pulselength",
9                  "90Amplitude13C",    "90 Pulse amplitude 13C (dB)",  "0","4",
                   "tbw","pulseamp",
10                 "180Amplitude13C",   "180 Pulse amplitude 13C (dB)","0","5",
                   "tbw","pulseamp",
11                 "b1Freq1H",          "1H Frequency (MHz)",           "1","0",
                   "tbw","freq",
12                 "decoupleAmp",       "Decouple amplitude 1H (dB)",   "2","3",
                   "tbw","pulseamp",
13                 "pulseLengthH180",   "180 Decouple length 1H (us)",  "2","4",
                   "tbw","pulselength",
14                 "90AmplitudeHC",     "90 Pulse amplitude 1H (dB)",   "1","2",
                   "tbw","pulseamp",
15                 "180AmplitudeHC",    "180 Pulse amplitude 1H (dB)",  "1","3",
                   "tbw","pulseamp",
16                 "jch",               "J(C,H) Coupling (Hz)",         "2","2",
                   "tbw","float",
17                 "repTime",           "Repetition time (ms)",         "3","4",
                   "tbw","reptime",
18                 "acqDelay",          "Pulse acqu. delay (us)",       "1","4",
                   "tbw","sdelay",
19                 "bDelta",            "Big DELTA (ms)",               "1","0",
                   "tbw","ldelayms",
20                 "lDelta",            "Little delta (ms)",            "1","1",
                   "tbw","float,[0.1,100]",
21                 "gradMax",           "Max. gradient (mT/m)",         "1","2",
                   "tbw","float,[0,2000]",
22                 "gradAmpPC",         "Gradient Strength Usage (%)",  "1","3",
                   "tbw","float,[0,100]",
23                 "gradRamp",          "Gradient ramp time (ms)",      "1","4",
                   "tbw","float,[0.1,100]",
24                 "rampSteps",         "Number of ramp steps",         "2","0",
                   "tbw","integer,[2,16]"]
25
26   # Relationships to determine remaining variable values
27      relationships = ["(DiffAmp,gradAmp) =
        ucsUtilities:getGradientsmod(gradAmpPC,oshim)",
28                 "b1Freq = b1Freq13C",
29                 "a1 = 90AmplitudeHC",
30                 "a2 = 180AmplitudeHC",
31                 "a3 = 90Amplitude13C",
32                 "a4 = 180Amplitude13C",
33                 "a6 = decoupleAmp",
34                 "d2 = pulseLength13C",
35                 "d3 = 1",
36                 "d4 = pulseLengthH180",
37                 "d5 = 100",
38                 "d6 =
                   1000*gradRamp/rampSteps",
39                 "d7 =
                   1000*lDelta",
40                 "d10 = 1e6/jch/4-2*pgo-pulseLength13C",
41                 "d12 =
                   pulseLengthH180/2",
42                 "d13 =
                   3*pulseLengthH180/2",
43                 "d14 =
                   2*pulseLengthH180",
44                 "d20 = 1e6*5/jch/8-2*pgo-pulseLength13C",
```

```
45                              "d21 = 1+acqShift",
46                              "n1 = nrPnts",
47                              "n2 =
                                trunc(1000*acqTime/(12*pulseLengthH180+9*pgo+8*d3+d3+1)/4)+1",
48                              "n3 =
                                rampSteps",
49                              "n4 =
                                oshim",
50                              "n5 =
                                DiffAmp+oshim",
51                              "w1 =
                                0.5*(1000*bDelta-1000*gradRamp-1000*lDelta-1000*gradRamp-d2)",
52                              "O1 = offFreq",
53                              "f1 = double(b1Freq13C)+double(offFreq/1e6d)",
54                              "f2 = 10d*f1",
55                              "f3 = double(b1Freq1H)",
56                              "totPnts = nrPnts",
57                              "totTime = acqTime"]
58
59    # Define the tabs and their order
60        tabs = ["Pulse_sequence","Progress","Acquisition",
61                "Processing_Std","Display_Std","File_Settings"]
62
63    # These parameters will be changed between experiments
64        variables = ["w1"]
65
66    # x and y spacing between controls
67        dim = [190,26]
68
69    # Pulse sequence
70        initpp(dir) # Reset internal parameter list
71        cleardata(n1)
72        delay(5000)                     # allow time to finish lock scan
73        settxfreqs(f3,f1)
74
75        pulse(1,a1,p1,f3,2,a3,p2,f1,d2)  # PENDANT: 90 H, 90 C pulse
76
77        delay(d10)
78
79        pulse(1,a2,p3,f3,2,a4,p4,f1,d2)  # PENDANT: 180 H, 180 C pulse
80
81        delay(d10)
82
83        pulse(1,a1,p5,f3,2,a3,p6,f1,d2)  # PENDANT: 90 H, 90 C pulse
84
85        delay(d20)
86
87        pulse(1,a2,p7,f3,2,a4,p8,f1,d2)   # PENDANT: 180 H, 180 C pulse
88
89        delay(d20)
90
91        gradramp(n4,n5,n3,d6)
92        delay(d7)
93        gradramp(n5,n4,n3,d6)
94
95        wait(w1)
96
97        pulse(2,a4,p8,d2)
98
99        wait(w1)
100
101       gradramp(n4,n5,n3,d6)
102       delay(d7)
103       gradramp(n5,n4,n3,d6)
104
105       delay(d21)
106
107       acquireon(n1)
108
109       loop(l1,n2)
110
```

```
111        pulse(1,a6,p10,d13); delay(d3); pulse(1,a6,p9,d14); delay(d3);
           pulse(1,a6,p10,d4); delay(d3); pulse(1,a6,p9,d13); delay(d3);
           pulse(1,a6,p10,d12); delay(d3); pulse(1,a6,p9,d4); delay(d3);
           pulse(1,a6,p10,d14); delay(d3); pulse(1,a6,p9,d4); delay(d3);
           pulse(1,a6,p10,d13);
112        delay(d3);
113        pulse(1,a6,p9,d13); delay(d3); pulse(1,a6,p10,d14); delay(d3);
           pulse(1,a6,p9,d4); delay(d3); pulse(1,a6,p10,d13); delay(d3);
           pulse(1,a6,p9,d12); delay(d3); pulse(1,a6,p10,d4); delay(d3);
           pulse(1,a6,p9,d14); delay(d3); pulse(1,a6,p10,d4); delay(d3); pulse(1,a6,p9,d13);
114        delay(d3);
115        pulse(1,a6,p9,d13); delay(d3); pulse(1,a6,p10,d14); delay(d3);
           pulse(1,a6,p9,d4); delay(d3); pulse(1,a6,p10,d13); delay(d3);
           pulse(1,a6,p9,d12); delay(d3); pulse(1,a6,p10,d4); delay(d3);
           pulse(1,a6,p9,d14); delay(d3); pulse(1,a6,p10,d4); delay(d3); pulse(1,a6,p9,d13);
116        delay(d3);
117        pulse(1,a6,p10,d13); delay(d3); pulse(1,a6,p9,d14); delay(d3);
           pulse(1,a6,p10,d4); delay(d3); pulse(1,a6,p9,d13); delay(d3);
           pulse(1,a6,p10,d12); delay(d3); pulse(1,a6,p9,d4); delay(d3);
           pulse(1,a6,p10,d14); delay(d3); pulse(1,a6,p9,d4); delay(d3);
           pulse(1,a6,p10,d13);
118        delay(d3);
119
120     endloop(l1)
121     acquireoff("overwrite",n1)
122
123     lst = endpp(mode) # Return parameter list
124
125  # Phase cycle list
126     phaseList = [0; # 1H-90
127                  0; # 13C-90
128                  0; # 1H-180
129                  0; # 13C-180
130                  1; # 1H-90
131                  1; # 13C-90
132                  0; # 1H-180
133                  0; # 13C-180
134                  0; # Decouple phase 1
135                  2; # Decouple phase 2
136                  0] # Acquire phase
137
138  endproc(lst,tabs,interface,relationships,variables,dim,phaseList)
```

A Stejskal-Tanner equation, which considers the shape of the trapezoidal gradient pulse of the benchtop NMR spectrometer in the ^{13}C BT PENPFG and ^{1}H BT PFGSTE experiments, is given in Equation 27. The correction was suggested by the manufacturer of the benchtop NMR spectrometer Magritek.

$$I_i = I_0 \exp\left(-D_i \gamma^2 G^2 \left(\delta_{\text{eff}}^2 \left(\Delta - \frac{\delta_{\text{eff}}}{3}\right)\right) + \frac{1}{30}\tau_{\text{grad}}^3 - \frac{\delta_{\text{eff}}\tau_{\text{grad}}^2}{6}\right) \tag{27}$$

The repetition delays applied in the ^{1}H HF PFGSTE, ^{13}C HF PFGSTE and ^{1}H HF PENPFG experiments for the different mixtures are given in Table A.13. The delays were set according to the molecule which has the longest T_1 as pure component. An additional safety margin was added to ensure a complete relaxation.

Table A.13: Repetition delays d_1 of different mixtures and experiments applied for the measurements on the high-field NMR spectrometer.

	Pure Component	
	^{1}H HF PFGSTE & ^{13}C HF PENPFG	^{13}C HF PFGSTE
	d_1 / s	d_1 / s
ACN	42	110
EtOH	25	50
PrOH	25	50

Binary Mixture: ACN + EtOH	
x_{ACN}	^{1}H HF PFGSTE & ^{13}C HF PENPFG
/ mol mol^{-1}	d_1 / s
1	42
0.75	42
0.5	42
0.25	42
Binary Mixture: EtOH + PrOH	
x_{EtOH}	^{1}H HF PFGSTE & ^{13}C HF PENPFG
/ mol mol^{-1}	d_1 / s
1	25
0.75	25
0.5	25
0.25	25
Binary Mixture: ACN + PrOH	
x_{PrOH}	^{1}H HF PFGSTE & ^{13}C HF PENPFG
/ mol mol^{-1}	d_1 / s
1	42
0.75	42
0.5	42
0.25	42

| Ternary Mixture: ACN + EtOH + PrOH		
x_{ACN}	x_{EtOH}	^{1}H HF PFGSTE & ^{13}C HF PENPFG
/ mol mol^{-1}		d_1 / s
0.333	0.333	42
0.33	0.165	42
0.33	0.505	42
0.165	0.33	42
0.505	0.33	42
0.505	0.165	42
0.165	0.505	42

C.2 Results and Discussion

C.2.1 Pure Components

Table A.14 displays self-diffusion coefficients of the pure components acetonitrile (ACN), ethanol (EtOH) and 1-propanol (PrOH) measured with different experiments with the high-field as well as with the benchtop NMR spectrometer. The calculated root mean squared error (RMSE) is additionally given. In each experiment, only the signals of the CH$_3$-groups were used for the analysis. The self-diffusion coefficients obtained with ^{1}H HF PFGSTE are considered as the ground truth in this work and are used to evaluate the results of the other experiments.

Table A.14: Self-diffusion coefficients of pure components ACN, EtOH and PrOH at T = 301.65 K. Comparison of the results measured by different methods (HF high-field, BT benchtop; PFGSTE standard experiment, PENPFG experiment with polarization transfer). The RMSE is given in parantheses and refers to the last digit.

| | $D_i \cdot 10^{-9}$ / m^2 s^{-1} | | | | |
	^{1}H HF PFGSTE	^{13}C HF PFGSTE	^{13}C HF PENPFG	^{1}H BT PFGSTE	^{13}C BT PENPFG
ACN	4.489 (1)	4.473 (61)	4.557 (2)	4.485 (10)	4.416 (22)
EtOH	1.129 (1)	1.123 (35)	1.126 (2)	1.111 (1)	1.165 (5)
PrOH	0.639 (1)	0.642 (5)	0.647 (3)	0.629 (1)	0.650 (12)

In Figure A.16 the RMSEs of the three repetitions by different NMR techniques are shown as error bars. Furthermore, in Figure A.16 the mean error of the Stejskal-Tanner fit is illustrated. It can be seen that both errors are very small which proves the repeatability of all methods.
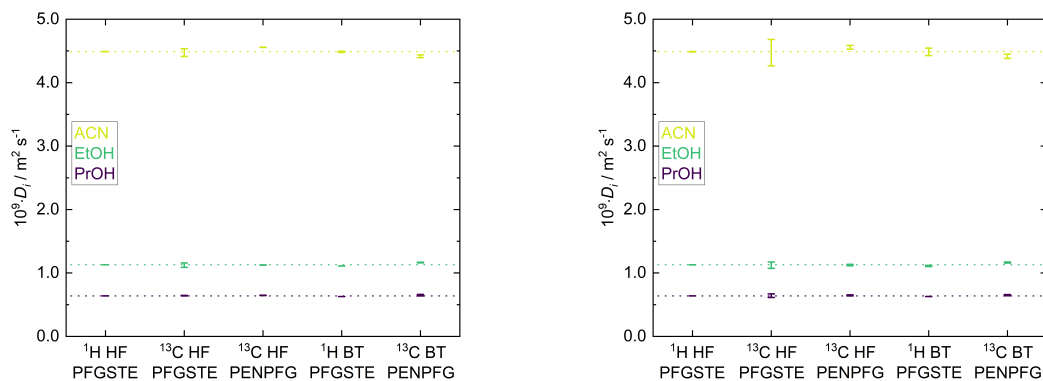
Figure A.16: Comparison of the results of the pure components ACN, EtOH and PrOH at T = 301.65 K measured by different methods (HF high-field, BT benchtop; PFGSTE standard experiment, PENPFG experiment with polarization transfer). Left: The RMSE of three repetitions are depicted as error bars. The dashed horizontal lines represent the reference measurement with ^{1}H HF PFGSTE. Right: The mean errors of the fitting procedure to the Stejskal-Tanner equation are depicted as error bars. The dashed horizontal lines represent the reference measurement with ^{1}H HF PFGSTE.

C.2.2 Binary Mixtures

Table A.15, A.16 and A.17 display self-diffusion coefficients of ACN, EtOH and PrOH in the three binary mixtures measured with ^{1}H HF PFGSTE as well as with ^{13}C BT PENPFG. The calculated RMSE is additionally given. In each experiment, only the signal of the CH$_3$-group of the specific molecules were used for the determination of self-diffusion coefficients. The self-diffusion coefficients obtained with ^{1}H HF PFGSTE are considered as the ground truth in this work and are used to evaluate the results of ^{13}C BT PENPFG.

Table A.15: Self-diffusion coefficients of ACN and EtOH in binary mixtures of ACN + EtOH at T = 301.65 K. Comparison of the results measured by different methods (HF high-field, BT benchtop; PFGSTE standard experiment, PENPFG experiment with polarization transfer). The RMSE is given in parentheses and refers to the last digit.

| x_{ACN} | ^{1}H HF PFGSTE | | ^{13}C BT PENPFG | |
| | D_{ACN} | D_{EtOH} | D_{ACN} | D_{EtOH} |
/ mol mol^{-1}	$\cdot 10^{-9}$ / m^2 s^{-1}		$\cdot 10^{-9}$ / m^2 s^{-1}	
1	4.489 (1)		4.416 (22)	
0.75	4.241 (1)	3.419 (1)	4.166 (42)	3.441 (58)
0.5	3.719 (1)	2.598 (1)	3.593 (29)	2.610 (50)
0.25	3.037 (3)	1.834 (1)	3.153 (222)	1.876 (16)

Table A.16: Self-diffusion coefficients of EtOH and PrOH in binary mixtures of EtOH + PrOH at T = 301.65 K. Comparison of the results measured by different methods (HF high-field, BT benchtop; PFGSTE standard experiment, PENPFG experiment with polarization transfer). The RMSE is given in parentheses and refers to the last digit.

| x_{EtOH} | ^{1}H HF PFGSTE | | ^{13}C BT PENPFG | |
| | D_{EtOH} | D_{PrOH} | D_{EtOH} | D_{PrOH} |
/ mol mol^{-1}	$\cdot 10^{-9}$ / m^2 s^{-1}		$\cdot 10^{-9}$ / m^2 s^{-1}	
1	1.129 (1)		1.165 (5)	
0.75	1.027 (1)	0.946 (1)	1.049 (12)	0.930 (8)
0.5	0.895 (1)	0.827 (1)	0.944 (35)	0.858 (8)
0.25	0.792 (1)	0.730 (1)	0.839 (19)	0.742 (8)

Table A.17: Self-diffusion coefficients of ACN and PrOH in binary mixtures of ACN + PrOH at T = 301.65 K. Comparison of the results measured by different methods (HF high-field, BT benchtop; PFGSTE standard experiment, PENPFG experiment with polarization transfer). The RMSE is given in parentheses and refers to the last digit.

| x_{PrOH} / mol mol^{-1}	¹H HF PFGSTE		¹³C BT PENPFG	
	D_{ACN}	D_{PrOH}	D_{ACN}	D_{PrOH}
	$\cdot 10^{-9}$ / m² s^{-1}		$\cdot 10^{-9}$ / m² s^{-1}	
1		0.639 (1)		0.650 (12)
0.75	2.338 (2)	1.239 (1)	2.228 (39)	1.253 (7)
0.5	3.080 (9)	1.862 (1)	3.018 (54)	1.861 (11)
0.25	3.888 (1)	2.758 (2)	3.842 (35)	2.744 (41)

C.2.3 Ternary Mixtures

Table A.18 displays self-diffusion coefficients of ACN, EtOH and PrOH of the seven investigated ternary mixtures measured with ¹H HF PFGSTE as well as with ¹³C BT PENPFG. The calculated RMSE is additionally given. In each experiment, only the signal of the CH₃-group of the specific molecules were used for the determination of self-diffusion coefficients. The self-diffusion coefficients obtained with ¹H HF PFGSTE are considered as the ground truth in this work and are used to evaluate the results of ¹³C BT PENPFG.

Figure A.17 summarizes all self-diffusion coefficients of the pure components ACN, EtOH and PrOH as well as the obtained values in the binary and ternary mixtures determined with ¹³C BT PENPFG in this work. The self-diffusion coefficients range from about $0.7 \cdot 10^{-9}$ m² s^{-1} (PrOH) to $4.4 \cdot 10^{-9}$ m² s^{-1} (ACN). It can be observed that the self-diffusion coefficients of ACN are the highest in all mixtures whereas PrOH is the slowest diffusing component in all mixtures. The self-diffusion coefficients of the specific molecules increase gradually as more of the fast diffusing component is added to the mixture.

Table A.18: Self-diffusion coefficients of ACN, EtOH and PrOH in ternary mixtures at T = 301.65 K. Comparison of the results measured by different methods (HF high-field, BT benchtop; PFGSTE standard experiment, PENPFG experiment with polarization transfer). The RMSE is given in parentheses and refers to the last digit.

Composition		^{1}H HF PFGSTE			^{13}C BT PENPFG		
x_{ACN}	x_{EtOH}	D_{ACN}	D_{EtOH}	D_{PrOH}	D_{ACN}	D_{EtOH}	D_{PrOH}
/ mol mol^{-1}		$\cdot 10^{-9}$ / m^2 s^{-1}			$\cdot 10^{-9}$ / m^2 s^{-1}		
0.333	0.333	2.852 (3)	1.753 (1)	1.601 (1)	2.807 (37)	1.795 (50)	1.662 (36)
0.33	0.165	2.776 (10)	1.701 (1)	1.551 (2)	2.667 (48)	1.665 (66)	1.544 (9)
0.33	0.505	3.094 (1)	1.923 (1)	1.758 (1)	3.024 (93)	1.984 (15	1.771 (33)
0.165	0.33	2.284 (13)	1.267 (1)	1.163 (1)	2.185 (41)	1.308 (27)	1.184 (8)
0.505	0.33	3.535 (4)	2.423 (1)	2.203 (3)	3.460 (24)	2.565 (11)	2.243 (3)
0.505	0.165	3.302 (2)	2.227 (1)	2.022 (1)	3.274 (34)	2.279 (25)	2.079 (14)
0.165	0.505	2.496 (15)	1.373 (1)	1.259 (2)	2.353 (46)	1.445 (10)	1.329 (13)
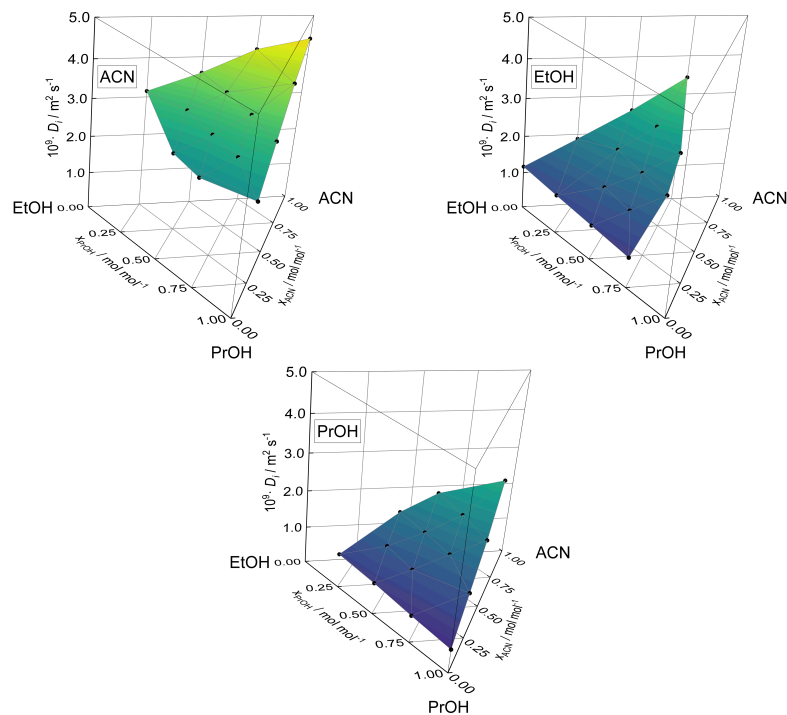
Figure A.17: Overview of all self-diffusion coefficients of the pure components ACN, EtOH and PrOH as well as in the binary and ternary mixtures at T = 301.65 K measured with ^{13}C BT PENPFG.

Table A.19 displays self-diffusion coefficients of ACN, EtOH and PrOH, which are obtained from the analysis of individual peaks of the ^{13}C benchtop NMR spectrum of the equimolar ternary system ACN + EtOH + PrOH. Again, the self-diffusion coefficients were measured with ^{1}H HF PFGSTE as well as with ^{13}C BT PENPFG. The calculated RMSE is additionally given. For ^{1}H HF PFGSTE, only the signal of the CH$_3$-group of the specific molecules were used for the determination of self-diffusion coefficients. The self-diffusion coefficients obtained with ^{1}H HF PFGSTE are considered as the ground truth in this work and are used to evaluate the results of ^{13}C BT PENPFG.

Table A.19: Self-diffusion coefficients of of an equimolar mixture ACN + EtOH + PrOH at T = 301.65 K. Comparison of the results measured by different methods (HF high-field, BT benchtop; PENPFG experiment with polarization transfer). The RMSE is given in parentheses and refers to the last digit.

	$D_i^{^{13}\text{C HF PENPFG}} \cdot 10^{-9}$ / m^2 s^{-1}			$D_i^{^{13}\text{C BT PENPFG}} \cdot 10^{-9}$ / m^2 s^{-1}		
	CH$_3$-Peak	CH$_2$-Peak	CH$_2$-Peak	CH$_3$-Peak	CH$_2$-Peak	CH$_2$-Peak
ACN	2.900 (24)			2.807 (37)		
EtOH	1.751 (27)	1.763 (25)		1.795 (50)	1.765 (36)	
PrOH	1.608 (46)	1.585 (18)	1.623 (47)	1.662 (36)	1.647 (18)	1.572 (20)

D Supporting Information for Chapter 5

D.1 Experimental Section

Figure A.18 illustrates the used pulse sequence PENDANT for the polarization transfer from ^{1}H to the ^{13}C nuclei. The applied evolution delays are given in Equation (28) and (29).
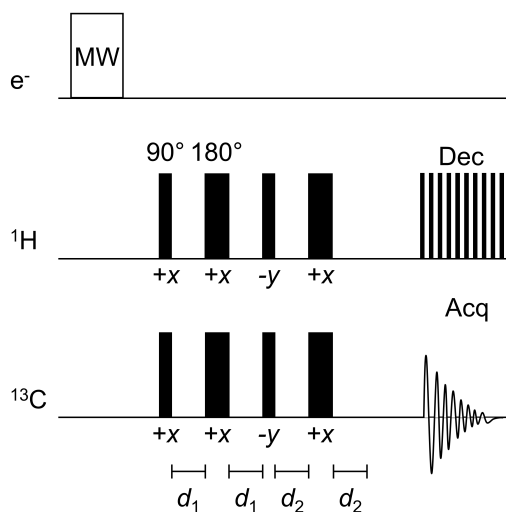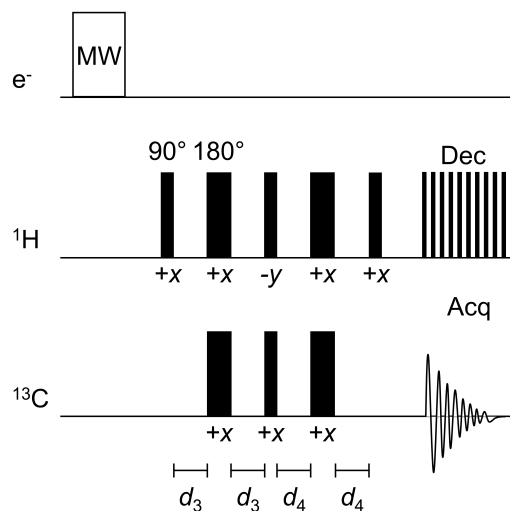

Figure A.18: Illustration of the used polarization transfer pulse sequence PENDANT.

$$d_1 = \frac{1}{4\,^1J_{\mathrm{C,H}}} \tag{28}$$

$$d_2 = \frac{5}{8\,^1J_{\mathrm{C,H}}} \tag{29}$$

Figure A.19 displays the pulse sequence refocused INEPT$^+$ also for the polarization transfer from ^{1}H to the ^{13}C nuclei. The applied evolution delays are given in Equation (30) and (31).

Figure A.19: Illustration of the used polarization transfer pulse sequence INEPT.

$$d_3 = \frac{1}{4\,^1J_{\mathrm{C,H}}} \tag{30}$$

$$d_4 = \frac{1}{6\,^1J_{\mathrm{C,H}}} \tag{31}$$

The error as well as the error bars of the signal enhancements are calculated with an error propagation which is given in Equation 32. For the estimation of ΔI_{ODNP} and $\Delta I_{\mathrm{thermal}}$ the specific standard uncertainty of three experiments is applied.

$$\Delta E = \left|\left(\frac{\sqrt{n_{\mathrm{thermal}}}}{\sqrt{n_{\mathrm{ODNP}}}} \cdot \frac{1}{I_{\mathrm{thermal,\,scaled}}}\right)\right| \cdot \Delta I_{\mathrm{ODNP}} + \left|\left(-\frac{\sqrt{n_{\mathrm{thermal}}}}{\sqrt{n_{\mathrm{ODNP}}}} \cdot \frac{I_{\mathrm{ODNP}}}{I^2_{\mathrm{thermal,\,scaled}}}\right)\right| \cdot \Delta I_{\mathrm{thermal}} \tag{32}$$

D.2 Results and Discussion

D.2.1 Characterization of the Flow Cell

In a step experiment in which a fluid in the detection cell was replaced by another the fluid dynamic within the flow cell was characterized. For this study, the flow cell, which was exactly positioned in the benchtop NMR spectrometer as in the later ODNP experiments, was filled with ACN in the first step. ACN was replaced by water (W) after activating the pump and, hence, the flow ($\dot{V}$ = 2.0 ml min^{-1} corresponding to v = 0.68 m s^{-1}). The change of the composition in the flow cell was monitored by ^{1}H NMR experiments (1 scan every 5 s, 90° excitation pulse, 1.6 s acquisition time, 8192 data points) for 400 s. The experiment was performed three times. Figure A.20 illustrates the result of the tracer experiment and displays the relative signal change of W (S_W) in dependence of the relative time (Θ). The definition for Θ is given in Equation 33. Here, t denotes the experimental time and t_total the total experimental time of the step experiment, which was t_total = 395 s.

The signal of W increases during the time as W is replacing ACN in the flow cell. A large deviation from an ideal flow cell without any back-mixing effect (ACN is instantly replaced by W) is observed. This results in a detection of a mixture of ODNP hyperpolarized and thermally polarized molecules which underestimates the calculated signal enhancements.

$$\Theta = \frac{t}{t_\text{total}} \tag{33}$$
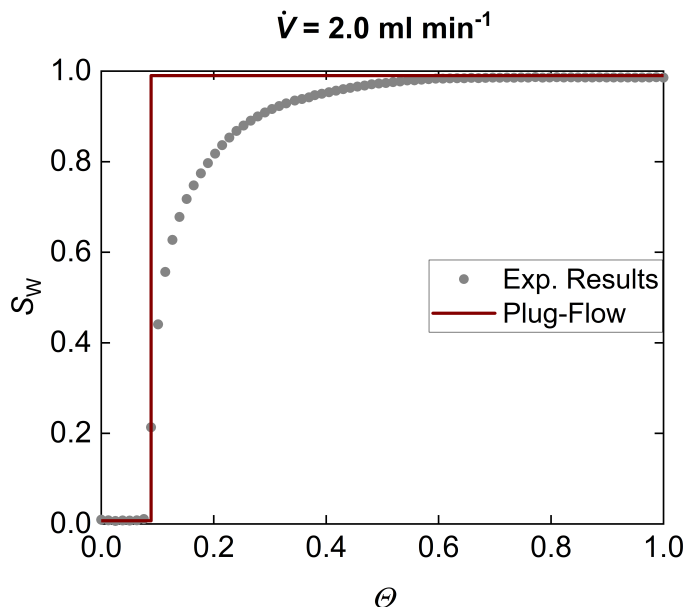
Figure A.20: The cell was initially filled with ACN which was then replaced by W
for the fluid dynamic characterisation of the flow cell at a flow rate of
$\dot{V}$ = 2.0 ml min^{-1} (corresponding to a flow velocity of v = 0.68 m s^{-1}).
The relative signal of W (S_W) is obtained by ^{1}H NMR experiments in
dependence of the relative time Θ. For comparison the signal of an ideal
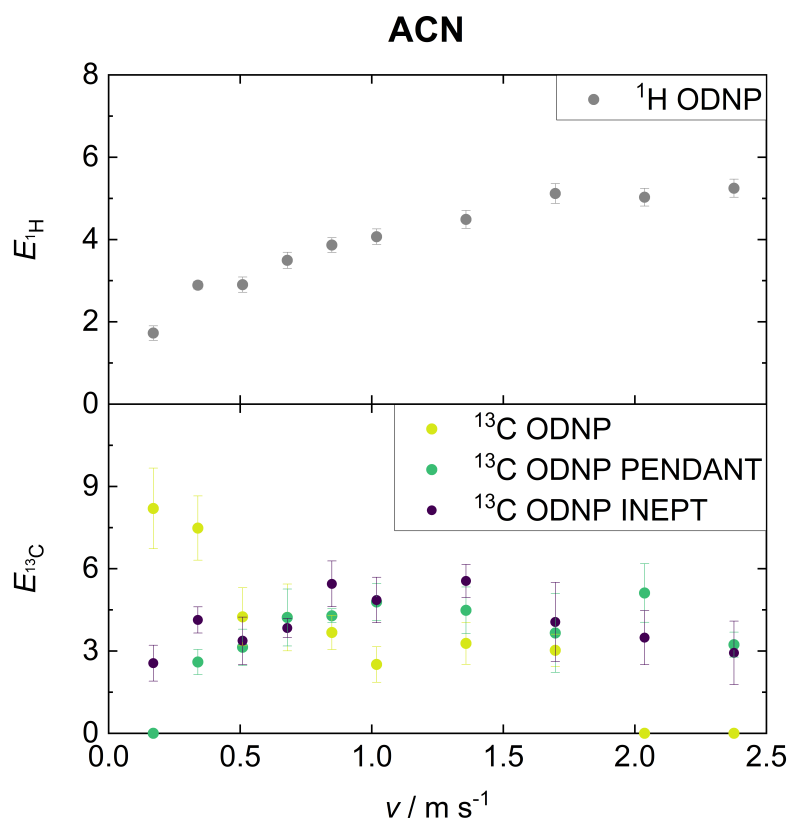plug-flow is given.

D.2.2 ODNP Experiments with ACN

Table A.20 displays the signal integrals and the signal enhancements of ACN acquired
with ^{1}H ODNP, ^{13}C ODNP, ^{13}C ODNP PENDANT, and ^{13}C ODNP INEPT at different
flow velocities. Note that the integral of the Boltzmann thermal equilibrium experiment,
which is used for the calculation of the signal enhancement of all ^{13}C ODNP experi-
ments, was obtained without any flow and with 256 scans. The signal enhancements
are additionally visualized in Figure A.21.

Table A.20: Numerical results of the ODNP experiments with ACN (C1) at different flow velocities. The scaled integral of the Boltzmann thermal equilibrium experiment ($I_{\text{thermal, scaled}}$) as well as of the signals of the ODNP experiments ^{1}H ODNP, ^{13}C ODNP, ^{13}C ODNP PENDANT, and ^{13}C ODNP INEPT ($I_{\text{ODNP, scaled}}$) are given. Errors are calculated from three repetitions using standard uncertainty. The signal enhancement E is provided as well as the result of the error propagation.

v	^{1}H ODNP			^{13}C ODNP		
	$I_{\text{thermal, scaled}}$	$I_{\text{ODNP, scaled}}$	E	$I_{\text{thermal, scaled}}$	$I_{\text{ODNP, scaled}}$	E
/ m s^{-1}	/ a.u.	/ a.u.		/ a.u.	/ a.u.	
0.17	6.5±0.1	11.2±1.0	1.7±0.2		13.8±1.9	8.2±1.5
0.34	7.1±0.1	20.7±0.6	2.9±0.1		12.6±1.5	7.5±1.2
0.51	7.4±0.1	21.4±1.1	2.9±0.2		7.1±1.5	4.2±1.1
0.68	7.5±0.1	26.1±1.4	3.5±0.2		7.1±1.8	4.2±1.2
0.85	7.2±0.1	27.9±1.1	3.9±0.2	1.7±0.1	6.2±0.8	3.7±0.6
1.02	6.9±0.1	28.2±1.0	4.1±0.2		4.2±0.9	2.5±0.6
1.36	6.2±0.1	27.9±1.1	4.5±0.2		5.5±1.1	3.3±0.8
1.70	5.7±0.1	29.3±1.2	5.1±0.2		5.1±0.8	3.0±0.6
2.04	5.2±0.1	26.2±0.9	5.0±0.2		0	0
2.38	5.0±0.1	26.5±0.9	5.2±0.2		0	0

v / m s^{-1}	^{13}C ODNP PENDANT			^{13}C ODNP INEPT		
	$I_{\text{thermal, scaled}}$ / a.u.	$I_{\text{ODNP, scaled}}$ / a.u.	E	$I_{\text{thermal, scaled}}$ / a.u.	$I_{\text{ODNP, scaled}}$ / a.u.	E
0.17		0	0		4.3±0.9	2.6±0.7
0.34		4.4±0.6	2.6±0.5		6.9±0.5	4.1±0.5
0.51		5.3±0.9	3.1±0.7		5.7±1.2	3.4±0.9
0.68		7.1±1.5	4.2±1.0		6.4±0.3	3.8±0.3
0.85	1.7±0.1	7.2±0.1	4.3±0.3	1.7±0.1	9.2±1.0	5.4±0.8
1.02		8.0±0.8	4.8±0.7		8.2±1.1	4.9±0.8
1.36		7.5±1.1	4.5±0.8		9.3±0.6	5.6±0.6
1.70		6.1±2.2	3.7±1.4		6.8±2.1	4.1±1.4
2.04		8.6±1.4	5.1±1.1		5.9±1.4	3.5±1.0
2.38		5.4±0.5	3.2±0.5		4.9±1.7	2.9±1.2

Figure A.21: Signal enhancements of ACN (C1) obtained by ^{1}H ODNP, ^{13}C ODNP, ^{13}C ODNP PENDANT, and ^{13}C ODNP INEPT at different flow velocities.
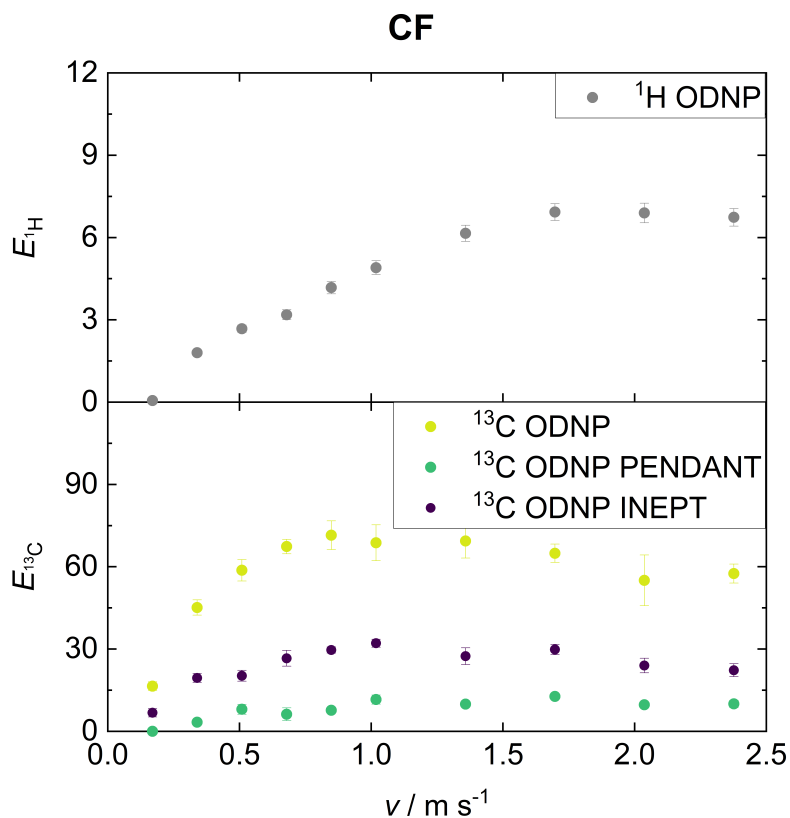
D.2.3 ODNP Experiments with CF

Table A.21 displays the signal integrals and the signal enhancements of CF acquired with ^{1}H ODNP, ^{13}C ODNP, ^{13}C ODNP PENDANT, and ^{13}C ODNP INEPT at different flow velocities. Note that the integral of the Boltzmann thermal equilibrium experiment, which is used for the calculation of the signal enhancement of all ^{13}C ODNP experiments, was obtained without any flow and with 256 scans. The signal enhancements are additionally visualized in Figure A.22.

Table A.21: Numerical results of the ODNP experiments with CF (C1) at different flow velocities. The scaled integral of the Boltzmann thermal equilibrium experiment ($I_{\text{thermal, scaled}}$) as well as of the signals of the ODNP experiments ^{1}H ODNP, ^{13}C ODNP, ^{13}C ODNP PENDANT, and ^{13}C ODNP INEPT ($I_{\text{ODNP, scaled}}$) are given. Errors are calculated from three repetitions using standard uncertainty. The signal enhancement E is provided as well as the result of the error propagation.

v	^{1}H ODNP			^{13}C ODNP		
	$I_{\text{thermal, scaled}}$	$I_{\text{ODNP, scaled}}$	E	$I_{\text{thermal, scaled}}$	$I_{\text{ODNP, scaled}}$	E
/ m s^{-1}	/ a.u.	/ a.u.		/ a.u.	/ a.u.	
0.17	2.1±0.1	0.1±0.1	0.1±0.1		17.8±1.2	16.5±1.6
0.34	2.1±0.1	3.7±0.2	1.8±0.1		48.7±1.7	45.1±2.8
0.51	2.2±0.1	6.0±0.2	2.7±0.1		63.4±2.5	58.7±3.9
0.68	2.2±0.1	7.0±0.3	3.2±0.2		72.7±0.9	67.3±2.6
0.85	2.1±0.1	9.0±0.4	4.2±0.2	1.1±0.1	77.2±3.6	71.5±5.2
1.02	2.1±0.1	10.4±0.4	4.9±0.3		74.2±5.1	68.7±6.5
1.36	2.0±0.1	12.4±0.5	6.2±0.3		74.9±4.7	69.4±6.2
1.70	1.9±0.1	13.5±0.5	7.0±0.3		70.1±1.8	64.9±3.3
2.04	1.9±0.1	13.1±0.6	6.9±0.4		59.4±8.4	55.0±9.3
2.38	1.8±0.1	12.3±0.4	6.7±0.3		62.1±2.1	57.5±3.5

v / m s^{-1}	^{13}C ODNP PENDANT			^{13}C ODNP INEPT		
	$I_{\text{thermal, scaled}}$ / a.u.	$I_{\text{ODNP, scaled}}$ / a.u.	E	$I_{\text{thermal, scaled}}$ / a.u.	$I_{\text{ODNP, scaled}}$ / a.u.	E
0.17		0	0		7.3±1.4	6.8±1.5
0.34		3.6±0.2	3.3±0.3		21.0±1.2	19.5±1.6
0.51		8.7±1.7	8.0±1.8		21.9±1.6	20.3±2.0
0.68		6.7±2.4	6.2±2.3		28.7±2.4	26.6±2.9
0.85	1.1±0.1	8.3±0.5	7.6±0.6	1.1±0.1	32.0±0.3	29.6±1.1
1.02		12.5±1.4	11.6±1.6		34.7±0.7	32.1±1.5
1.36		10.7±0.5	9.9±0.7		29.6±2.5	27.4±3.0
1.70		13.8±0.6	12.7±0.9		32.2±1.2	29.8±1.9
2.04		10.4±0.6	9.7±0.8		25.9±2.2	24.0±2.7
2.38		10.8±1.2	10.0±1.3		24.0±1.9	22.3±2.4

Figure A.22: Signal enhancements of CF (C1) obtained by ¹H ODNP, ¹³C ODNP, ¹³C ODNP PENDANT, and ¹³C ODNP INEPT at different flow velocities.
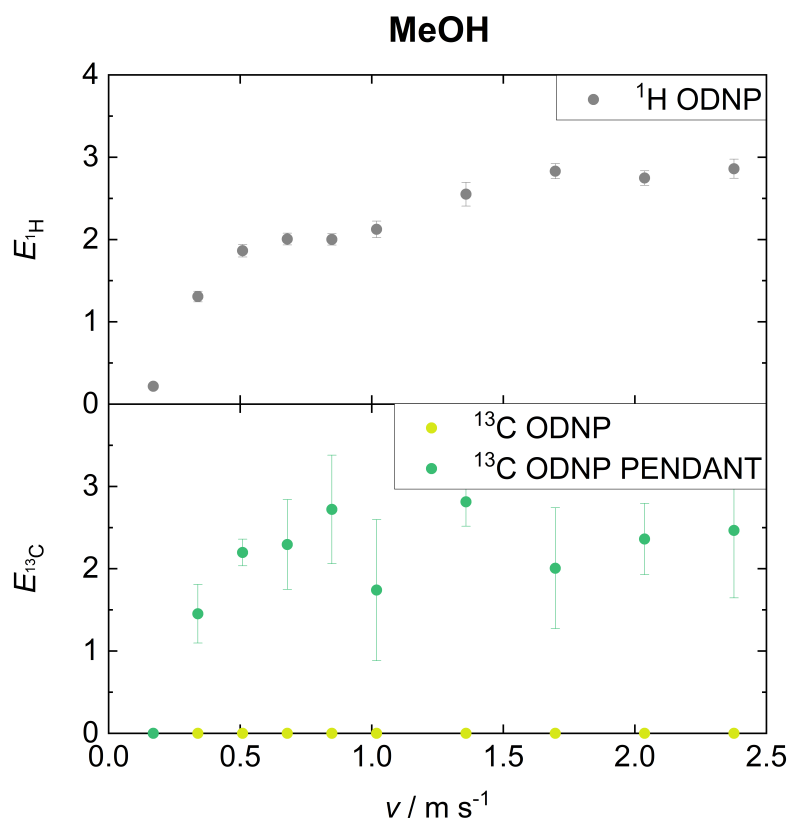
D.2.4 ODNP Experiments with MeOH

Table A.22 displays the signal integrals and the signal enhancements of MeOH acquired with ¹H ODNP, ¹³C ODNP, and ¹³C ODNP PENDANT at different flow velocities. Note that the integral of the Boltzmann thermal equilibrium experiment, which is used for the calculation of the signal enhancement of all ¹³C ODNP experiments, was obtained without any flow and with 256 scans.

Table A.22: Numerical results of the ODNP experiments with MeOH (C1) at different flow velocities. The scaled integral of the Boltzmann thermal equilibrium experiment ($I_{\text{thermal, scaled}}$) as well as of the signals of the ODNP experiments ^{1}H ODNP, ^{13}C ODNP, and ^{13}C ODNP PENDANT ($I_{\text{ODNP, scaled}}$) are given. Errors are calculated from three repetitions using standard uncertainty. The signal enhancement E is provided as well as the result of the error propagation.

v	^{1}H ODNP			^{13}C ODNP		
	$I_{\text{thermal, scaled}}$	$I_{\text{ODNP, scaled}}$	E	$I_{\text{thermal, scaled}}$	$I_{\text{ODNP, scaled}}$	E
/ m s^{-1}	/ a.u.	/ a.u.		/ a.u.	/ a.u.	
0.17	14.6±0.3	3.2±0.3	0.2±0.1		0	0
0.34	13.7±0.3	17.9±0.5	1.3±0.1		0	0
0.51	14.1±0.2	26.2±0.7	1.9±0.1		0	0
0.68	14.6±0.1	29.3±0.8	2.0±0.1		0	0
0.85	15.4±0.1	30.9±0.8	2.0±0.1		0	0
1.02	14.8±0.1	31.4±1.4	2.1±0.1	2.2±0.1	0	0
1.36	13.9±0.2	35.4±1.6	2.6±0.1		0	0
1.70	12.7±0.1	35.9±1.0	2.8±0.1		0	0
2.04	11.8±0.1	32.4±0.8	2.8±0.1		0	0
2.38	11.2±0.1	32.1±1.0	2.9±0.1		0	0

| v | ^{13}C DNP PENDANT | | |
| | $I_{\text{thermal, scaled}}$ | $I_{\text{ODNP, scaled}}$ | E |
/ m s^{-1}	/ a.u.	/ a.u.	
0.17		0	0
0.34		3.3±0.7	1.5±0.4
0.51		4.9±0.2	2.2±0.2
0.68		5.2±1.1	2.3±0.5
0.85	2.2±0.1	6.1±1.3	2.7±0.7
1.02		3.9±1.8	1.7±0.9
1.36		6.3±0.5	2.8±0.3
1.70		4.5±1.5	2.0±0.7
2.04		5.3±0.8	2.4±0.4
2.38		5.5±1.7	2.5±0.8

Figure A.23: Signal enhancements of MeOH (C1) obtained by ^{1}H ODNP, ^{13}C ODNP, and ^{13}C ODNP PENDANT at different flow velocities.

D.2.5 ODNP Experiments with ACN + CF

Table A.23 displays the signal integrals and the signal enhancements of ACN and CF in the binary mixture (x_{ACN} = 0.75 mol mol^{-1}) acquired with ^{1}H ODNP, ^{13}C ODNP, and ^{13}C ODNP PENDANT at different flow velocities. Note that the integral of the Boltzmann thermal equilibrium experiment, which is used for the calculation of the signal enhancement of all ^{13}C ODNP experiments, was obtained without any flow and with 256 scans. The signal enhancements are additionally visualized in Figure A.24.

Table A.23: Numerical results of the ODNP experiments with the binary mixture of ACN and CF (x_{ACN} = 0.75 mol mol^{-1}, C1 for both molecules) at different flow velocities. The scaled signals of the integral of the Boltzmann thermal equilibrium experiment ($I_{\mathrm{thermal,\,scaled}}$) as well as of the ODNP experiments ^{1}H ODNP, ^{13}C ODNP, and ^{13}C ODNP PENDANT ($I_{\mathrm{ODNP,\,scaled}}$) are given. Errors are calculated from three repetitions using standard uncertainty. The signal enhancement E is provided as well as the result of the error propagation.

	ACN					
	^{1}H ODNP			^{13}C ODNP		
v	$I_{\mathrm{thermal,\,scaled}}$	$I_{\mathrm{ODNP,\,scaled}}$	E	$I_{\mathrm{thermal,\,scaled}}$	$I_{\mathrm{ODNP,\,scaled}}$	E
/ m s^{-1}	/ a.u.	/ a.u.		/ a.u.	/ a.u.	
0.17	4.4±0.1	3.2±0.1	0.7±0.1		9.6±0.6	11.5±0.9
0.34	4.6±0.1	8.1±0.1	1.8±0.1		7.3±0.3	8.8±0.6
0.51	4.4±0.1	9.3±0.1	2.1±0.1		5.6±0.4	6.8±0.7
0.68	4.5±0.1	12.0±0.1	2.7±0.1		5.4±1.1	6.5±1.5
0.85	4.7±0.1	14.4±0.1	3.0±0.1	0.8±0.1	4.5±0.7	5.4±1.0
1.02	4.3±0.1	13.8±0.1	3.2±0.1		2.5±0.3	3.1±0.5
1.36	4.2±0.1	13.9±0.1	3.3±0.1		3.4±0.3	4.1±0.5
1.70	3.8±0.1	14.0±0.1	3.6±0.1		0	0
2.04	3.5±0.1	13.9±0.1	4.0±0.1		0	0
2.38	3.4±0.1	13.4±0.1	3.9±0.1		0	0

	ACN		
	^{13}C ODNP PENDANT		
v	$I_{\text{thermal, scaled}}$	$I_{\text{ODNP, scaled}}$	E
/ m s^{-1}	/ a.u.	/ a.u.	
0.17		0	0
0.34		0	0
0.51		2.2±0.6	2.6±0.7
0.68		3.6±0.5	4.3±0.7
0.85	0.8±0.1	3.9±0.7	4.6±1.0
1.02		3.3±1.3	3.9±1.6
1.36		3.4±0.9	4.1±1.1
1.70		3.7±0.9	4.5±1.2
2.04		3.6±1.1	4.3±1.5
2.38		0	0

	CF					
	^{1}H ODNP			^{13}C ODNP		
v	$I_{\text{thermal, scaled}}$	$I_{\text{ODNP, scaled}}$	E	$I_{\text{thermal, scaled}}$	$I_{\text{ODNP, scaled}}$	E
/ m s^{-1}	/ a.u.	/ a.u.		/ a.u.	/ a.u.	
0.17	0.4±0.1	0.4±0.1	1.2±0.2		3.8±0.7	8.2±1.7
0.34	0.4±0.1	0.9±0.1	2.1±0.1		9.4±0.7	20.0±1.9
0.51	0.4±0.1	1.0±0.1	2.4±0.2		13.2±0.8	27.9±2.2
0.68	0.4±0.1	1.3±0.1	3.1±0.2		13.9±1.1	29.2±2.8
0.85	0.5±0.1	1.8±0.1	3.5±0.2	0.5±0.1	13.6±0.8	28.7±2.2
1.02	0.5±0.1	1.7±0.1	3.8±0.3		13.2±0.2	27.7±1.0
1.36	0.5±0.1	2.0±0.1	4.0±0.3		15.0±0.9	31.5±2.5
1.70	0.4±0.1	1.9±0.1	4.4±0.3		12.1±1.9	25.5±4.4
2.04	0.5±0.1	2.3±0.2	4.7±0.3		8.5±0.6	17.9±1.6
2.38	0.4±0.1	1.7±0.1	4.8±0.4		10.7±1.4	22.6±3.3

	CF		
		^{13}C ODNP PENDANT	
v	$I_{\text{thermal, scaled}}$	$I_{\text{ODNP, scaled}}$	E
/ m s^{-1}	/ a.u.	/ a.u.	
0.17		0	0
0.34		6.3±1.0	13.2±2.4
0.51		5.8±2.0	12.2±4.5
0.68		7.1±0.7	14.9±1.7
0.85	0.5±0.1	5.7±1.2	12.0±2.8
1.02		6.4±1.2	13.5±2.8
1.36		6.1±0.6	12.9±1.6
1.70		7.1±0.4	15.0±1.1
2.04		5.1±0.5	10.7±1.3
2.38		0	0
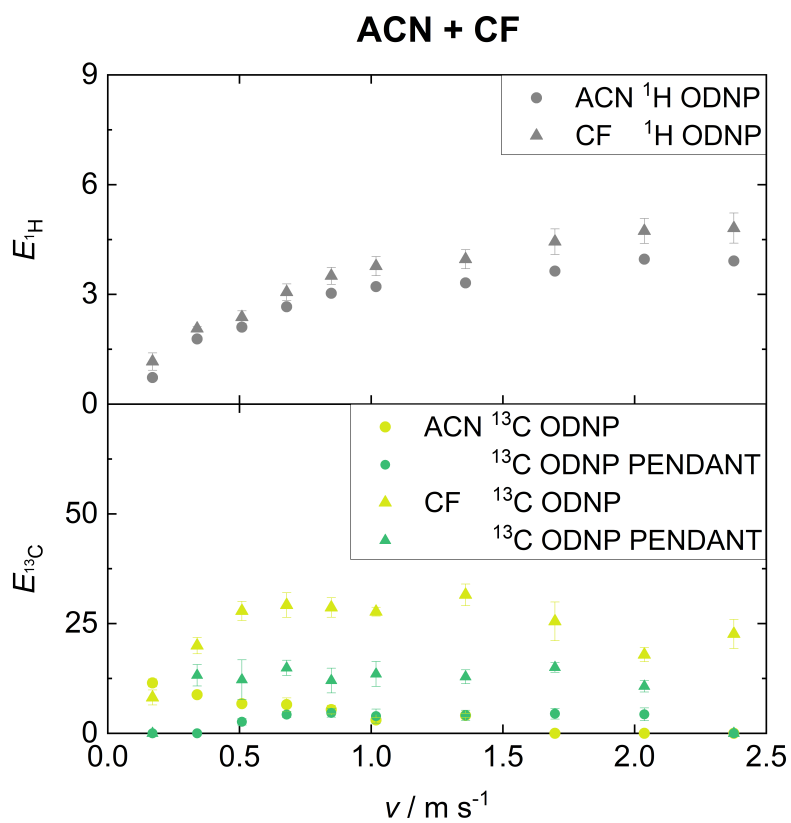
Figure A.24: Signal enhancements of ACN and CF (C1 for both molecules) in a binary mixture (x_{ACN} = 0.75 mol mol^{-1}) obtained by ^{1}H ODNP, ^{13}C ODNP, and ^{13}C ODNP PENDANT at different flow velocities.

E Supporting Information for Chapter 6

E.1 Experimental Section

E.1.1 Chemicals and Materials

Table A.24 summarizes the chemicals which were used in this work without further purification. In addition, ultrapure water (W) was provided by Starpure's OmniaPure UV/UF-TOC water treatment system with a resistivity of 18.2 MΩ cm.

Table A.24: Chemicals used in this work including the suppliers and the purities as specified by the suppliers.

Chemical	Supplier	Purity
Acetonitrile	Carl Roth	≥ 99.9%
Chloroform	Merck	≥ 99.0%
1,4-Dioxane	Sigma Aldrich	≥ 99.8%

The immobilized radical matrix used in this work was made of nitroxide radicals glycidyloxy-tetramethylpiperidinyloxyl immobilized via a polyethylene-imine-linker (molecular mass 25,000 g mol-1) on aminopropyl-functionalized controlled porous glasses (CPG) with a pore size of 50 nm.

E.1.2 Experimental Setup

The liquid sample mixture was taken from a storage vessel (volume V = 100 ml) at ambient pressure and temperature. A double piston high pressure pump with damping piston (WADose Plus HP, Flusys, accuracy: < 3 %), which was calibrated for a flow range of 0.5 to 10 ml min^{-1}, was used for the transport of the sample. The pressure

increase by the pump was between 1 and 40 bar indicated by the pressure gauge integrated in the pump (accuracy: 0.5 %). The probe for ODNP hyperpolarization (Bruker BioSpin EN 4148X-MD4 electron nuclear double resonance ENDOR probe) was not thermostated; it was connected to the MW source (details of the hardware are given in Kircher et al. [206]. The paramagnetic fixed bed was mounted in a PEEK tube (inner diameter 1.0 mm) and was installed inside the ODNP probe filling its 4 mm cavity resonator. For System 3, the 2.9 mm detection cell was positioned inside the benchtop NMR spectrometer so that the sensitive region of the NMR coil was located close to the expansion from 0.25 to 2.9 mm to minimize hyperpolarization losses by T_1 relaxation. A detailed description of the fluid characteristics of this setup is given in Phuong et al. (Zitat Phuong et al. 2024).

E.1.3 Experimental Procedure and Calculation of the Signal Enhancements

All NMR experiments were controlled by the Spinsolve Expert software (Magritek). ^{1}H NMR ODNP experiments were performed with an acquisition time of 0.4 s, 2048 data points, 1 scan, and a 90° excitation pulse. ^{13}C NMR ODNP experiments were performed with an acquisition time of 1.6 s, 16 k data points, 1 scan and a 90° excitation pulse; an inverse-gated decoupling sequence (WALTZ-16) was applied during acquisition. To calculate the achieved ^{1}H ODNP signal enhancements ($E_i^{^1\text{H}}$), ^{1}H NMR experiments with the same acquisition parameters were performed under the same flow conditions. For the ^{13}C ODNP signal enhancements ($E_i^{^{13}\text{C}}$), the results of the ^{13}C NMR ODNP experiment were referenced to the ^{13}C NMR experiments which were acquired with the same acquisition parameters but with 256 scans in the absence of flow as the premagnetization is not sufficient for a detection of flowing samples. Manual correction of baseline, phase and peak integration was performed in MestReNova (Mestrelab Research).

For the calculation of the signal enhancement E of the ODNP experiments, the spectra were scaled to the same noise level. The signal and the noise of the thermally polarized NMR spectra as well as of the NMR spectra with ODNP enhancement were divided by the square root of the number of accumulated scans. The calculation of the signal enhancement is given in Equation (34):

$$E = \frac{I^{\text{ODNP, scaled}}}{I^{\text{thermal, scaled}}} \cdot \frac{\sqrt{n^{\text{thermal}}}}{\sqrt{n^{\text{ODNP}}}} \tag{34}$$

Here, $I^{\text{ODNP, scaled}}$ denotes the integral of the scaled signal obtained with ODNP enhancement, $I^{\text{thermal, scaled}}$ the integral of the scaled thermally polarized signal, and n the

number of scans. Note that a correction for the receiver gain is not necessary since this parameter was kept constant in within the respective ^{1}H and ^{13}C experiments.

The error of the signal enhancements are calculated with an error propagation which is given in Equation (35). For the estimation of ΔI^{ODNP} and $\Delta I^{\text{thermal}}$ the specific standard uncertainty of the experiments is applied.

$$\Delta E = \left| \left(\frac{\sqrt{n^{\text{thermal}}}}{\sqrt{n^{\text{ODNP}}}} \cdot \frac{1}{I^{\text{thermal, scaled}}} \right) \right| \cdot \Delta I^{\text{ODNP}} + \left| \left(-\frac{\sqrt{n^{\text{thermal}}}}{\sqrt{n^{\text{ODNP}}}} \cdot \frac{I^{\text{ODNP}}}{(I^{\text{thermal, scaled}})^2} \right) \right| \cdot \Delta I^{\text{thermal}}$$

(35)

Inversion recovery experiments were performed to determine the spin-lattice relaxation time $T_{1,\,^1\text{H}}$ of the ^{1}H nuclei for each mixture. The experiments were carried out with the standard operating software Spinsolve of the benchtop NMR spectrometer in NMR sample tubes with an inner diameter of 5 mm (Magritek) and were repeated 3 times.

Furthermore, the relative deviations of the data points from the calibration curve are calculated according to Equation (36).

$$\Delta_{\text{rel}} = \frac{f\left(x_{\text{ACN}}^{\text{ref}}\right) - x_{\text{ACN}}^{\text{ODNP}}}{x_{\text{ACN}}^{\text{ODNP}}} \cdot 100\%$$

(36)

E.2 Results and Discussion

E.2.1 System 1: Acetonitrile (ACN) + Water (W)

In Figure A.25, the obtained signal integrals of ACN and W of System 1, which are acquired with the ^{1}H NMR ODNP experiment, are shown as a function of the composition. The corresponding signal enhancements are displayed in Figure A.26. The relative deviations of the data points from the calibration curve are shown in Figure A.27. Table A.25 provides the numerical values for the signal integrals and the uncorrected mole fractions x_i^{ODNP} acquired with the ^{1}H NMR ODNP experiment as well as the spin-lattice relaxation time $T_{1,\,^1\text{H}}$ of ACN and W in the mixtures.
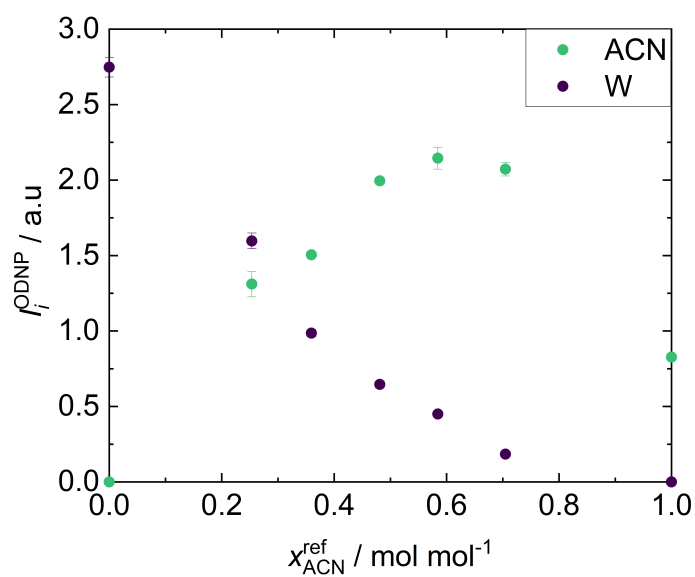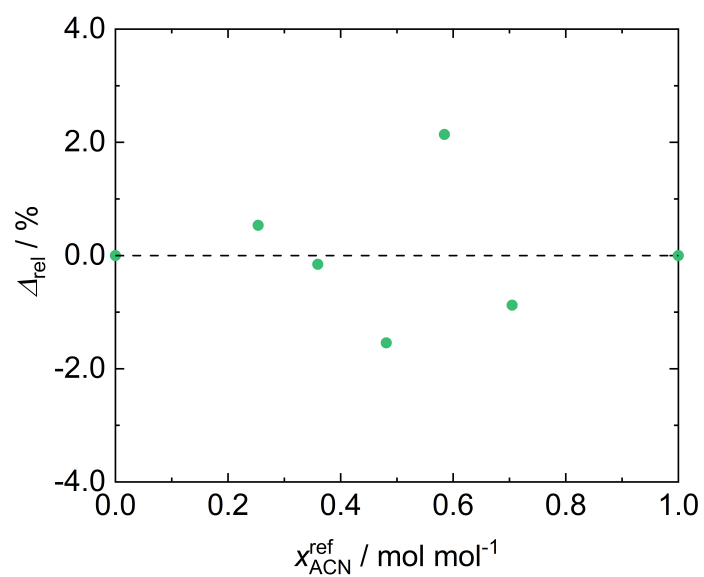
Figure A.25: Signal integrals of ACN and W of System 1 as a function of the mixtures's composition acquired with the ^{1}H NMR ODNP experiment.
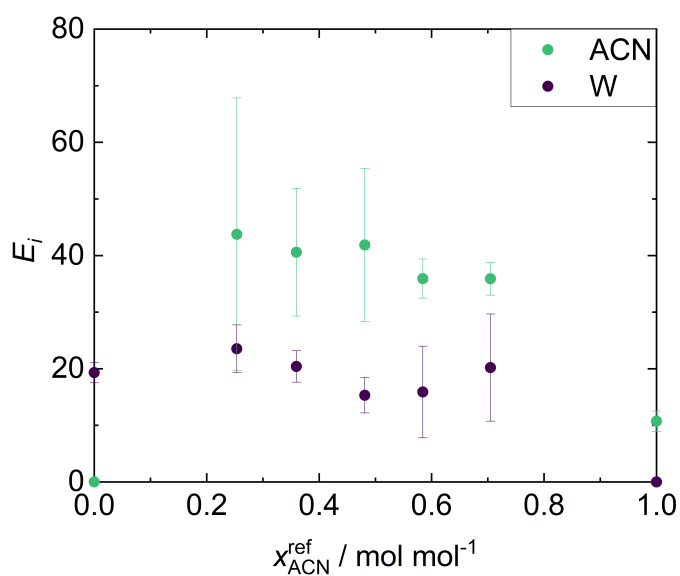
Figure A.26: Signal enhancements of ACN and W of System 1 as a function of the mixtures's composition acquired with the ^{1}H NMR ODNP experiment.

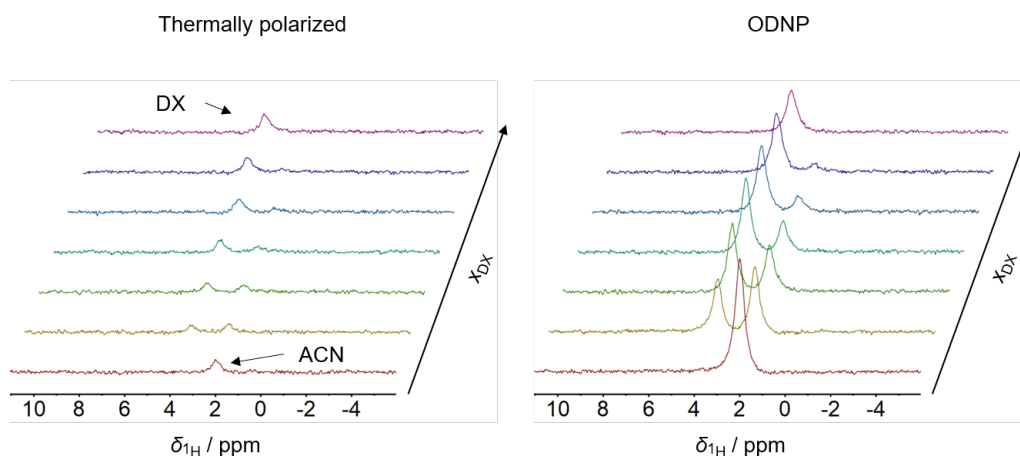**Figure A.27:** Relative deviations of the data points obtained with the ^{1}H NMR ODNP experiment from the calibration curve of System 1: ACN + W.

Table A.25: Signal integrals I^{ODNP} of ACN and W of System 1 acquired with the ^{1}H NMR ODNP experiment, the signal enhancements E^{1H} and the uncorrected mole fraction x_i^{ODNP} in dependence of the composition. Spin-lattice relaxation time $T_{1,\,^1H}$ at a magnetic field strength of 1 T of selected mixtures are given. The ^{1}H NMR ODNP experiments were repeated 5 times; $T_{1,\,^1H}$ were obtained with 3 repetitions. Standard uncertainties and errors are given, respectively.

| Mixture	ACN				W		
x_{ACN} / mol mol^{-1}	I^{ODNP} / a.u.	E^{1H}	x^{ODNP} / mol mol^{-1}	$T_{1,\,^1H}$ / s	I^{ODNP} / a.u.	E^{1H}	$T_{1,\,^1H}$ / s
0	-	-	0	-	2.75±0.07	19.3±1.8	3.10±0.05
0.254	1.31±0.08	43.8±24.1	0.354±0.016	4.81±0.03	1.60±0.05	23.5±4.2	2.99±0.01
0.359	1.50±0.01	40.6±11.3	0.504±0.006	-	0.99±0.02	20.4±2.8	-
0.481	1.99±0.02	41.9±13.5	0.673±0.008	4.47±0.02	0.65±0.02	15.3±3.1	3.10±0.01
0.584	2.14±0.07	35.9±3.5	0.760±0.012	-	0.45±0.02	15.9±8.1	-
0.705	2.07±0.05	35.9±2.9	0.882±0.005	4.27±0.01	0.18±0.01	20.2±9.5	3.33±0.02
1	0.83±0.02	10.7±1.8	1	3.99±0.01	-	-	-

E.2.2 System 2: Acetonitrile (ACN) + 1,4-Dioxane (DX)

Figure A.28 displays the ^{1}H NMR spectra of the different studied mixtures of System 2: ACN + DX obtained by the ^{1}H NMR and ^{1}H NMR ODNP experiments in continuous-flow. Two singlet peaks can be identified that are assigned to ACN and DX. By switching on the MW and performing the ^{1}H NMR ODNP experiment, a significant improvement in the SNR is achieved. The average signal enhancements are $E_{\text{ACN}}^{^1\text{H}}$ = 6 for ACN and $E_{\text{DX}}^{^1\text{H}}$ = 6 for DX for System 2.

Figure A.28: ^{1}H NMR spectra of System 2: ACN + DX for mixtures with different composition acquired with a single scan in continuous-flow (flow velocity v = 0.34 m s^{-1}). Left: thermal experiments. Right: ODNP experiments.
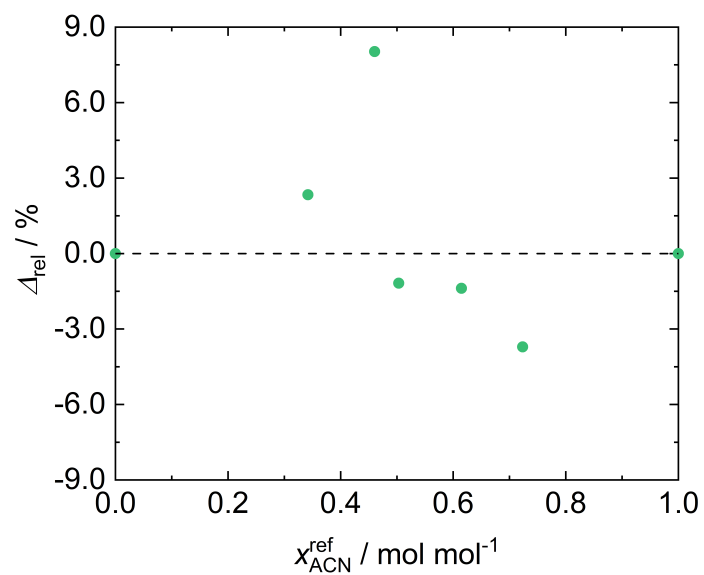
In Figure A.29, the obtained signal integrals of ACN and DX of System 2, which are acquired with the ^{1}H NMR ODNP experiment, are shown as a function of the composition. The corresponding signal enhancements are displayed in Figure A.30. The relative deviations of the data points from the calibration curve are shown in Figure A.31. Table A.26 provides the numerical values for the signal integrals and the uncorrected mole fractions x_i^{ODNP} acquired with the ^{1}H NMR ODNP experiment as well as the spin-lattice relaxation time $T_{1,\,^1\text{H}}$ of ACN and DX in the mixtures.
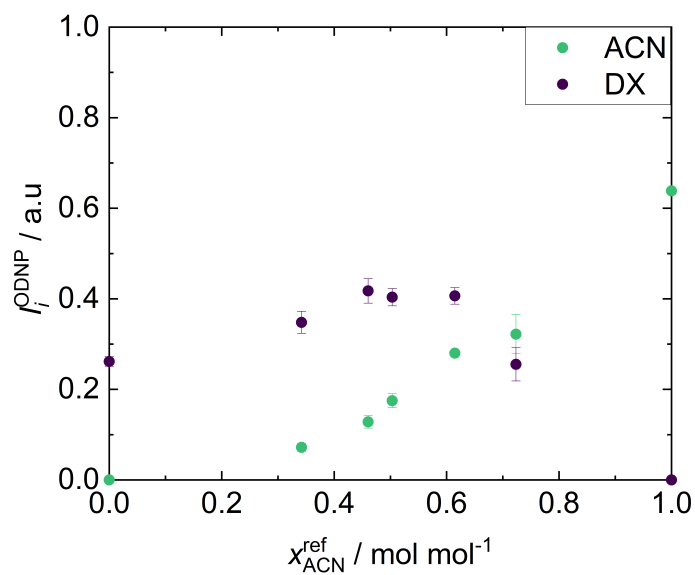
Figure A.29: Signal integrals of ACN and DX of System 2 as a function of the sample's composition acquired with the ^{1}H NMR ODNP experiment.
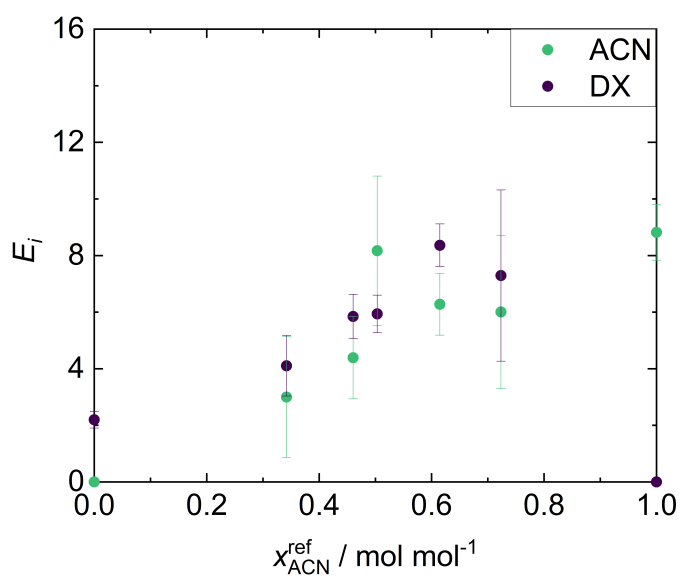
Figure A.30: Signal enhancements of ACN and DX of System 2 as a function of the sample's composition acquired with the ^{1}H NMR ODNP experiment.
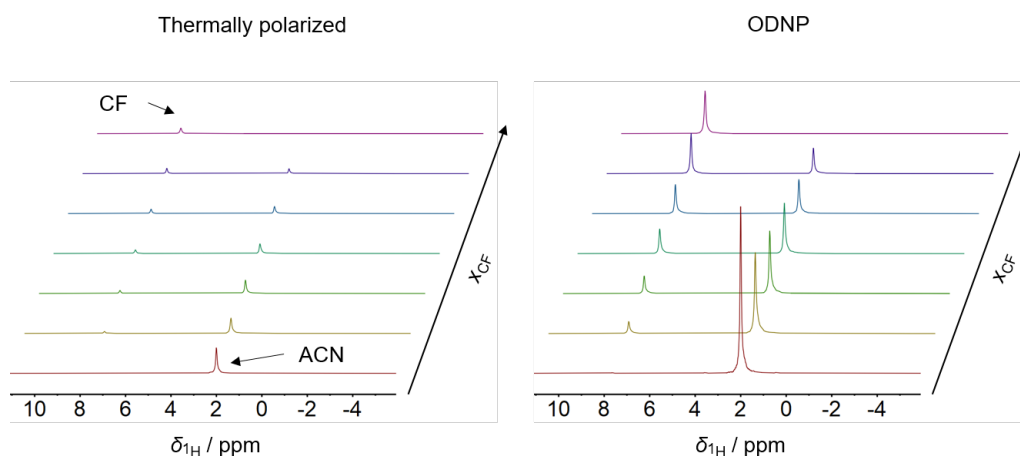
Figure A.31: Relative deviations of the data points obtained with the ^{1}H NMR ODNP experiment from the calibration curve of System 2: ACN + DX.

Table A.26: Measured signal integrals I^{ODNP} of ACN and DX, their signal enhancements E^{1H} and the uncorrected mole fraction x_i^{ODNP} as a function of the composition acquired with the ^{1}H NMR ODNP experiment. Spin-lattice relaxation time $T_{1,\,^{1}H}$ at a magnetic field strength of 1 T of selected mixtures are additionally given. The ^{1}H NMR ODNP experiments were repeated 5 times; $T_{1,\,^{1}H}$ were obtained with 3 repetitions. Standard uncertainties and errors are given, respectively.

| Mixture	ACN				DX		
x_{ACN} / mol mol^{-1}	I^{ODNP} / a.u.	E^{1H}	x^{ODNP} / mol mol^{-1}	$T_{1,\,^{1}H}$ / s	I^{ODNP} / a.u.	E^{1H}	$T_{1,\,^{1}H}$ / s
0	-	-	0	-	0.26±0.01	2.2±0.3	3.58±0.01
0.342	0.07±0.01	3.0±2.1	0.355±0.017	3.16±0.01	0.35±0.02	4.1±1.1	2.87±0.01
0.461	0.13±0.01	4.4±1.5	0.450±0.037	-	0.42±0.03	5.8±0.8	-
0.503	0.17±0.01	8.2±2.6	0.535±0.018	3.38±0.01	0.40±0.02	5.9±0.7	3.12±0.01
0.615	0.28±0.01	6.3±1.1	0.648±0.014	-	0.41±0.02	8.4±0.8	-
0.724	0.32±0.04	6.0±2.7	0.771±0.007	3.61±0.01	0.26±0.04	7.3±3.0	3.38±0.02
1	0.64±0.01	8.8±1.0	1	3.99±0.01	-	-	-

E.2.3 System 3: Acetonitrile (ACN) + Chloroform (CF)

Figure A.32 displays the ^{1}H NMR spectra of the different studied mixtures of System 3: ACN + CF obtained by the ^{1}H NMR and ^{1}H NMR ODNP experiments in continuous-flow. Two singlet peaks can be identified that are assigned to ACN and CF. By switching on the MW and performing the ^{1}H NMR ODNP experiment, a significant improvement in the SNR is achieved. The average signal enhancements are $E_{\mathrm{ACN}}^{^1\mathrm{H}}$ = 5 for ACN and $E_{\mathrm{DX}}^{^1\mathrm{H}}$ = 7 for CF for System 3.


Figure A.32: ^{1}H NMR spectra of System 3: ACN + CF for mixtures with different composition acquired with a single scan in continuous-flow (flow velocity $v = 2.38$ m s^{-1}). Left: thermal experiments. Right: ODNP experiments.

In Figure A.33, the obtained signal integrals of ACN and CF, which are acquired with the ^{1}H NMR ODNP experiment, are shown as a function of the composition. The corresponding signal enhancements are displayed in Figure A.34. The relative deviations of the data points from the calibration curve are shown in Figure A.35. Table A.27 provides the numerical values for the signal integrals and the uncorrected mole fractions x_i^{ODNP} acquired with the ^{1}H NMR ODNP experiment as well as the spin-lattice relaxation time $T_{1,\,^1\mathrm{H}}$ of ACN and CF in the mixtures.
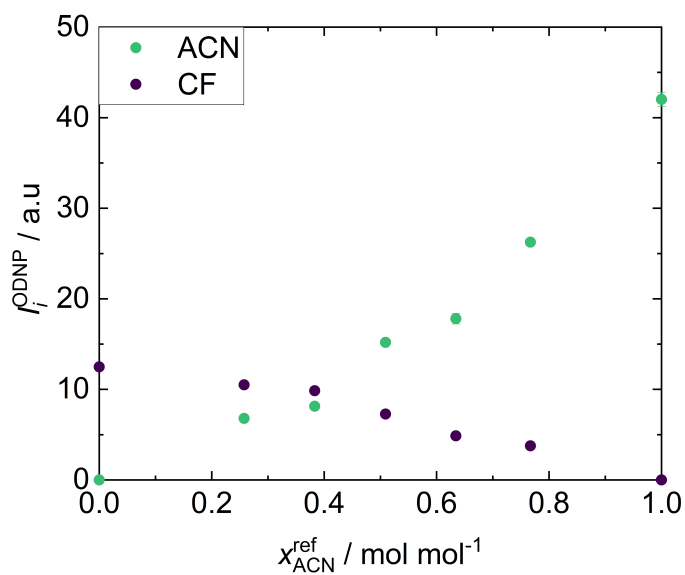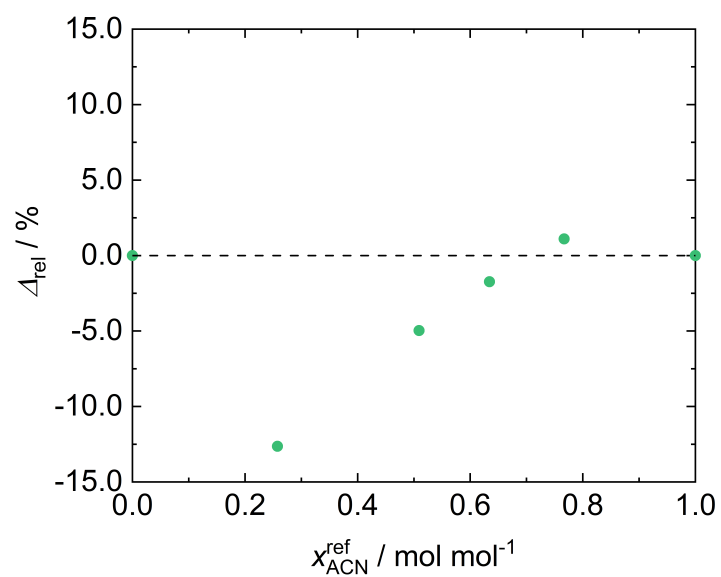
Figure A.33: Signal integrals of ACN and CF of System 3 as a function of the sample's composition acquired with the ^{1}H NMR ODNP experiment.
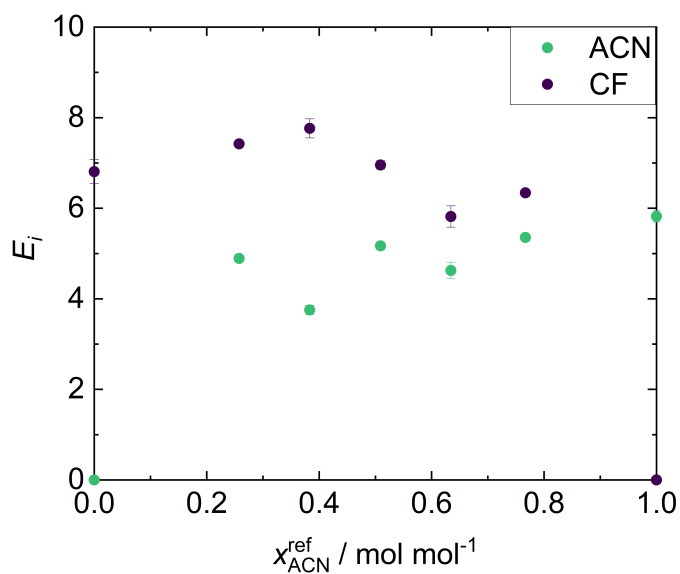
Figure A.34: Signal enhancements of ACN and CF of System 3 as a function of the sample's composition acquired with the ^{1}H NMR ODNP experiment.
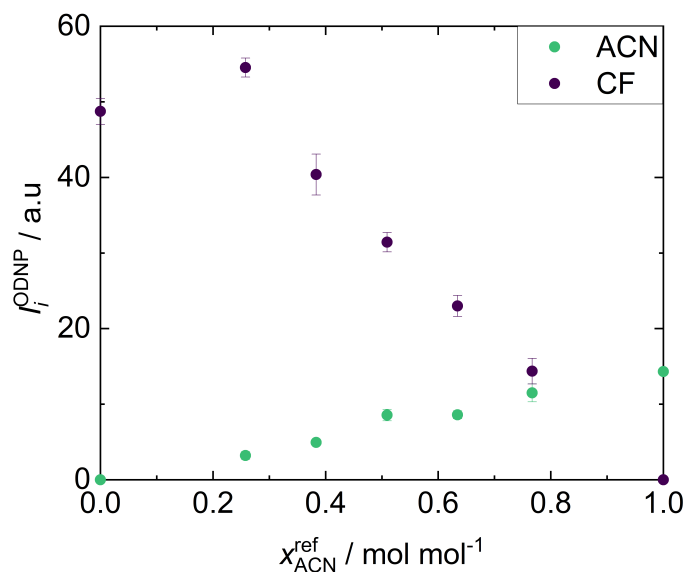
Figure A.35: Relative deviations of the data points obtained with the ^{1}H NMR ODNP experiment from the calibration curve of System 3: ACN + CF.
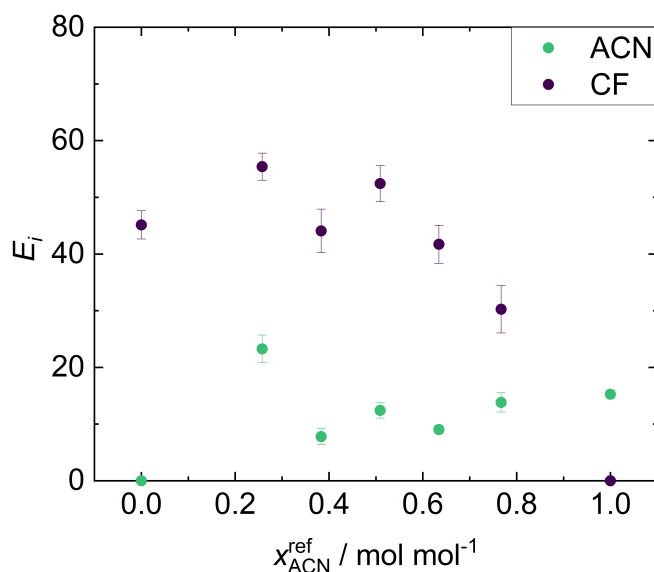
Table A.27: Measured signal integrals I^{ODNP} of ACN and CF, their signal enhancements $E^{1\text{H}}$ and the uncorrected mole fraction x_i^{ODNP} as a function of the composition acquired with the ^{1}H NMR ODNP experiment. Spin-lattice relaxation time $T_{1,\,^1\text{H}}$ at a magnetic field strength of 1 T of selected mixtures are additionally given. The ^{1}H NMR ODNP experiments were repeated 5 times; $T_{1,\,^1\text{H}}$ were obtained with 3 repetitions. Standard uncertainties and errors are given, respectively.

| Mixture	ACN				CF		
x_{ACN} /	I^{ODNP} /	$E^{1\text{H}}$	x^{ODNP} /	$T_{1,\,^1\text{H}}$ /	I^{ODNP} /	$E^{1\text{H}}$	$T_{1,\,^1\text{H}}$ /
mol mol^{-1}	a.u.		mol mol^{-1}	s	a.u.		s
0	-	-	0	-	12.49±0.31	6.8±0.3	5.25±0.06
0.258	6.79±0.06	4.9±0.1	0.177±0.001	3.59±0.05	10.51±0.08	7.4±0.1	4.41±0.04
0.383	8.13±0.41	3.8±0.1	0.216±0.001	-	9.84±0.34	7.8±0.2	-
0.509	15.18±0.16	5.2±0.1	0.410±0.001	3.23±0.05	7.27±0.07	7.0±0.1	4.03±0.04
0.634	17.81±0.88	4.6±0.2	0.549±0.001	-	4.87±0.24	5.8±0.2	-
0.767	26.26±0.26	5.4±0.1	0.699±0.001	3.58±0.05	3.77±0.03	6.3±0.1	4.41±0.04
1	42.01±0.79	5.8±0.1	1	3.99±0.01	-	-	-

In Figure A.36, the obtained signal integrals of ACN and CF, which are acquired with the ^{13}C NMR ODNP experiment, are shown as a function of the composition. The corresponding signal enhancements are displayed in Figure A.37. The relative deviations of the data points from the calibration curve are shown in Figure A.38. Table A.27 provides the numerical values of the signal integrals and the uncorrected mole fractions x_i^{ODNP} acquired with the ^{13}C NMR ODNP experiment.

Figure A.36: Signal integrals of ACN and CF of System 3 as a function of the mixtures's composition acquired with the ^{13}C NMR ODNP experiment.

Figure A.37: Signal enhancements of ACN and CF of System 3 as a function of the mixtures's composition acquired with the ^{13}C NMR ODNP experiment.
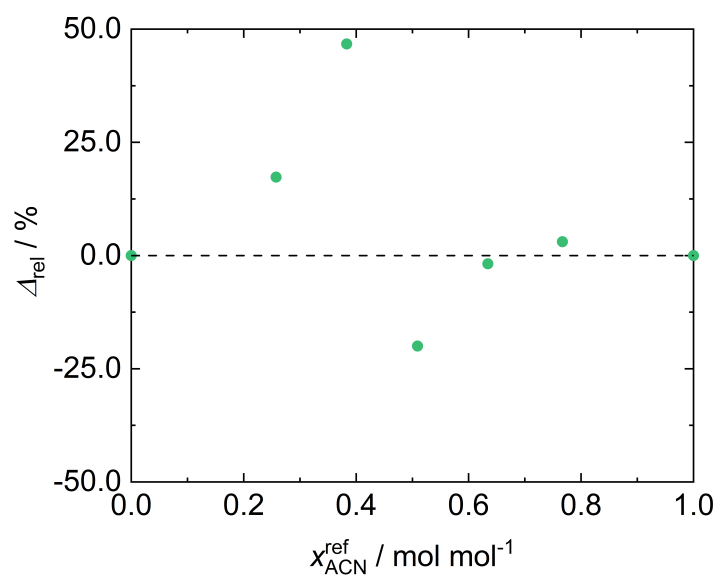
Figure A.38: Relative deviations of the data points obtained with the ^{13}C NMR ODNP experiment from the calibration curve of System 3: ACN + CF.

Table A.28: Measured signal integrals I^{ODNP} of ACN and CF, their signal enhancements E^{13C} and the uncorrected mole fraction x_i^{ODNP} as a function of the composition acquired with the ^{13}C NMR ODNP experiment. The ^{13}C NMR ODNP experiments were repeated 3 times. Standard uncertainties and errors are given, respectively.

Mixture	ACN			CF	
x_{ACN} / mol mol^{-1}	I^{ODNP} / a.u.	E^{13C}	x^{ODNP} / mol mol^{-1}	I^{ODNP} / a.u.	E^{13C}
0	-	-	0	48.74±1.71	45.1±2.5
0.258	3.21±0.52	23.3±2.4	0.074±0.009	54.53±1.25	55.4±2.4
0.383	4.95±0.42	7.8±1.4	0.083±0.005	40.38±2.71	44.1±3.8
0.509	8.56±0.76	12.4±1.4	0.214±0.014	31.43±1.28	52.4±3.2
0.634	8.59±0.52	9.0±0.7	0.272±0.006	23.00±1.39	41.7±3.4
0.767	11.50±1.19	13.8±1.7	0.445±0.041	14.37±1.70	30.2±4.2
1	14.32±0.35	15.3±0.7	1	-	-

Declaration

This dissertation contains material that has been published previously or that is included in submitted publications. In the following, these publications are listed together with a statement on the contributions of the author of the present dissertation.

- J. Phuong, S. Mross, D. Bellaire,. H. Hasse, K. Münnemann: Determination of self-diffusion coefficients in mixtures with benchtop ^{13}C NMR spectroscopy via polarization transfer, Magnetic Resonance in Chemistry 62, 5 (2024) 386-397, DOI: 10.1002/mrc.5412.

  The author developed the NMR pulse sequence together with Daniel Bellaire and carried out the corresponding benchtop NMR spectroscopy experiments. The experiments conducted on the high-field NMR spectrometer were carried out by Sarah Mross. The author evaluated the results. The author wrote the manuscript.

- J. Phuong, Z. Romero, H. Hasse, K. Münnemann: Polarization transfer methods for quantitative analysis of flowing mixtures with benchtop ^{13}C NMR spectroscopy, Magnetic Resonance in Chemistry 62, 5 (2024) 398-411, DOI: 10.1002/mrc.5417.

  The author implemented the NMR pulse sequence, carried out and supervised the experiments together with Zeno Romero. The author evaluated the results. The author wrote the manuscript.

- J. Phuong, B. Salgado, T. Labusch, H. Hasse, K. Münnemann: Overhauser Dynamic Nuclear Polarization Enables Single Scan Benchtop ^{13}C NMR Spectroscopy in Continuous-Flow, *submitted to Analytical Chemistry* (2024).

  The author carried out and supervised the experiments together with Billy Salgado and Tom Labusch. The author evaluated the results. The author wrote the manuscript.

- J. Phuong, B. Salgado, J. Heiß, E. Steimers, P. Nickolaus, L. Keller, U. Fischer, E. von Harbou, D. J. Holland, F. Jirasek, H. Hasse, K. Münnemann: Online Monitoring of Fermentation Processes in Wine Production with Benchtop ^{1}H NMR Spectroscopy, *to be submitted to Food Research International* (2024).

The author carried out and supervised the experiments. The postprocessing of the data was done by Billy Salgado. The author evaluated the results. The author wrote the manuscript.

- J. Phuong, R. Kircher, S. Mross, B. Salgado, H. Hasse, K. Münnemann: Quantitative NMR Spectroscopy with Overhauser Dynamic Nuclear Polarization, *to be submitted to Angewandte Chemie* (2024).

The author carried out and supervised the experiments together with Raphael Kircher. The implementation of the calibration function and the fitting routine were done by the author. The author evaluated the results. The author wrote the manuscript.

Student Theses

The following student theses were prepared under the supervision of the author of the present doctoral thesis in the frame of his research:

- Z. Romero: Application of polarisation transfer methods for process monitoring with medium-field ^{13}C NMR-spectroscopy. Student thesis, Laboratory of Engineering Thermodynamics (LTD), TU Kaiserslautern (2021).

- B. Salgado: Comissioning of a new DNP probe head. Student thesis, Laboratory of Engineering Thermodynamics (LTD), TU Kaiserslautern (2022).

- A. Müller: Application of polarisation transfer methods for quantification of multi-component-mixtures with benchtop ^{13}C NMR-spectroscopy. Student thesis, Laboratory of Engineering Thermodynamics (LTD), TU Kaiserslautern (2022).

- T. Labusch: Systematic investigation of ^{1}H and ^{13}C NMR signal enhancement using ODNP hyperpolarisation techniques in continuous flow. Master thesis, Laboratory of Engineering Thermodynamics (LTD), RPTU Kaiserslautern (2024).

Curriculum Vitae

Name:	Johnnie The Phuong
Place of birth:	Ludwigshafen am Rhein
Nationality:	German

Education

2001 – 2005	Elementary school in Ludwigshafen am Rhein
2005 – 2013	Carl-Bosch-Gymnasium in Ludwigshafen am Rhein
	Degree: Allgemeine Hochschulreife
2013 – 2017	Bachelor studies at TU Kaiserslautern
	Program: Biochemical and Chemical Engineering
	Degree: Bachelor of Science
2017 – 2019	Master studies at TU Kaiserslautern
	Program: Biochemical and Chemical Engineering
	Degree: Master of Science

Professional

11/2019 – 09/2024	Research Associate
	Laboratory of Engineering Thermodynamics
	RPTU Kaiserslautern
	Prof. Dr.-Ing. Hans Hasse
since 11/2024	Research Engineer
	BASF SE, Ludwigshafen am Rhein